

## ABSTRACT

BAUCOM, JARED NEWTON. Initiation and Evolution of Dynamic Failure Mechanisms in Woven Composite Systems. (Under direction of Professor M. A. Zikry)

The unique reinforcement geometry of three-dimensional orthogonally woven fabric-reinforced composites offers the potential of significantly improved penetration resistance and damage tolerance, in comparison with other composite systems, for a myriad of civilian and military applications at different velocity regimes. However, there has been a lack of understanding and quantification of how energy dissipation, momentum, and failure modes are affected by fiber orientation and distribution, as well as by loading rates that span the quasi-static to the high-velocity regimes. The major objective of this experimental investigation is to obtain a detailed understanding and characterization of damage progression in woven composite panels under transverse impact at three different velocity regimes: quasi-static (10-80  $\mu\text{m/s}$ ), low velocity (1-5 m/s), and high velocity (200-500 m/s). The broad classes of glass-fiber-reinforced composite systems that were investigated included two-dimensional plain woven laminates, three-dimensional orthogonally woven monoliths, and three-dimensional orthogonally woven laminates. The unique fabric structure of the three-dimensional orthogonal weave has also been utilized with a recently developed matrix-cellularization processing technique and to investigate how pore formation can be tailored for enhanced energy absorption and crack deflection of carbon-fiber-reinforced cellular-matrix-epoxy composites for quasi-static three-point bending and ballistic impact loading conditions.

At the quasi-static regime, normal perforation experiments were conducted, and the puncture load was monitored to provide load history and energy dissipation. The deformation and failure history was also recorded by backlit videography, which allowed

a novel method to monitor internal damage initiation and progression. The three-dimensional laminates were found to require a higher maximum punch force and absorbed more energy than the two-dimensional laminates and three-dimensional monolithic woven systems.

Low-velocity impact damage progression was investigated by the use of an instrumented drop-weight impactor. Measurements were obtained for impact force and energy dissipation for repeated strikes. The radial spread of damage was smallest for the two-dimensional laminates and largest for the three-dimensional woven composites. The three-dimensional composites had the greatest resistance to penetration and dissipated more total energy than the other systems.

A powder gun was used for the high-velocity experiments to determine energy absorption, to provide approximate ballistic limit, and to identify and characterize failure modes of two-dimensional and three-dimensional composite systems subjected to ballistic impact. The energy absorption was comparable for the two-dimensional and three-dimensional woven composite systems. However, the damage was much more localized for the two-dimensional woven system, which suggests that this system may be more damage-tolerant than the three-dimensional woven systems but less resistant to perforation than the three-dimensional laminate.

The flexural strength, impact response, and perforation resistance of three-dimensional orthogonally woven cellular carbon-fiber-reinforced epoxy panels were also investigated. These cellular composites have lower areal densities, and as the experimental results indicate, an increase in specific energy absorption, in comparison with three-dimensionally woven resin-matrix composites.

The results of this investigation indicate that, for the three different velocity regimes, the three-dimensional laminates consistently had greater damage tolerance than the two-dimensional laminates and the three-dimensional monolithic composites. This damage tolerance is due to unique energy absorption mechanisms, which involve the crimped portion of *z*-tows in the three-dimensional composites. This implies that failure can be controlled by manipulation of the properties of the *z*-tows. It also indicates that the surface condition of three-dimensional orthogonally woven composites can strongly affect the progression of impact-induced damage. This is significant, since three-dimensional architectures can provide both an inherent capability to dissipate energy over a large radial area and a greater perforation strength than comparable two-dimensional laminate and three-dimensional monolithic composite systems.

**INITIATION AND EVOLUTION OF DYNAMIC FAILURE  
MECHANISMS IN WOVEN COMPOSITE SYSTEMS**

by

**JARED NEWTON BAUCOM**

A thesis submitted to the Graduate Faculty of  
North Carolina State University  
In partial fulfillment of the Degree of  
Doctor of Philosophy

**MECHANICAL ENGINEERING**

Raleigh

2002

APPROVED BY:

\_\_\_\_\_  
\_\_\_\_\_  
\_\_\_\_\_

\_\_\_\_\_  
Chair of Advisory Committee

## **ABOUT THE AUTHOR**

At the time of this writing, the author has been a student for approximately eighty-eight percent of his life. Although this volume may represent a closure of the formal portion of his education, he intends to remain a student, at least in heart.

## ACKNOWLEDGEMENTS

The ideas and assistance of colleagues are greatly appreciated. Many people deserve mention, but two stand out above the rest: Dr. Waeil Ashmawi and Rolin Barrett, Jr., P.E. Dr. Ashmawi has been an endless source of encouragement and advice. Mr. Barrett has contributed an extensive knowledge of interior and exterior ballistics, many insights into electrical circuit design, and photographic expertise.

Dr. Wei Xu provided the samples, 3-point bending data, photographs and SEM micrographs of the carbon/epoxy composites. The E-glass and S2-glass composite systems were provided on behalf of 3TEX by Dr. James Singletary. His cooperative concern to provide materials meeting the requirements of this work is deeply appreciated.

The efficient assistance of Roberto Garcia and Rich Fiore of the NCSU Analytical Instrumentation Facility is gratefully acknowledged. Their help with sample preparation and ESEM operation both accelerated and economized the micrographic characterization. The staff of the MAE Machine Shop (Rufus ‘Skip’ Richardson and Mike Breedlove) is greatly appreciated for its skill and experience. They produced all of the projectiles, most of the newly designed machine elements, and occasionally dissected material samples.

The Advisory Committee Chair, Dr. Mohammed Zikry, has been an invaluable resource in the author’s pursuit of research and career goals. The author is also gratefully appreciative of the advice, time, and patience of the other members of his Advisory Committee: Drs. John Bailey, Harvey Charlton, Eric Klang, and Yiping Qiu.

This work was supported under ARO MURI, DAAH-04-96-0018 for Functionally Tailored Textile Systems. That support is gratefully acknowledged.

The most important contributors to this work are the members of the author's extended and immediate family, father and mother, and especially his wife, Maria. Without their moral and financial support this report would never have been written.

# TABLE OF CONTENTS

LIST OF TABLES.....	viii
LIST OF FIGURES.....	ix
1. INTRODUCTION .....	1
1.1 3D Cellular-Matrix Composite Systems.....	3
1.2 Quasi-Static Perforation of 2D and 3D Composite Systems .....	5
1.3 Low-Velocity Impact Damage Progression.....	6
1.4 High-Velocity Impact and Perforation.....	7
2. 3D CELLULAR-MATRIX COMPOSITE SYSTEMS.....	9
2.1 Material Preparation and Fabrication.....	9
2.2 Experimental Procedures .....	11
2.2.1 Quasi-Static Three-Point Bending Experiments.....	11
2.2.2 Dynamic Experiments.....	12
2.3 Results and Discussion .....	14
2.3.1 Quasi-Static Results .....	14
2.3.2 Dynamic Results .....	15
2.4 Conclusions.....	17
2.5 Figures (Chapter 2) .....	20

3. QUASI-STATIC PERFORATION OF 2D AND 3D COMPOSITE SYSTEMS .....	31
3.1 Material Preparation and Fabrication.....	32
3.1.1 Fabric Architectures.....	32
3.1.2 Constituent Materials.....	33
3.2 Experimental Procedures .....	34
3.3 Results and Discussion. ....	35
3.4 Conclusions.....	42
3.5 Figures (Chapter 3) .....	43
4. LOW-VELOCITY IMPACT DAMAGE PROGRESSION.....	76
4.1 Material Preparation and Fabrication.....	76
4.1.1 E-Glass Systems.....	76
4.1.2 S2-Glass Systems.....	78
4.2 Experimental Procedures .....	79
4.3 Results and Discussion: E-Glass Systems .....	82
4.4 Results and Discussion: S2-Glass Systems.....	86
4.5 Conclusions.....	89
4.5 Figures (Chapter 4) .....	91
5. HIGH-VELOCITY IMPACT AND PERFORATION.....	118
5.1 Material Preparation and Fabrication.....	118
5.2 Experimental Procedures .....	120
5.3 Results and Discussion. ....	121

5.4 Conclusions.....	125
5.5 Figures (Chapter 5).....	127
6. SUMMARY .....	146
6.1 Failure Mechanisms .....	146
6.2 Energy Dissipation.....	147
6.3 Damage Progression .....	147
6.4 Conclusion .....	148
6.5 Figures (Chapter 6).....	151
7. RECOMMENDATIONS FOR FUTURE STUDIES .....	153
8. LIST OF REFERENCES .....	154

## LIST OF TABLES

Table 2.1	Carbon-Fiber/Epoxy Cellular- and Resin-Matrix Composite Systems .....	11
Table 2.2	Three-Point Bending, Average Results.....	17
Table 3.1	S2-Glass/Rubber-Toughened-Epoxy-Vinyl-Ester Composites Systems for Quasi-Static Puncture.....	34
Table 3.2	Post-Contact Penetrator Displacement at Transition Points of Quasi-Static Load-Displacement Curves, Corresponding to Captured Frames from Digital Video .....	37
Table 3.3	Peak Force and Work of Perforation, Average Values for Each Material System .....	38
Table 4.1	E-Glass/Vinyl-Ester Composite Systems for Low-Velocity Impact and Perforation.....	77
Table 4.2	S2-Glass/Rubber-Toughened-Epoxy-Vinyl-Ester Composite Systems for Low-Velocity Impact and Perforation .....	78
Table 5.1	S2-Glass/Rubber-Toughened-Epoxy-Vinyl-Ester Composite Systems for High-Velocity Impact and Perforation .....	120
Table 5.2	Striking Velocity, Residual Velocity, and Energy Dissipation .....	122

## LIST OF FIGURES

Figure 2.1	Three-Dimensional Orthogonal Weave .....	21
Figure 2.2	Resin-Matrix Composite .....	22
Figure 2.3	Cellular Matrix Composite .....	22
Figure 2.4	19-mm Powder-Charge Accelerator .....	23
Figure 2.5	Flat-Nose Steel 19-mm Projectile (77.8 g) .....	23
Figure 2.6	Measurement of Impact Velocity by Velocity-Pin Switches.....	24
Figure 2.7	Measurement of Residual Velocity by Coil-Type Inductors .....	24
Figure 2.8	Target Holder for 19-mm Accelerator .....	25
Figure 2.9	Three-Point Bend for Resin-Matrix Composites .....	26
Figure 2.10	Three-Point Bend for Cellular-Matrix Composites .....	26
Figure 2.11	Post-Perforation Photographs: Left - Resin-Matrix Composite (Rear Face), Right - Cellular-Matrix Composite (Impacted Face) .....	27
Figure 2.12	Perforated Resin-Matrix Composite .....	28
Figure 2.13	Perforated Cellular Matrix Composite.....	28
Figure 2.14	Absorbed Energy: Fiber Volume (f) and Porosity Effects.....	29
Figure 2.15	Normalized Energy Absorption .....	29
Figure 2.16	Absorbed Energy as a Function of Areal Density .....	30
Figure 3.1	Thin S2-Glass Fabric Architectures: (a) 4-Ply 2D Laminate (2D-S-24x4, 3.25 kg/m <sup>2</sup> ), (b) 3D Orthogonally Woven Monolith (3D-S-93, 3.15 kg/m <sup>2</sup> ).....	44

Figure 3.2	Thick S2-Glass Fabric Architectures: (a) 12-Ply 2D Laminate ( <i>2D-S-24x12</i> , 9.77 kg/m <sup>2</sup> ), (b) 3-Ply Laminate ( <i>3D-S-93x3</i> , 9.46 kg/m <sup>2</sup> ) of 3D Orthogonally Woven Monoliths (c) 3D Orthogonally Woven Monolith ( <i>3D-S-270</i> , 9.15 kg/m <sup>2</sup> ).....	44
Figure 3.3	Displacement-Controlled Quasi-Static Transverse Puncture (INSTRON 4400R).....	45
Figure 3.4	Perforator for Quasi-Static Puncture.....	46
Figure 3.5	Target Fixture for Quasi-Static Puncture.....	47
Figure 3.6	Perforating Load as a Function of Tup Displacement .....	48
Figure 3.7	Perforating Load-Displacement for Thin 2D Laminates ( <i>2D-S-24x4</i> ) and 3D Monoliths ( <i>3D-S-93</i> ) at Two Rates of Loading: 10 and 80 μm/s .....	49
Figure 3.8	Perforating Load-Displacement for Thick 2D Laminates ( <i>2D-S-24x12</i> ) at Two Rates of Loading: 40 and 80 μm/s.....	50
Figure 3.9	Perforating Load-Displacement for Thick 3D Monoliths ( <i>3D-S-270</i> ) at Two Rates of Loading: 40 and 80 μm/s.....	51
Figure 3.10	Perforating Load-Displacement for Thick 3-Ply 3D Laminates ( <i>3D-S-93x3</i> ) at Two Rates of Loading: 40 and 80 μm/s .....	52
Figure 3.11	Stages of Quasi-Static Punch Loading and Perforation Failure .....	53
Figure 3.12	Representative Video Frames Captured during Quasi-Static Perforation of <i>2D-S-24x12-2</i> , Near Transition Points .....	54
Figure 3.13	Representative Video Frames Captured during Quasi-Static Perforation of <i>3D-S-270-3</i> , Near Transition Points .....	55
Figure 3.14	Representative Video Frames Captured during Quasi-Static Perforation of <i>3D-S-93x3-3</i> , Near Transition Points .....	56
Figure 3.15	Work of Quasi-Static Perforation .....	57

Figure 3.16	Load-Displacement Behavior, Normalized by Target Areal Density .....	58
Figure 3.17	Work of Quasi-Static Perforation, Normalized by Target Areal Density .....	58
Figure 3.18	Post-Mortem Photographs of <i>2D-S-24x4-2</i> : (a) Front Face, (b) Rear Face, (c) Rear Face under Back-Lighting.....	59
Figure 3.19	Closer Views of Front Target Face ( <i>2D-S-24x4-2</i> ) .....	60
Figure 3.20	Closer Views of Rear Target Face ( <i>2D-S-24x4-2</i> ).....	61
Figure 3.21	Post-Mortem Photographs of <i>3D-S-93-1</i> : (a) Front Face, (b) Rear Face, (c) Rear Face under Back-Lighting.....	62
Figure 3.22	Closer Views of Front Target Face ( <i>3D-S-93-1</i> ) .....	63
Figure 3.23	Closer Views of Rear Target Face ( <i>3D-S-93-1</i> ) .....	64
Figure 3.24	Post-Mortem Photographs of <i>2D-S-24x12-1</i> : (a) Front Face, (b) Rear Face, (c) Rear Face under Back-Lighting .....	65
Figure 3.25	Closer Views of Front Target Face ( <i>2D-S-24x12-1</i> ).....	66
Figure 3.26	Closer Views of Rear Target Face ( <i>2D-S-24x12-1</i> ).....	67
Figure 3.27	Post-Mortem Photographs of <i>3D-S-270-2</i> : (a) Front Face, (b) Rear Face, (c) Rear Face under Back-Lighting.....	68
Figure 3.28	Closer Views of Front Target Face ( <i>3D-S-270-2</i> ) .....	69
Figure 3.29	Closer Views of Rear Target Face ( <i>3D-S-270-2</i> ) .....	70
Figure 3.30	Post-Mortem SEM ( <i>3D-S-270</i> ).....	71
Figure 3.31	Post-Mortem Photographs of <i>3D-S-93x3-2</i> : (a) Front Face, (b) Rear Face, (c) Rear Face under Back-Lighting.....	72
Figure 3.32	Closer Views of Front Target Face ( <i>3D-S-93x3-2</i> ).....	73
Figure 3.33	Closer Views of Rear Target Face ( <i>3D-S-93x3-2</i> ).....	74
Figure 3.34	Post-Mortem SEM ( <i>3D-S-93x3</i> ) .....	75

Figure 4.1	Surface Crimp of z-Tows in 3D Orthogonally Woven Preforms.....	92
Figure 4.2	Instrumented Drop-Weight Impactor.....	92
Figure 4.3	Representative Impactor Height History for E-Glass Composite Systems (Sample: <i>3D-E-96-1</i> ).....	93
Figure 4.4	Representative Impactor Acceleration History for E-Glass Composite Systems (Sample: <i>3D-E-96-1</i> ).....	93
Figure 4.5	Peak Impact Force of E-Glass Composite Systems as a Function of Strike Number .....	94
Figure 4.6	Energy Dissipation of E-Glass Composite Systems as a Function of Strike Number .....	94
Figure 4.7	Cumulative Energy Dissipation Resulting in Perforation of E-Glass Composite Systems .....	95
Figure 4.8	Post-Perforation Photographs of E-Glass Systems, Rear Target Faces: <i>2D-E-24x4</i> (Left), <i>BRWK</i> (Center), <i>3D-E-96</i> (Right).....	95
Figure 4.9	Post-Perforation Photographs of the 2D Plain Woven Laminate (Sample: <i>2D-E-24x4-1</i> ).....	96
Figure 4.10	Post-Perforation Photographs of the Biaxially Reinforced Warp-Knit (Sample: <i>BRWK-1</i> ) .....	96
Figure 4.11	Post-Perforation Photographs of the 3D Orthogonally Woven System (Sample: <i>3D-E-96-1</i> ).....	96
Figure 4.12	Representative Impactor Height History for S2-Glass Composite Systems (Sample: <i>2D-S-24x4-1</i> ) .....	97
Figure 4.13	Representative Impactor Acceleration History for S2-Glass Composite Systems (Sample: <i>2D-S-24x4-1</i> ) .....	97
Figure 4.14	Peak Impact Force of S2-Glass Composite Systems as a Function of Strike Number .....	98

Figure 4.15	Energy Dissipation of S2-Glass Composite Systems as a Function of Strike Number .....	98
Figure 4.16	Cumulative Energy Dissipation Resulting in Perforation of S2-Glass Composite Systems .....	99
Figure 4.17	Sub-Perforation (1 Strike) Photography of <i>2D-S-24x4-3</i> : (a) Front Face, (b) Rear Face, (c) Rear Face under Back-Lighting.....	100
Figure 4.18	Closer Views of Front Target Face ( <i>2D-S-24x4-3</i> ).....	101
Figure 4.19	Scanning Electron Micrographs Showing Surface Damage on Front Target Face near Impact Site ( <i>2D-S-24x4-3</i> ) .....	102
Figure 4.20	Closer Views of Rear Target Face ( <i>2D-S-24x4-3</i> ).....	103
Figure 4.21	Sub-Perforation (5 Strikes) Photography of <i>2D-S-24x4-4</i> : (a) Front Face, (b) Rear Face, (c) Rear Face, Oblique.....	104
Figure 4.22	Scanning Electron Micrographs Showing Surface Damage on Rear Target Face near Impact Site ( <i>2D-S-24x4-4</i> ) .....	105
Figure 4.23	Post-Perforation (23 Strikes) Photography of <i>2D-S-24x4-6</i> : (a) Front Face, (b) Rear Face, (c) Rear Face under Back-Lighting.....	106
Figure 4.24	Closer Views of Front Target Face ( <i>2D-S-24x4-6</i> ).....	107
Figure 4.25	Closer Views of Rear Target Face ( <i>2D-S-24x4-6</i> ).....	108
Figure 4.26	Sub-Perforation (1 Strike) Photography of <i>3D-S-93-3</i> : (a) Front Face, (b) Rear Face, (c) Rear Face under Back-Lighting.....	109
Figure 4.27	Closer Views of Front Target Face ( <i>3D-S-93-3</i> ) .....	110
Figure 4.28	Closer Views of Rear Target Face ( <i>3D-S-93-3</i> ) .....	111
Figure 4.29	Scanning Electron Micrographs Showing Surface Damage on Front Target Face near Impact Site ( <i>3D-S-93-3</i> ): Damaged z-Crimp (Top), Closer View of Left Edge (Middle), Close View of Central Region (Bottom) .....	112

Figure 4.30	Scanning Electron Micrographs Showing Internal Integrity near Impact Site (3D-S-93-3): (a) Sections of z-Tow and Weft Tows, (b) Sections of Warp and Weft Tows.....	113
Figure 4.31	Sub-Perforation (5 Strikes) Photography of 3D-S-93-4: (a) Front Face, (b) Rear Face, (c) Rear Face, Oblique.....	114
Figure 4.32	Post-Mortem Photography (39 Strikes) of 3D-S-93-7: (a) Front Face, (b) Rear Face, (c) Rear Face under Back-Lighting.....	115
Figure 4.33	Closer Views of Front Target Face (3D-S-93-7) .....	116
Figure 4.34	Closer Views of Rear Target Face (3D-S-93-7) .....	117
Figure 5.1	19-mm Hemispherical-Nose Steel Projectile, 55.6 g (design by Rolin F. Barrett, Jr.).....	128
Figure 5.2	Post-Mortem Photography of 3D-S-270-4 (154-m/s Striking Velocity): (a) Front Face, (b) Rear Face .....	129
Figure 5.3	Closer Views of Front Target Face (3D-S-270-4) .....	130
Figure 5.4	Post-Mortem SEM (3D-S-270-4).....	131
Figure 5.5	Post-Mortem Photography of 3D-S-270-5 (216-m/s Striking Velocity): (a) Front Face, (b) Rear Face .....	132
Figure 5.6	Oblique Views of 3D-S-270-5: (a) Front Face, (b) Rear Face.....	133
Figure 5.7	Closer Views of Rear Target Face (3D-S-270-5) .....	134
Figure 5.8	Post-Mortem Photography of 3D-S-270-6 (525-m/s Striking Velocity): (a) Front Face, (b) Rear Face, (c) Rear Face, Oblique .....	135
Figure 5.9	Post-Mortem Photography of 2D-S-24x12-4 (155-m/s Striking Velocity): (a) Front Face, (b) Rear Face, (c) Rear Face, Oblique .....	136
Figure 5.10	Post-Mortem Photography of 2D-S-24x12-5 (233-m/s Striking Velocity): (a) Front Face, (b) Rear Face, (c) Rear Face, Oblique .....	137

Figure 5.11	Post-Mortem Photography of <i>2D-S-24x12-6</i> (539-m/s Striking Velocity): (a) Front Face, (b) Rear Face, (c) Rear Face, Oblique .....	138
Figure 5.12	Post-Mortem Photography of <i>3D-S-93x3-4</i> (152-m/s Striking Velocity): (a) Front Face, (b) Rear Face, (c) Rear Face, Oblique .....	139
Figure 5.13	Post-Mortem Photography of <i>3D-S-93x3-5</i> (227-m/s Striking Velocity): (a) Front Face, (b) Rear Face .....	140
Figure 5.14	Oblique Views of <i>3D-S-93x3-5</i> : (a) Front Face, (b) Rear Face .....	141
Figure 5.15	Closer Views of Rear Target Face ( <i>3D-S-93x3-5</i> ) .....	142
Figure 5.16	Post-Mortem Photography of <i>3D-S-93x3-6</i> (508-m/s Striking Velocity): (a) Front Face, (b) Rear Face .....	143
Figure 5.17	Oblique Views of <i>3D-S-93x3-6</i> : (a) Front Face, (b) Rear Face, (c) Rear Face, Oblique .....	144
Figure 5.18	Closer View of Rear Target Face ( <i>3D-S-93x3-6</i> ) .....	145
Figure 6.1	Damage Mechanisms, Unique to 3D Orthogonally Woven Composites, Evident over a Wide Range of Penetration Velocities and for both 3D Monoliths and Laminates .....	152

## 1. INTRODUCTION

Advances in composite processing and fiber design have resulted in new applications for lightweight and high strength composite material systems (Seale *et al.* 1994; Cheremisinoff and Cheremisinoff 1995). Recently, fiber-reinforced systems have been found to be uniquely suited for use in certain smart material applications (Sirkis and Chang 1998; Anastasi and Lopatin 2001; Childers *et al.* 2001). General overviews of the current state of manufacturing and application of composite systems are available (Bogdanovich and Sierakowski 1999). As limits are reached in the specific strength and moduli of fibers and matrix materials, there is a need to understand how fabric *architectures* affect the behavior of composites such that optimal arrangements can be designed and utilized for specific applications. This investigation focuses on the characterization of damage initiation and progression in 2D and 3D composite panels subjected to transverse impact and perforation at various velocity regimes.

There are three basic configurations of reinforcement by continuous fibers: unidirectional reinforcement, two-dimensional fabrics, and three-dimensional fabrics (Cox and Flanagan 1997). Frequently, these basic architectures are stacked and then consolidated to form composite laminates. Laminates whose individual laminae are reinforced unidirectionally, so-called *uniweaves*, have been studied extensively and continue to be the subject of much investigation (Sun and Potti 1996; Schoeppner and Abrate 2000; Kim *et al.* 2001; Luo *et al.* 2001; Mili and Necib 2001; Mouritz 2001; Olsson 2001; Belingardi and Vadori 2002; Walker *et al.* 2002, accepted for publication).

Examples of the second basic construction, two-dimensional fabrics, exist in many forms (e.g., plain weave, satin weave, twill, 2D braid, *etc.*), but they share the common characteristic of fiber interlacing and undulation. These materials have also received much attention and continue to do so (O'Donnell 1993; Cunniff 1996; Davies *et al.* 1996; Chocron-Benloulou *et al.* 1997; Espinosa *et al.* 2000; Gellert *et al.* 2000; Azouaoui *et al.* 2001; Khan *et al.* 2001, accepted for publication). Examples of three-dimensional fabrics include stitched laminates, 3D orthogonal weaves, 3D braids, and angle-interlock weaves. Of the three basic architectures, 3D fabrics and composites have received the least attention (Cox 1995; Jenq and Mo 1996; Jenq *et al.* 1998; Kuo and Lee 1999; Singletary and Bogdanovich 2000; Xu 2000; Allix 2001; Qiu *et al.* 2001). In particular, the mechanisms of damage and energy transfer for these materials and their dependence upon striking velocity and energy have not been fully characterized. Moreover, little or no work has been done to examine the behavior of 3D laminates in comparison with 3D monolithic architectures.

The ultimate goal of this work is to provide new information about the behavior of fiber-reinforced composite materials under high rates of loading. It is hoped that the information will lead to the development of more efficient designs of structures and lightweight armor employing composite materials. The remainder of the first chapter includes an overview of the related work of other researchers, as well as a more detailed discussion of the specific objectives of each portion of this investigation.

## 1.1 3D Cellular-Matrix Composites

Macroporous polymeric materials are used in applications such as ion exchange, chromatographic separation, catalysis, and adsorption (Peters *et al.* 1997). However, porosity induced during the manufacture or repair of composite structures and components is generally viewed as a defect that can result in degraded material response (Guo and Cawley 1994). Significant reductions in elastic moduli and interlaminar shear strength due to matrix porosity have been observed by several investigators, including (Daniel *et al.* 1992; Mouritz and Hutchings 1992; Peters *et al.* 1995). However, if porosity can be controlled in such a way as to significantly improve the quasi-static and ballistic performance of composite systems, then the total weight of the system can be reduced, a highly desirable characteristic of structural systems that are needed for high-strength and resilient applications.

The exploration of the control of porosity in polymeric matrix composites has mainly emphasized the detection and minimization of porosity (Daniel *et al.* 1992; Guo and Cawley 1994). Mouritz and Hutchings (Mouritz and Hutchings 1992) induced porosity in silica-filled epoxy resins by the addition of glass microspheres, which resulted in a decrease in compressive strength. The low velocity perforation behavior of composite sandwich panels has been investigated (Mines *et al.* 1998), with a core material composed of resin-impregnated non-woven polyester felt with 50% microspheres, analogous to the creation of a highly porous central section. Peters *et al.* (Peters *et al.* 1997) recently introduced a new method to create macroporous cylinders of styrenic and methacrylic monomers. In another study (Peters *et al.* 1995), the porosity of

SiC/SiC ceramic matrix composites was controlled by the spacing of pre-impregnated fibers within the composite preform. In that study, the presence of porosity appeared to have a small effect on the tensile modulus, but the transverse shear and compressive moduli were severely reduced.

The chief modes of failure of fiber-reinforced polymeric matrix composites subjected to ballistic impact include fiber breakage, matrix cracking, fiber debonding, delamination, and shear plugging (Backman and Goldsmith 1978; Cunniff 1992; Cunniff 1996; Jenq and Mo 1996; Ellis *et al.* 1998; Jenq *et al.* 1998; Kumar and Bhat 1998; Walsh *et al.* 1998; Flanagan *et al.* 1999). Although porosity has been observed to promote delamination (Daniel *et al.* 1992), the role of porosity in fiber breakage and matrix cracking has not been well understood or characterized. Porosity may inhibit or deflect crack propagation through the matrix, and it may allow fibers to bear the load in tension rather than in shear. Several researchers (Cunniff 1992; Walsh *et al.* 1998) have observed a greater energy absorption capacity of fibers subjected to tension as compared with fibers subjected to shear.

The objective of the investigation of cellular-matrix composite systems is to examine the effects of induced porosity on the mechanical response of 3D woven carbon-fiber reinforced epoxy matrix composite panels subjected to quasi-static and dynamic loading conditions. Dynamic impact experiments for projectile velocities in the range from 100 to 200 m/s are used to determine material response as a function of absorbed energy, areal density, and perforation resistance.

## 1.2 Quasi-Static Perforation of 2D and 3D Composite Systems

The quasi-static loading of fiber-reinforced plastics is a common investigative tool. The large temporal scale permits easy viewing and measurement of material response under a wide range of loading conditions, including three-point bending (Baucom *et al.* 2000; Qiu *et al.* 2001), in-plane loading (Zhu *et al.* 1992; Evans and Zok 1994; Kammerer and Neme 1998; Kuo and Lee 1999), and transverse puncture (Lee and Zahuta 1991; Zhu *et al.* 1992; Lee and Sun 1993; Portanova 1995; Jenq and Mo 1996; Sun and Potti 1996; Jenq *et al.* 1998; Mines *et al.* 1998; Walsh *et al.* 1998; Ying 1998; Mines *et al.* 1999). Quasi-static perforation data have also been used to model and predict material behavior under dynamic impact (Taylor and Vinson 1990; Jenq and Mo 1996; Jenq *et al.* 1998).

The objectives of this part of the investigation include the measurement of the requisite force, energy, and transverse displacement for the quasi-static perforation of glass-fiber-reinforced plastic (GFRP) composite panels. Glass-fiber reinforced plastic composites have been highly desirable engineering materials, due to their high resistance to corrosion, ability to withstand relatively high temperatures, high specific strength, good machineability, and relatively low cost. Many GFRP composites, including the material systems examined here, are translucent when properly consolidated. Hence, damaged regions of impacted samples become opaque, and internal damage can be visually identified. This property is exploited to provide a visual record of damage progression during each quasi-static puncture experiment through the use of a video

recorder and back-lighting. The results are used for the direct comparison of perforation energies and damage mechanisms under low- and high-velocity impact.

### **1.3 Low-Velocity Impact Damage Progression**

Low-velocity impact of fiber-reinforced plastics has been the subject of many experimental and analytical investigations (Bogdanovich and Friedrich 1994; Shen 1997; Naik and Sekher 1998). This type of loading occurs when tools are dropped onto the surface of a composite structure or from the impact of debris, fragments, or projectiles. Experiments can provide quantitative insights and measurements of damage progression of material systems at higher loading rates (Baucom *et al.* 2000). Some investigators have used compression-after-impact and other static tests to obtain measures of damage tolerance and residual strength after low-velocity impact (Cantwell *et al.* 1983; Liu *et al.* 1998; Mahfuz *et al.* 1998; Zhou 1998).

By subjecting specimens to multiple instrumented impacts, residual strength and damage progression can be monitored, as well. In a study of the response of stitched and unstitched E-glass/epoxy laminates subjected to transverse impact (Wu and Wang 1995), specimens were impacted multiple times to examine the growth of damage, including delamination and transverse cracking.

The purpose of the present low-velocity impact study is to examine the progression of damage and capacity for energy-absorption of 2D and 3D woven composite systems subjected to multiple impacts, until the occurrence of complete perforation. Dynamic impact experiments for incident velocities from 2 to 4 m/s are used

to determine material response as a function of absorbed energy, areal density, and fabric architecture. Damage progression is assessed by post-mortem photography, scanning electron microscopy, and the evolution of contact force.

#### **1.4 High-Velocity Impact and Perforation**

For obvious reasons, high-velocity impact on structures and armor systems is a vital concern. This type of loading can be the result of impact by aircraft runway debris, small arms fire, flak and other fragmentation explosives, projectiles driven by high winds, and so on. As new material systems have been developed, the subject of the ballistic response of fabrics and composites has continued to provide fertile ground for research (Vinson and Zukas 1975; Taylor and Vinson 1990; Cunniff 1992; Cate 1993; Zee and Hsieh 1993; Bodner and Rajendran 1997; Vinson and Walker 1997; Gellert *et al.* 1998; Kumar and Bhat 1998; Navarro 1998; Baucom 1999; Mines *et al.* 1999; Mahfuz *et al.* 2000; Singletary and Bogdanovich 2000; Mouritz 2001; Okafor *et al.* 2001; Fujii *et al.* 2001, article accepted for publication; Tarim *et al.* 2002).

Examining the effects of reinforcement geometry on the ballistic response of composite laminates and fabrics, some researchers have compared and contrasted uniweave fabrics and laminates against 2D-plain-weave fabrics and laminates (Mines *et al.* 1999; Morye *et al.* 2000; Fujii *et al.* 2001, article accepted for publication). Others have looked at the effects of 3D braiding or stitching (Flanagan *et al.* 1999; Mines *et al.* 1999; Mouritz 2001; Fujii *et al.* 2001, article accepted for publication). The ballistic

limits of 3D-orthogonal-weave, uniweave, and plain weave Kevlar fabrics have also been compared (Balasundharam 1999).

For this investigation, ballistic impact experiments are conducted on 2D plain-weave laminates and 3D orthogonal-weave laminates and monoliths to determine the dynamic material response and to characterize and compare damage mechanisms as functions of absorbed energy, impact velocity, and fabric architecture. The projectile and target-holder have been designed to provide a boundary condition and impactor geometry that are comparable to those of the quasi-static and low-velocity experiments mentioned above.

## 2. 3D CELLULAR-MATRIX COMPOSITE SYSTEMS

The objective of this investigation is to examine the effects of induced porosity on the mechanical response of 3D woven carbon-fiber reinforced epoxy matrix composite panels subjected to quasi-static and dynamic loading conditions. Porous samples were synthesized by a new foaming technique that is specialized to three-dimensionally woven composites. Three-point bending experiments were used to determine strength and flexural resistance under quasi-static loading conditions. Dynamic impact experiments for projectile velocities in the range from 100 to 200 m/s were used to determine material response as a function of absorbed energy, areal density, and perforation resistance. This chapter is organized as follows: the details of the foaming process and sample preparation are given in Section 2.1, a description of the experimental procedures in Section 2.2, a discussion of the results in Section 2.3, and concluding remarks in Section 2.4.

### 2.1 Material Preparation and Fabrication

Porosity may be induced in epoxy matrix composites by a method of controlled nitrogen pressurization. This method was developed by Qiu et al. (Qiu *et al.* 2001) to reduce the density of 3D woven composites and to fabricate 3D fiber-reinforced cellular polymer matrix composites (3DCPMC). A schematic of the fiber preform is shown in Figure 2.1. An environmental scanning electron microscope (ESEM) micrograph of a sample cross-section of the non-porous 3D system is shown in Figure 2, and a similar micrograph of the cellular matrix composite system is shown in Figure 3.

The 3DCPMC systems were consolidated by impregnating 3D orthogonally woven carbon fiber preforms with epoxy resin and then pressurizing the system with nitrogen gas. After three hours of gas saturation, the temperature was elevated until the resin had cross-linked to a desired stiffness. The gas pressure was then released to induce cells (material voids) of various sizes. Cell nucleation and growth were triggered by the sudden quenching of the applied pressure at specific time intervals. Through careful control of process variables, a reduction in density by approximately 30% ( $1.0 \text{ g/cm}^3$ ) was attained.

Four types of sample materials were produced, as shown in Table 2.1. Samples of similar areal density, but different fabric preforms, were made both *with* and *without* the pore-induction technique. This variation and control of properties provided a framework to understand and differentiate of the effects of fiber volume fraction and porosity on overall behavior under different loading conditions.

**Table 2.1 Carbon-Fiber/Epoxy Cellular- and Resin-Matrix Composite Systems**

<b>Sample</b>	<b>Description</b>	<b>Fiber-Volume Fraction</b>	<b>Areal Density (kg/m<sup>2</sup>)</b>
<b>TM</b>	Low fiber-volume, cellular-matrix	0.41	4.3
<b>TS</b>	High fiber-volume, cellular-matrix	0.46	4.8
<b>TMR</b>	Low fiber-volume, resin-matrix	0.36	6.7
<b>TSR</b>	High fiber-volume, resin-matrix	0.42	7.2

## **2.2 Experimental Procedures**

The effects of porosity on the mechanical response of 3D woven fiber-reinforced epoxy panels were investigated and characterized for quasi-static and dynamic loading conditions. Quasi-static behavior was examined by three-point bending experiments, such that maximum and failure loads could be determined for porous and non-porous 3D woven composite systems. The energy absorption, dynamic response, and perforation resistance of the composite systems were investigated for impact velocities of 120 and 220 m/s.

### **2.2.1 Quasi-Static Three-Point Bending Experiments**

Flexural stiffness and strength were determined under three-point bending, pursuant to ASTM standard D790-97. Six rectangular coupons, 13 mm x 200 mm, were supported symmetrically by fixed lateral pins with a span of 76.2 mm. An Instron model 1125 was used to push a central lateral pin in the opposite direction at a rate of 10

mm/min. The load as a function of displacement of the cross-head was monitored until the material ruptured.

### **2.2.2 Dynamic Experiments**

A 19-mm powder-charge accelerator (Figure 2.4) was used to examine the perforation resistance of various composite systems at ballistic velocity regimes. The gun was designed with a barrel length of 2.2 m, which can accelerate a variety of 19-mm projectiles to velocities approaching 1 km/s. A flat-nose, cylindrical steel projectile (Figure 2.5) with a mass of 77.8 g was designed for this series of experiments. The projectile velocity was measured before and after perforation of the target, and the energy absorbed by the target was calculated by a balance of the incident and residual kinetic energy of an essentially rigid projectile. This experimental apparatus has been used successfully by other investigators in the examination of various material systems, including woven and braided composites (Flanagan 1997). The ability to measure the residual velocity of the projectile permits an estimate of the absorbed energy of the target at projectile speeds significantly above the ballistic limit. The understanding and characterization of energy absorption and damage mechanisms, at impact speeds well above the ballistic limit, can provide important insights into the performance of structural composite systems (Cunniff 1992; Cunniff 1996; Schonberg 1998).

The impact velocity of the projectile, as well as its residual velocity, are measured for each impact. The impact velocity is determined by monitoring the response of two switches (*velocity pins*) that are placed along the bore, near the muzzle. As it closes the

first switch, the projectile triggers an oscilloscope, which monitors the status (high or low voltage) of the second switch (Figure 2.6). The velocity is inferred from the known switch spacing and the measured time between closings of the switches. The residual velocity of the projectile is measured with inductive coils (Figure 2.7). The ferritic steel projectile passes through each coil, inducing a voltage as it passes. This residual velocity sensor detects only the ferritic projectile, but it is unaffected by the debris of ejected target material and the exhaust cloud of burned powder both ahead of and behind the projectile. The target is clamped along a circular boundary (Figure 2.8), and the energy absorbed by the target is estimated through a simple balance of translational kinetic energy of the projectile,

$$E = \frac{1}{2} m (V_i^2 - V_r^2) \quad (2.1)$$

where  $E$  is the energy absorbed by the target,  $m$  is the mass of the projectile,  $V_i$  is the incident projectile velocity, and  $V_r$  is the residual projectile velocity.

Each projectile is a right-circular cylinder with a diameter of 19 mm, 38-mm length, and 78-g mass. Mild ferritic steel was chosen for its machineability, its relatively high hardness, and its iron content, so that the residual-velocity sensor can detect it. In the energy balance of Equation (2.1), the plastic work of projectile deformation is neglected, since the projectiles are essentially rigid. The projectiles are placed in 12-gauge shotgun cartridge cases, and they are loaded with standard primers and smokeless powder charges.

Target panels are clamped between two thick aluminum annuli, 76.2-mm inner diameter and 152-mm outer diameter, and tightened to prevent slippage. The target is held at a fixed distance (90 mm) from the muzzle and normal to the line of trajectory of the projectile. The frame of the target holder was designed to prevent rearward motion of the grip.

## **2.3 Results and Discussion**

Quasi-static three-point bending and dynamic impact experiments were used to understand how the variation of porosity and fiber-volume fraction affect the material response of 3D orthogonally woven composite systems as a function of different velocity regimes and loading conditions.

### **2.3.1 Quasi-Static Results**

Six samples of each type (Table 2.1) were subjected to quasi-static three-point bending. The resulting load-deflection curves for the resin-matrix and cellular composite systems with higher fiber-volume-fractions are shown in Figures 2.9 and 2.10. The load-deflection curves for the porous and non-porous samples with the lower fiber-volume-fraction were analogous in shape but with maximum loads of approximately one-half of the maximum load corresponding to the high fiber-volume-fraction samples.

All three-point bending load-deflection curves exhibit an initial nonlinear loading region through a deflection of about 0.5 mm. This is followed by a linear load path and terminates with a peak load value. A summary of the average peak load, flexural

stiffness based upon the linear loading region, and the deflection at peak load is shown in Table 2.2.

Beyond the peak load, the behavior of porous systems differs from that of non-porous systems. In the case of non-porous systems, the peak load is followed by rupture of the sample. For the porous systems, an abrupt drop follows the maximum load to a value that is approximately 25% of the peak load. The load then increases in an essentially linear fashion, at a lower rate than the first linear loading, until a second peak value is reached. The second peak load is followed by rupture of the specimen.

These results indicate that porosity may mitigate damage progression by the pores acting as sites that can deflect failure surface propagation with a strength that is comparable to non-porous systems. Furthermore, as the results indicate, the porosity results in a gradual unloading to rupture, which would be a desirable characteristic for an indication and control of material failure.

### **2.3.2 Dynamic Results**

Ballistic impact tests were conducted at two nominal velocities, 120 and 220 m/s, for the four sample types listed in Table 2.1. As can be seen in the post-perforation photographs of resin-matrix and cellular-matrix samples (Figure 2.11), the material deformation and damage are confined to a much smaller area for the non-porous system. In contrast, the cellular matrix systems had substantially more transverse deflection and dishing over a larger area than the non-porous system.

Post-perforation ESEM micrographs of sample cross-sections, shown in Figures 2.12 and 2.13, further indicate significant differences in the vicinity of the perforation edge. The non-porous systems appear to have failed in a manner similar to shear-plugging (Flanagan *et al.* 1999), with little damage beyond the edge of the hole. However, the cellular matrix systems exhibited extensive debonding and relative motion of fiber tows, resulting in greater dispersion of the impact energy over a larger area.

The energy absorbed by the target was calculated from Equation (2.1), based on the incident and residual projectile velocities. A plot of the absorbed energy, as a function of projectile velocity, is given in Figure 2.14. At lower velocities, both the porous and non-porous samples with higher fiber volumes absorbed about 10% more energy than the samples with lower fiber-volume fractions. Only the low fiber-volume samples were tested at the higher velocity. At higher velocities, the samples with induced porosity absorbed approximately 60% less energy than the non-porous samples. These results indicate that higher fiber volume fractions and non-cellularization enhance ballistic perforation resistance of composite materials.

However, if the absorbed energy is normalized by the areal density, material response can be clearly delineated for a direct comparison between systems of different areal densities. This would provide an indication of the relative performance of composite systems of *comparable* areal densities. Figure 2.15 shows a plot of the normalized absorbed energy as a function of projectile velocity. As these results indicate, the impact response is segregated by porosity, not fiber-volume fraction. Per unit of areal density, highly porous materials absorbed more energy than less porous materials.

When the absorbed energy is plotted as a function of the target areal density (Figure 2.16) the potential advantage of induced porosity becomes even more apparent. The samples with induced porosity absorbed energy comparable to the non-porous samples. These results suggest that it may be possible to substantially decrease the weight of composite systems through the induction of porosity without degradation of ballistic performance, if the fiber volume fraction is not below a critical threshold value. Furthermore, the ESEM micrographs and post-mortem analysis indicate that the pores can be sites for the dissipation of energy over a large area.

**Table 2.2 Three-Point Bending, Average Results**

<b>Series</b>	<b>Peak Load (kN)</b>	<b>Flexural Stiffness (kN/mm)</b>	<b>Deflection at Initial Yield (mm)</b>
<b>TM</b>	0.68	0.19	4.0
<b>TS</b>	0.74	0.27	3.2
<b>TMR</b>	1.2	0.20	6.4
<b>TSR</b>	1.5	0.32	5.2

## **2.4 Conclusions**

Quasi-static and dynamic experiments were conducted to investigate how porosity, fiber-volume fraction, absorbed energy, and strength affect the mechanical response of cellular 3D woven samples for different velocity regimes and loading conditions. The results of this investigation indicate that the induction of porosity by

nitrogen gas pressurization in 3DCPMC-based composite systems results in significant weight reduction, while structural performance and durability are maintained and energy is dissipated.

For quasi-static three-point bending, the pore sites may act as sites where the failure surfaces are deflected and mitigated. The force unloading beyond the post-maximum load behavior was gradual until rupture. In contrast, the non-porous samples' behavior beyond the maximum load was abrupt and rupture occurred rapidly after the maximum load. This further suggests that failure can be controlled in the porous samples without significant strength differences between the porous and non-porous samples.

For dynamic loading conditions at different impact velocities, the normalization of the absorbed energy by the areal density of the target provided a direct comparison of the ballistic performance of panels with different areal densities. By normalizing the absorbed energy, the sample response segregated by porosity and not by fiber volume fraction. Per unit of areal density, the more highly porous samples *absorbed more energy* than the non-porous materials. As in the three-point bending experiments, this may be due to the deflection of transverse cracks by pores, thereby inhibiting and dissipating failure under ballistic impact over large radial areas. Furthermore, a higher density of matrix material in non-porous composites may serve to confine the damage area and, hence, limit the energy absorption capacity of the material over small radial areas. The weak interfaces between pores and the matrix material can act as failure surfaces that can absorb and dissipate energy. Therefore, porosity not only results in significantly reduced

areal densities, but it also results in substantially different failure and dissipative energy mechanisms and behavior without strength degradation.

**2.5 Figures**  
**(Chapter 2)**

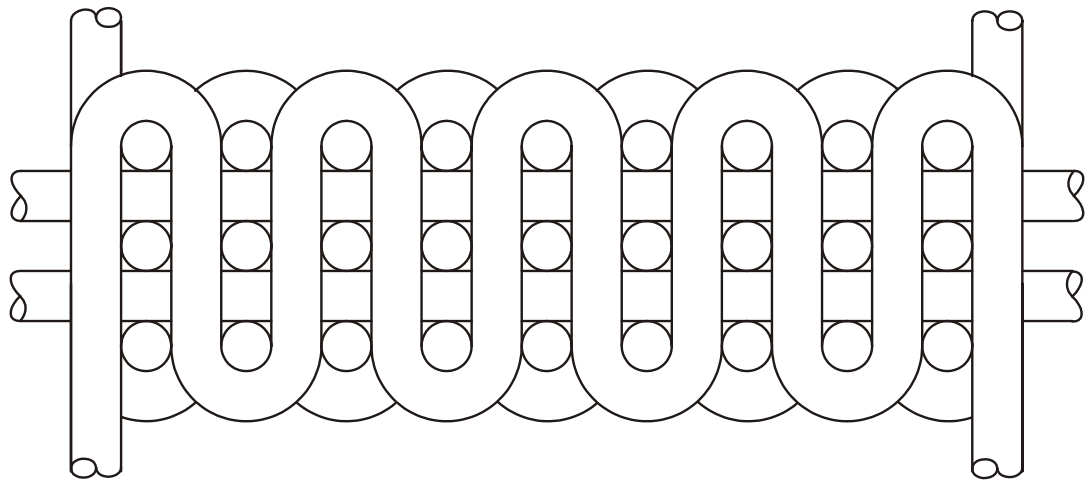


**Figure 2.1 Three-Dimensional Orthogonal Weave**

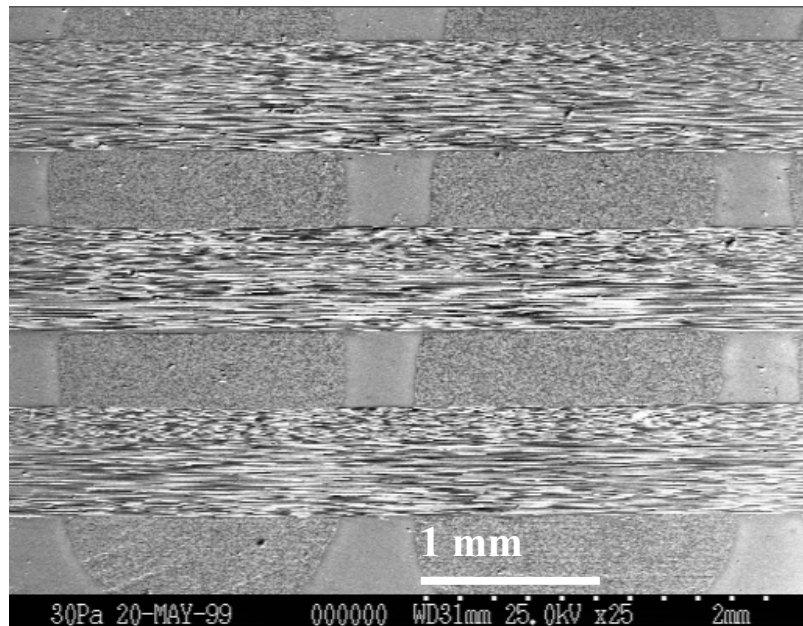


**Figure 2.2 Resin-Matrix Composite**

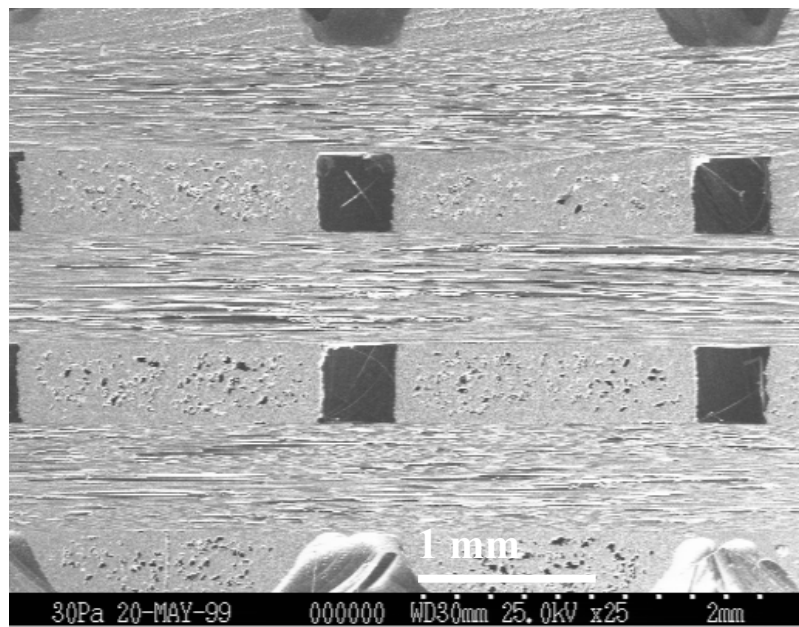


**Figure 2.3 Cellular Matrix Composite**

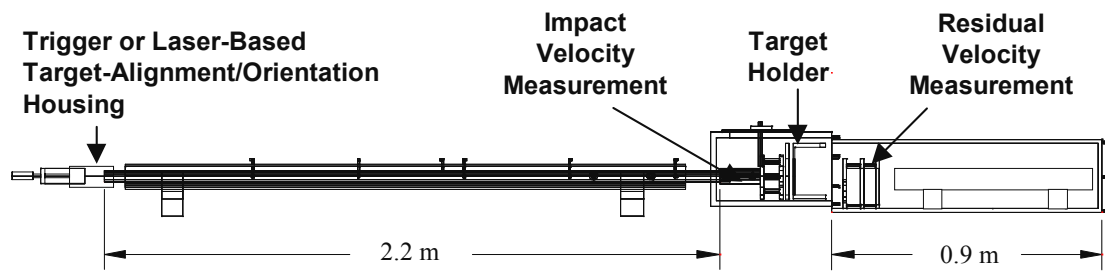


**Figure 2.4 19-mm Powder-Charge Accelerator**

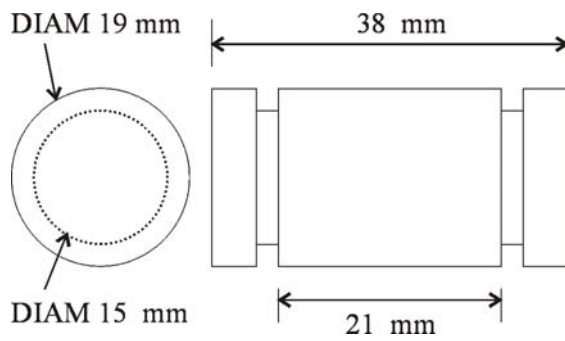


**Figure 2.5 Flat-Nose Steel 19-mm Projectile (77.8 g)**

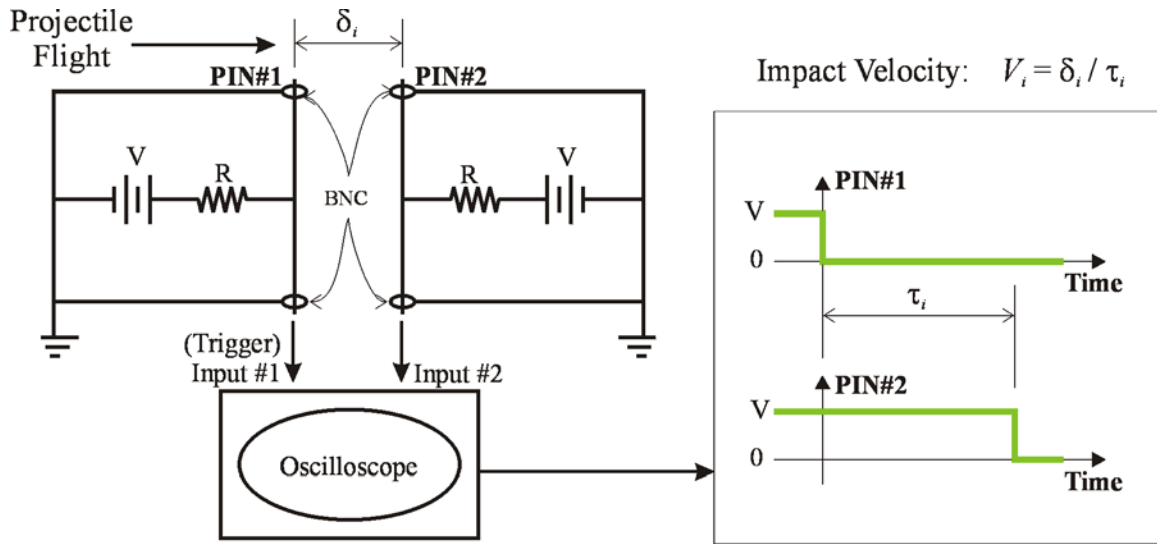


Figure 2.6 Measurement of Impact Velocity by Velocity-Pin Switches

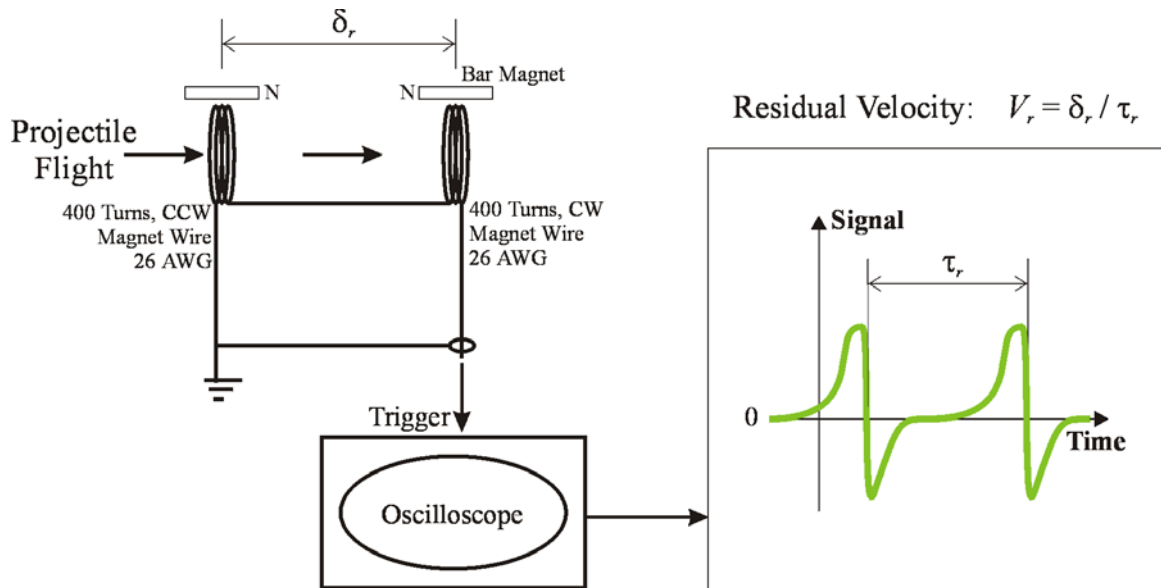


Figure 2.7 Measurement of Residual Velocity by Coil-Type Inductors

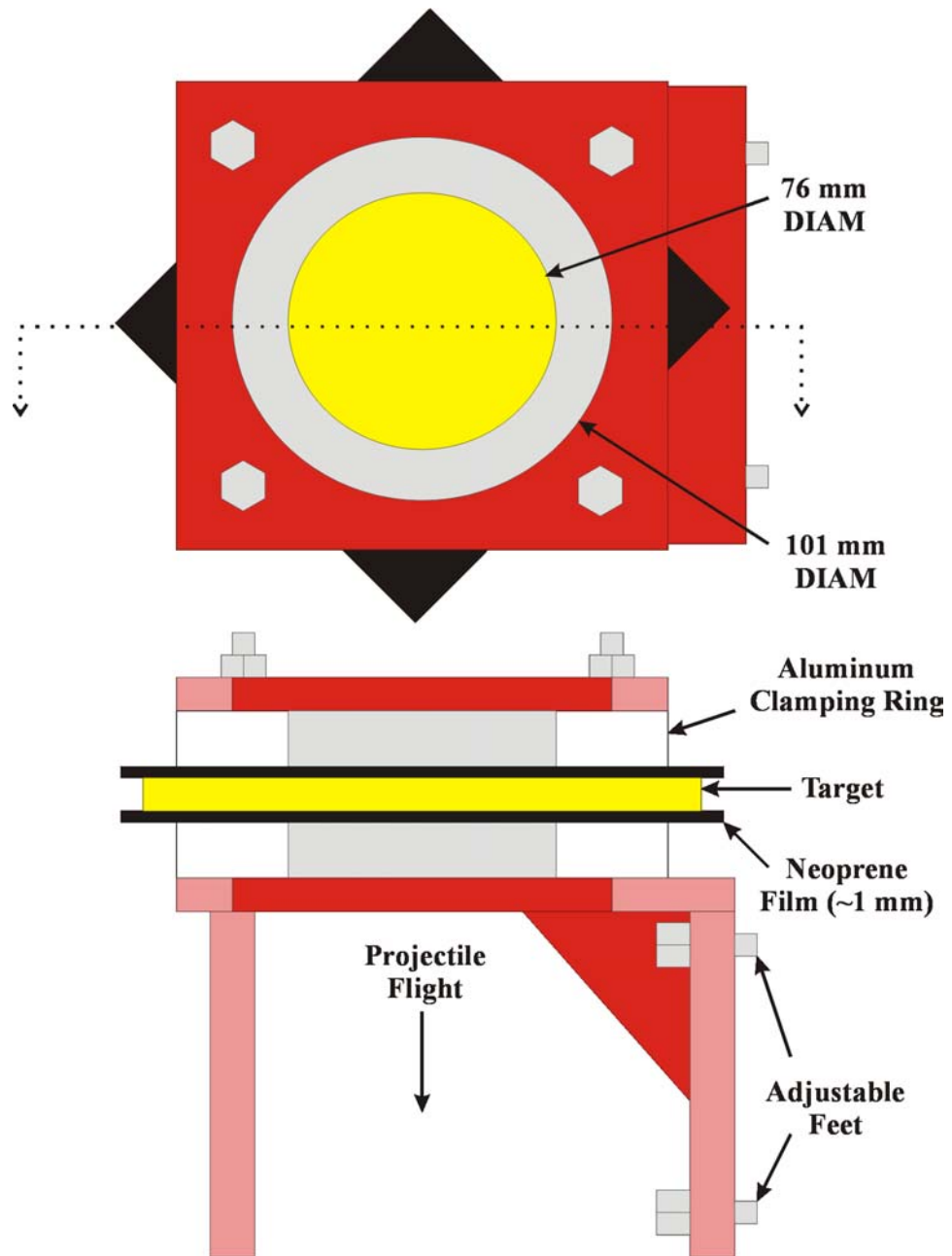
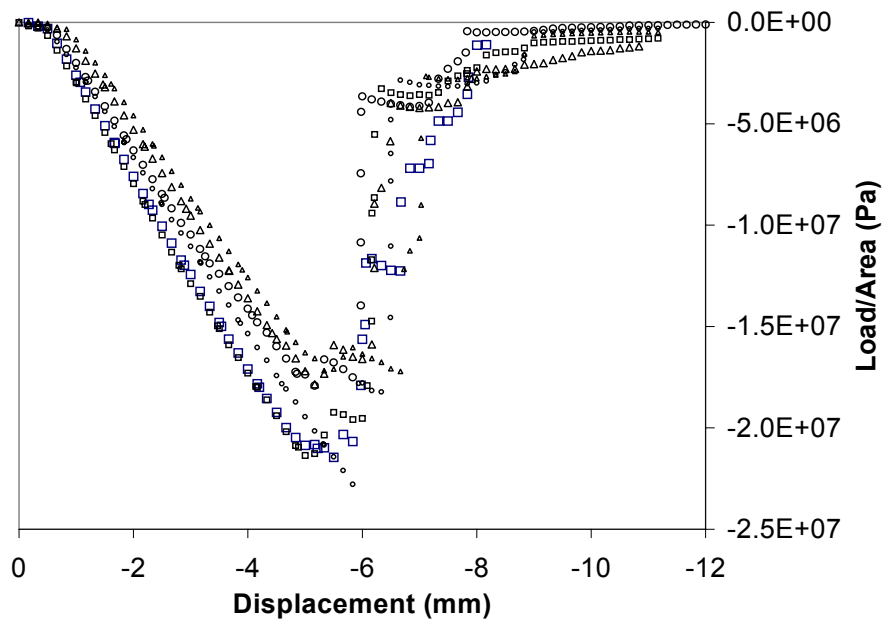
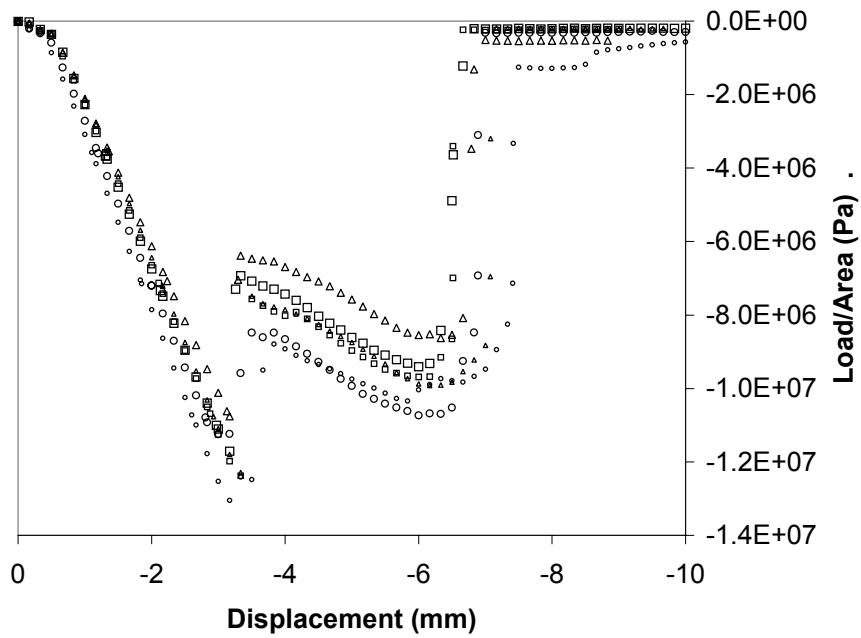


Figure 2.8 Target Holder for 19-mm Accelerator



**Figure 2.9 Three-Point Bend for Resin-Matrix Composites**



**Figure 2.10 Three-Point Bend for Cellular-Matrix Composites**

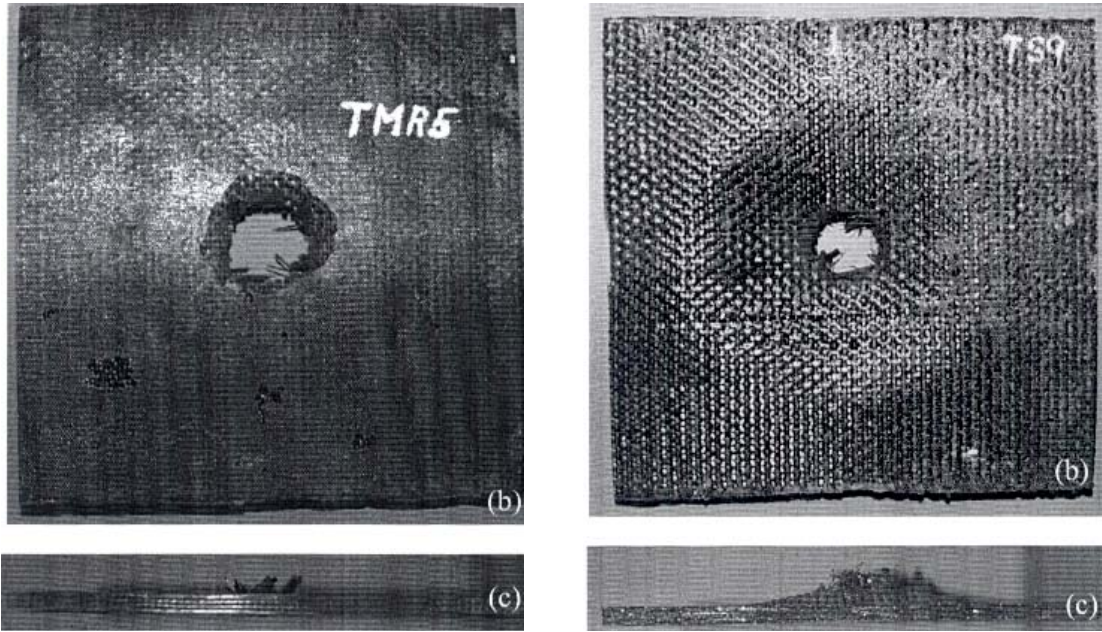


**Figure 2.11 Post-Perforation Photographs: Left - Resin-Matrix Composite (Rear Face), Right - Cellular-Matrix Composite (Impacted Face)**

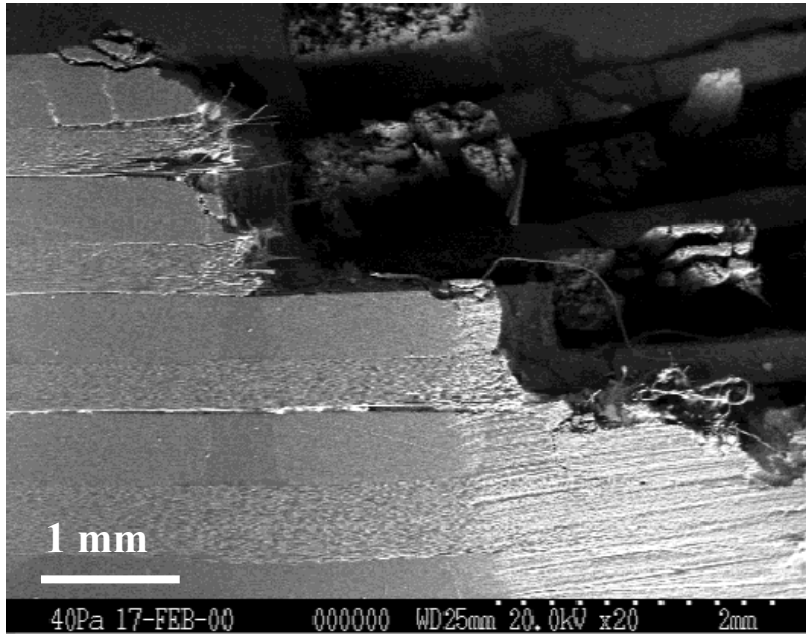


**Figure 2.12 Perforated Resin-Matrix Composite**

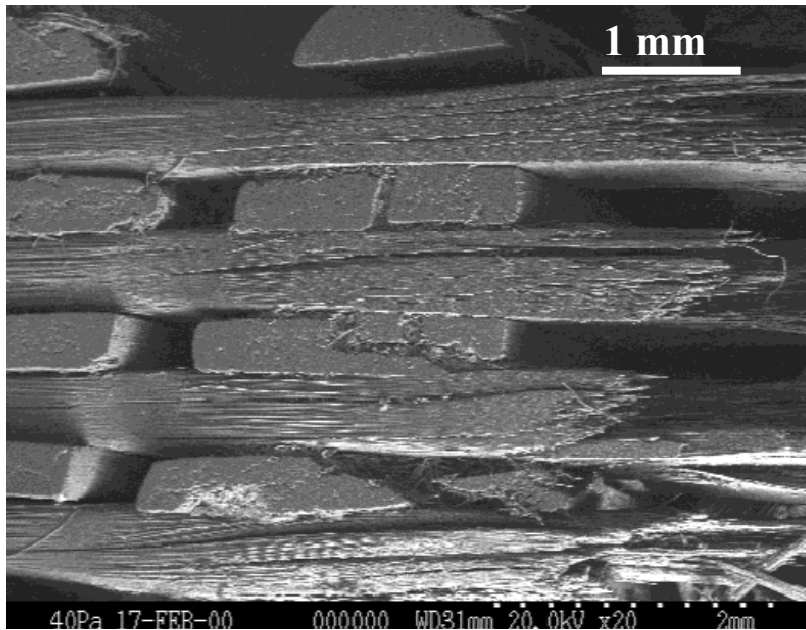


**Figure 2.13 Perforated Cellular-Matrix Composite**

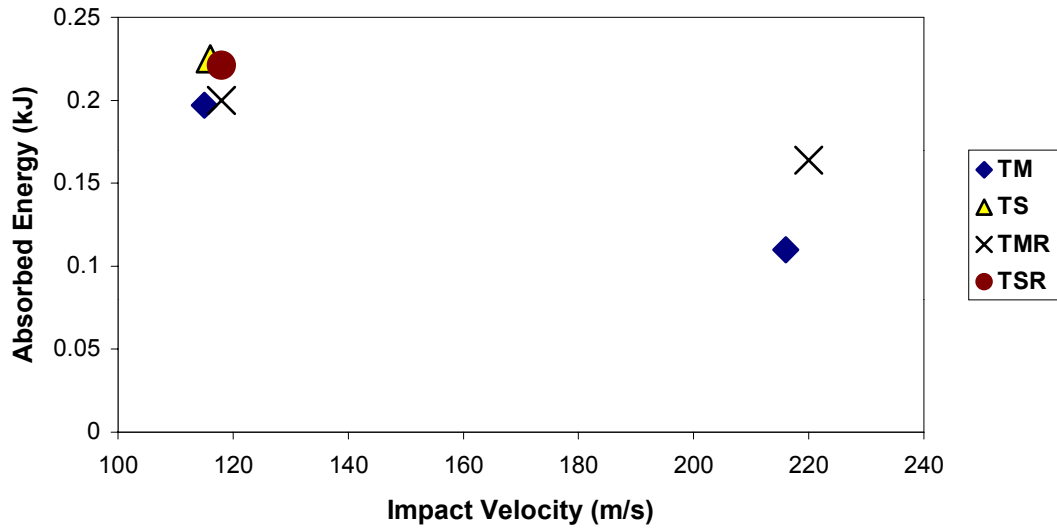


**Figure 2.14 Absorbed Energy: Fiber Volume (f) and Porosity Effects**

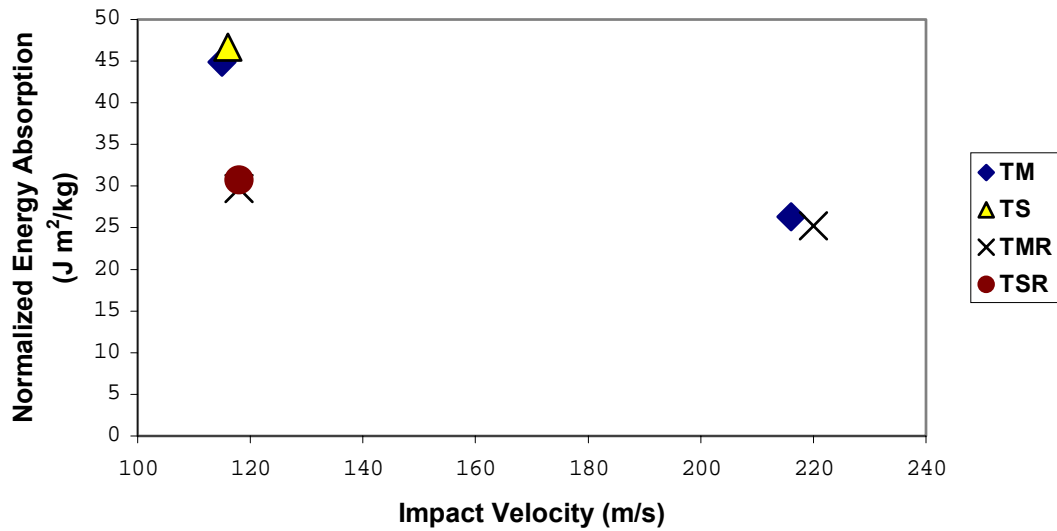


**Figure 2.15 Normalized Energy Absorption**

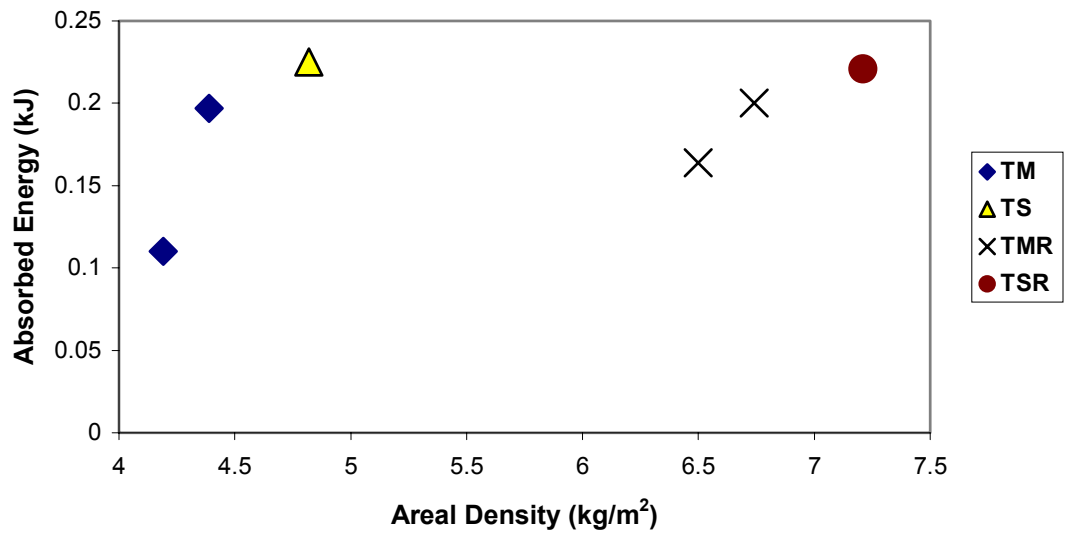


**Figure 2.16 Absorbed Energy as a Function of Areal Density**

### 3. QUASI-STATIC PERFORATION OF 2D AND 3D COMPOSITE SYSTEMS

This part of the investigation examines how the variation of fabric architecture in composite systems with comparable areal densities affects perforation resistance, strength, energy dissipation, and damage mechanisms of GFRP composite panels subjected to quasi-static perforation, at velocities in the range from 10 to 80  $\mu\text{m/s}$ . Five woven architectures were chosen as the fabric preforms: two 2D plain-woven laminates, two 3D orthogonally woven monoliths, and a 3-ply laminate of 3D orthogonally woven laminae. The composite fibers were chosen as S2-glass, and a rubber-toughened vinyl-ester/epoxy resin was selected for the matrix material. These materials were produced to compare systems of similar areal-density and constituent material but varying fiber-architecture (Table 3.1).

The 3D systems are orthogonally woven. For the 3D laminates (*3D-S-93x3*), two through-the-thickness planes are introduced which break the  $z$ -reinforcement. These 3D laminates also have three times the number of sites of crimp in the  $z$ -yarns. The remainder of the chapter is organized as follows: the details of the material preparation and fabrication are given in Section 3.1, a description of the experimental apparatus and method is presented in Section 3.2, the results are discussed in Section 3.3, and concluding remarks are made in Section 3.4.

### 3.1 Material Preparation And Fabrication

Five composite systems were examined, with different fabric architectures but with comparable areal densities, fiber-volume fractions, and thicknesses. Glass-fiber reinforced plastics have been widely accepted for use as engineering materials, due to their superior properties and affordability. Many GFRP composites are translucent when consolidated, but material damage, such as the separation of fibers and matrix material, results in a reduction of the transmissivity of visible light. Hence, damaged interior regions of impacted samples become opaque, and internal damage can be visually identified under back-lighting (Baucom *et al.* 2001). This property is exploited to provide a record of internal damage progression.

#### 3.1.1 Fabric Architectures

Fabric preforms were selected to provide samples of various fabric architectures but common areal density. The fabric architecture of the first system was a conventional 2D plain-woven laminate with 4 layers (*2D-S-24x4*). A similar, but thicker, 2D laminate was produced with 12 layers of plain woven fabric (*2D-S-24x12*); this laminate may be considered as the consolidation of 3 layers of *2D-S-24x4*. The fabric preform of the next material system was a monolithic 3D orthogonal weave (*3D-S-93*) of approximately the same areal density as the 4-layer 2D laminate (Figure 3.1). Three layers of the *3D-S-93* preform were consolidated to yield the next material system (*3D-S-93x3*), a 3-layer laminate of laminae with 3D orthogonally woven fabric reinforcement. The preform of the final material system consisted of a monolithic 3D orthogonally woven fabric (*3D-S-*

270), such that the total areal density was nearly the same as for systems *2D-S-24x12* and *3D-S-93x3* (Figure 3.2).

### 3.1.2 Constituent Materials

All composite systems were derived from S2-glass fiber rovings in a matrix of Dow Derakane 8084 rubber-toughened epoxy/vinyl-ester. The fiber-volume-fraction ranged from 0.49 to 0.58. Hence, this selection of material systems permitted an isolation of the effects of fabric architecture, especially the effects of orthogonal *z*-reinforcement. A listing of the material systems is provided in Table 3.1, including the composite areal density, fiber-volume-fraction, and average measured thickness of each system. In Table 3.1, the fraction of fiber volume is estimated in the following manner:

$$FVF = \frac{AD_f}{\rho_f t_{nom}} \quad (3.1)$$

where *FVF* is the estimated fiber-volume-fraction for a particular sample, *AD<sub>f</sub>* is the areal density of the fabric reinforcement,  $\rho_f$  is the volumetric density of the fibers, and *t<sub>nom</sub>* is the nominal thickness of the panel. Consolidation was achieved by vacuum-assisted resin-transfer molding, with a four- to eight-hour post-cure at 85°C.

**Table 3.1 S2-Glass/Rubber-Toughened-Epoxy-Vinyl-Ester Composites Systems for Quasi-Static Puncture**

Composite System	Sample Designation	Areal Density (kg/m <sup>2</sup> )	Fiber Volume Fraction	Thickness (mm)
<b>2D-S-24x4</b> (4-ply, 2D Laminate)	<i>2D-S-24x4-1</i>	4.60	0.532	2.44
	<i>2D-S-24x4-2</i>	4.62	0.491	2.64
<b>2D-S-24x12</b> (12-ply, 2D Laminate)	<i>2D-S-24x12-1</i>	13.7	0.509	7.65
	<i>2D-S-24x12-2</i>	13.6	0.526	7.65
<b>3D-S-93</b> (3D Monolith)	<i>3D-S-93-1</i>	4.41	0.556	2.26
<b>3D-S-93x3</b> (3-Ply, 3D Laminate)	<i>3D-S-93x3-1</i>	13.2	0.519	7.26
	<i>3D-S-93x3-2</i>	13.3	0.517	7.29
	<i>3D-S-93x3-3</i>	12.7	0.536	7.04
<b>3D-S-270</b> (3D Monolith)	<i>3D-S-270-1</i>	12.7	0.522	6.99
	<i>3D-S-270-2</i>	12.5	0.530	6.88
	<i>3D-S-270-3</i>	12.7	0.520	7.01

### 3.2 Experimental Procedures

An Instron 4400R universal testing machine (Figure 3.3) was used to subject the composite samples to quasi-static transverse central puncture and to collect load-deflection data. The crosshead was driven along one axis under displacement rate control, and a 9.0-kN load cell was used to monitor the compressive force between the cross-head and the frame. Given the constant rate of crosshead displacement, the load

cell data is used to generate load-displacement curves, yielding the total work of the cross-head required for perforation of the panel.

A specialized penetrator (*tup*) and target fixture were designed to adapt the universal testing machine for quasi-static perforation. The tup developed for these experiments was a steel cylinder with a 19-mm diameter and a hemispherical nose (Figure 3.4). This geometry was chosen for comparison of results obtained for other quasi-static, low-velocity, and high-velocity impact and perforation in this report, as well as from other studies (Cantwell *et al.* 1983; Jang *et al.* 1990; Jenq and Mo 1996; Jenq *et al.* 1998; Liu *et al.* 2000). Square target panels (edge-lengths of 13 cm) were clamped between steel plates with central circular apertures, 76.2 mm in diameter (Figure 3.5). The clamps were supported by four 20-mm steel legs, which rested upon the load cell. An angled mirror was placed in the open space between the legs of the target holder, permitting a view suitable to capture video of the rear target-face. To provide backlighting for the video, the tup was surrounded by a circular fluorescent light tube and mounted to the crosshead. This arrangement provided a record of internal damage initiation and progression throughout the quasi-static event.

### **3.3 Results And Discussion**

Displacement-controlled quasi-static transverse puncture of 2D laminates, 3D composite monoliths, and 3D laminates was performed while monitoring the puncture load. Damage initiation and progression was monitored by backlit videography. The

energy required to perforate each sample was calculated for comparison with higher-velocity impacts.

The crosshead speed, rate of data sampling, and load history were used to derive a load-deflection curve. The load-deflection curve was integrated from the point of contact, until the moment of perforation, to yield the work required for the perforation of the target as

$$W_p = \int_0^{s_f} F ds \quad (3.2)$$

where  $W_p$  is the total work of perforation by the tup,  $F$  is the force measured by the load cell,  $ds$  is the incremental displacement of the perforator, and  $s_f$  is the displacement at which perforation has been achieved. The condition,  $s = 0$ , corresponds to the moment at which the penetrator contacts the target and was identified by the positive increase of load-cell output.

When perforation occurs, the target continues to resist through frictional sliding of the cylindrical penetrator which creates a widening hole in the target, and it is difficult to determine the displacement corresponding to the onset of perforation. In this report, the target was considered to be perforated when the post-contact displacement of the tup reaches a value that is equal to the sum of the target thickness and the diameter, 19 mm, of the hemispherical nose. This condition determined the integration limit,  $s_f$ , in Equation (3.2).

The punch load is plotted in Figures 3.6-10 as a function of tup displacement. Certain general trends were observed, and a representative load-displacement curve was developed (Figure 3.11). The curve is divided at four points, labeled A, B, C, and D. The tup-displacements corresponding to these points of transition are listed in Table 3.2 for the experiments in which a video recording was made (Figures 3.12-14). Each video was synchronized with the load-cell data through the audio track of the audio/video recording, at the moment of contact. Frames of the video recording, captured in proximity to each transition point, support the description of the general penetration process for the composite systems under investigation.

**Table 3.2 Post-Contact Penetrator Displacement at Transition Points of Quasi-Static Load-Displacement Curves**

<b>Specimen</b>	<b>Point <i>A</i> (mm)</b>	<b><i>B</i> (mm)</b>	<b><i>C</i> (mm)</b>	<b><i>D</i> (mm)</b>
<b><i>2D-S-24x12-2</i></b> (2D Laminate)	1.27	10.25	15.75	30.32
<b><i>3D-S-270-3</i></b> (3D Monolith)	1.23	10.42	17.28	30.57
<b><i>3D-S-93x3-3</i></b> (3D Laminate)	1.19	12.41	17.74	30.49

The first transition, point *A*, marks the end of elastic deformation and the onset of internal damage, as indicated by the appearance of a dark spot under the point of contact. The damaged area grows to reach the boundary, at which time a sudden increase in damaged area is observed (point *B*). Point *C* marks the time at which the penetrator has ruptured the panel and begins to appear, widening the rupture site as it continues. Finally, point *D* marks the moment at which the passage of the shank has reached a steady state.

**Table 3.3 Peak Force and Work of Perforation, Average Values for Each Material System**

<b>Composite System</b>	<b>Peak Force (kN)</b>	<b>Normalized Peak Force (kN · m<sup>2</sup>/kg)</b>	<b>Perforation Work (J)</b>	<b>Normalized Perforation Work (J · m<sup>2</sup>/kg)</b>
<b><i>3D-S-93</i></b> (3D Monolith)	10.2	2.31	105	23.9
<b><i>2D-S-24x4</i></b> (4-ply, 2D Laminate)	11.3	2.44	89.5	19.5
<b><i>3D-S-270</i></b> (3D Monolith)	32.0	2.48	410	32.1
<b><i>3D-S-24x12</i></b> (12-ply, 2D Laminate)	37.5	2.74	434	31.7
<b><i>3D-S-93x3</i></b> (3-Ply, 3D Laminate)	37.9	2.91	467	35.7

As shown in Figures 3.6-10, the load-displacement curves were very repeatable. Average values for peak force and punch work are listed in Table 3.3. Of the thin panels, *3D-S-93* and *2D-S-24x4*, the peak punch force was 14% higher for the 2D laminate. The peak force for the thick 2D and 3D laminates was about the same and exceeded the peak of the 3D monolith by 16%. After normalizing these values by target areal density, the peak force of the 3D laminate was highest, followed by the thick 2D laminate (*2D-S-24x12*), the thick 3D monolith (*3D-S-270*), and then the thin panels. The normalized punch force (Figure 3.16) was comparable for all systems, the highest and lowest peak values differing by only 23%.

The work of perforation was calculated according to Equation 3.2 and is plotted in Figure 3.15. Average values of the punch work are given in Table 3.3. For the thin panels, the 3D system absorbed an average of 16% more energy than the 2D laminate. For the thick panels, the 3D laminate absorbed the most energy (467 J), followed by the 2D laminate (434 J) and the 3D monolith (410 J). This trend is magnified when the punch work is normalized by panel areal density (Figure 3.17).

Photography was used to identify and record post-perforation damage. Internal damage was revealed under backlighting. Photographs of the thin 2D laminate (*2D-S-24x4*) are shown in Figures 3.18-20. For this material system, the internal and external damage is highly localized. The backlit image of Figure 3.18 shows that the bulk of the damage (the darkest area) occurred in a circular area surrounding the rupture site. Lesser

damage spreads radially in the warp and weft directions. The chief damage mechanisms appear to be delamination and fiber fracture.

Photographs of the thin 3D monolith (*3D-S-93*) are shown in Figures 3.21-23. As in the case of the thin 2D laminate, the most heavily damaged region is in proximity to the hole. The shape of this darkest region, however, is more rectangular (Figure 3.21c). Fiber-debonding has occurred throughout the circular area exposed by the aperture of the target clamp. In contrast with the 2D laminate, less damage appears to have occurred along radial bands, in the warp and weft directions, intersecting the rupture site. On each side these bands of minimal damage the rear-face weft has delaminated beyond the boundary of the target clamp. Damage also has been clearly incurred by the surface crimp of *z*-tows retaining the delaminated rear-face weft.

Photographs of the thick 2D laminate (*2D-S-24x12*) are shown in Figures 3.24-26. Reflective lighting showed that surface damage had extended to the clamp boundary on both sides of the panel (Figure 3.24a,b). However, backlighting revealed that internal delamination had grown beyond the clamp boundary in the warp and weft directions (Figure 3.24c). As in the case of the thin 2D laminate, an intensification of damage was observed in a cross-shape pattern along warp and weft directions (Figure 3.25). Some delamination was also evident at the edges of the panel (Figure 3.26).

Photographs of the thick 3D monolith (*3D-S-270*) are shown in Figures 3.27-29. Similar to the thick 2D laminate, damage has extended to the edge of the clamp and beyond (Figure 3.27). On the front face (Figure 3.28) only fiber debonding and matrix cracking were observed. However, on the rear target face (Figure 3.29) damage modes

were more complex. These modes included large straining of *z*-tows, debonding of surface weft extending to the edge of the panel, and sliding of the surface weft through the crimp of *z*-tows toward the perforation site.

Photographs of the 3D laminate (*3D-S-93x3*) are shown in Figures 3.30-32. Again, backlighting revealed internal delamination and fiber-debonding that had grown beyond the clamp boundary (Figure 3.30c). Similar to the 3D monolith, the front face of the panel exhibited the same dominant failure modes: fiber debonding and matrix cracking (Figure 3.31). Examination of the rear target face showed that one of the rear surface weft tows had been pulled inward through *z*-tow crimps, some of which had been broken near the perforation site (Figure 3.32). The residual transverse dishing of the panel was noticeably greater in comparison with the other material systems.

Through-the-thickness damage was inspected by environmental scanning electron microscopy (Hitachi S-3200). This mode of SEM uses low-pressure helium to alleviate sample charging for electrically nonconductive samples and avoids the necessity of coating the sample surface with gold. A hacksaw was used to cut the perforated panels into strips that were approximately 1 cm in width and 2 cm in length. The cut faces were then smoothed using 400-grit sandpaper and rinsed with water. Interesting micrographs are presented for the thick 3D monolith and the 3D laminate (Figures 3.33-34). The plane of the displayed cut face is normal to the weft direction for each micrograph. In the case of the 3D monolith (Figure 3.33) extensive internal fiber-debonding was observed. Micrographs of the 3D laminate showed delamination, debonding, and the internal fracture of a *z*-tow.

### 3.4 Conclusions

This investigation examined how variations of fabric architecture in GFRP composite systems with comparable areal density, thickness, and fiber-volume-fraction affected perforation resistance, strength, and distributions of energy dissipation of panels subjected to quasi-static perforation. Three woven fabric preforms were investigated: a 24-ply 2D plain-weave laminate, a monolithic 3D orthogonal weave, and a 3-ply 3D orthogonally woven laminate. The material consisted of a rubber-toughened-epoxy-vinyl-ester reinforced by S2-glass fibers. Coupons were subjected to transverse quasi-static puncture at fixed rates from 10 to 80  $\mu\text{m/s}$ . The penetration load was recorded and a novel view of internal damage progression was obtained by backlit videography.

Distinctions in failure modes of the various material systems were observed. Matrix cracking, delamination or fiber debonding, and fiber fracture were observed in all systems. Damage mechanisms unique to the 3D systems included the straining and fracture of  $z$ -reinforcement tows. Also, the radial spread of damage was larger for the 3D systems than for the 2D laminates; often, fiber debonding of the 3D systems extended to the edges of the test panel.

Considering the thicker material systems, load data indicated that the strength and capacity to absorb energy under transverse puncture were comparable for the 2D and 3D laminates and superior to the 3D monolith. Normalization by areal density magnified the superiority of the 3D laminate. This is attributed to the damage mechanisms unique to these geometries. Furthermore, the introduction of two planes in the 3D laminates increased the number of  $z$ -crimps by a factor of three.

**4.5 Figures**  
**(Chapter 3)**

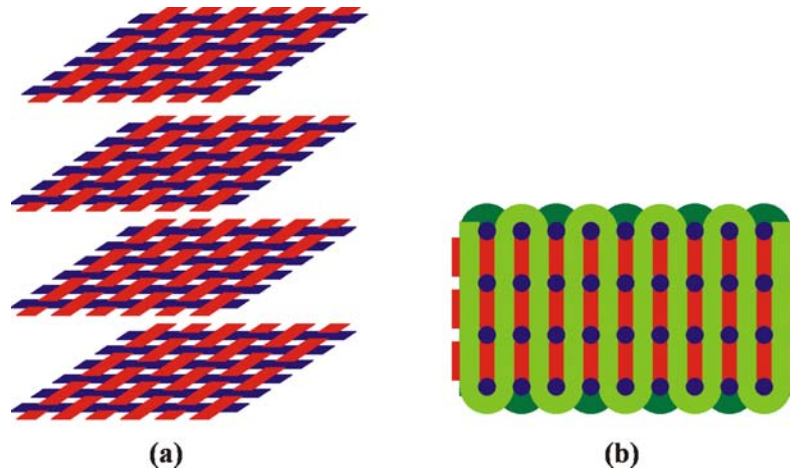


Figure 3.1 Thin S2-Glass Fabric Architectures: (a) 4-Ply 2D Laminate ( $2D-S-24x4$ ,  $3.25 \text{ kg/m}^2$ ), (b) 3D Orthogonally Woven Monolith ( $3D-S-93$ ,  $3.15 \text{ kg/m}^2$ )

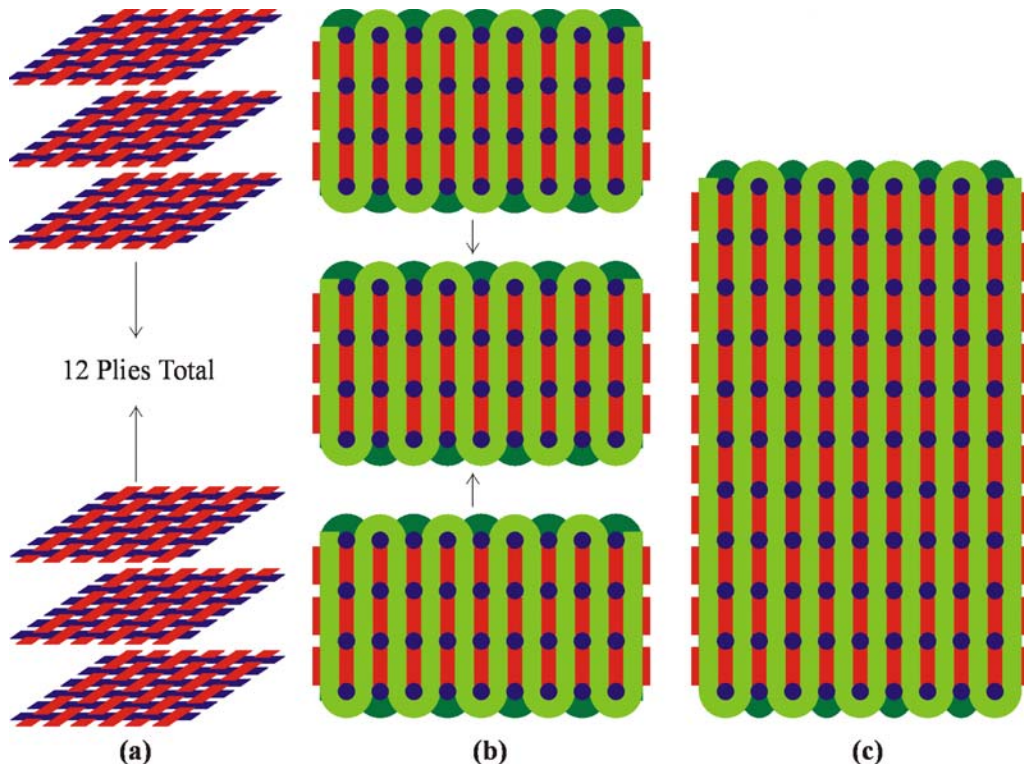
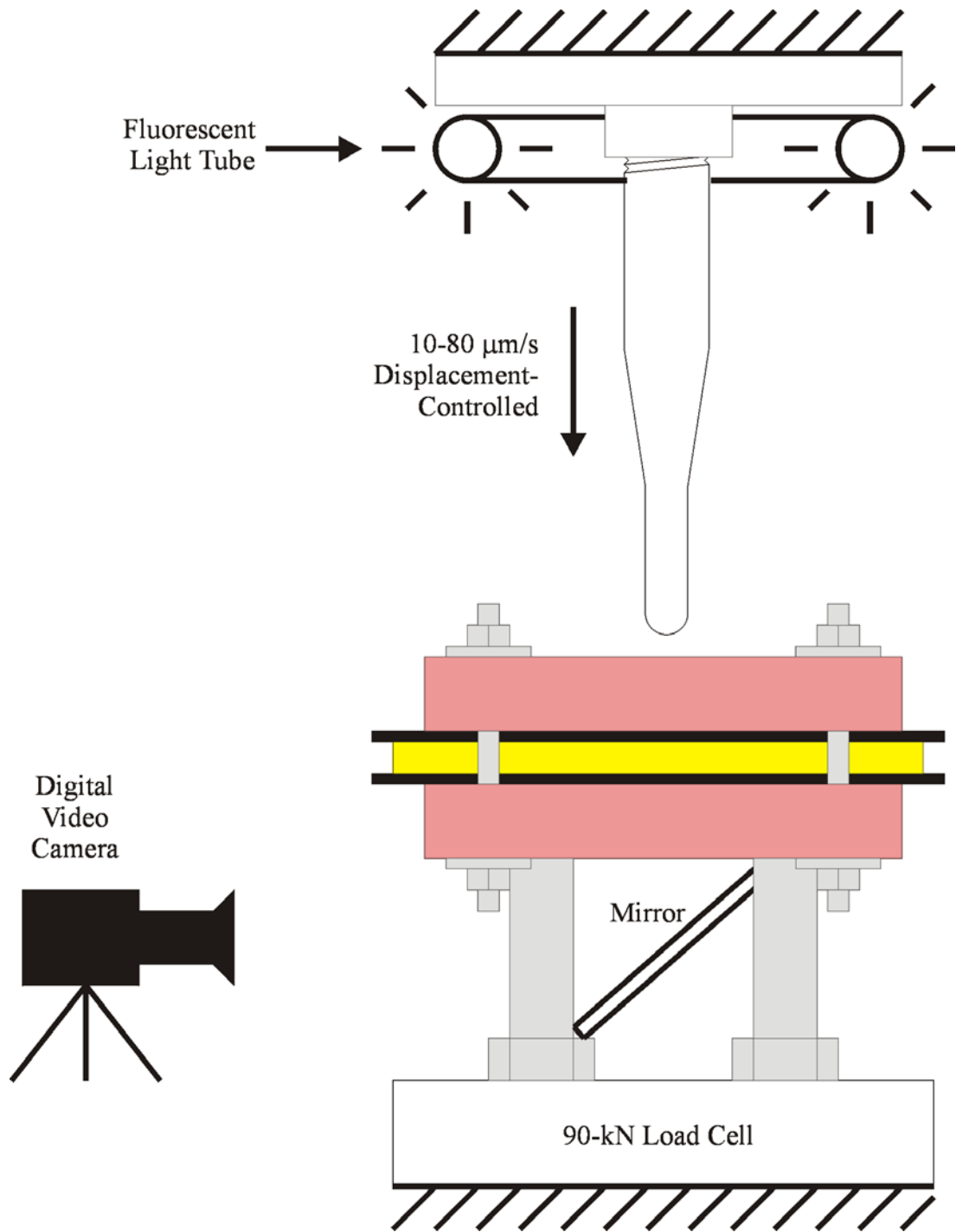
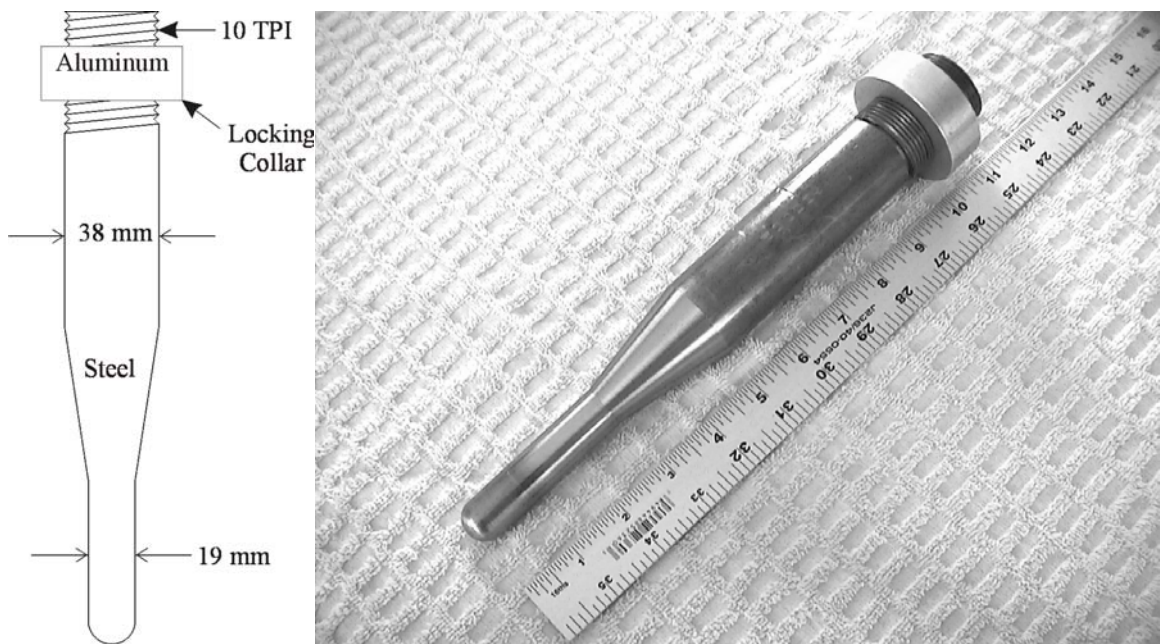


Figure 3.2 Thick S2-Glass Fabric Architectures: (a) 12-Ply 2D Laminate ( $2D-S-24x12$ ,  $9.77 \text{ kg/m}^2$ ), (b) 3-Ply Laminate of 3D Orthogonally Woven Monoliths ( $3D-S-93x3$ ,  $9.46 \text{ kg/m}^2$ ), (c) 3D Orthogonally Woven Monolith ( $3D-S-270$ ,  $9.15 \text{ kg/m}^2$ )



**Figure 3.3 Displacement-Controlled Quasi-Static Transverse Puncture (INSTRON 4400R)**



**Figure 3.4 Perforator for Quasi-Static Puncture**

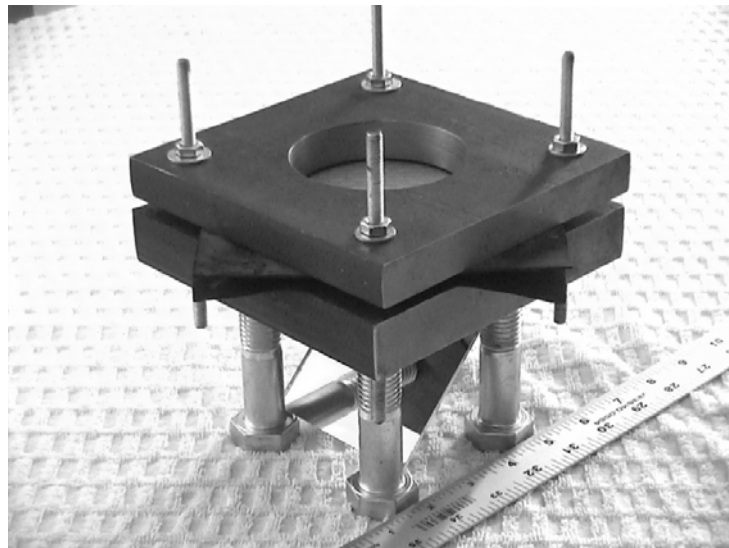
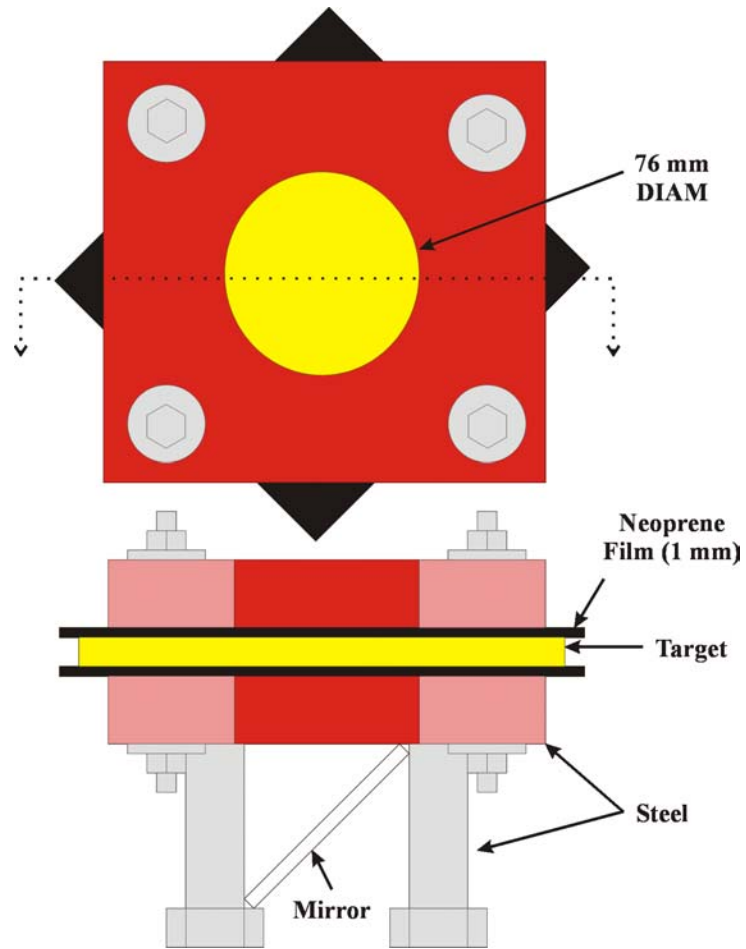


**Figure 3.5 Target Fixture for Quasi-Static Puncture**

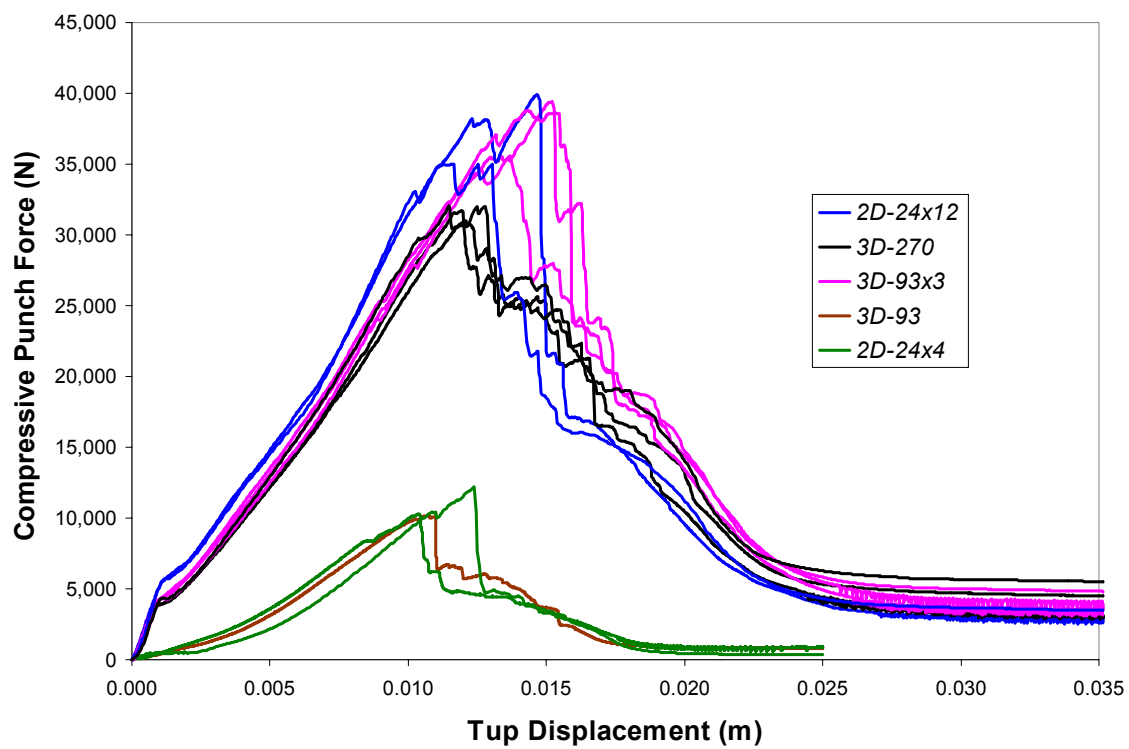


**Figure 3.6 Perforating Load as a Function of Tup Displacement**

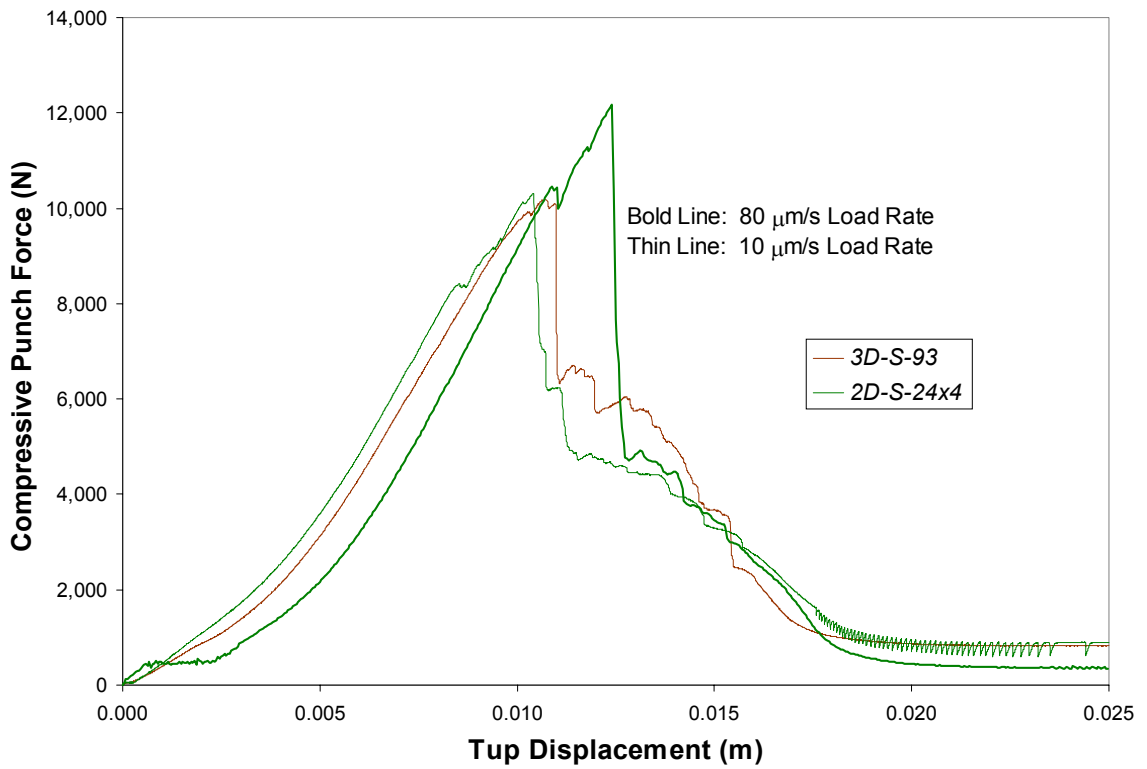


**Figure 3.7** Perforating Load-Displacement for Thin 2D Laminates (*2D-S-24x4*) and 3D Monoliths (*3D-S-93*) at Two Rates of Loading: 10 and 80 μm/s

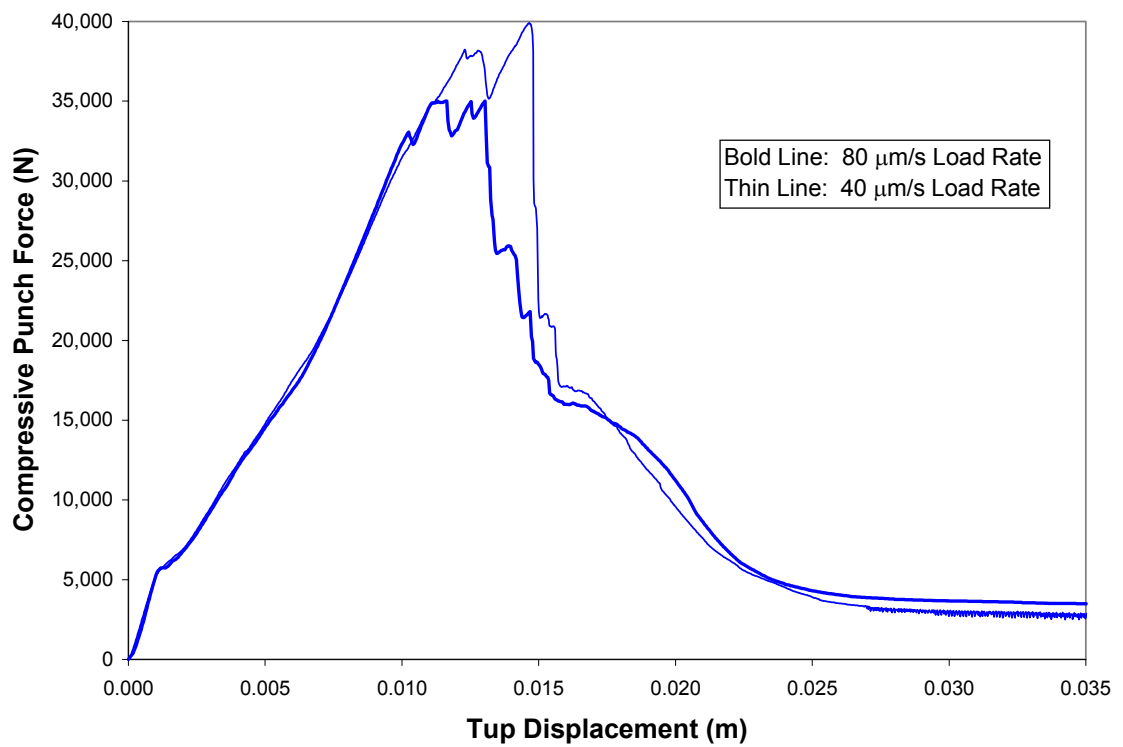


**Figure 3.8 Perforating Load-Displacement for Thick 2D Laminates (*2D-S-24x12*) at Two Rates of Loading: 40 and 80 μm/s**

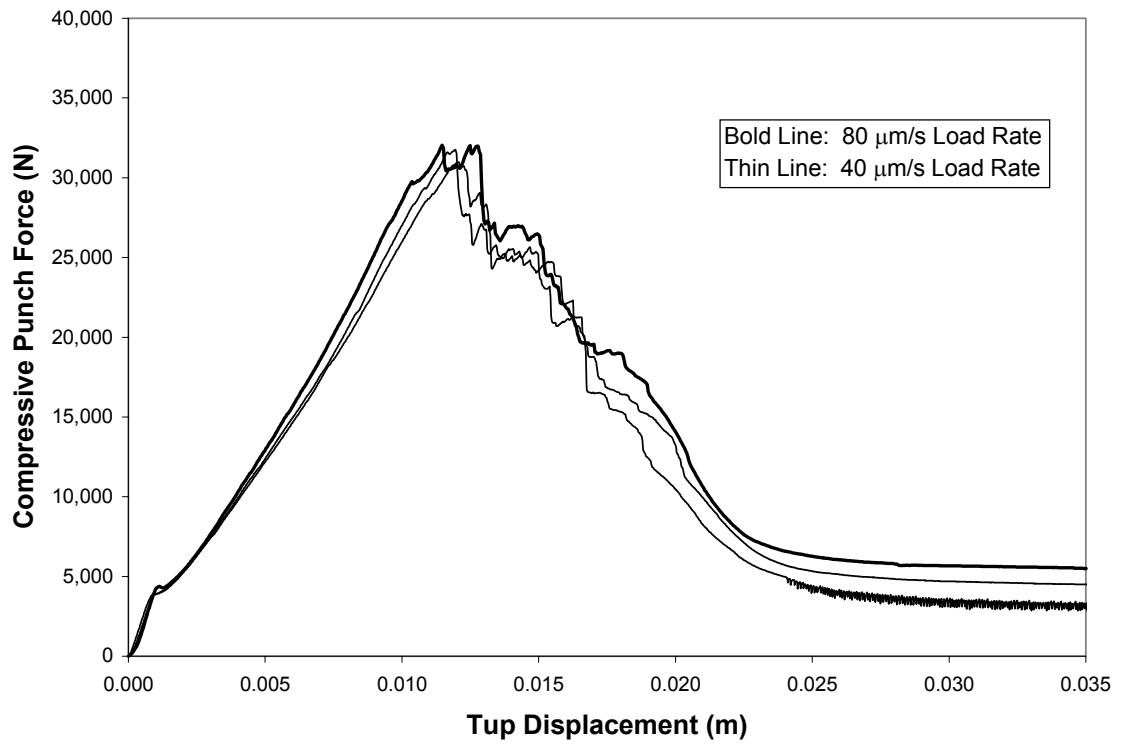


**Figure 3.9 Perforating Load-Displacement for Thick 3D Monoliths (3D-S-270) at Two Rates of Loading: 40 and 80 μm/s**

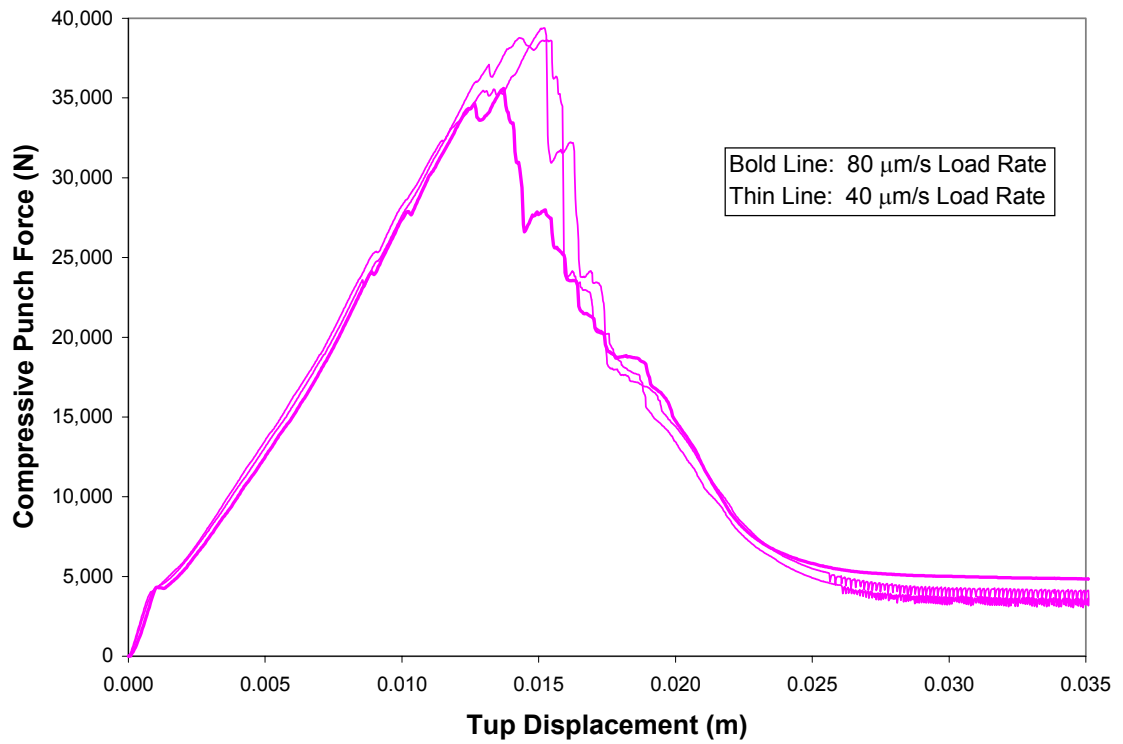


**Figure 3.10** Perforating Load-Displacement for Thick 3-Ply 3D Laminates (*3D-S-93x3*) at Two Rates of Loading: 40 and 80  $\mu\text{m/s}$

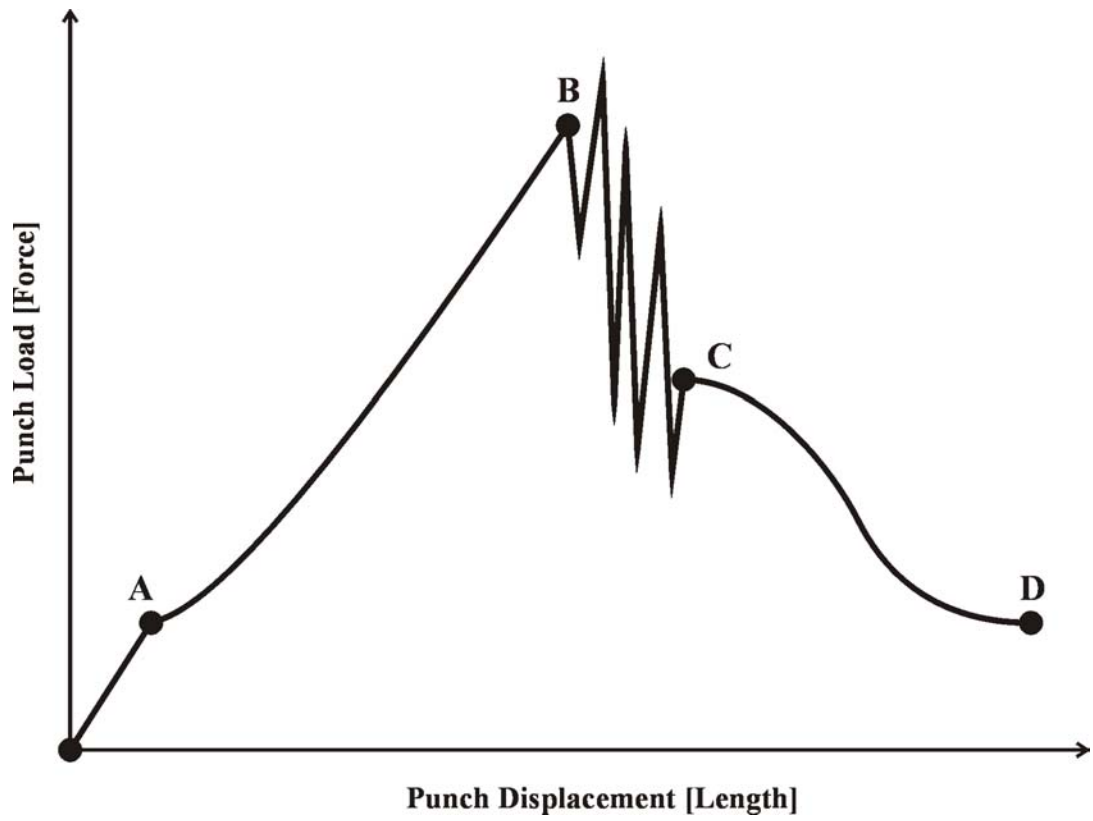


**Figure 3.11 Stages of Quasi-Static Punch Loading and Perforation Failure**

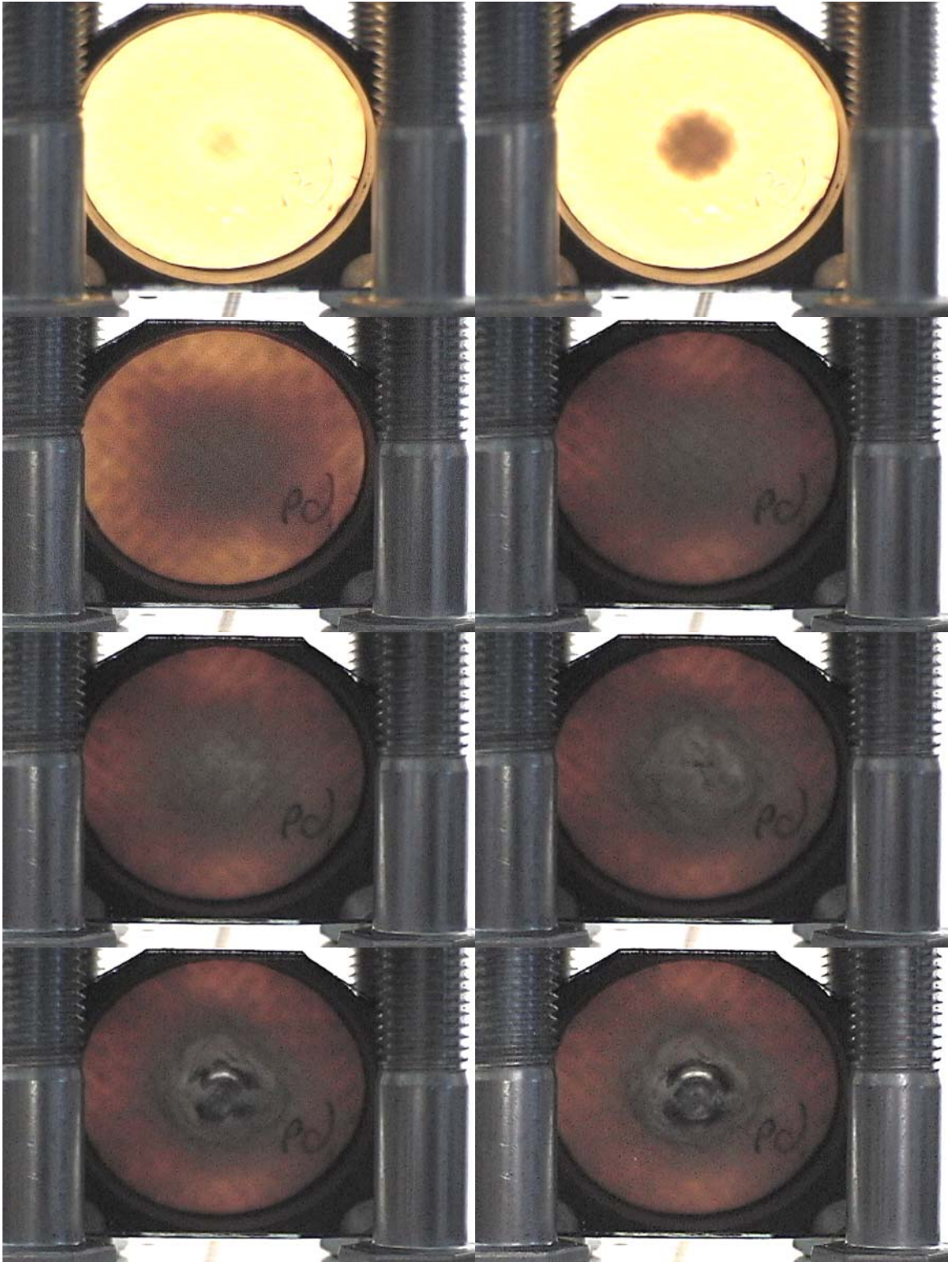


**Figure 3.12 Representative Video Frames Captured during Quasi-Static Perforation of 2D-S-24x12-2, Near Transition Points**

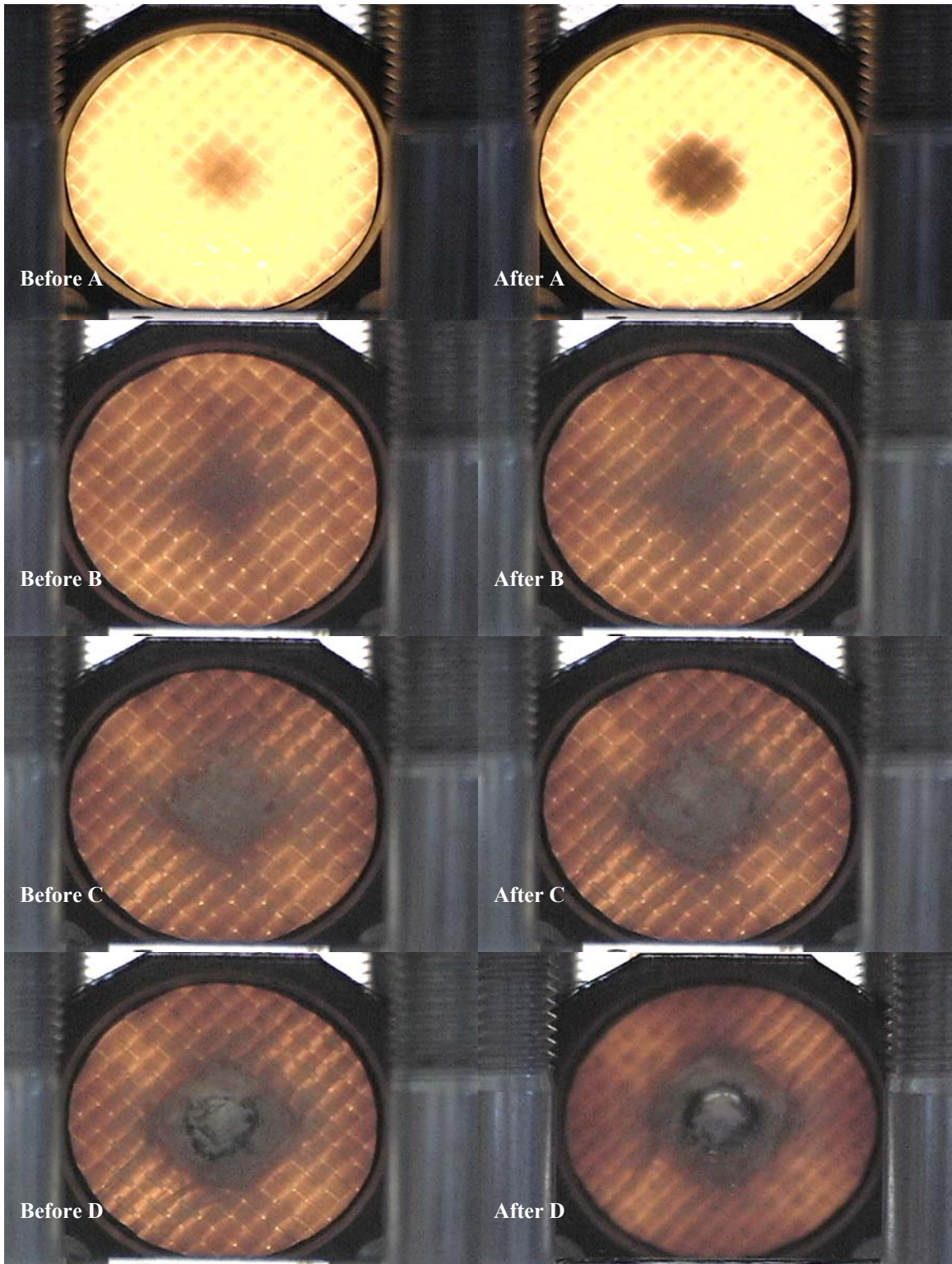


**Figure 3.13 Representative Video Frames Captured during Quasi-Static Perforation of 3D-S-270-3, Near Transition Points**

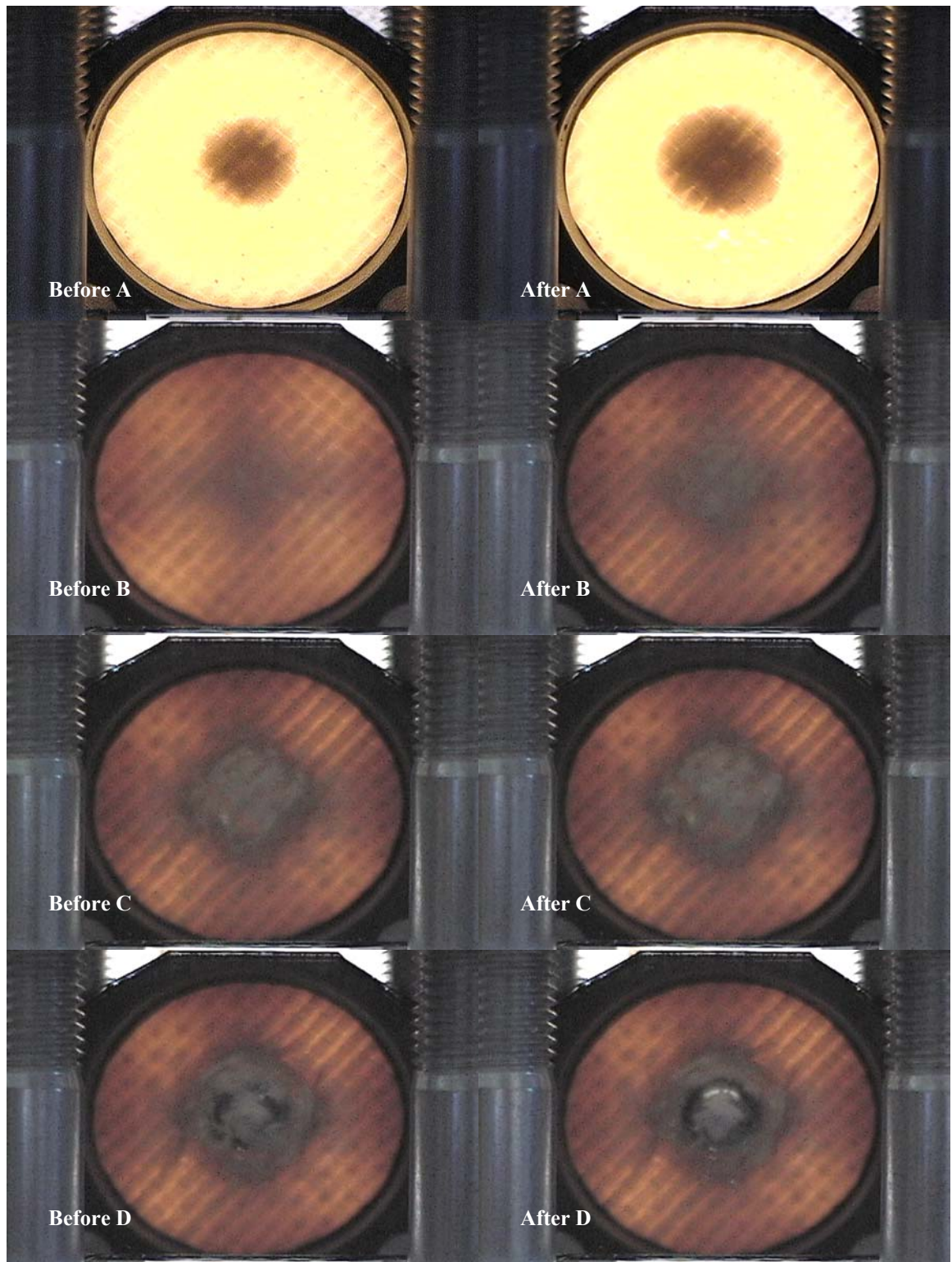


**Figure 3.14 Representative Video Frames Captured during Quasi-Static Perforation of 3D-93x3-3, Near Transition Points**

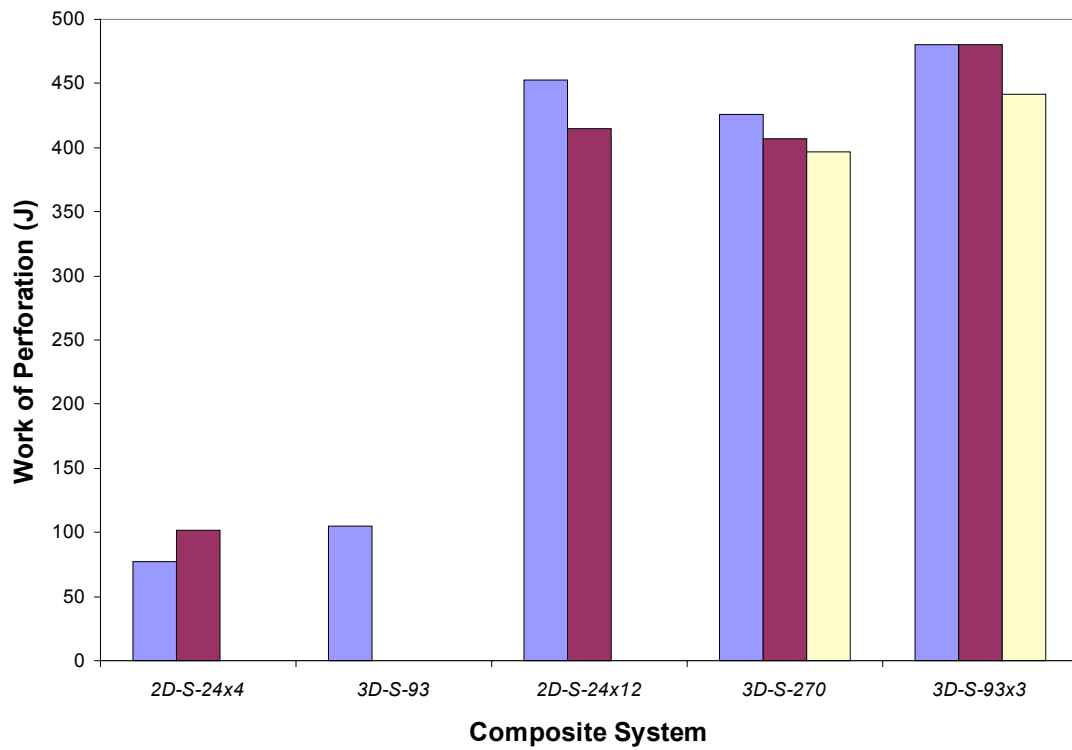


**Figure 3.15 Work of Quasi-Static Perforation**

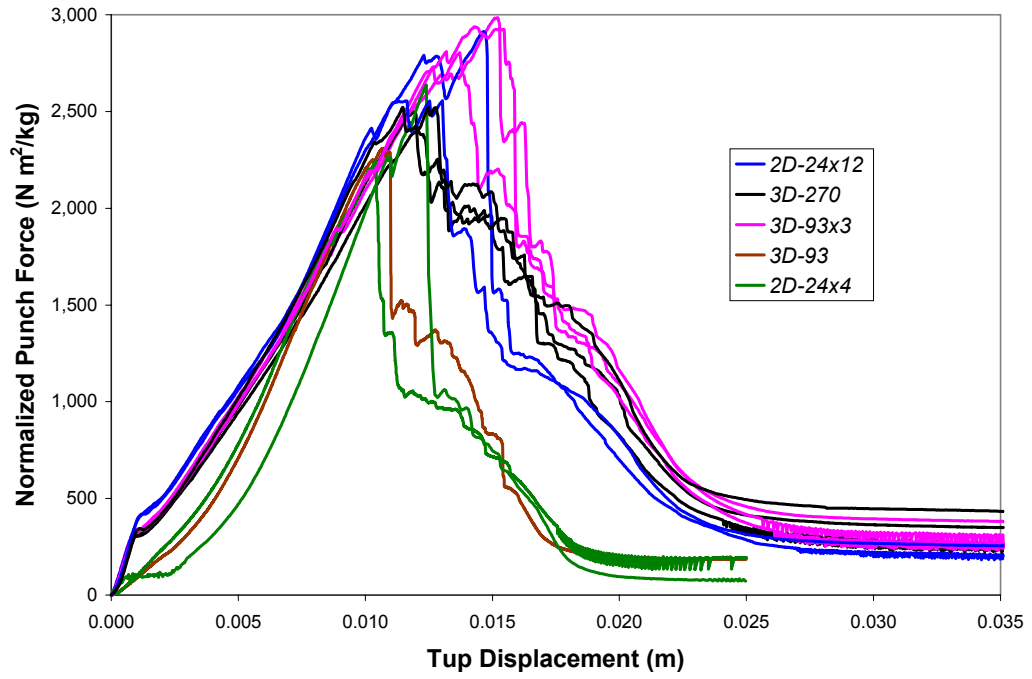


**Figure 3.16 Load-Displacement Behavior, Normalized by Target Areal Density**

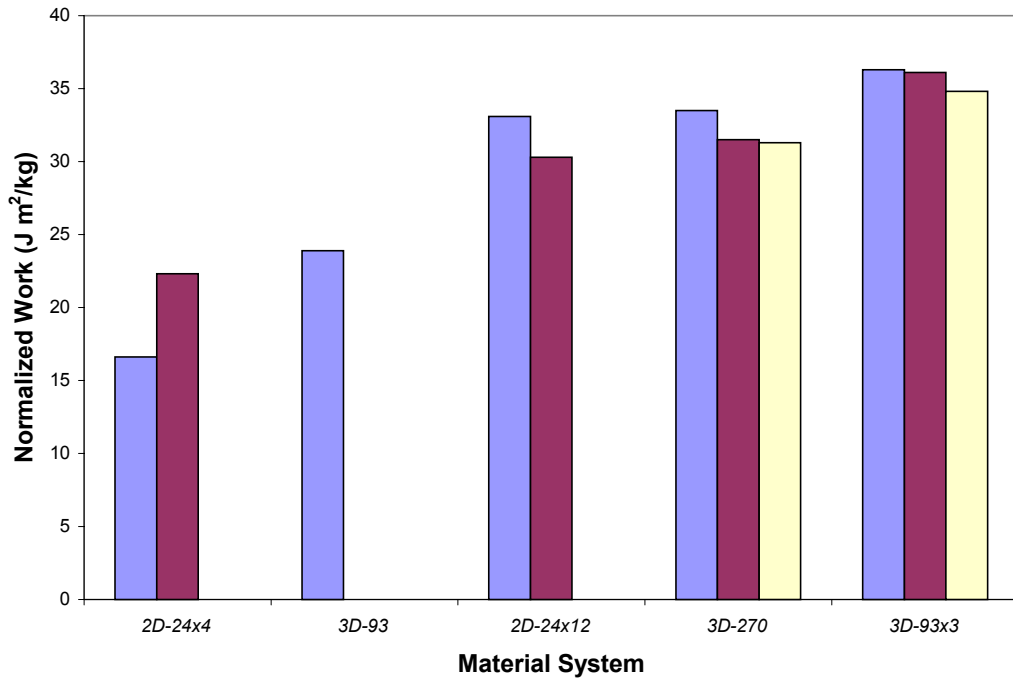
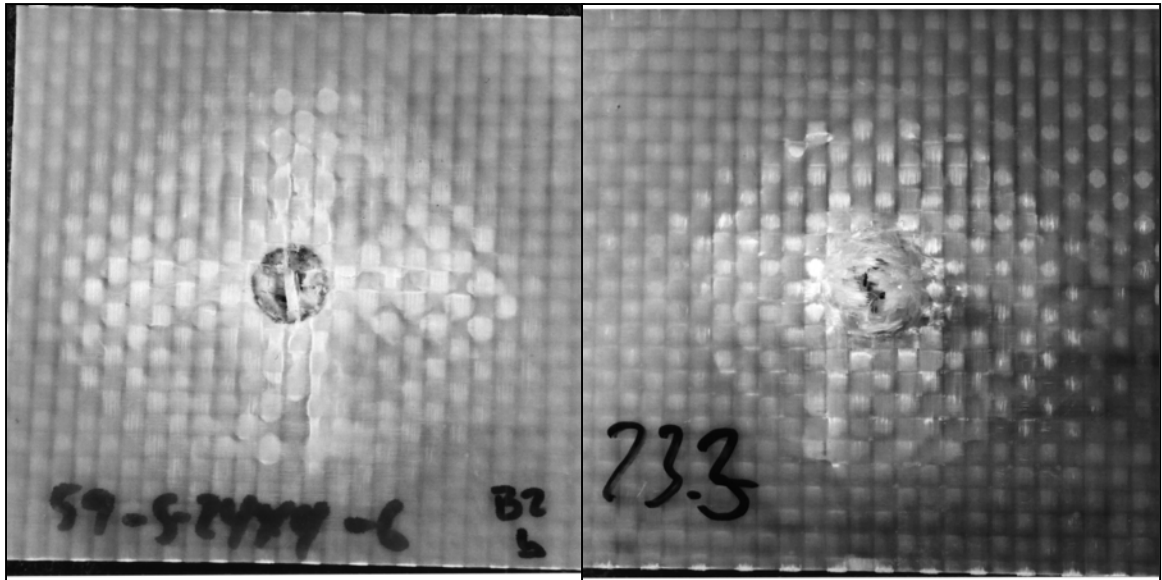
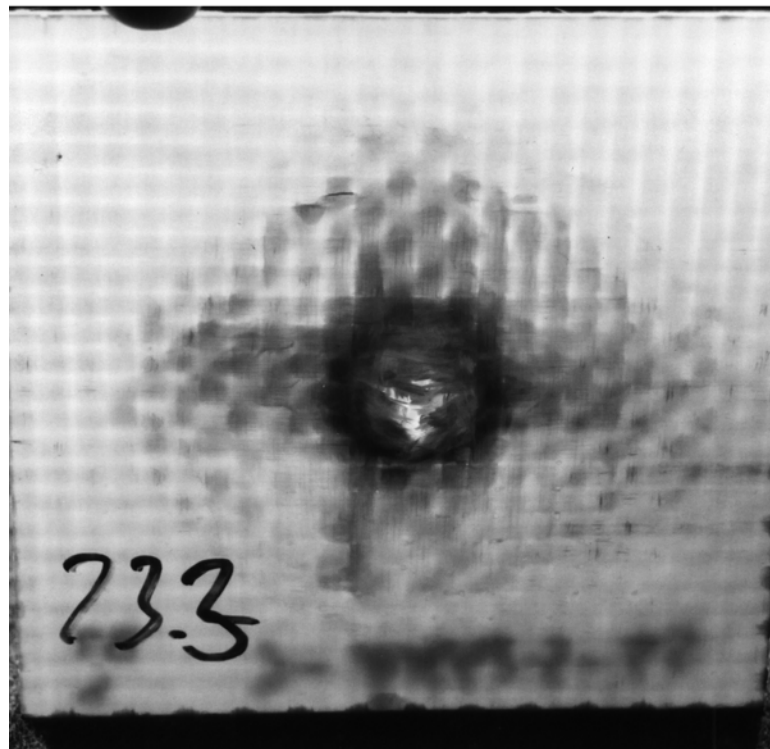


**Figure 3.17 Work of Quasi-Static Perforation, Normalized by Target Areal Density**



(a)

(b)



(c)

**Figure 3.18 Post-Mortem Photographs of 2D-S-24x4-2: (a) Front Face, (b) Rear Face, (c) Rear Face under Back-Lighting**

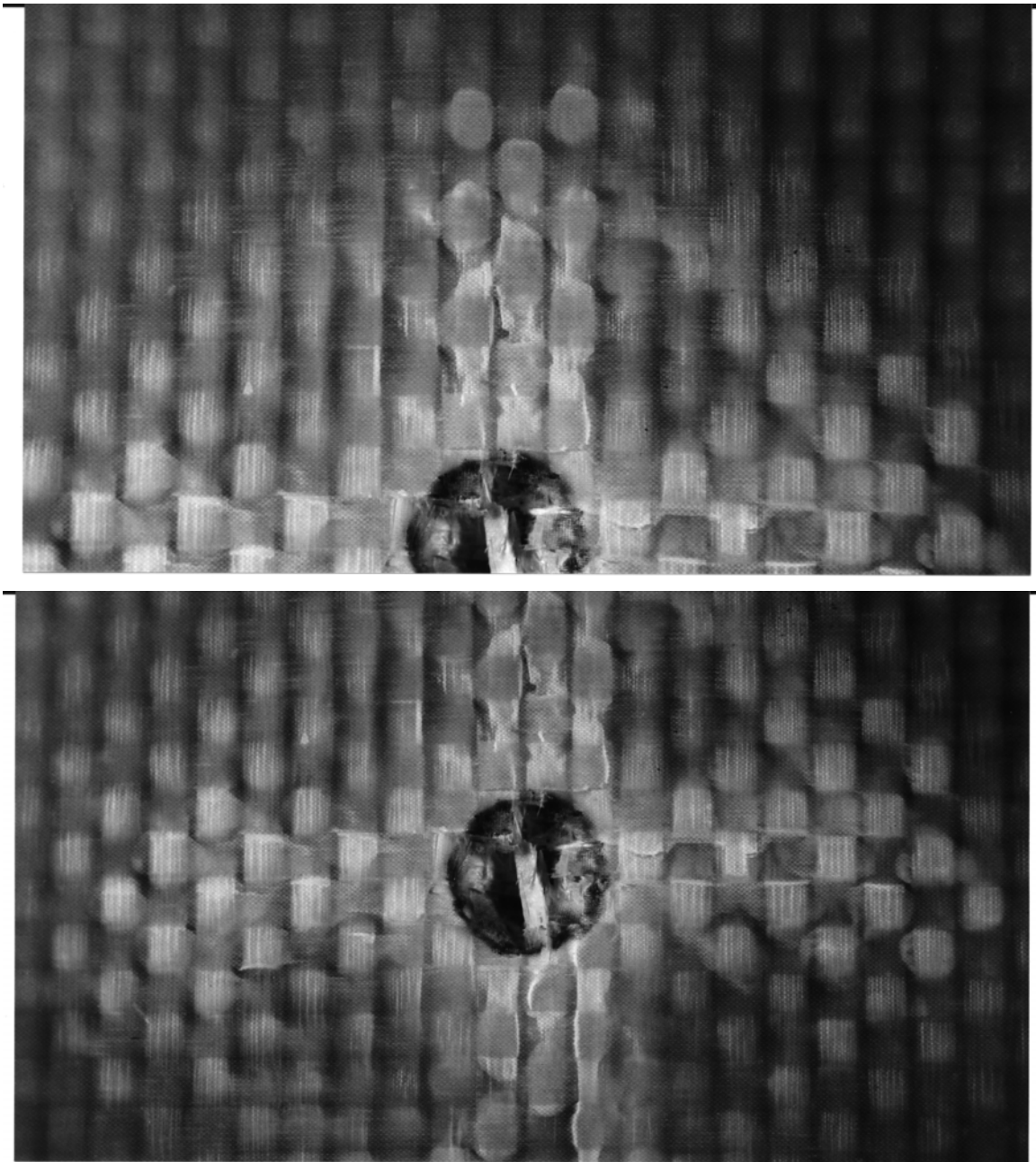


**Figure 3.19** Closer Views of Front Target Face (*2D-S-24x4-2*)

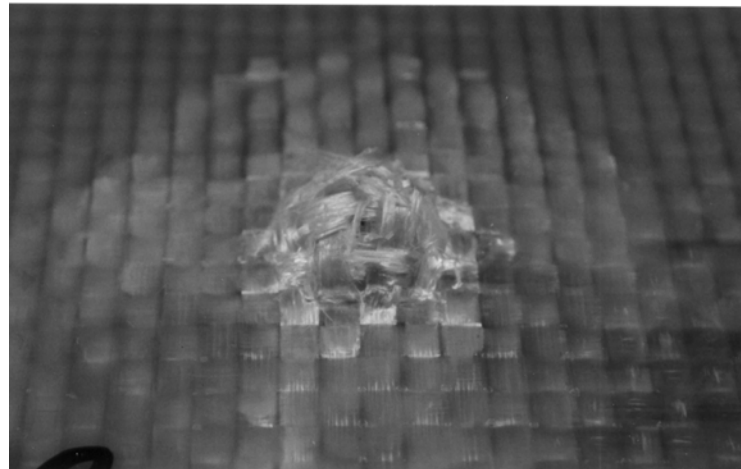
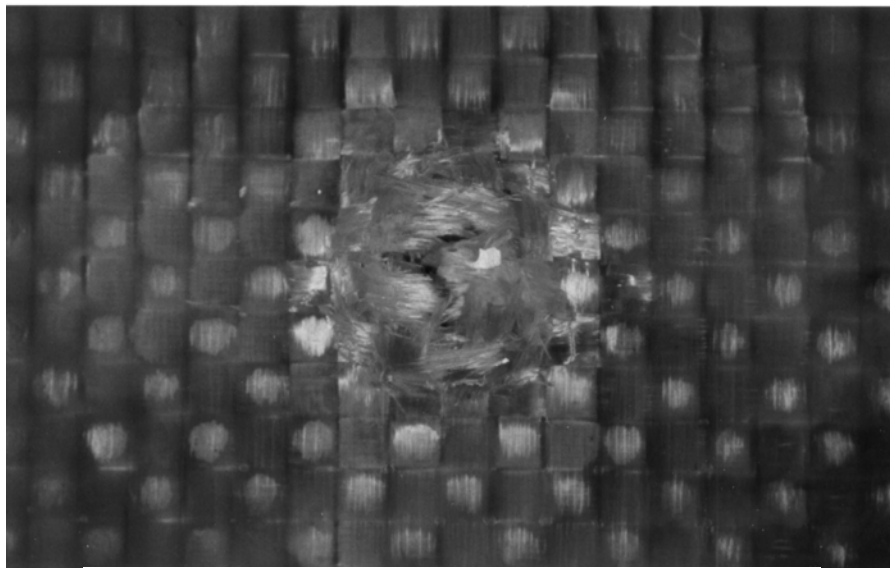
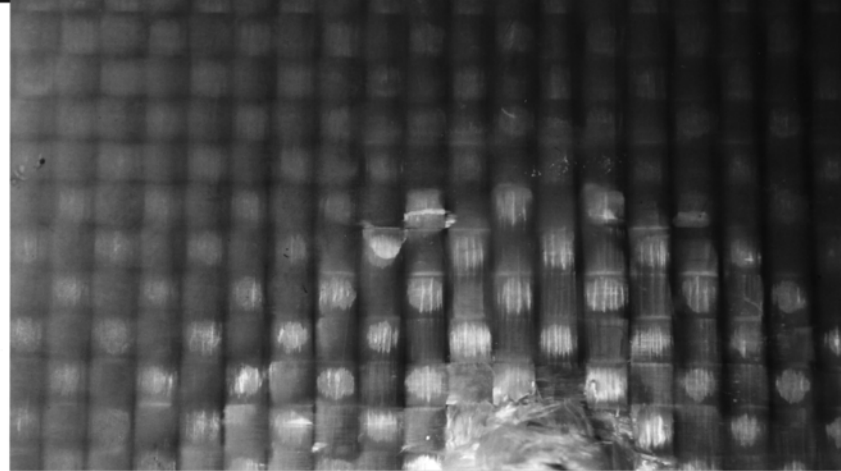
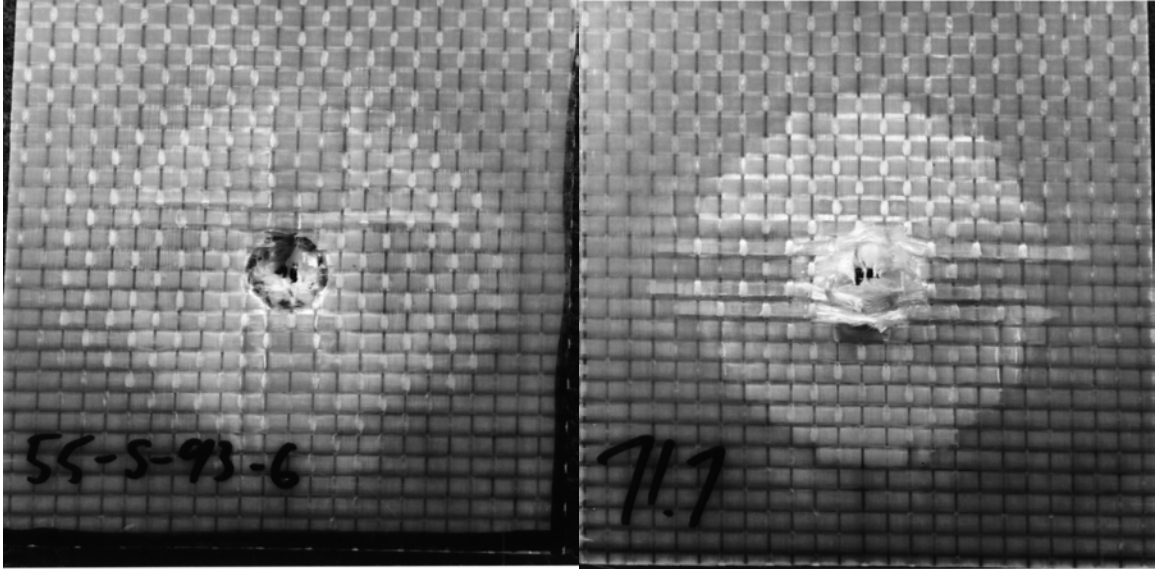
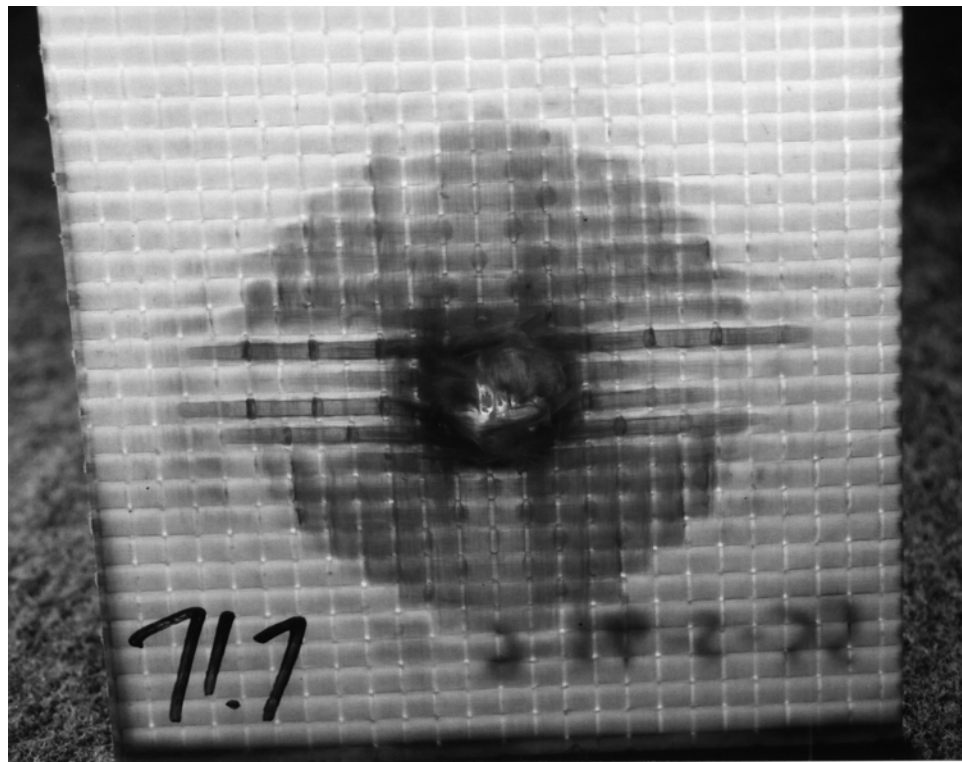


**Figure 3.20 Closer Views of Rear Target Face (2D-S-24x4-2)**



(a)

(b)



(c)

**Figure 3.21 Post-Mortem Photographs of 3D-S-93-1: (a) Front Face, (b) Rear Face, (c) Rear Face under Back-Lighting**

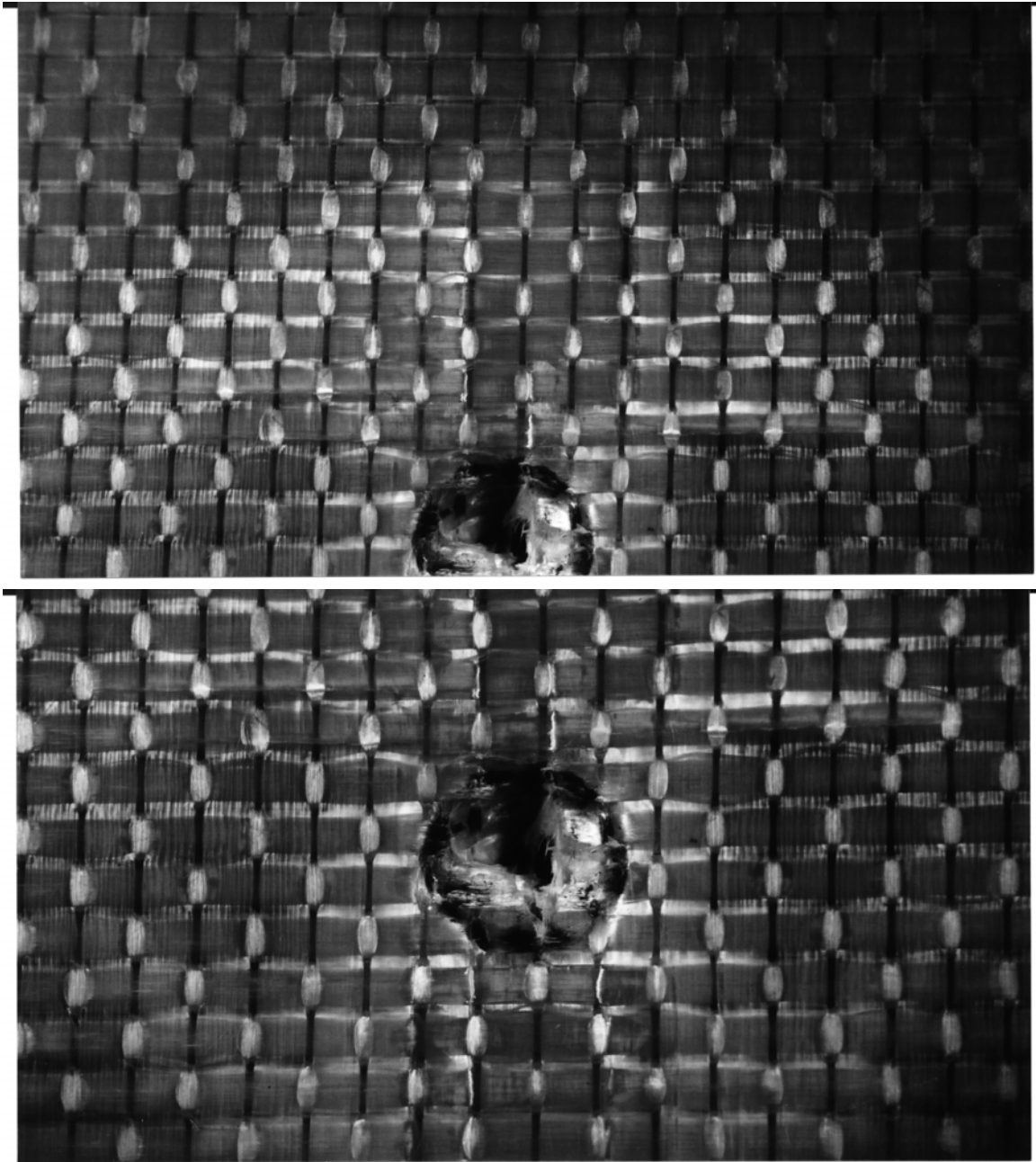


**Figure 3.22 Closer Views of Front Target Face (3D-S-93-1)**

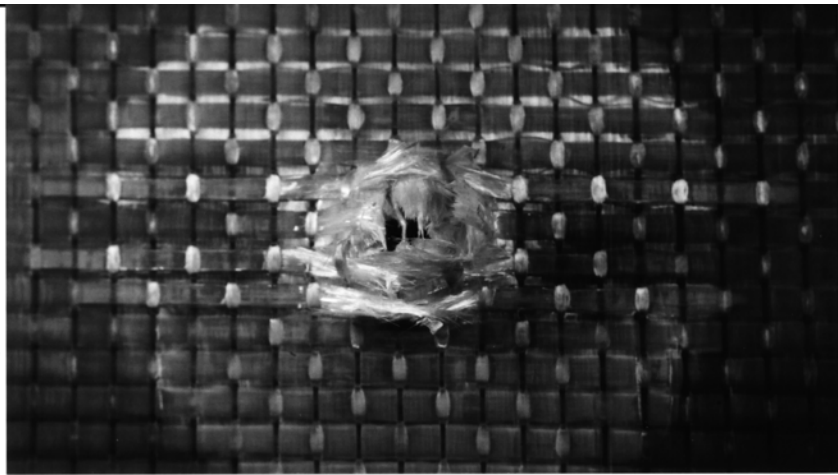
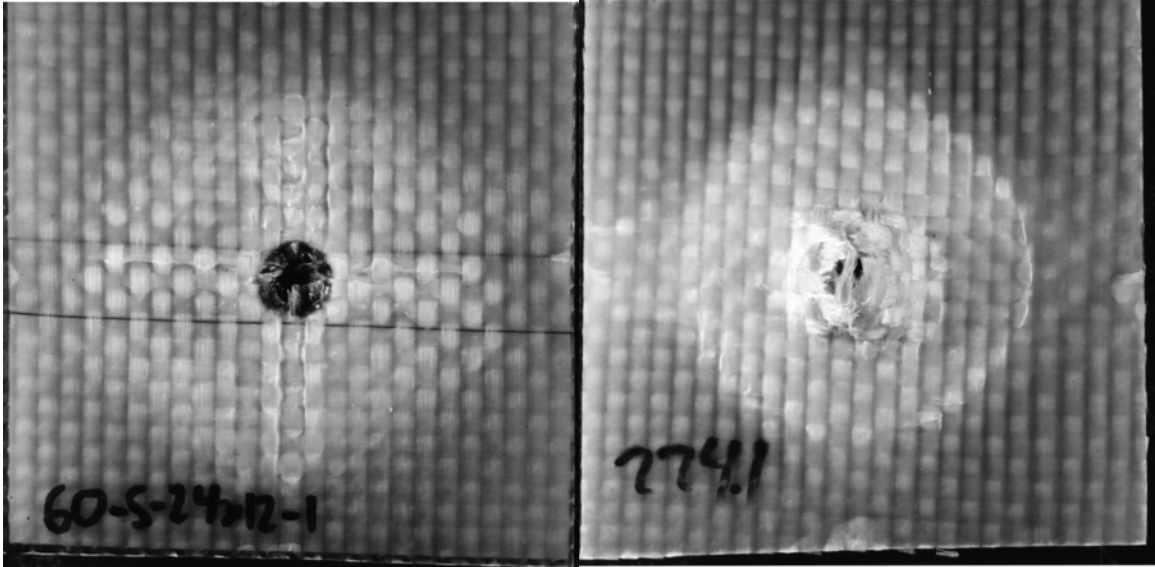
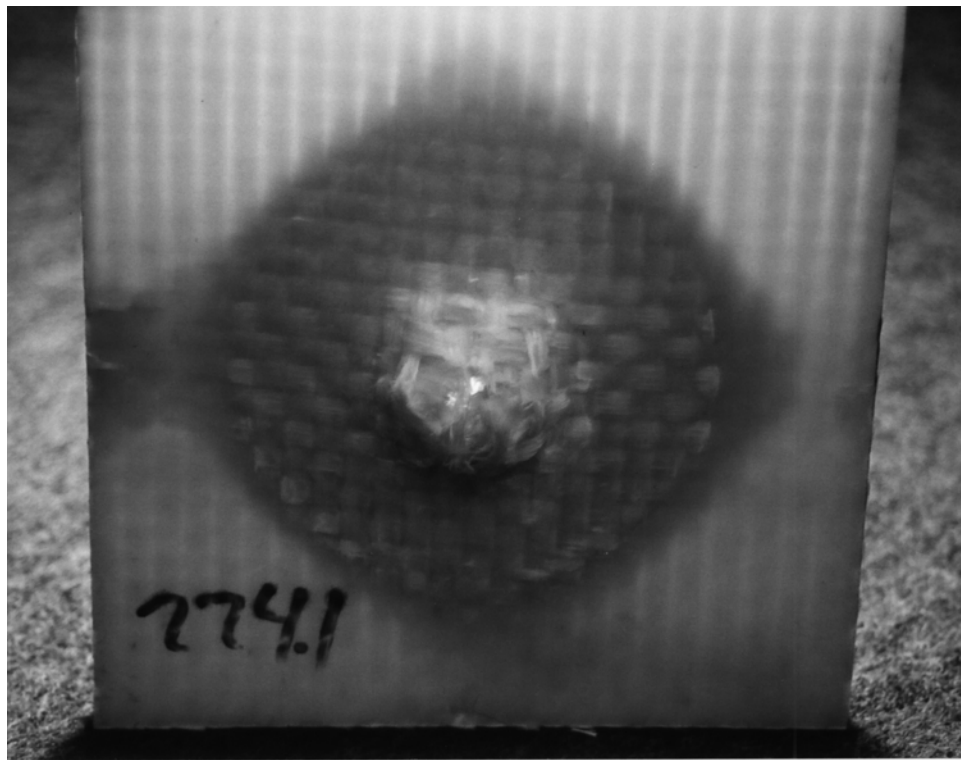


**Figure 3.23 Closer Views of Rear Target Face (3D-S-93-1)**



(a)

(b)



(c)

**Figure 3.24 Post-Mortem Photographs of 2D-S-24x12-1: (a) Front Face, (b) Rear Face, (c) Rear Face under Back-Lighting**

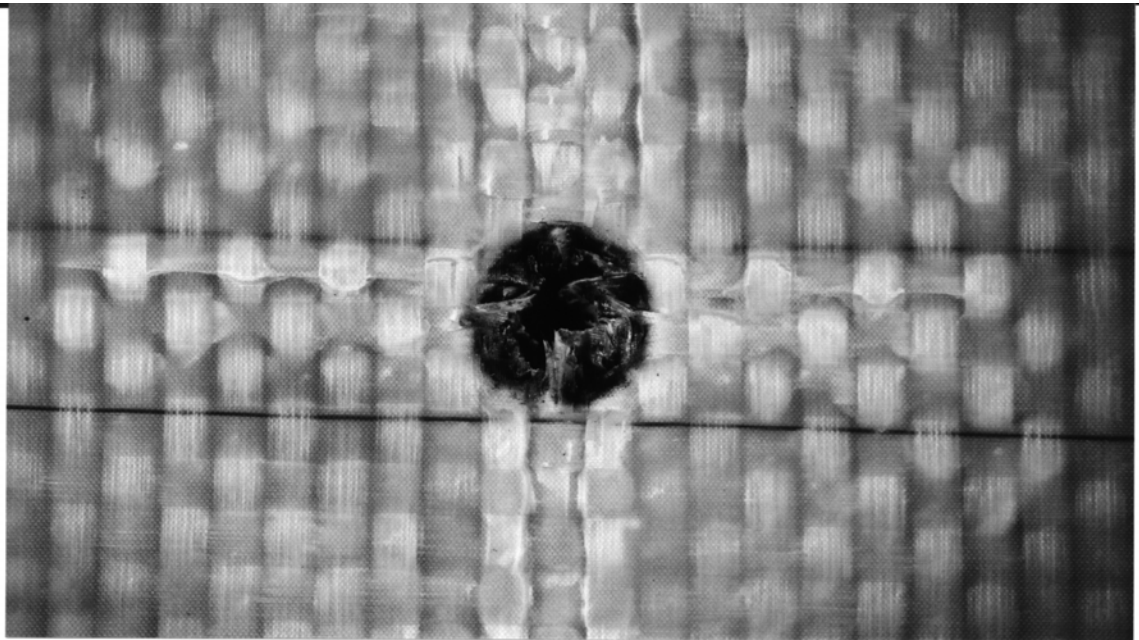


**Figure 3.25** Closer Views of Front Target Face (*2D-S-24x12-1*)

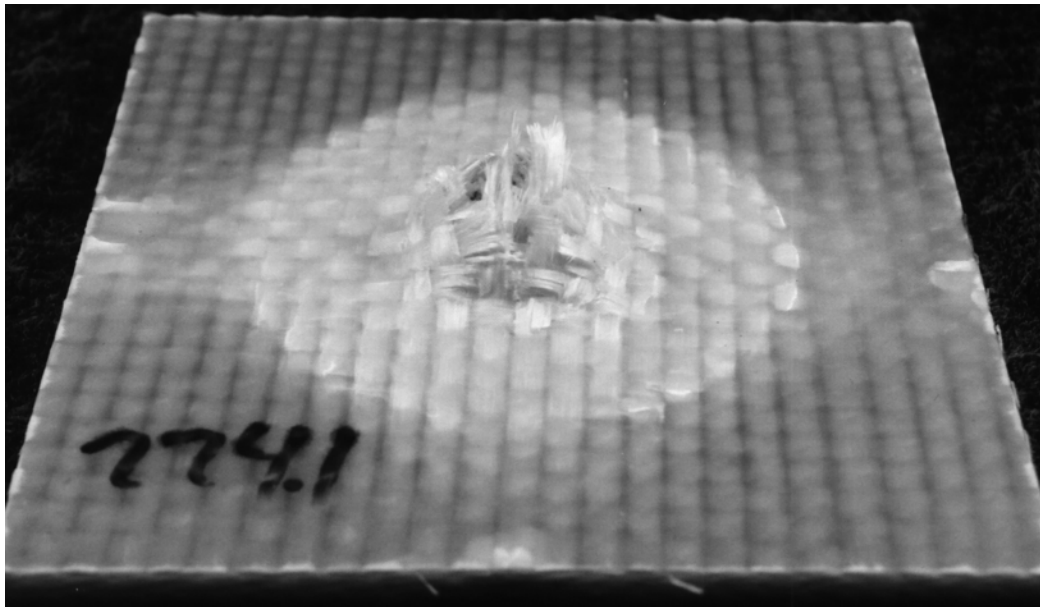
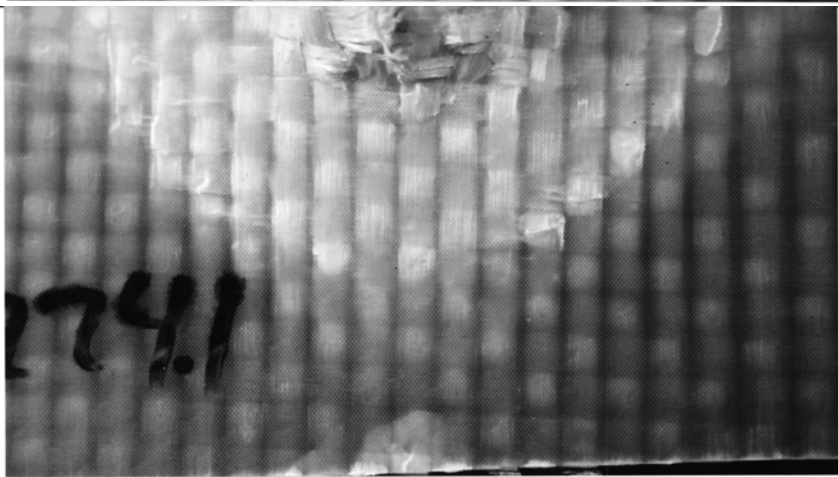
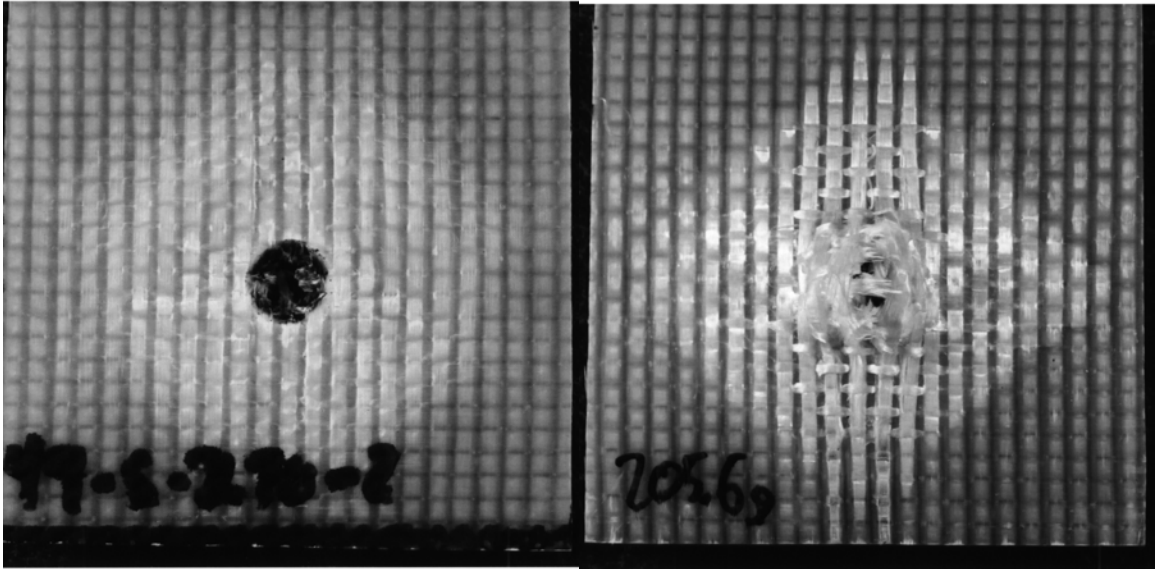


**Figure 3.26 Closer Views of Rear Target Face (2D-S-24x12-1)**



(a)

(b)



(c)

**Figure 3.27 Post-Mortem Photographs of 3D-S-270-2: (a) Front Face, (b) Rear Face, (c) Rear Face under Back-Lighting**

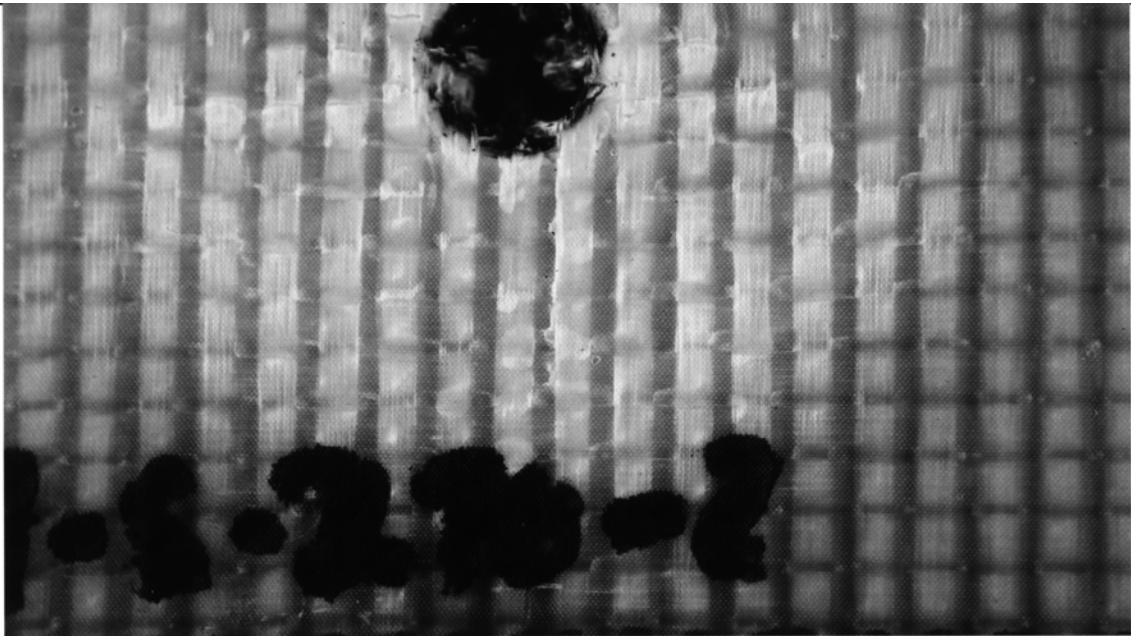


**Figure 3.28 Closer Views of Front Target Face (3D-S-270-2)**

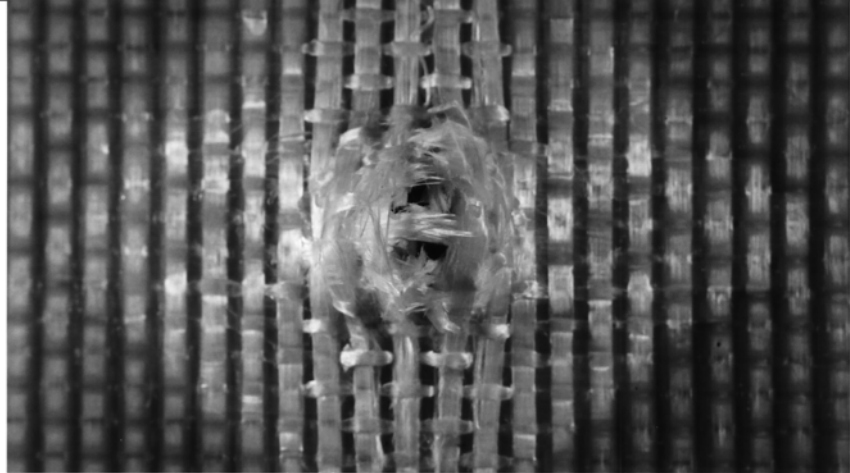
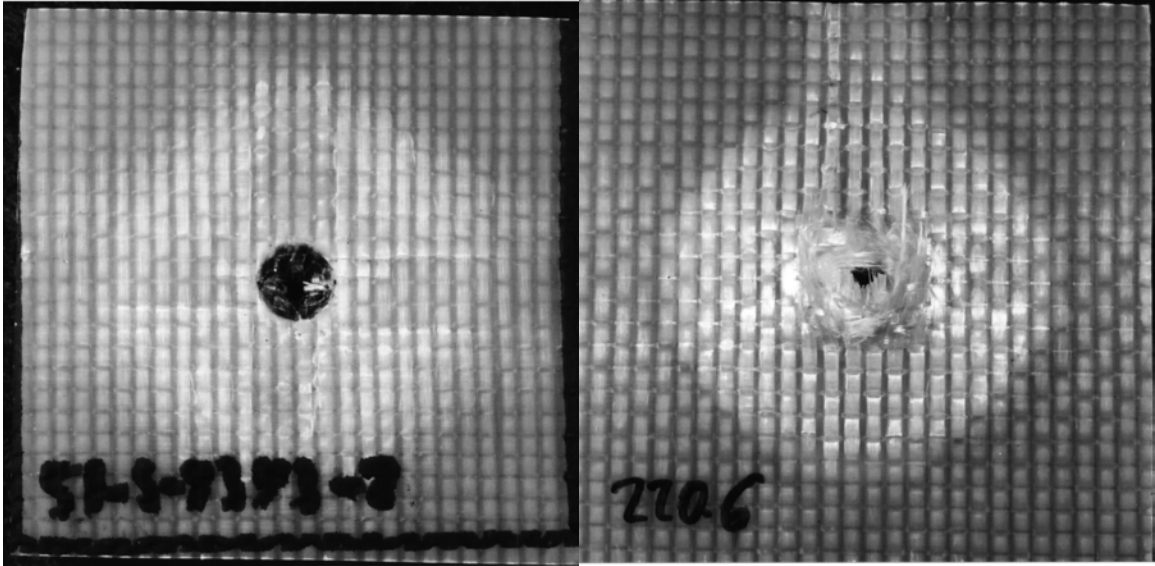
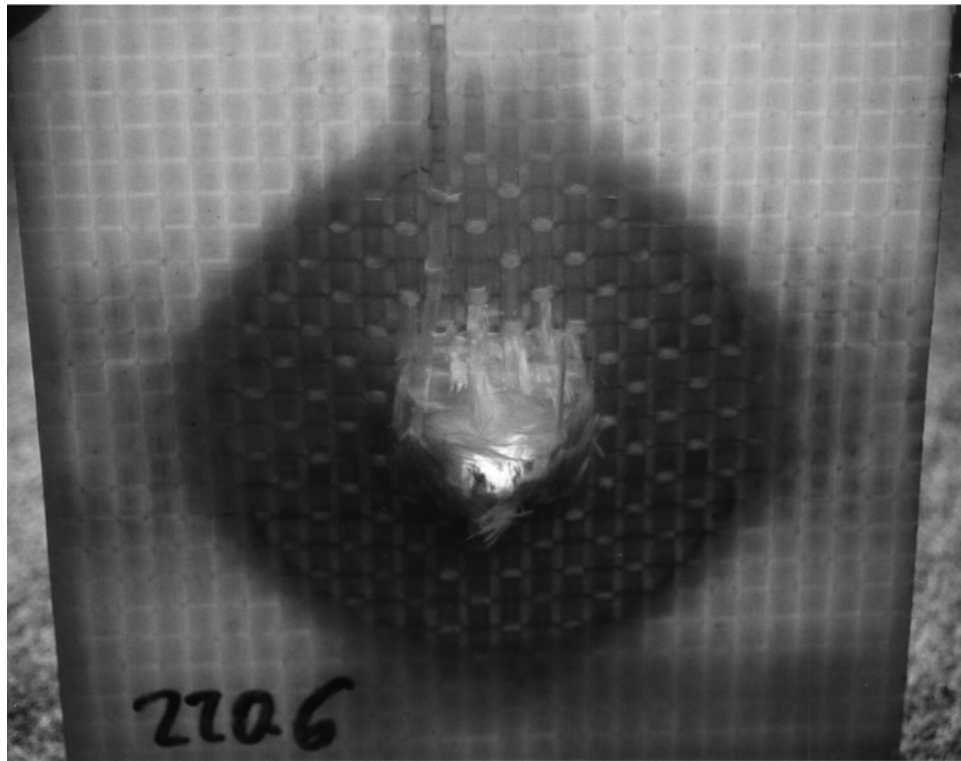


**Figure 3.29** Closer Views of Rear Target Face (3D-S-270-2)



(a)

(b)



(c)

**Figure 3.30 Post-Mortem Photographs of 3D-S-93x3-2: (a) Front Face, (b) Rear Face, (c) Rear Face under Back-Lighting**

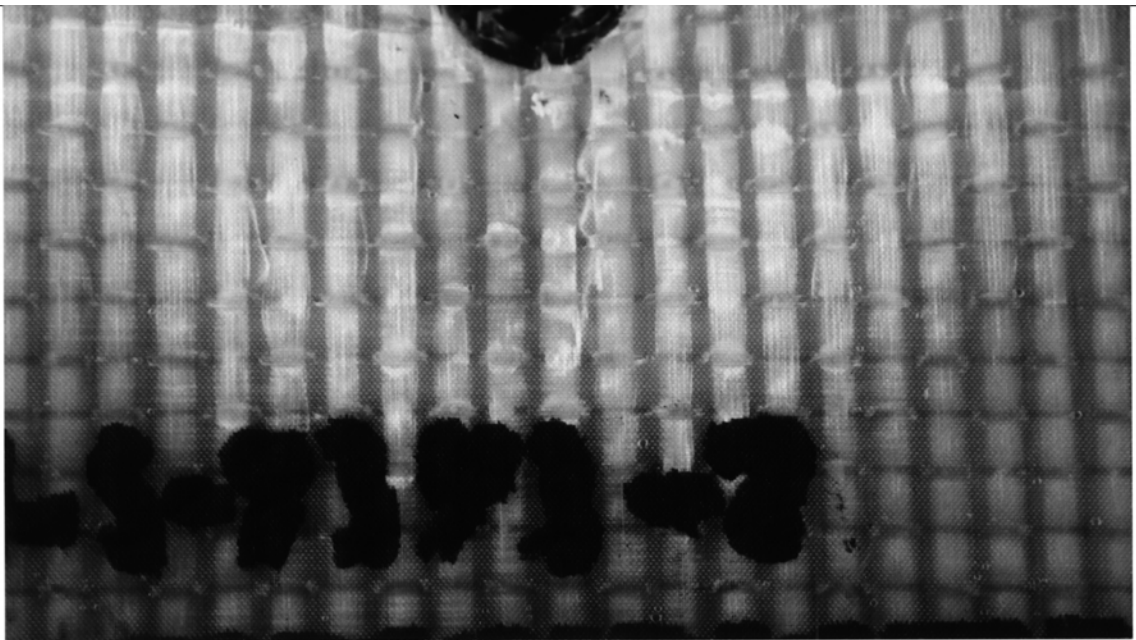
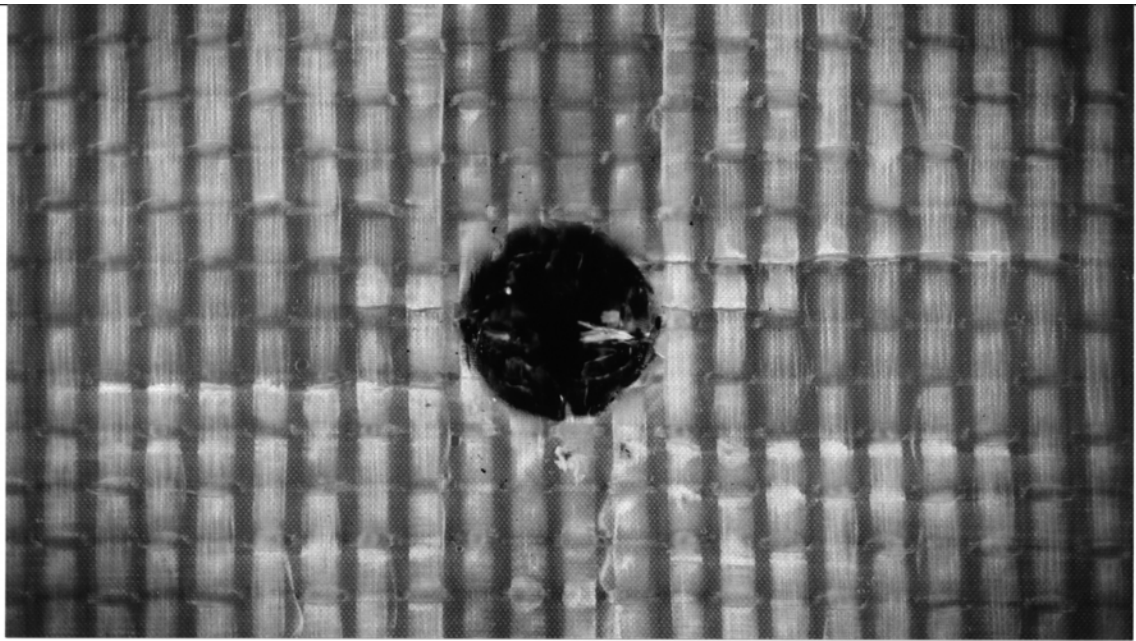


**Figure 3.31 Closer Views of Front Target Face (3D-S-93x3-2)**

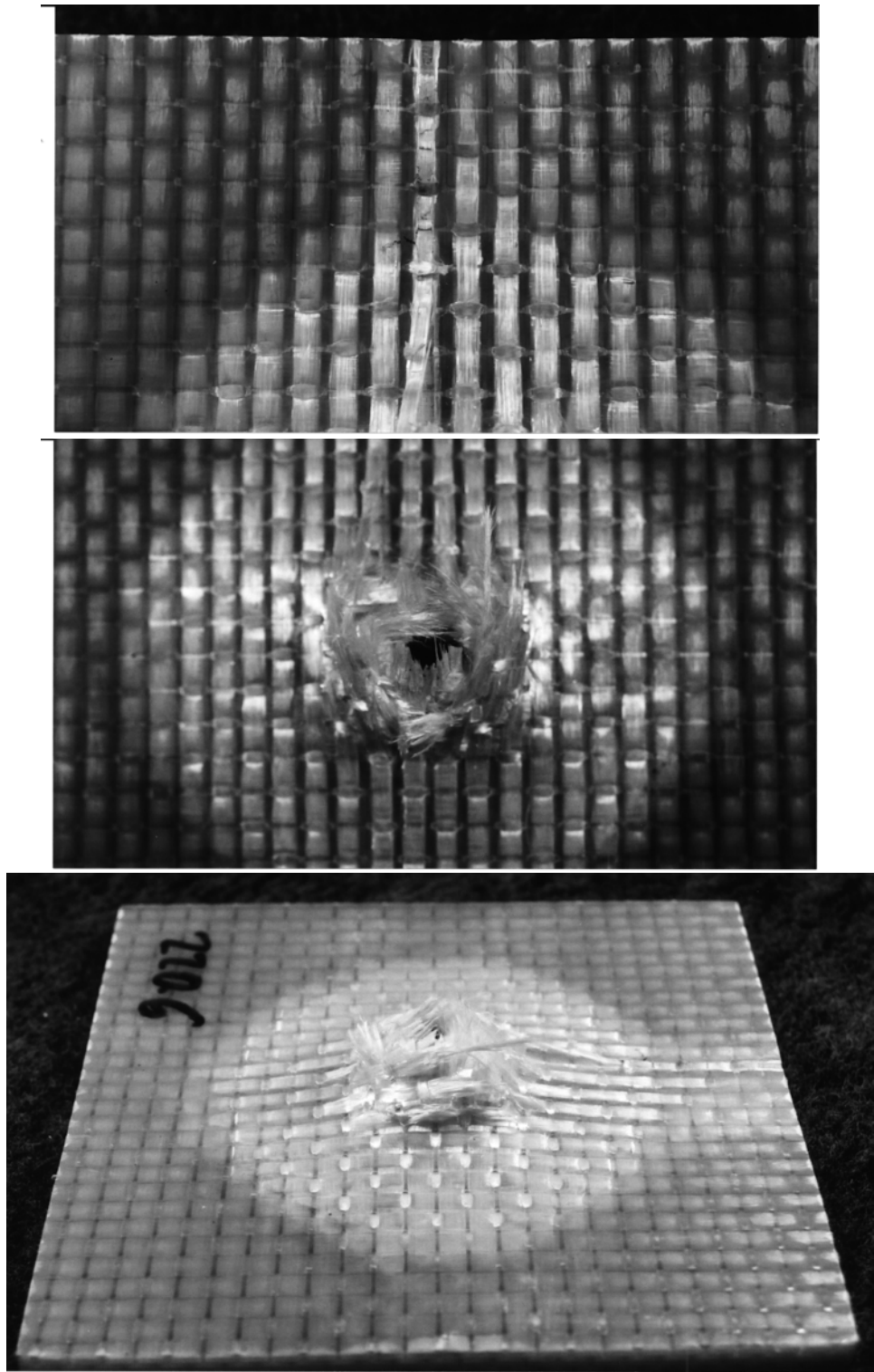
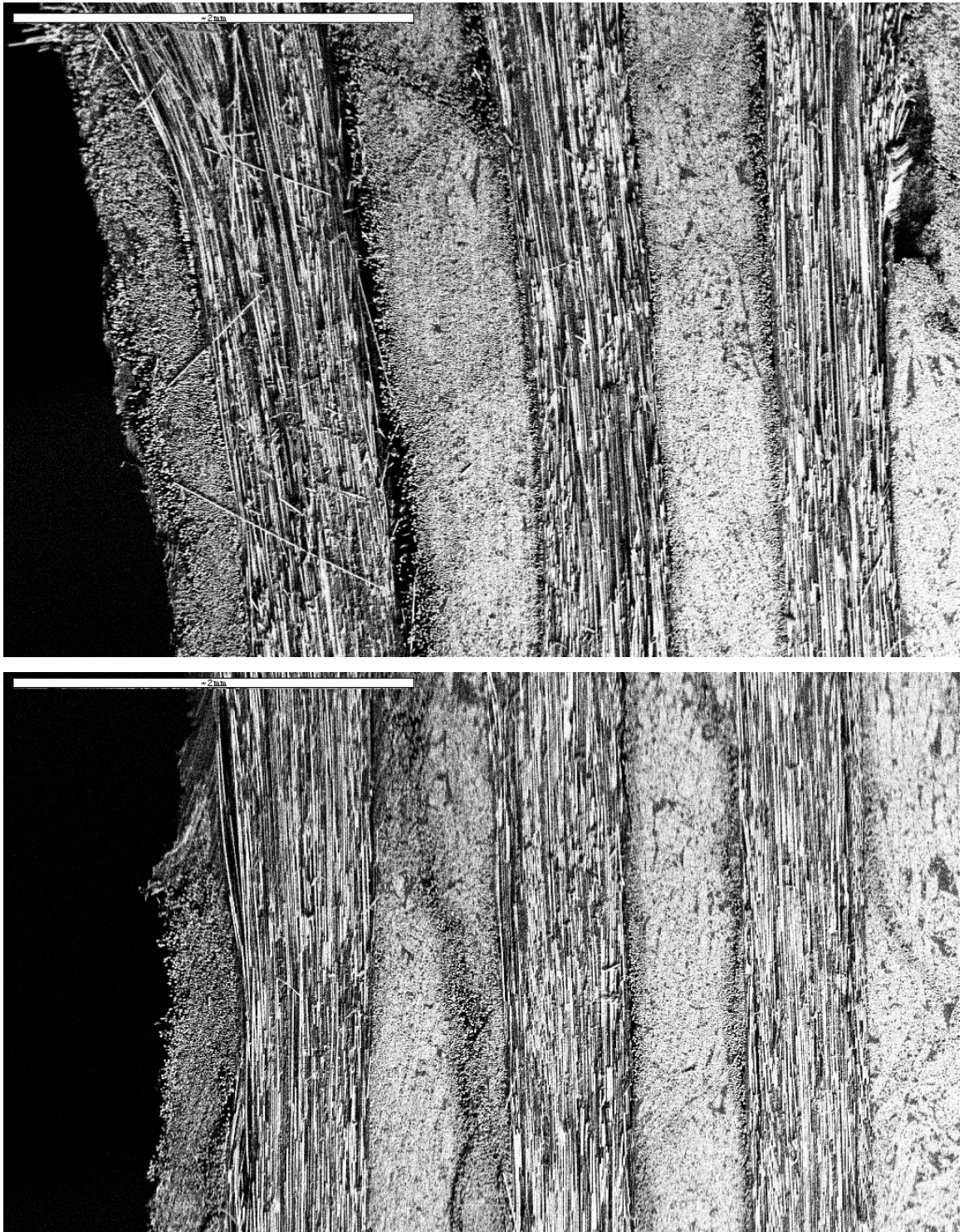
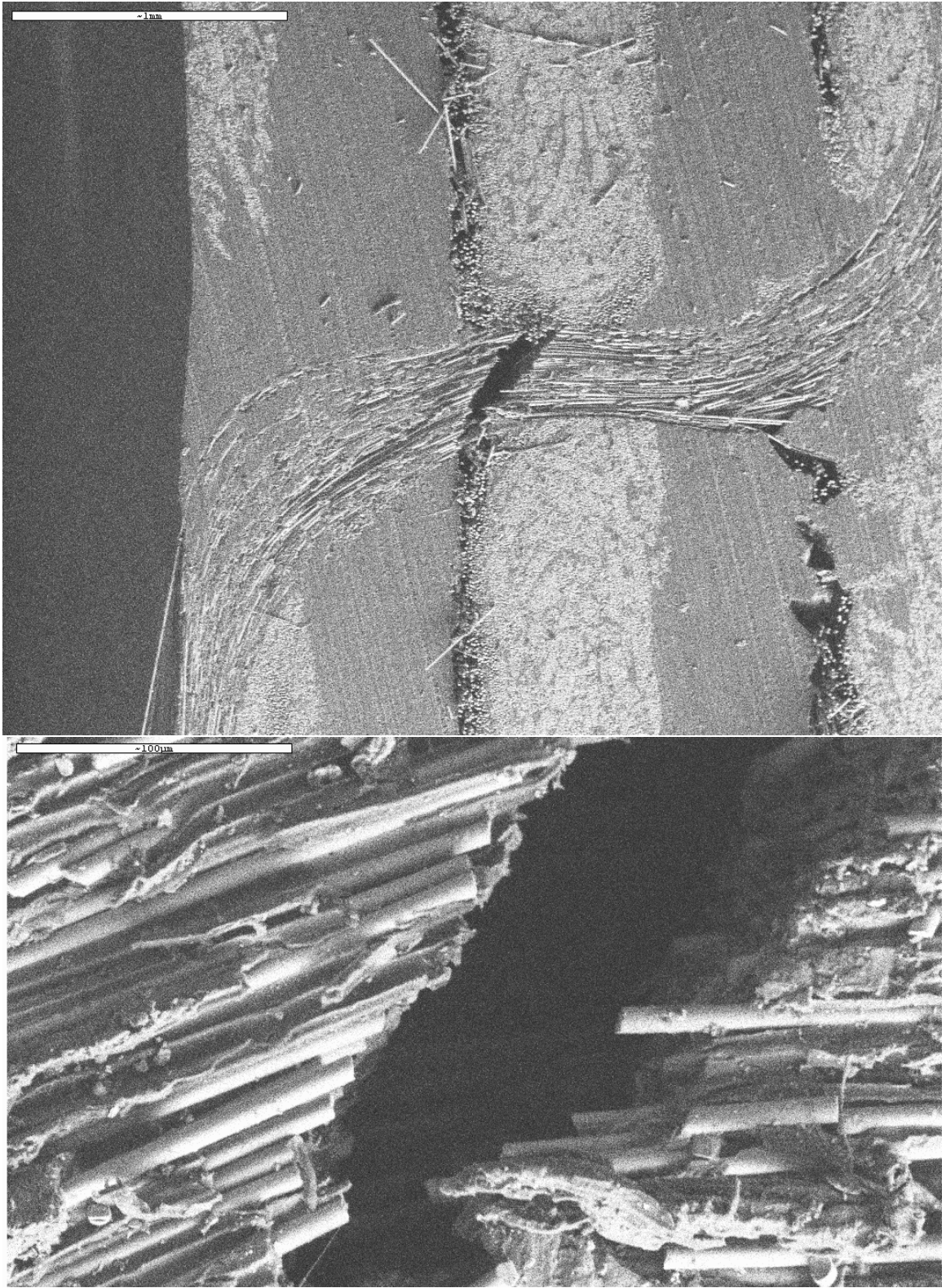


Figure 3.32 Closer Views of Rear Target Face (3D-S-93x3-2)



**Figure 3.33 Post-Mortem SEM (3D-S-270-2)**



**Figure 3.34 Post-Mortem SEM (3D-S-93x3-2)**

## 4. LOW-VELOCITY IMPACT DAMAGE PROGRESSION

By subjecting specimens to repeated instrumented impacts, residual strength and damage progression can be monitored. The purpose of the low-velocity impact experiments is to examine the progression of damage and capacity for energy-absorption of 2D and 3D woven GFRP composite systems subjected to multiple impacts. Dynamic impact experiments for incident velocities from 2 to 4 m/s are conducted to determine material response as a function of absorbed energy, areal density, and fabric architecture. Photography, scanning electron microscopy, and analysis of contact force evolution are used to assess the progression of damage.

### 4.1 Material Preparation And Fabrication

Five composite systems were examined. Various fabric architectures and constituent materials were selected. In an effort to isolate the effects of reinforcement geometry, samples were produced with comparable areal densities and thicknesses. Two types of fiber were used: E-glass (density,  $\rho_E \approx 2590 \text{ kg/m}^3$ ) and S2-glass (density,  $\rho_{S2} \approx 2510 \text{ kg/m}^3$ ).

#### 4.1.1 E-Glass Systems

Three reinforcement geometries were employed in the construction E-glass-reinforced vinyl-ester composite panels. The fabric architecture of the first material system (*3D-E-96*) was a monolithic, 3D orthogonal weave; see Figure 4.1 for a schematic

of the preform. The second material system (*2D-E-24x4*) was a conventional 2D plain-weave laminate. The fabric preform of the third system consisted of a commercially available, biaxially reinforced warp-knit (*BRWK*). All three composite systems have E-glass fiber rovings and a vinyl-ester resin matrix, Reichhold Hydrex® 100. Consolidation was achieved by vacuum-assisted resin-transfer molding, with a four- to eight-hour post-cure at 85°C. A listing of the material systems is given in Tables 4.1 and 4.2. The areal density of each sample was determined by dividing the mass of each sample by its area, taken to be the product of the two-point averages of the width and length of each square coupon. The stated thickness is a four-point average.

**Table 4.1 E-Glass/Vinyl-Ester Composite Systems for Low-Velocity Impact**

<b>Composite System</b>	<b>Sample Designation</b>	<b>Areal Density (kg/m<sup>2</sup>)</b>	<b>Fiber Volume Fraction</b>	<b>Average Thickness (mm)</b>
<b><i>2D-E-24x4</i> (4-Ply, 2D Laminate)</b>	<i>2D-E-24x4-1</i>	4.45	0.52	2.44
	<i>2D-E-24x4-2</i>	4.53	0.53	2.39
<b><i>BRWK</i> (Biaxially-Reinforced Warp-Knit)</b>	<i>BRWK-E-1</i>	3.99	0.58	2.34
<b><i>3D-E-96</i> (3D Monolith)</b>	<i>3D-E-96-1</i>	4.36	0.53	2.41
	<i>3D-E-96-2</i>	4.32	0.54	2.36
	<i>3D-E-96-3</i>	4.37	0.52	2.44

#### 4.1.2 S2-Glass Systems

A description of the preparation and fabrication of the S2-glass systems is provided in Section 3.1. Only the thin composite systems (*2D-S-24x4* and *3D-S-93*) are used for the low-velocity impact experiments. These systems are listed in Table 4.2, including the areal density, fiber-volume-fraction, and 4-point average thickness for each sample.

**Table 4.2 S2-Glass/Rubber-Toughened-Epoxy-Vinyl-Ester Composite Systems for Low-Velocity Impact**

Composite System	Sample Designation	Areal Density (kg/m <sup>2</sup> )	Fiber Volume Fraction	Thickness (mm)
<b><i>2D-S-24x4</i></b> (4-ply, 2D Laminate)	<i>2D-S-24x4-3</i>	4.44	0.55	2.36
	<i>2D-S-24x4-4</i>	4.49	0.54	2.41
	<i>2D-S-24x4-5</i>	4.82	0.49	2.64
	<i>2D-S-24x4-6</i>	4.64	0.49	2.64
	<i>2D-S-24x4-7</i>	4.77	0.49	2.67
<b><i>3D-S-93</i></b> (3D Monolith)	<i>3D-S-93-3</i>	4.37	0.56	2.24
	<i>3D-S-93-4</i>	4.40	0.57	2.21
	<i>3D-S-93-5</i>	4.37	0.56	2.24
	<i>3D-S-93-6</i>	4.35	0.56	2.24
	<i>3D-S-93-7</i>	4.32	0.57	2.21

## 4.2 Experimental Procedures

An instrumented drop-weight apparatus (Figure 4.2) was used to subject the composite coupons to multiple normal impacts, at the center of each coupon, until perforation of the target was observed.

This drop-weight apparatus can be used to generate impact velocities up to 5 m/s. The impacting tup is modular, and by varying the crosshead mass and the height of release, impact energies from 1 to 500 Joules are possible. For the E-glass-reinforced composites, the impact velocity was held at approximately 2 m/s, and the total mass of the impactor was fixed at 9.0 kg. For the S2-glass reinforced composite systems, the impact velocity was held at approximately 4 m/s, and the total mass of the impactor was fixed at 5.5 kg. The position and acceleration of the impactor were continuously monitored. The reason for the disparity between the two material systems, with regard to the mass and velocity of the impactor, can be attributed to the improvement of the position and acceleration measurements by the removal of off-axis mass. This mass consisted mainly of the arrest device (the actuated member of a garage-door control system) and structural members attaching it to the impactor. The other motivating factor was the greater specific strength of S2-glass in comparison with that of E-glass. The available energy of the slower, heavier impactor is 18 J. By comparison, the available energy of the faster, lighter impactor is 44 J. This type of arrangement has been used successfully for impact testing of composites by many researchers, including (Cantwell *et al.* 1983; Jang *et al.* 1990; Wu and Wang 1995; Mahfuz *et al.* 1998; Walsh *et al.* 1998)

The tup velocity was determined using a magnetostrictive position sensor, MTS Temposonics III. The acceleration of the impactor was obtained by a piezoelectric accelerometer, Sensotec PEL. The ability to monitor the position and acceleration of the falling mass permits measurement of dynamic energy dissipation. The total energy dissipation for each impact was determined by a balance of translational kinetic energy of the impactor as

$$E = \frac{1}{2} m (V_i^2 - V_r^2) \quad (4.1)$$

where  $E$  is the energy dissipated by the target during impact,  $m$  is the mass of the impactor,  $V_i$  is the incident velocity, and  $V_r$  is the residual velocity after rebound or perforation.

For specimen perforation, the residual velocity continuously decreases due to the friction between the target and penetrator as the shank slides through the hole, and it is difficult to measure the residual velocity accurately from the position signal. Therefore, the acceleration is numerically integrated to yield the change in velocity,  $\Delta V$ . Then the dissipated energy can be expressed in terms of the initial velocity and the change in the velocity as

$$E = -mV_i(\Delta V) - \frac{1}{2}m(\Delta V)^2 \quad (4.2)$$

where  $V_i$  is measured with the position sensor and  $\Delta V$  is calculated from the accelerometer signal. This procedure was also used to check the accuracy of the accelerometer signal, and good agreement was found (less than 3% difference).

For the experiments involving the E-glass systems, the drop-weight apparatus was equipped with a motorized lifting track. The crosshead was designed to engage or disengage the track by remote control. This arrangement provided the means to arrest the impactor between strikes. The collected data was stored after each strike, and the impactor was returned to its original starting height. Using this technique, a striking velocity of approximately 2 m/s (18 J) was consistently obtained. Because the target holder was rigidly attached to the frame of the testing device, the tup struck the target each time at the same location.

After the series of E-glass experiments had been conducted, electrical and mechanical modifications to the apparatus were implemented to reduce noise in the position and acceleration signals. The electrical modifications included adjustments in the physical spacing of electronic components, alterations to the grounding circuit, and improvements in cable shielding. Having completed these changes, it was discovered that a significant portion of the signal noise could be attributed mechanical sources, including bearing/guide-rod friction and asymmetry of the crosshead mass. This asymmetry was due mainly to the attachment of the motorized lift. Symmetry of the impactor was restored by the removal of extraneous material, including the motorized lift. The improvement in the quality of the position signal can be appreciated by comparing Figures 4.3 and 4.12. Before making the alterations described above, the acceleration

signal for the E-glass experiments had been numerically cleaned, using discrete Fourier transforms to suppress high-frequency contributions. Unfortunately, this filtering process can also remove potentially significant information. Fortunately, the quality of the improved acceleration permitted use of the raw signal; compare Figures 4.4 and 4.13. The function of impactor arrest was restored by the installation of a spring-loaded pivoting bar, attached to the upper target grip. The bar is pivoted out of the way of the impactor and then released after the first strike. The bar absorbs subsequent strikes until the impactor comes to rest.

The tup chosen for this investigation was circular-cylindrical, with a 19-mm diameter and a hemispherical nose. Stainless steel was chosen for its relatively high hardness and resistance to corrosion. In the energy balance of Equations (4.1-2), the work of tup deformation is neglected. Square target panels, with 12.7-cm edges, were clamped between two thick aluminum annuli, with 76-mm inner diameter and 152-mm outer diameter, and fixed to a rigid base to prevent slippage of the target material.

### **4.3 Results And Discussion: E-Glass Systems**

The E-glass composite coupons were subjected to multiple 18-J impacts until perforation. The tup velocity for each impact was 2.0 m/s, and the total mass of the impactor was fixed at 9.0 kg. For each impact, the position and acceleration of the impactor were continuously monitored. Hence, dynamic energy dissipation was measured from the displacement and acceleration signals. Representative signals are shown in Figures 4.3 and 4.4. The incident energy was calculated based on the height

history, while the dissipation of energy was derived from both acceleration and height histories of the impactor, assuming rigid-body motion (Equation 4.2). From the velocity histories, a general trend was observed: the impactor rebounded at a relatively constant rate until the last two or three strikes, when impulse suddenly dropped off.

To compare the strength and energy dissipation of the three systems, the acceleration histories were used to determine the peak force imparted to the rigid impactor by the target. A plot of the peak force for all impacts is shown in Figure 4.5. All three material systems have an initial peak force of 6.5 kN, which increased on the second strike and then decreased as the number of strikes was increased. The maximum peak was nearly the same, 7 kN, for all samples. Also, the rate at which peak force dropped for the last three strikes was approximately 3 kN per strike for all three material systems. However, the main difference between the material systems is in the number strikes before the decrease in the peak-load occurred. For the 2D laminate, the load decreased rapidly on the third strike; for the biaxially reinforced warp-knit, the load decreased rapidly on the sixth strike. These results are consistent with the findings of (Wu and Wang 1995) for glass-fiber-reinforced epoxy laminates. For the 3D composite system, however, the peak force gradually drops from the second until the eighth strike. After this strike, there was a rapid decrease.

The measured velocity and acceleration were then used to determine the amount of energy dissipated during each impact (Figure 4.6). Again, similarities among the three material systems include the initial energy of approximately 10 J, and the maximum value of approximately 18 J (perforation). The amount of dissipated energy generally

increased from the initial value until perforation was observed. The maximum value for all samples was equal to the available energy and corresponded to arrest of the impactor by sliding friction. However, the main difference between the various E-glass systems was the rate at which the energy dissipation increased. The energy dissipation of the 2D laminates most rapidly, followed by the biaxially reinforced warp-knit and, finally, the 3D orthogonally woven composite. A plot of the total energy dissipation (Figure 4.7) was obtained by summing the dissipation for multiple impacts of each sample. The 3D orthogonally woven composite dissipated approximately 140 J, nearly twice as much energy as for the 2D plain-weave laminate of comparable areal density. The biaxially reinforced warp-knit dissipated approximately 105 J.

The various samples were assessed for damage development by post-mortem photographic analysis. The damage on the impacted face was very similar for all samples: a sharply defined circular hole with very little damage beyond. The fiber rovings were sharply bent to form the edge of each hole. Post-perforation photographs of the rear target faces of three representative samples are shown in Figure 4.8.

Two samples were examined from the group of 2D plain-weave laminates, both of which were perforated on the fifth strike. Observed failure modes include debonding, tensile failure and splitting of rovings, and delamination (Figure 4.9). The damaged region of the two-dimensional laminates was comparatively smaller than that of the other two material systems. This reduced radial expansion of damage can be attributed to the self-confinement of interlaced rovings.

For the biaxially reinforced warp-knit, perforation occurred on the eighth strike. As for the case of the 2D plain-weave laminates, the modes of failure include debonding, tensile fiber-failure, and splitting of the rovings (Figure 4.10). However, peeling of fiber rovings was observed nearest to the rear face. The rovings intersecting the area of contact between the impactor and target debonded to the very edge of the sample, and the observed radial expansion of material damage was significantly larger than that of the 2D plain-weave laminates.

For the 3D orthogonally woven composites, three samples were subjected to multiple impacts. All three samples were perforated on the tenth strike. The shape of the damaged region was almost identical to that of the biaxially reinforced warp-knit, but the area was slightly larger. The dominant observed failure modes were the same as for the biaxially reinforced warp-knit, with two additional modes. The surface crimp of the *z*-tows, depicted in Figure 4.1, provided *two more* mechanisms of energy dissipation. The first was the tensile failure of *z*-rovings at the crimp on the rear face; these failures occurred most frequently in the vicinity of the area of contact between the impactor and target. The second mechanism occurred as the penetrator caused rovings nearest to the rear face to be *pulled through* the surface crimp of the *z*-rovings, which deformed but did not break (Figure 4.11). This mode of failure typically occurred for only one or two rovings, near the axis of the impactor. Rovings that intersected the area of contact were broken or pushed to the side of the penetrator. The tensile failure and frictional sliding under the *z*-rovings provide an energy dissipation mechanism that is uniquely inherent to 3D woven architectures.

#### 4.4 Results and Discussion: S2-Glass Systems

The S2-glass composite coupons were subjected to multiple 44-J impacts until perforation. The tup velocity for each impact was approximately 4.0 m/s, and the total mass of the impactor was fixed at 5.5 kg. As for the E-glass experiments, the position and acceleration of the impactor were monitored, resulting in measurement of dynamic energy dissipation. Representative position and acceleration signals are shown in Figures 4.12 and 4.13. The same general trend was observed: the impactor rebounded at a relatively constant rate until the last three strikes, when impulse progressively decreased.

The peak force for all impacts is shown in Figure 4.14. The 2D laminates (*2D-S-24x4*) had initial peak forces in the range from 14 to 16 kN, while the peak force for the 3D monoliths (*3D-S-93*) fell in the range from 12 to 14 kN. The maximum peak was nearly the same, 18 kN, for all samples. Three samples of each material type were struck repeatedly until they were perforated; the 2D laminates required 14, 14, and 23 strikes to perforate, while the 3D monoliths required 23, 29, and 39 strikes. Two additional samples of each material system were removed for inspection after the first and fifth strikes.

The measured velocity and acceleration were used to determine the amount of energy dissipated during each impact (Figure 4.15). Zero energy dissipation, which was never observed, corresponds to a perfectly elastic impact. For the 2D laminates, the energy dissipated on the first strike ranged from about 21 to 24 J. For the 3D monoliths, however, the initial energy dissipation was consistently 25 J, indicating that the 3D monoliths suffered a greater amount damage on the first strike. Again, the cumulative

energy dissipation (Figure 4.16) was obtained by summing the dissipation of all impacts for each sample that was perforated. The 3D orthogonally woven composite dissipated an average of 777 J (588, 750, and 994 J), nearly twice as much energy as for the 2D plain-weave laminate, whose average cumulative energy dissipation was 393 J (334, 508, and 337 J).

Samples were also inspected for damage initiation and progression by photographic and microscopic analysis after the first, fifth, and final (perforating) strikes. Due to the difficulty of target realignment, a sample was removed after the first strike and another after the fifth strike; returning a sample to the target holder could result in an altered impact site. The 2D laminates are considered first.

After the initial strike, considerable damage was observed (Figures 4.17-21). Backlighting revealed a cross-shape pattern of internal delamination that was similar to the pattern observed after quasi-static perforation of the 2D laminates (Figure 3.18). This delamination extended to the boundary of the clamp aperture. At the site of impact on the front face, a small indentation crater was observed (Figure 4.18). Scanning electron microscopy of a surface warp tow close to the impact site showed that matrix material had been shed from the yarn at the surface (Figure 4.19). On the rear face, a similar cross-shape delamination pattern was observed (Figure 4.20).

After the fifth strike, this cross-shape pattern was more developed, and the rear face showed signs of fiber fracture opposite the impact site (Figure 4.21). This location was examined in more detail by SEM (Figure 4.22). Matrix cracking was observed, and fibers appeared to have failed in tension.

Post-perforation photographs of one of the 2D laminates showed a fully developed cross-shape damage pattern, very similar to the pattern observed after quasi-static perforation (Figure 4.23). The dominant damage mechanisms for the 2D laminates (2D-S-24x4) included delamination, matrix cracking (Figures 4.24 and 4.25), and tensile fiber fracture.

The mechanisms and patterns of damage for the 3D monoliths (3D-S-93) were analogous to the cases of quasi-static perforation of the same material system, described in Section 3.3. Examining the 3D monolith subjected to a single strike, reflected-light photographs showed that fiber debonding had occurred throughout the area exposed by the clamp aperture (Figure 4.26a,b). Backlighting revealed that two lines of intense fiber debonding had occurred in the warp direction, on either side of the point of impact (Figure 4.26c). Backlighting also revealed a circular indentation, similar to the indentation observed after the initial strike upon the 2D laminate, at the impact site (Figure 4.26c). This indentation was not easily observed under normal lighting (Figure 4.27). Matrix cracking between neighboring surface crimps of z-tows on both front and rear faces of the panel (Figures 4.27 and 4.28). The crimps also showed signs of damage, as can be seen in SEM images of the surface (Figure 4.29) and of through-the-thickness sections (Figure 4.30a). Debonding of a surface weft tow was observed, as well (Figure 4.30b).

After five strikes upon a 3D monolith, a similar pattern of matrix cracking between z-crimps was observed on the front face, near the point of impact (Figure 4.31a).

Debonding of one of the rear surface weft tows had spread beyond the inside edge of the clamp (Figure 4.31b,c). This delaminated weft tow was centrally located.

After perforation of the 3D monoliths, progression of damage had noticeably shifted (Figures 4.32-34). Although similar but more extensive debonding of rear surface weft was observed (Figures 4.32b and 4.34), the debonding had moved to weft tows *on either side* of the perforation hole. Lines of intense delamination of warp tows and *z*-tows *on either side* of the perforation hole were also observed under backlighting. As the fabric reinforcement (warp, weft, and *z*) is ruptured at the impact site, the load exerted by the impactor shifts to warp and weft tows adjacent to the ruptured reinforcement. As can be seen in the backlit photograph (Figure 4.32c), two weft tows on either side of the hole have delaminated to the edge of the panel. By comparison, weft tows intersecting the ruptured area have delaminated beyond the inside edge of the clamp but not to the edge of the panel (Figures 4.32b and 4.34). As before, extensive matrix cracking between *z*-crimps was observed on both front and rear faces (Figures 4.33 and 4.34).

#### **4.5 Conclusions**

This investigation examined how variation of the fabric architecture in composite systems with comparable areal densities and fiber-volume-fractions affects perforation resistance, strength, and damage mechanisms of GFRP composite panels subjected to multiple impacts, at velocities of approximately 2 m/s and 4 m/s, corresponding to impact energies of approximately 18 J and 44 J, respectively. Three classes of woven

architectures were chosen as the fabric preforms for this investigation: a 2D plain-woven laminate, a biaxially reinforced warp-knit system, and a 3D orthogonally woven system.

Again, distinctive modes of failure for the various material systems were observed. Matrix cracking, delamination or debonding, and fiber fracture were dominant in all systems, but the unique damage mechanisms of the 3D systems, included the straining and fracture of *z*-tows, acted as additional means of energy absorption. As in the case of quasi-static perforation, the radial spread of damage was larger for the 3D systems than for the 2D laminates. After the occurrence of perforation, debonding of the 3D systems often extended to the edges of the test panel.

For the systems examined under repeated low-velocity impact, the 3D systems survived more strikes before perforating and absorbed more total energy than the 2D laminates. This was true for both the E-glass/vinyl-ester and S2-glass/rubber-toughened-epoxy-vinyl-ester systems. Normalization by areal density magnified the superiority of the 3D systems. This is attributed to the damage mechanisms unique to these reinforcement geometries. The tendency of the 3D orthogonal weaves to spread damage over a larger area is mainly due to the straightness of the fibers. This spread was already evident after the first and fifth strikes.

**4.5 Figures**  
**(Chapter 4)**

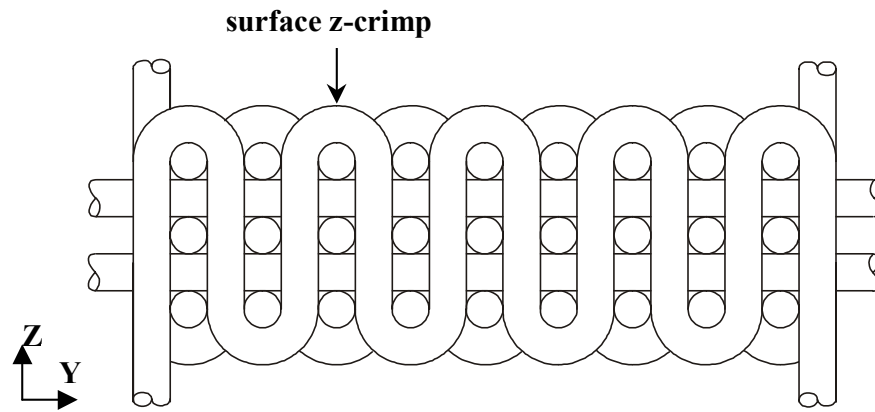


**Figure 4.1 Surface-Crimp of z-Tows in 3D Orthogonal Fabric Preform**

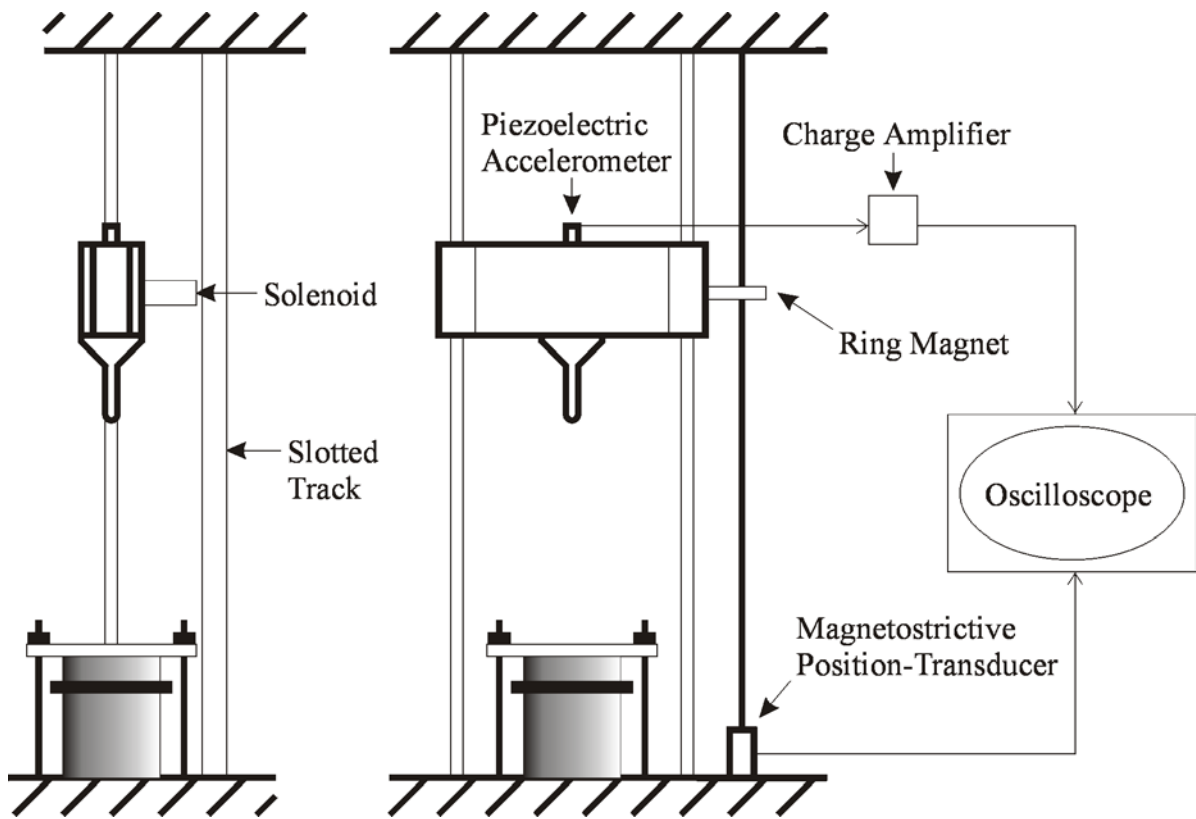


**Figure 4.2 Instrumented Drop-Weight Impactor**

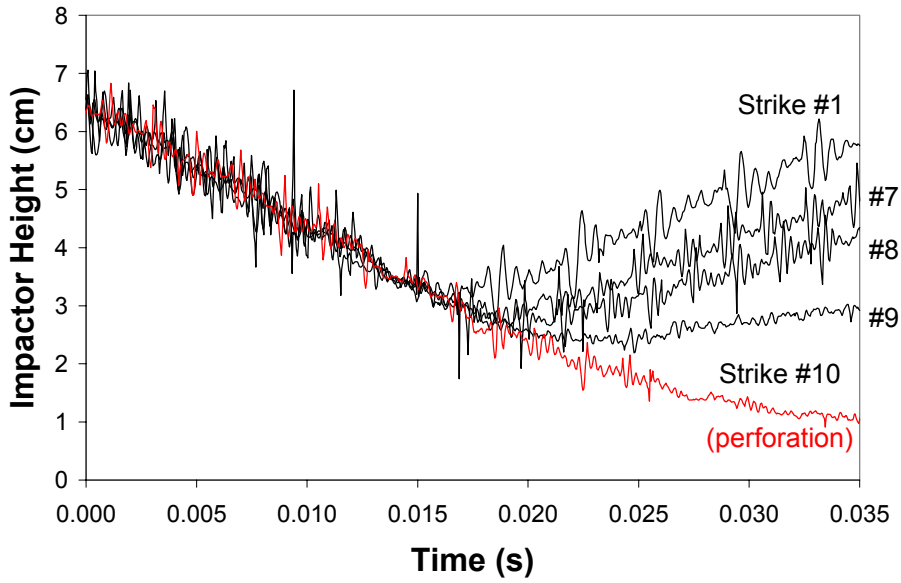


**Figure 4.3 Representative Impactor Height History for E-Glass Composite Systems (Sample: 3D-E-96-1)**

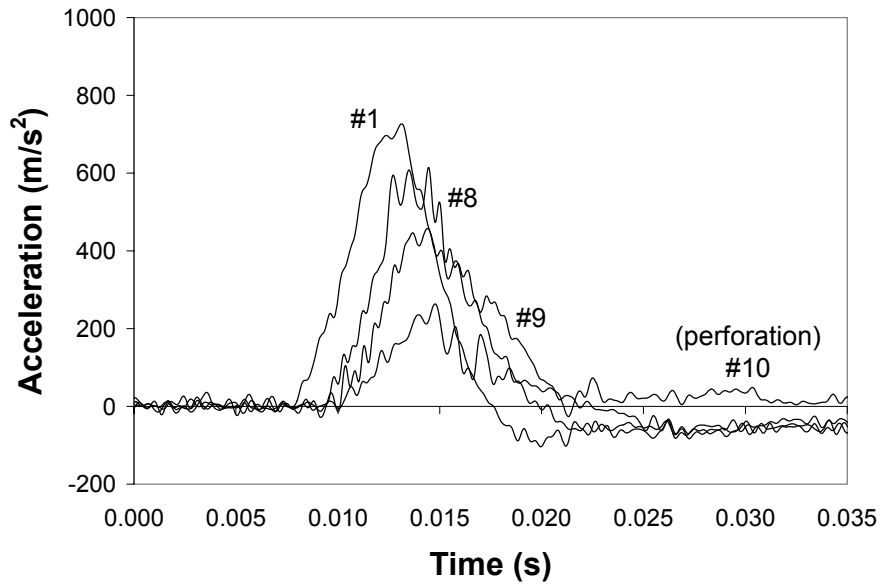


**Figure 4.4 Representative Impactor Acceleration History for E-Glass Composite Systems (Sample: 3D-E-96-1)**

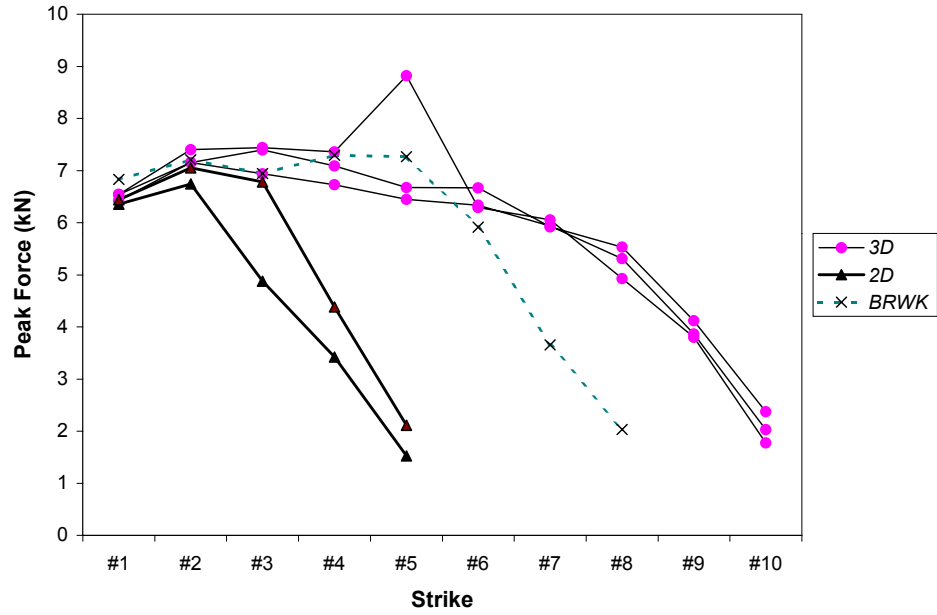


**Figure 4.5 Peak Impact Force of E-Glass Composite Systems as a Function of Strike Number**

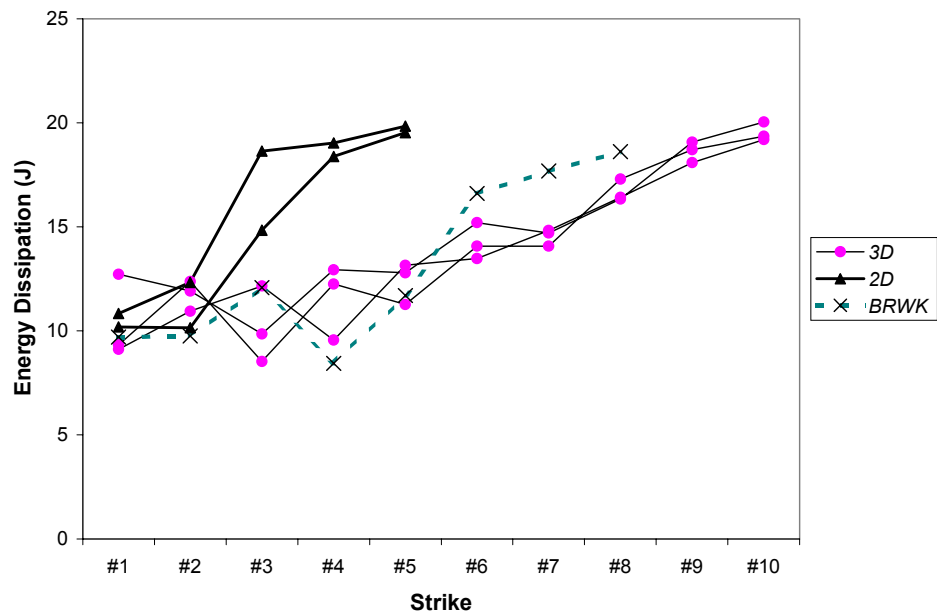


**Figure 4.6 Energy Dissipation of E-Glass Composite Systems as a Function of Strike Number**

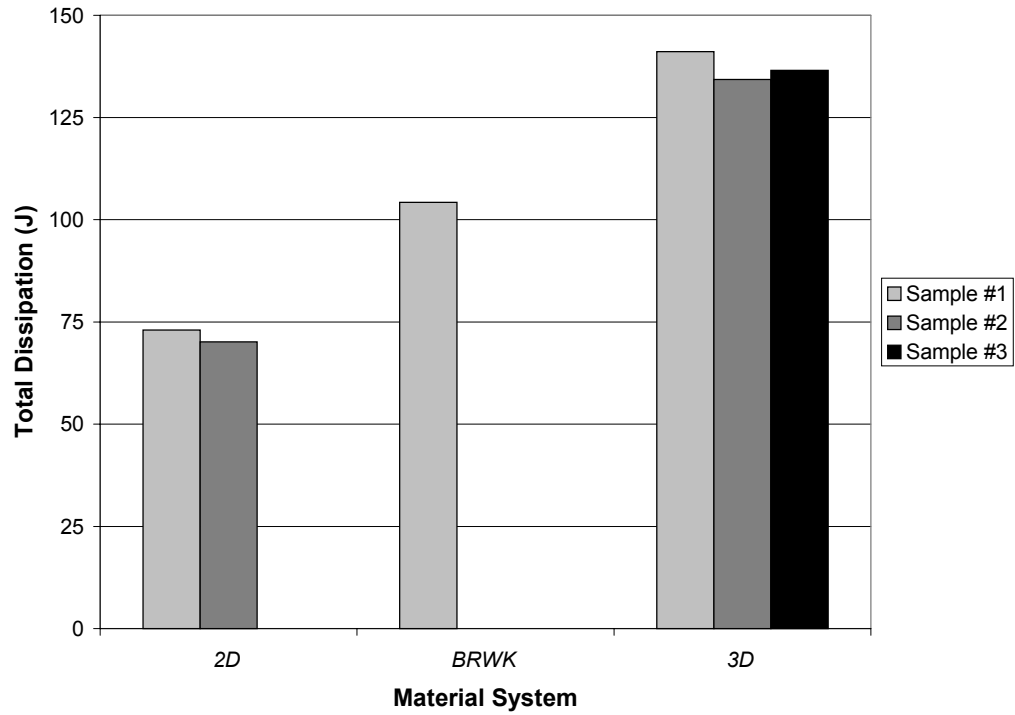


**Figure 4.7 Cumulative Energy Dissipation Resulting in Perforation of E-Glass Composite Systems**

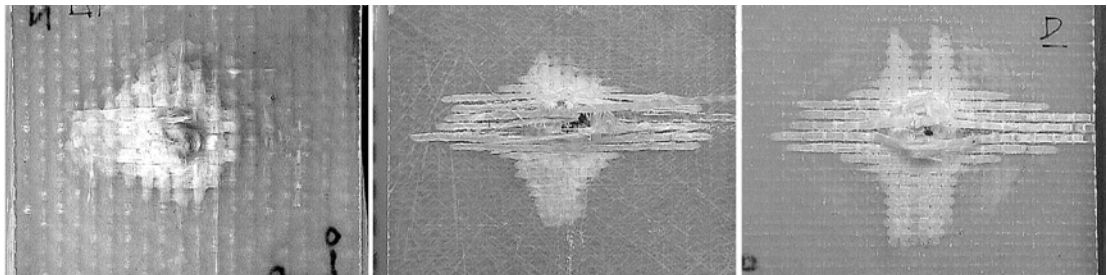


**Figure 4.8 Post-Perforation Photographs of E-Glass Systems, Rear Target Faces: 2D-E-24x4 (Left), BRWK (Center), 3D-E-96 (Right)**

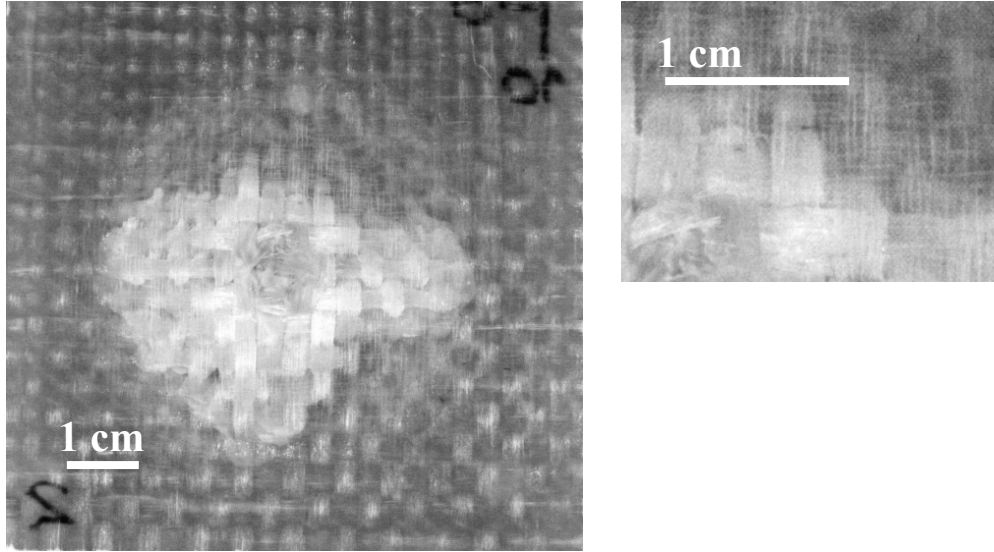


**Figure 4.9 Post-Perforation Photographs of the 2D Plain Woven Laminate (2D-E-24x4-1)**

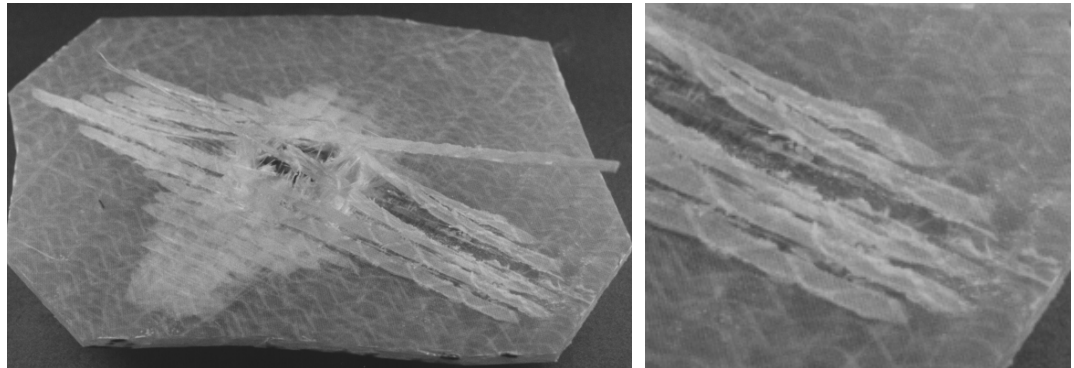


**Figure 4.10 Post-Perforation Photographs of the Biaxially Reinforced Warp-Knit (BRWK-1)**

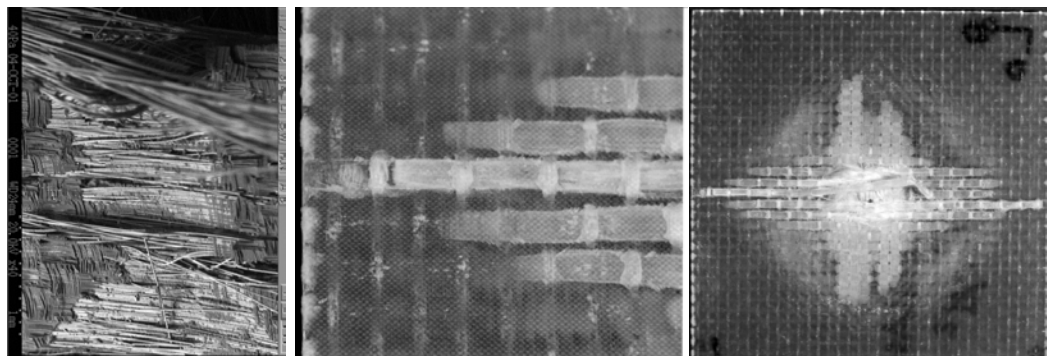


**Figure 4.11 Post-Perforation SEM and Photographs of the 3D Orthogonally Woven System (3D-E-96-1)**

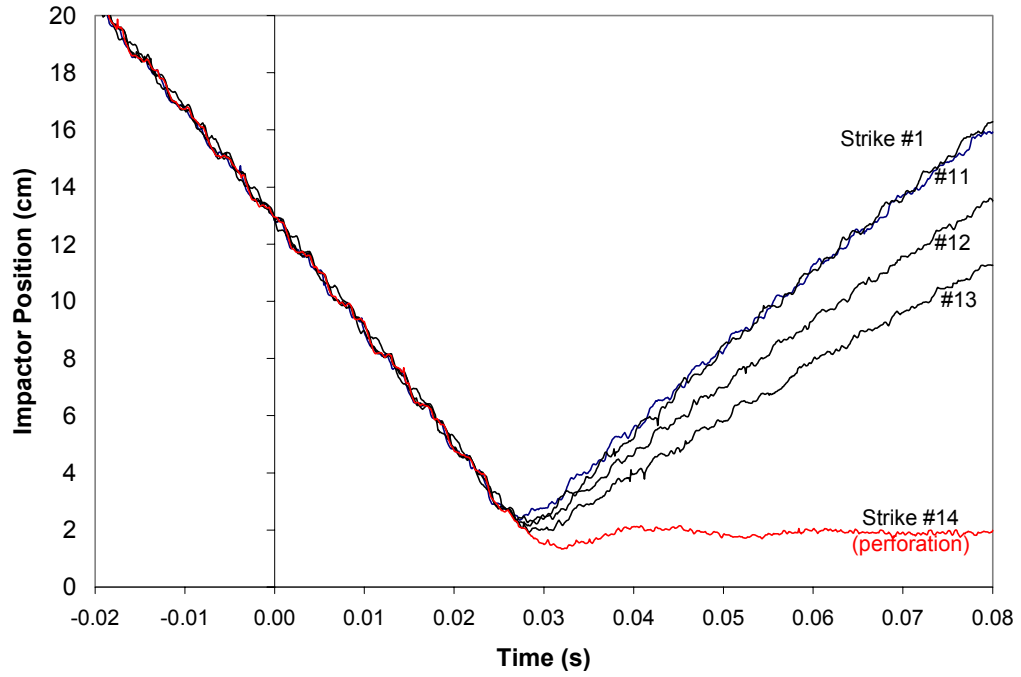


**Figure 4.12 Representative Impactor Height History for S2-Glass Composite Systems (Sample: 2D-S-24x4-1)**

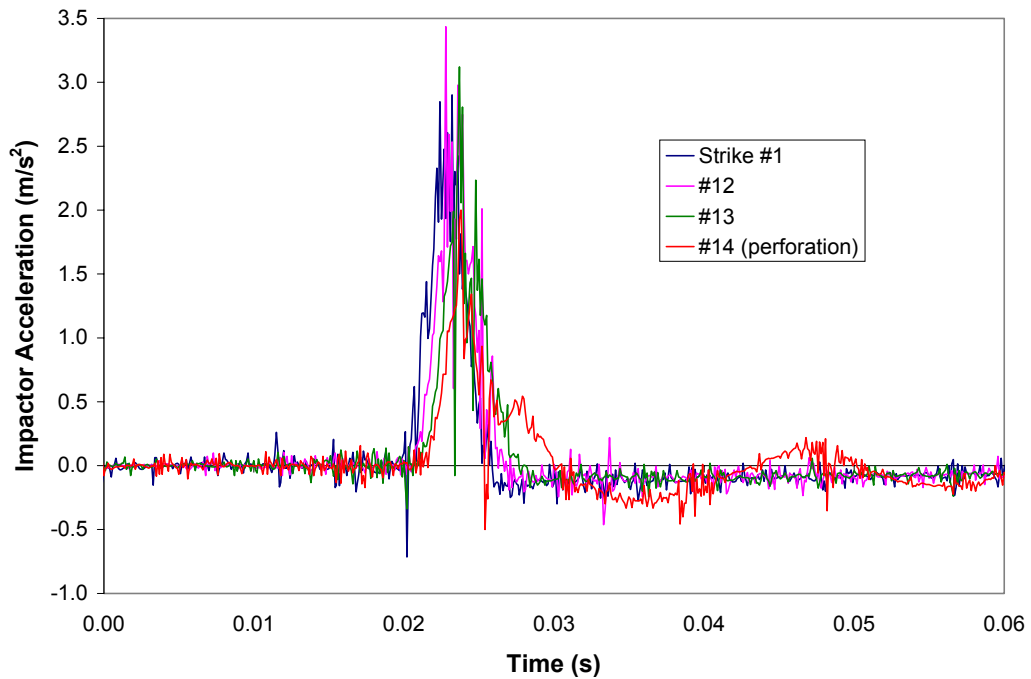


**Figure 4.13 Representative Impactor Acceleration History for S2-Glass Composite Systems (Sample: 2D-S-24x4-1)**

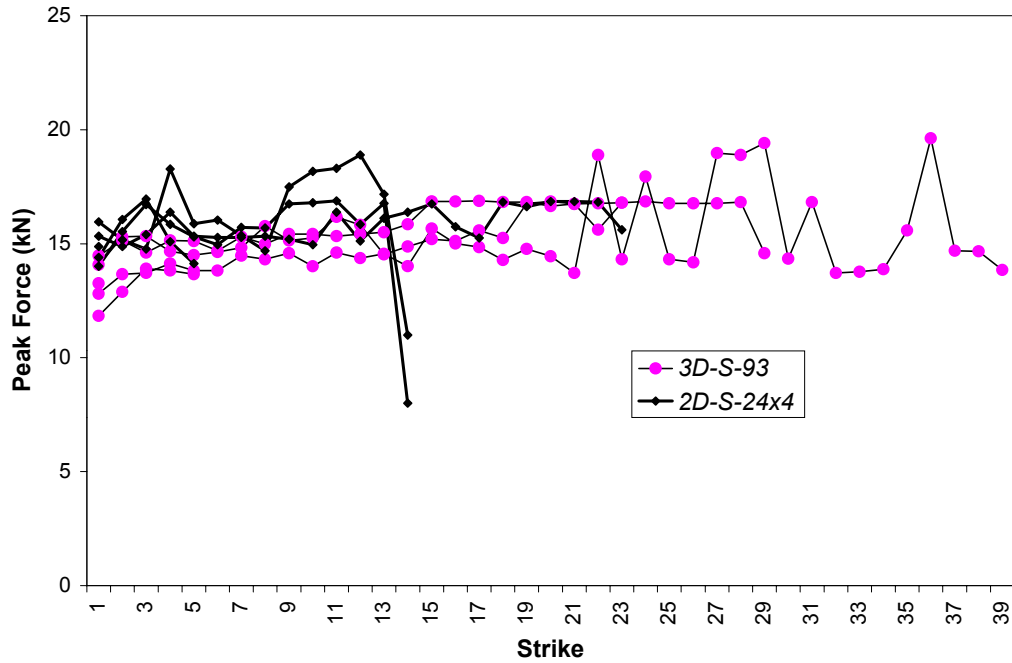


**Figure 4.14 Peak Impact Force of S2-Glass Composite Systems as a Function of Strike Number**

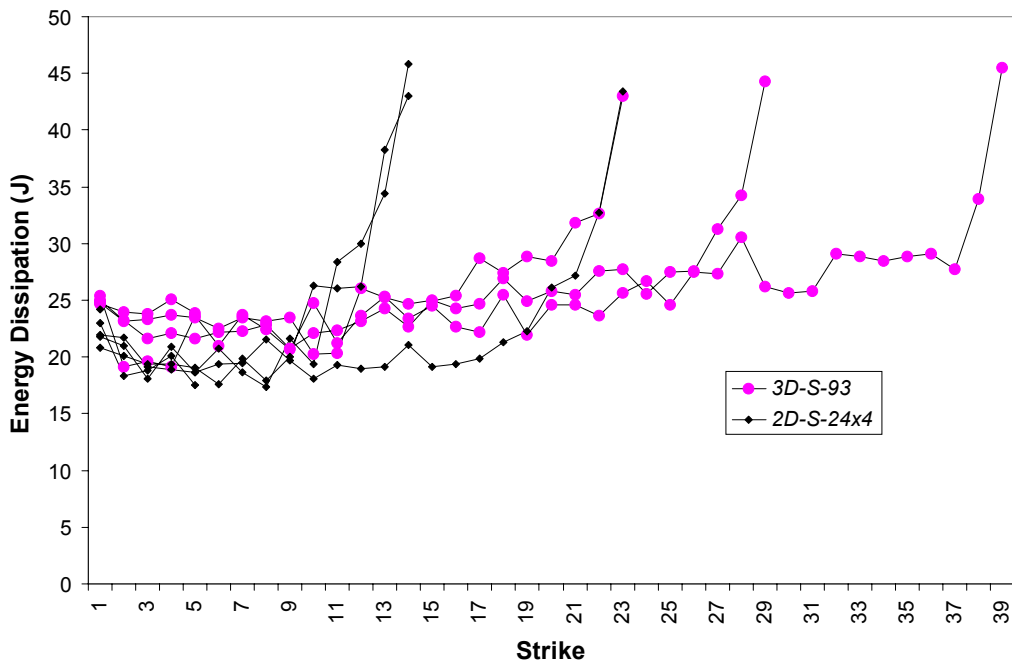


**Figure 4.15 Energy Dissipation of S2-Glass Composite Systems as a Function of Strike Number**

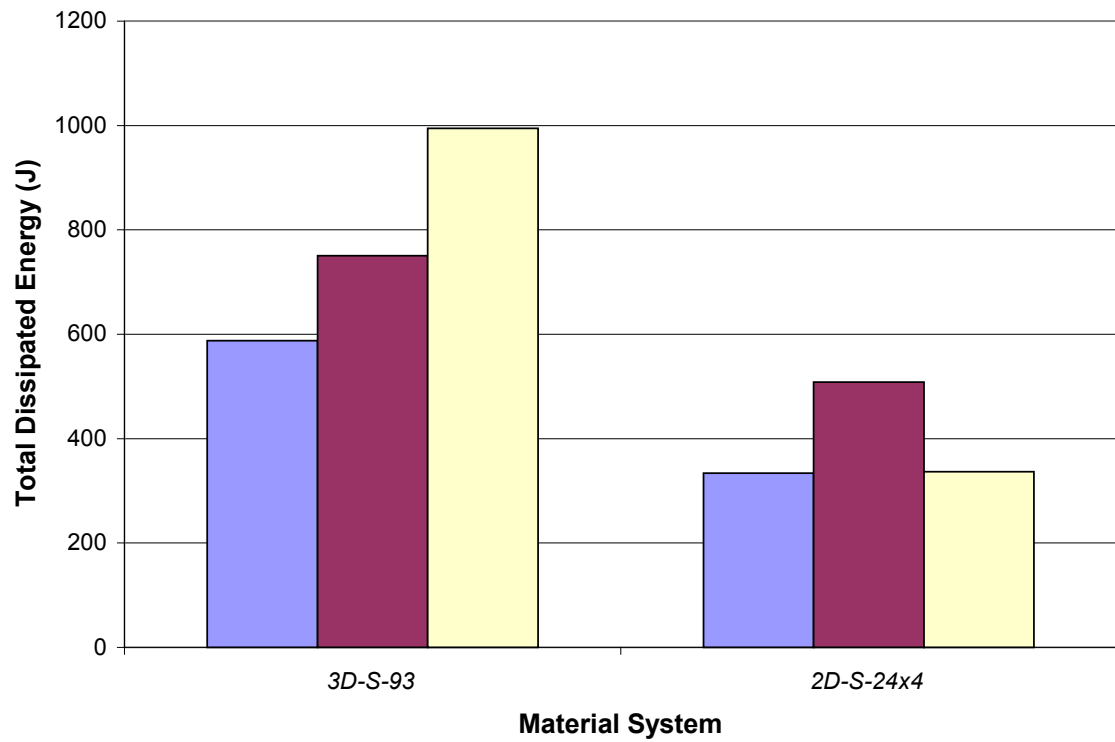
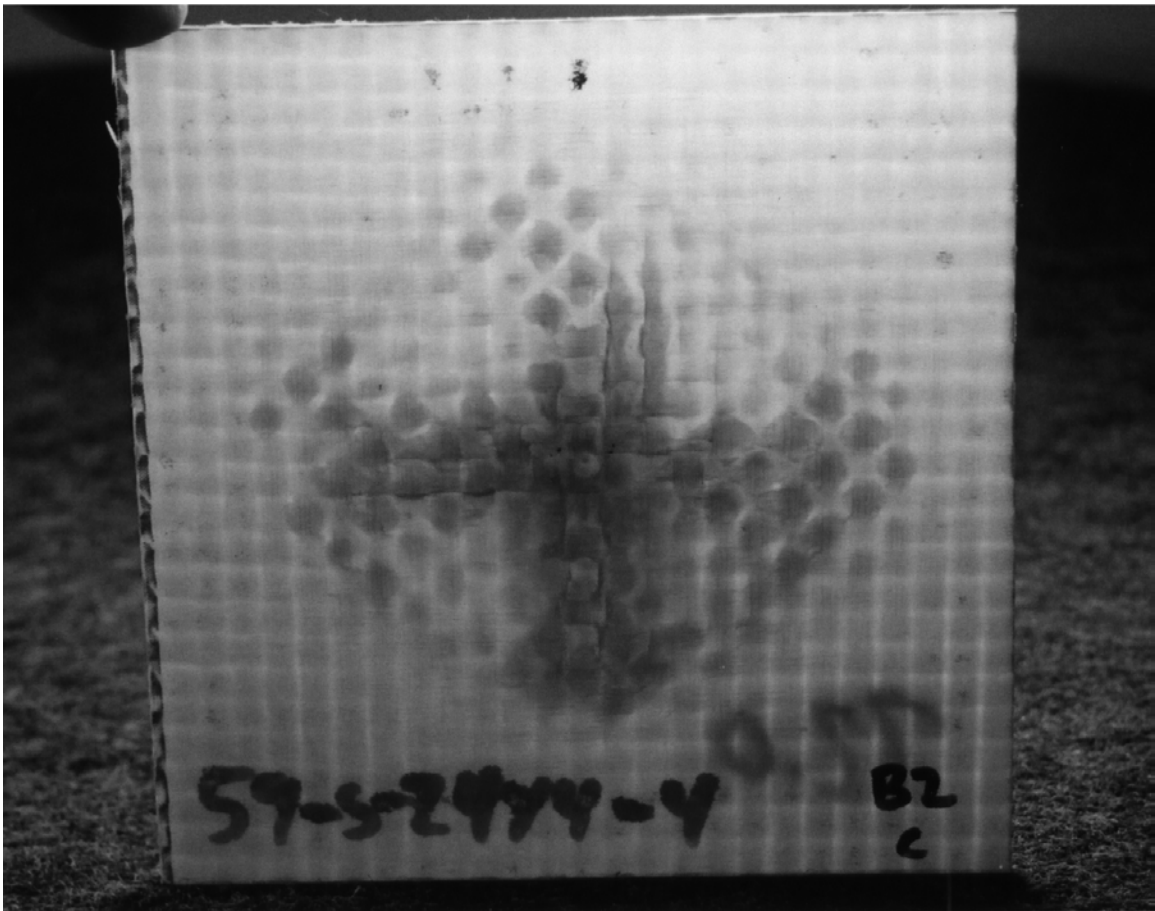


**Figure 4.16 Cumulative Energy Dissipation Resulting in Perforation of S2-Glass Composite Systems**



(a)

(b)



(c)

**Figure 4.17 Sub-Perforation (1 Strike) Photography of 2D-S-24x4-3:  
(a) Front Face, (b) Rear Face, (c) Rear Face under Back-Lighting**

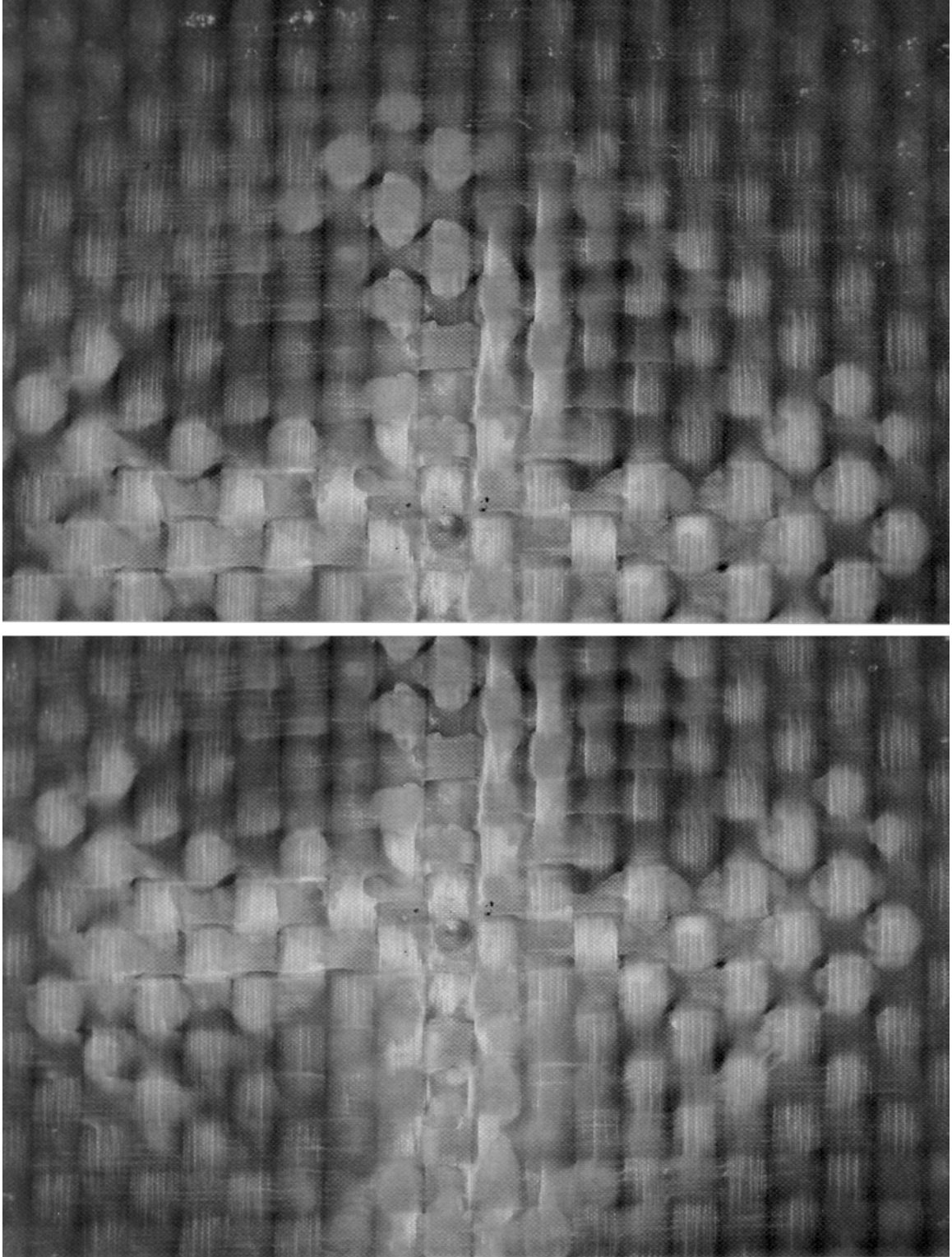


**Figure 4.18** Closer Views of Front Target Face (*2D-S-24x4-3*)

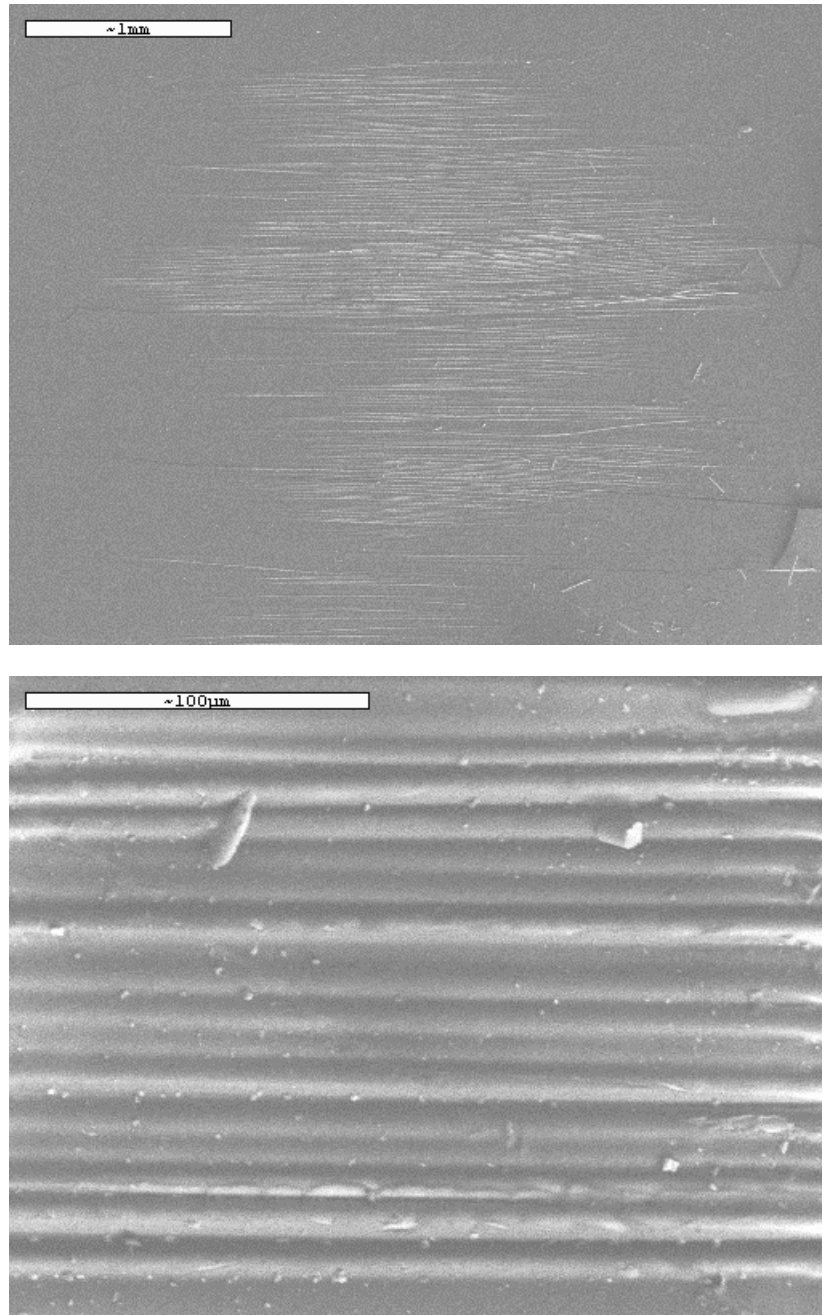


**Figure 4.19 Scanning Electron Micrographs Showing Surface Damage on Front Target Face near Impact Site (2D-S-24x4-3)**

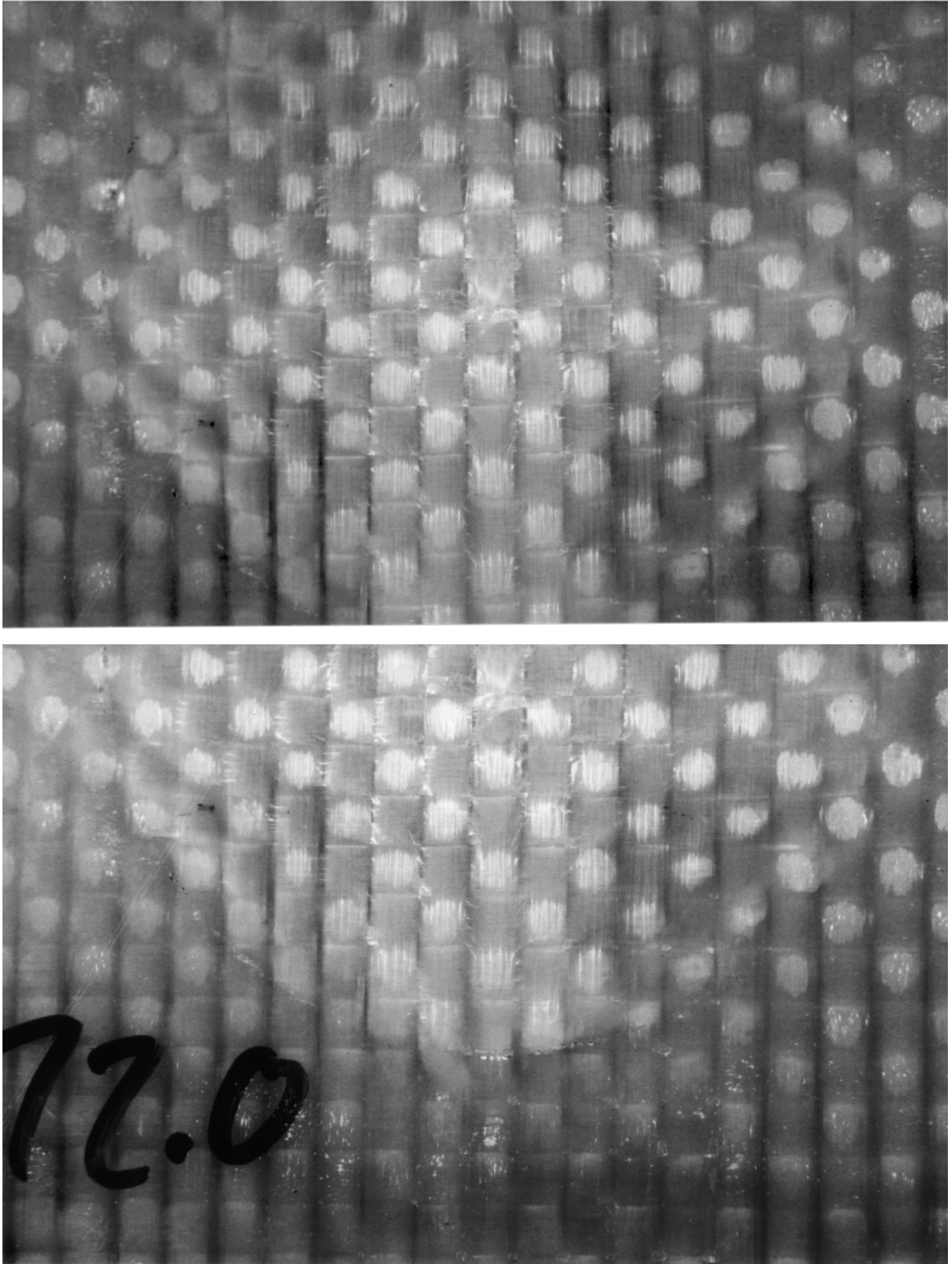
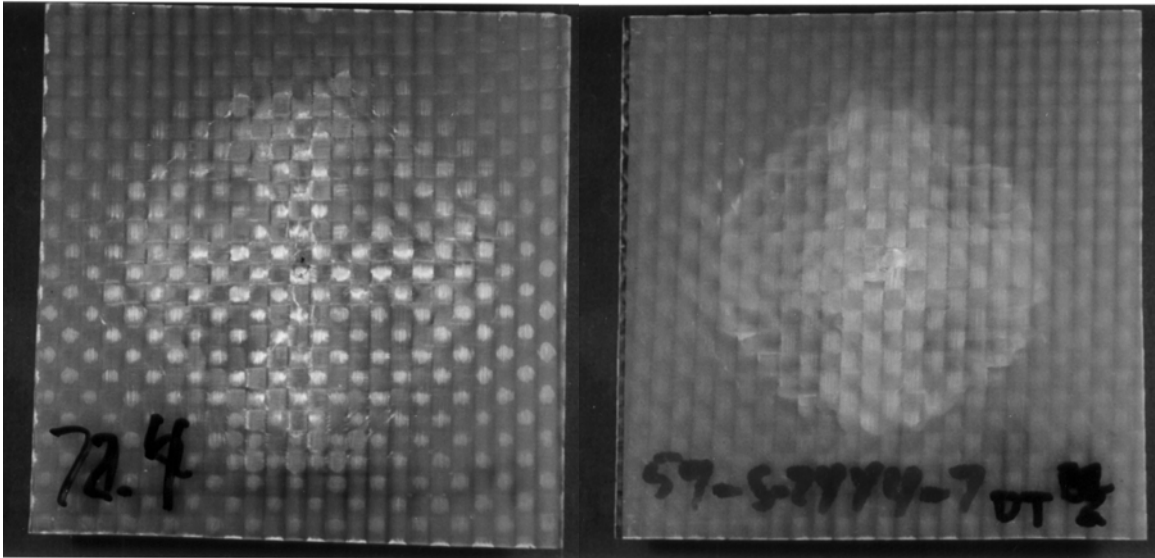
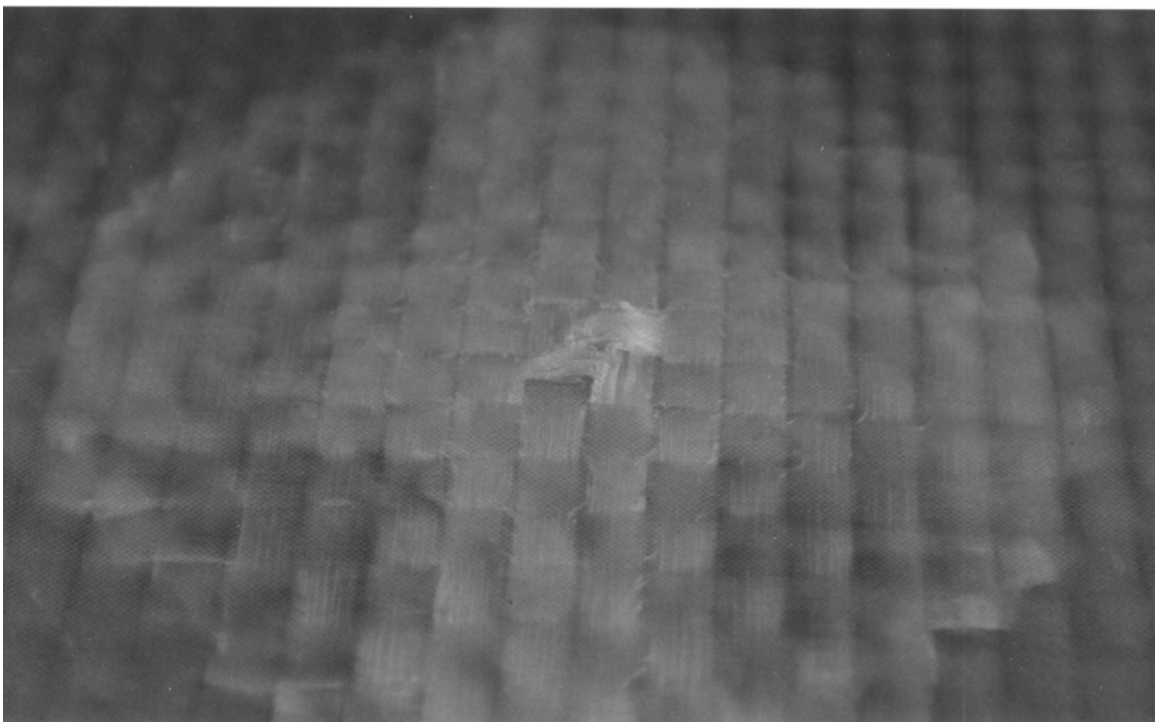


**Figure 4.20** Closer Views of Rear Target Face (*2D-S-24x4-3*)



(a)

(b)



(c)

**Figure 4.21 Sub-Perforation (5 Strikes) Photography of 2D-S-24x4-4: (a) Front Face, (b) Rear Face, (c) Rear Face, Oblique**

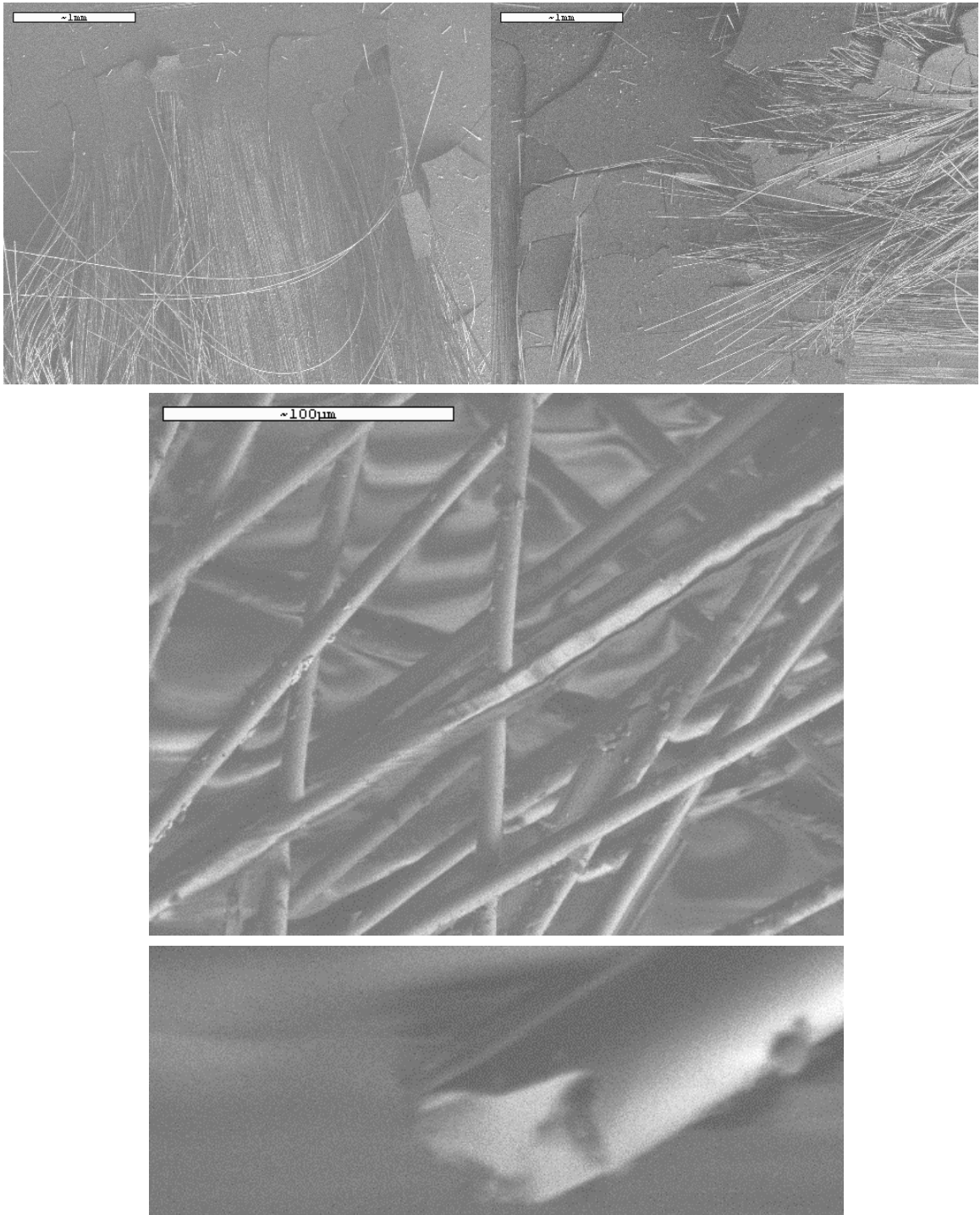
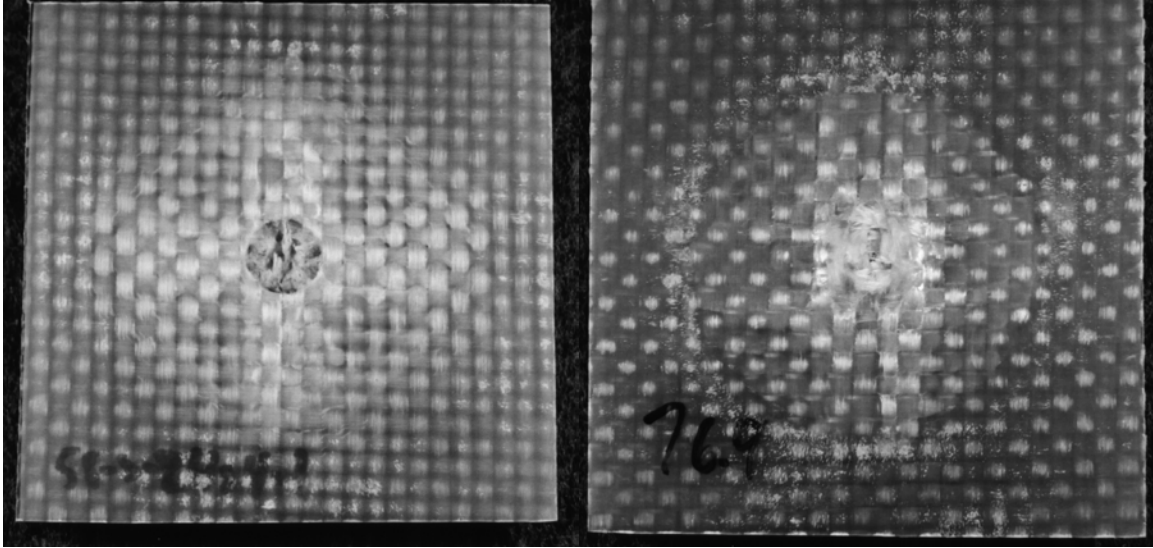
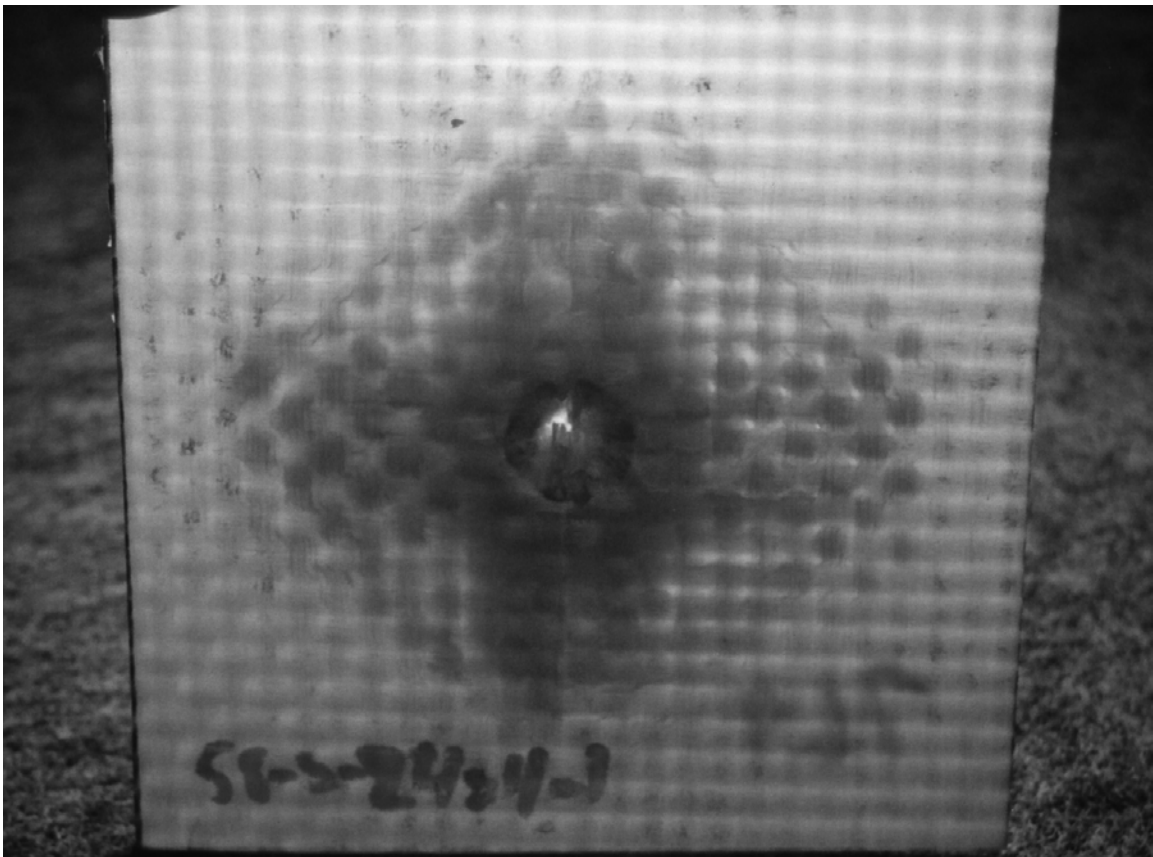


**Figure 4.22 Scanning Electron Micrographs Showing Surface Damage on Rear Target Face near Impact Site (2D-S-24x4-4)**



(a)

(b)



(c)

**Figure 4.23 Post-Perforation (23 Strikes) Photography of 2D-S-24x4-6:  
(a) Front Face, (b) Rear Face, (c) Rear Face under Back-Lighting**

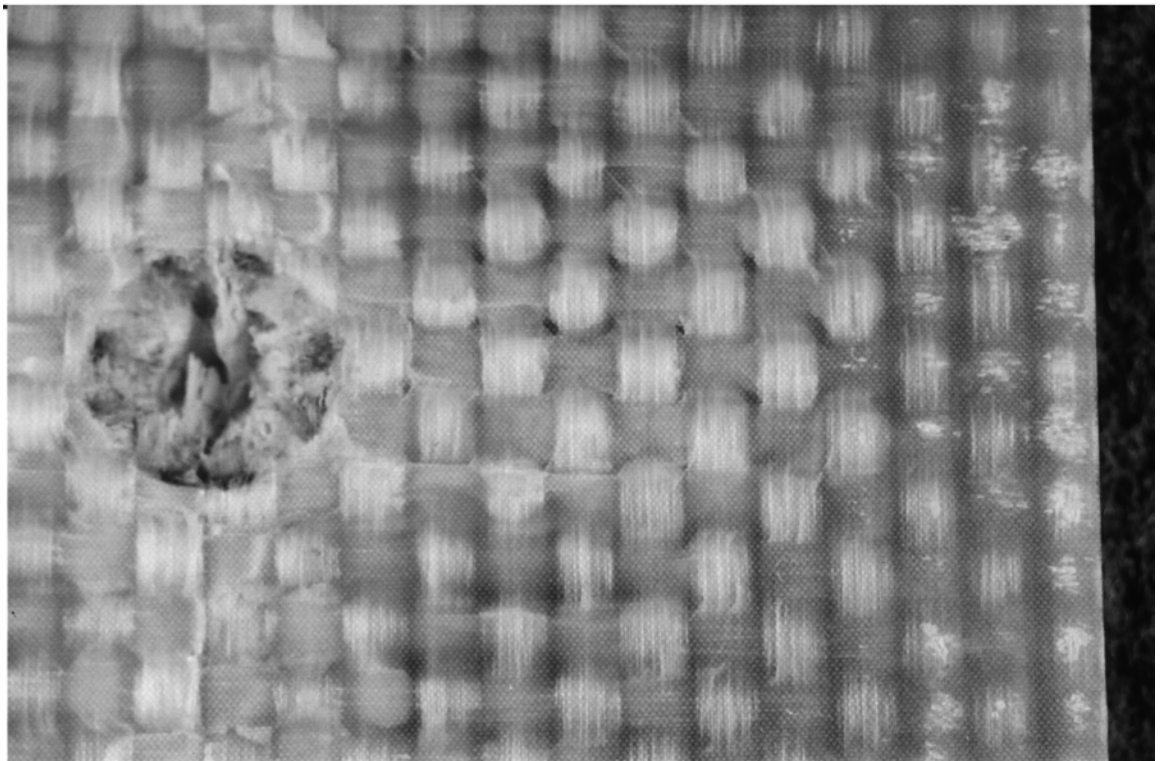
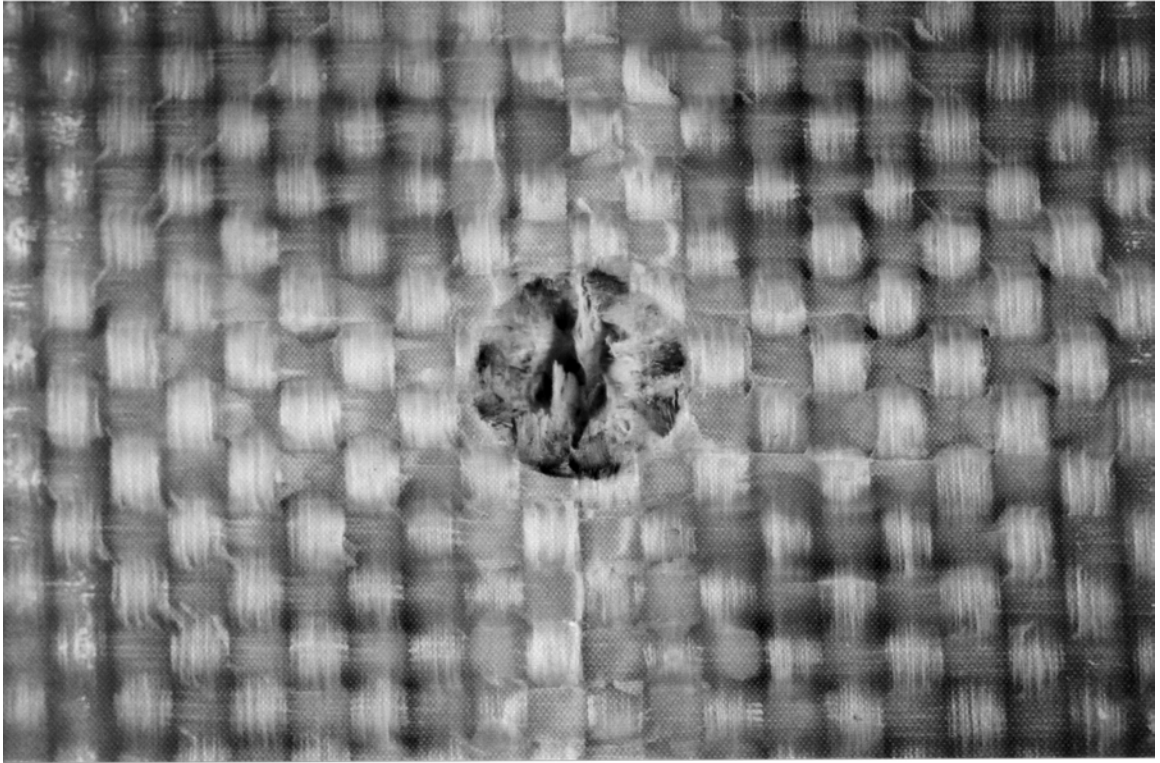


**Figure 4.24** Closer Views of Front Target Face (2D-S-24x4-6)

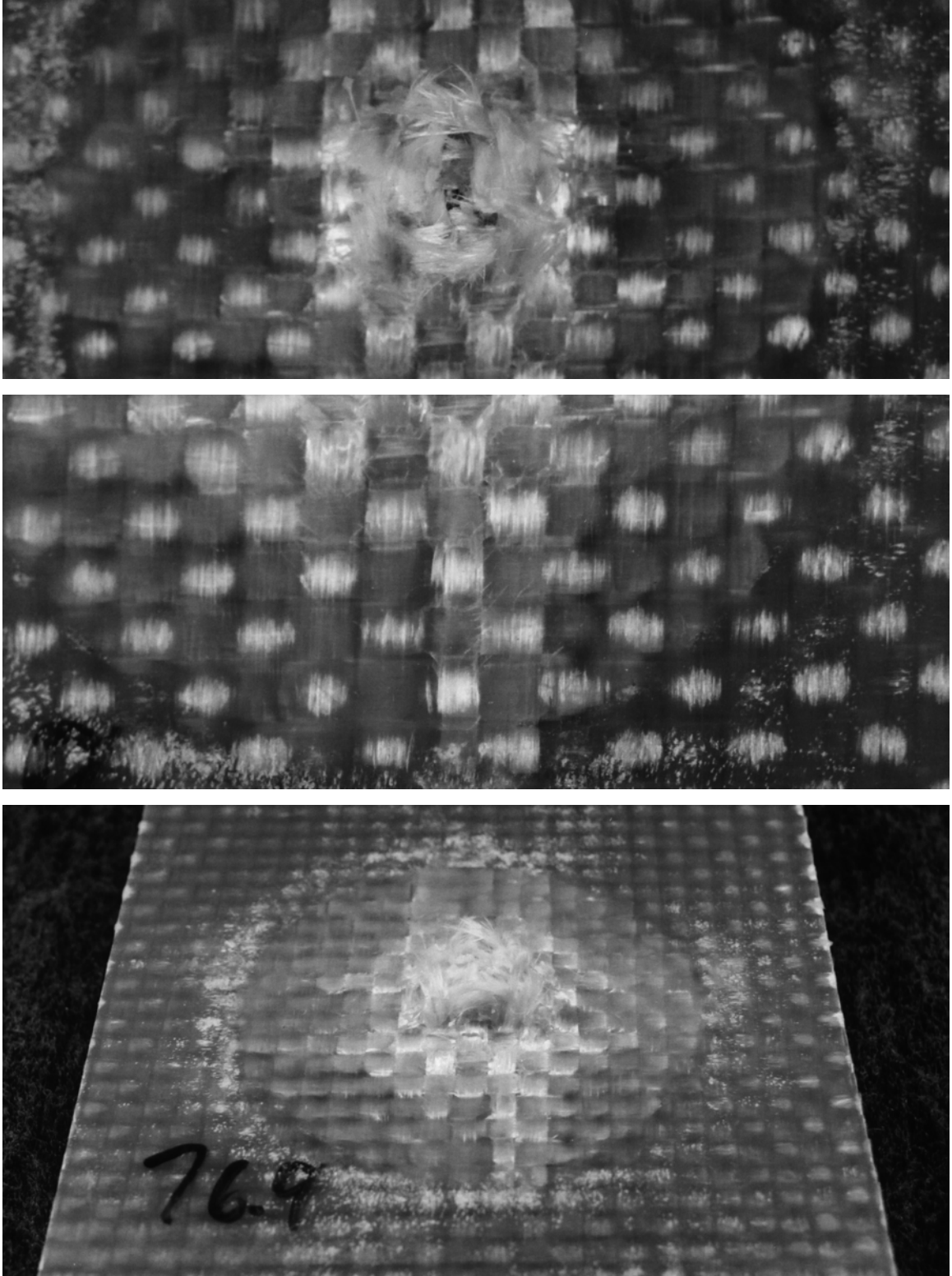
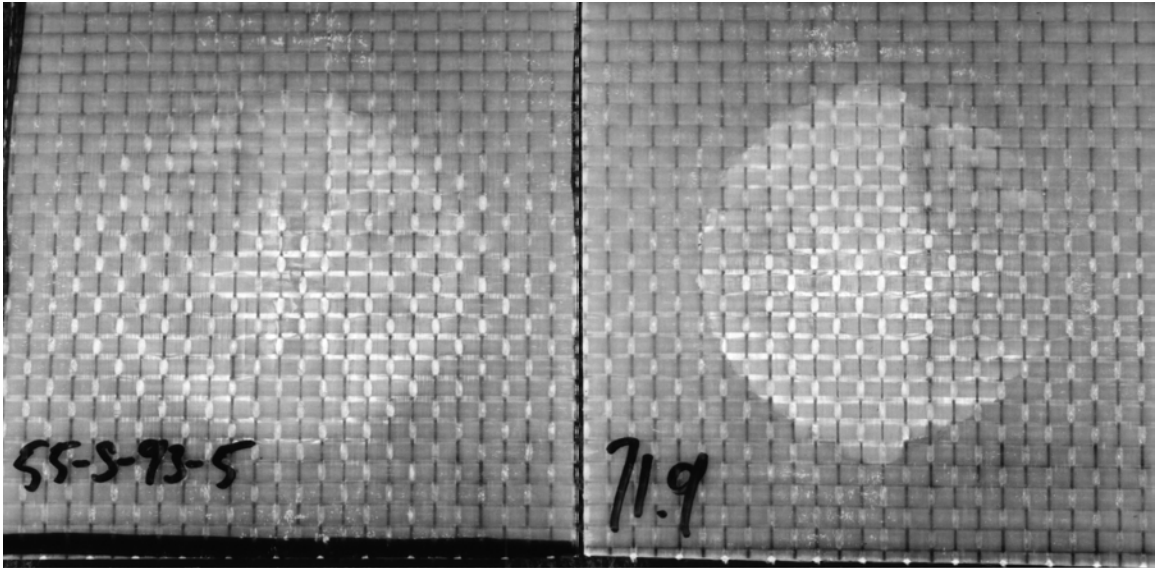
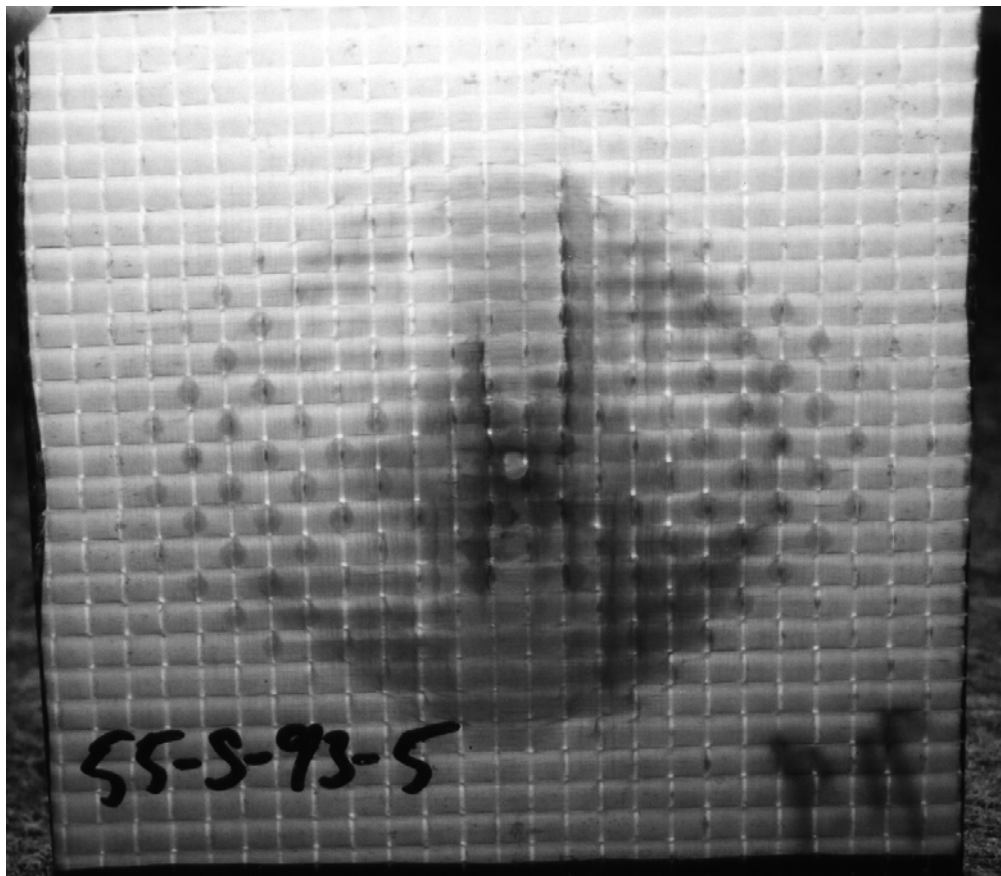


**Figure 4.25 Closer Views of Rear Target Face (2D-S-24x4-6)**



(a)

(b)



(c)

**Figure 4.26 Sub-Perforation (1 Strike) Photography of 3D-S-93:  
(a) Front Face, (b) Rear Face, (c) Rear Face under Back-Lighting**

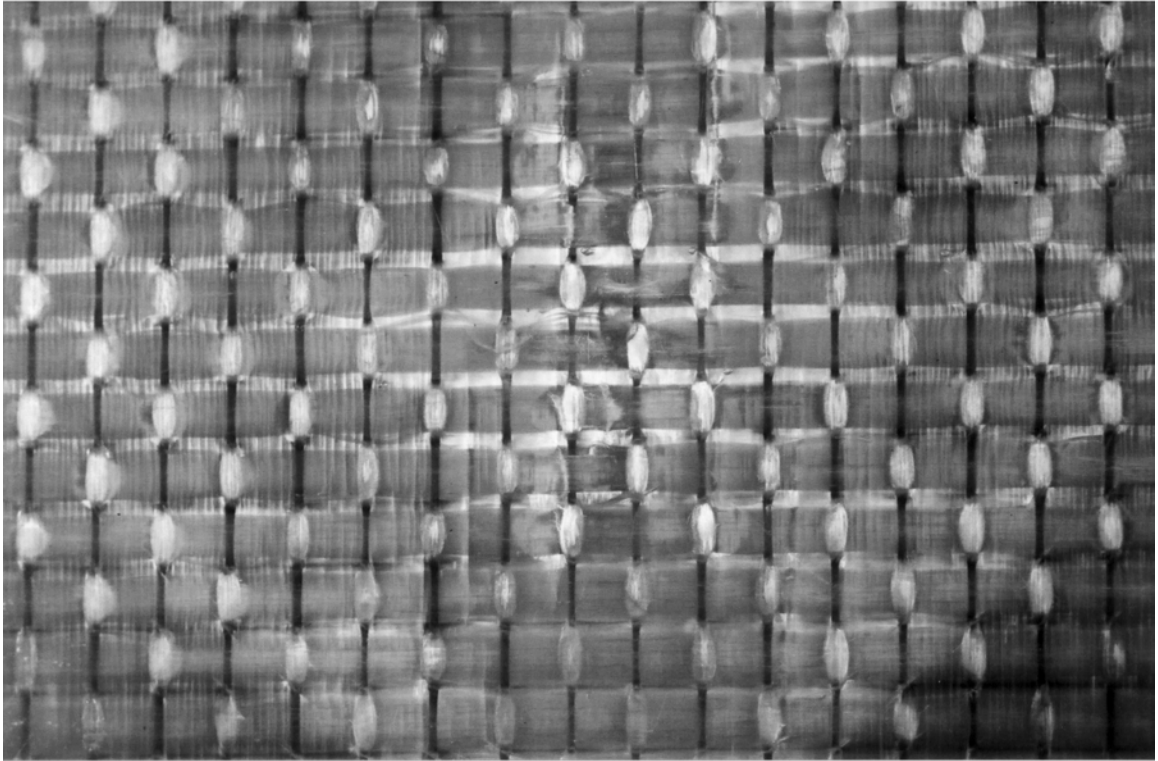


**Figure 4.27 Closer Views of Front Target Face (3D-S-93-3)**

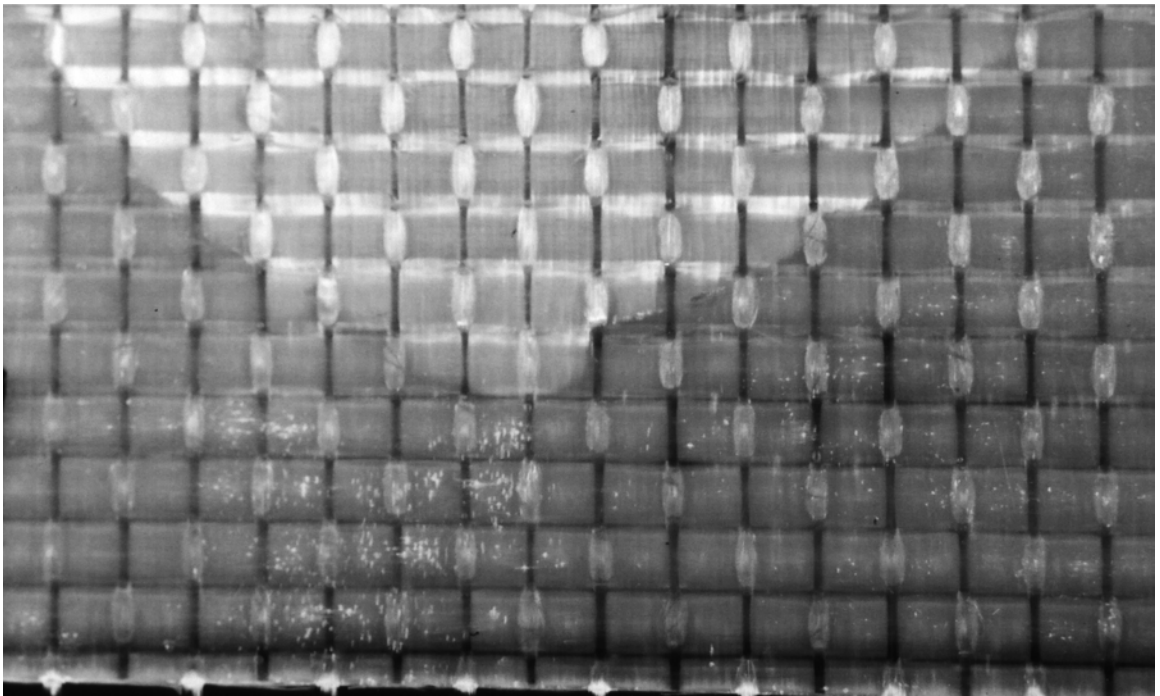
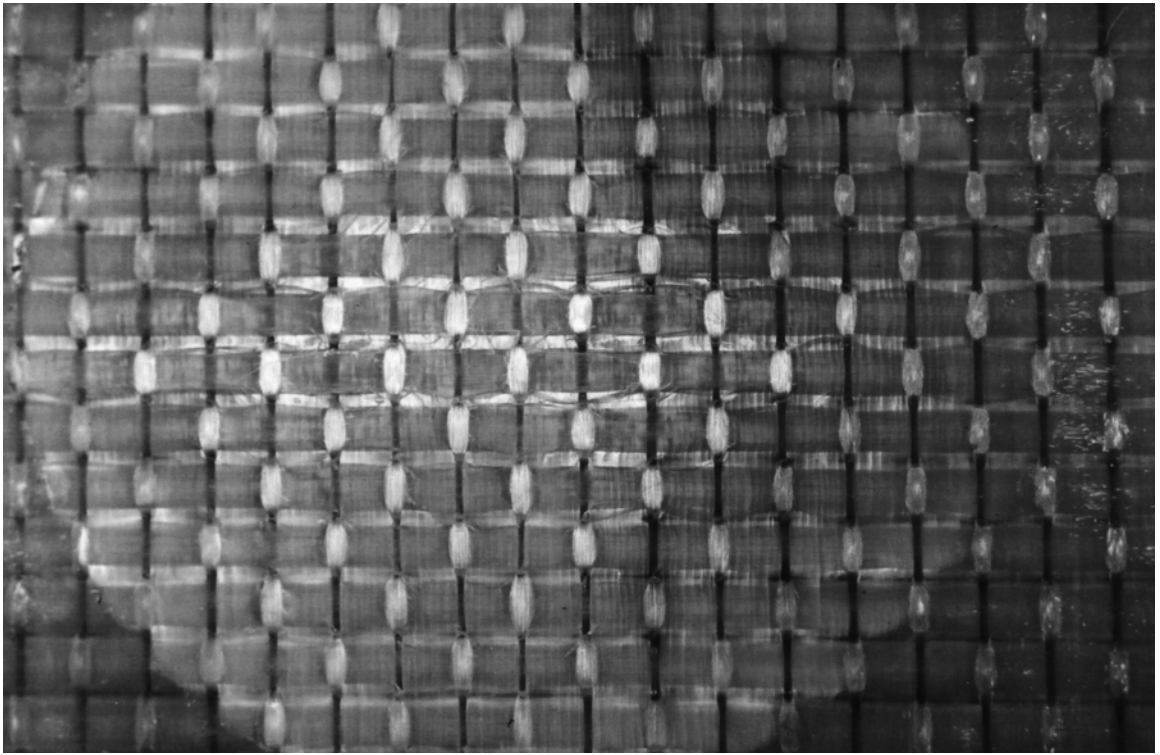


**Figure 4.28 Closer Views of Rear Target Face (3D-S-93-3)**

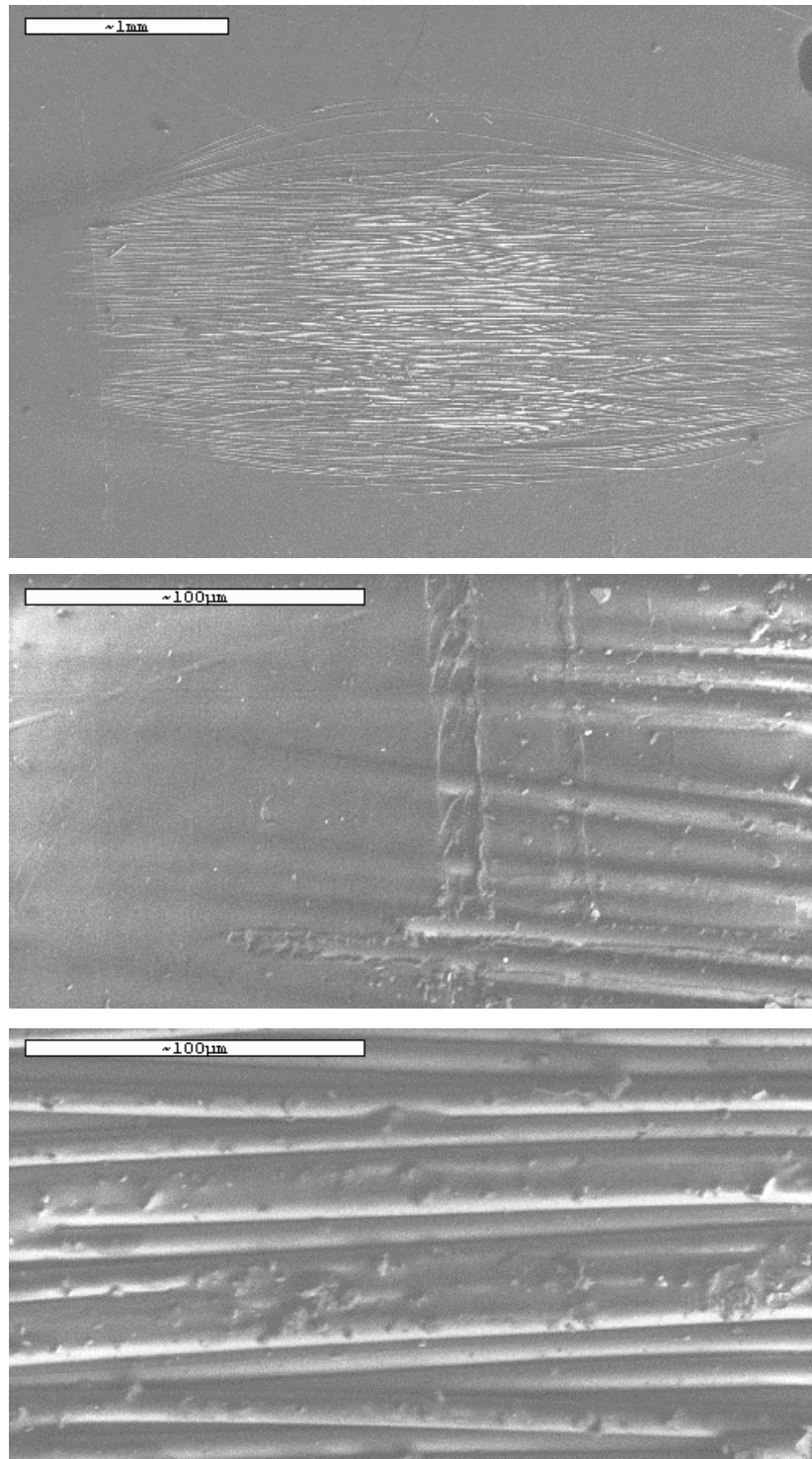
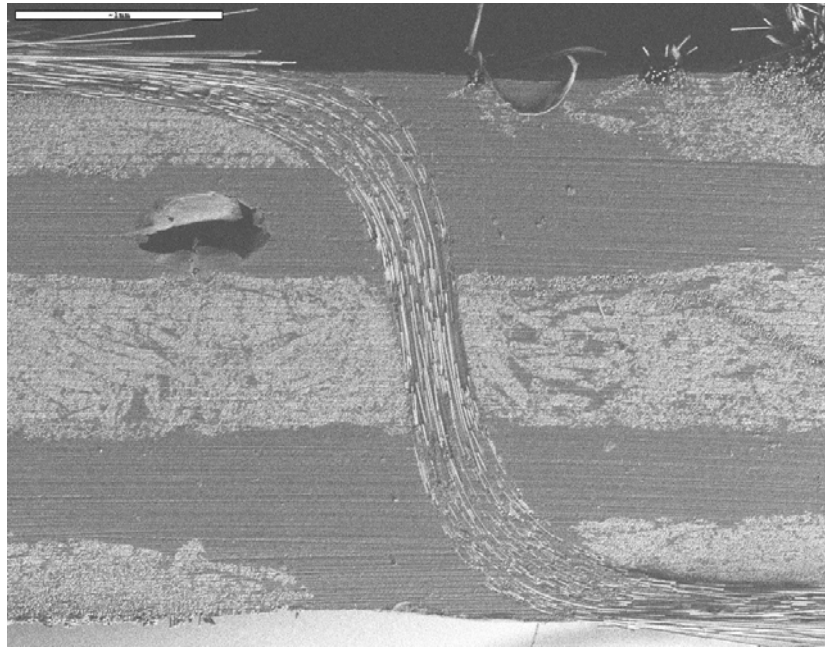
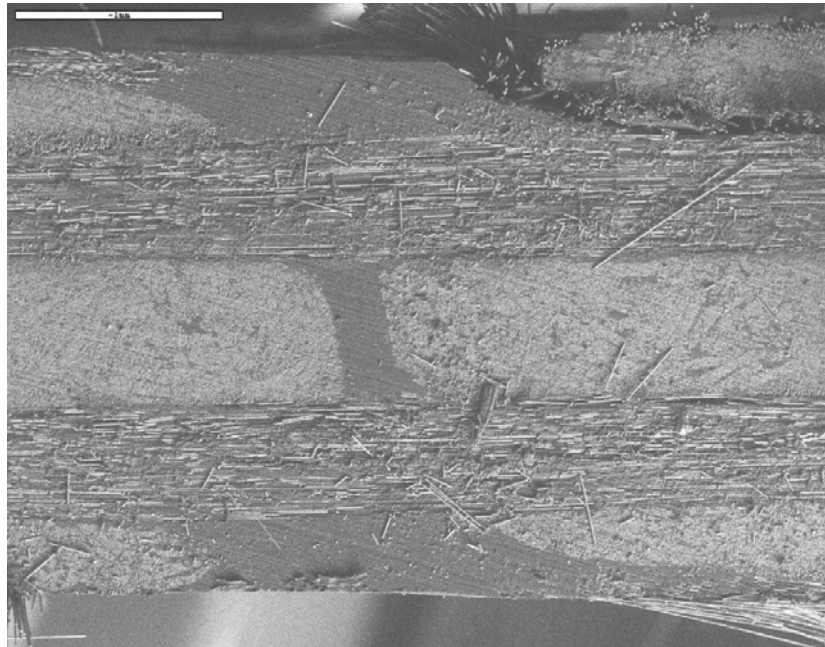


**Figure 4.29 Scanning Electron Micrographs Showing Surface Damage on Front Target Face near Impact Site (3D-S-93-3): Damaged z-Crimp (Top), Closer View of Left Edge (Middle), Close View of Central Region (Bottom)**

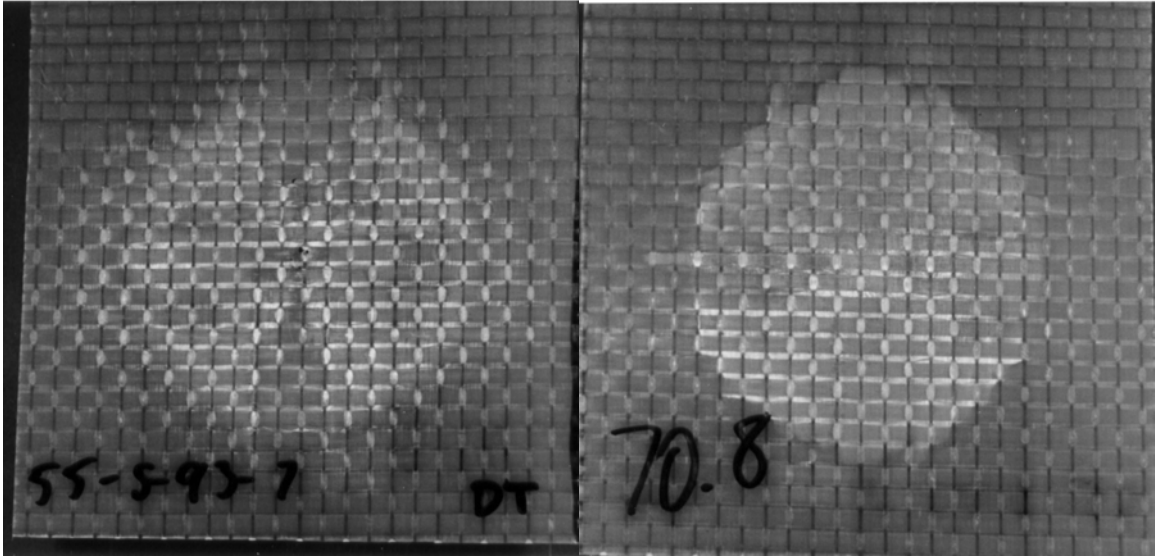


(a)



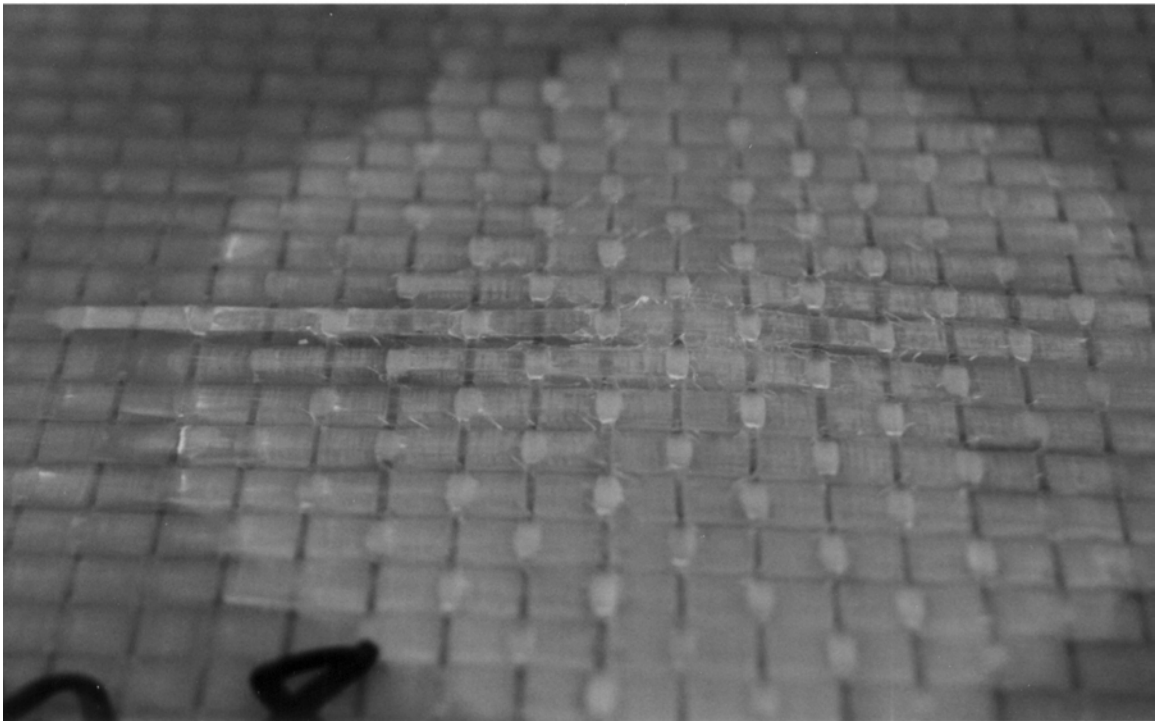
(b)

**Figure 4.30 Scanning Electron Micrographs Showing Internal Integrity near Impact Site (3D-S-93-3): (a) Sections of z-Tow and Weft Tows, (b) Sections of Warp and Weft Tows**



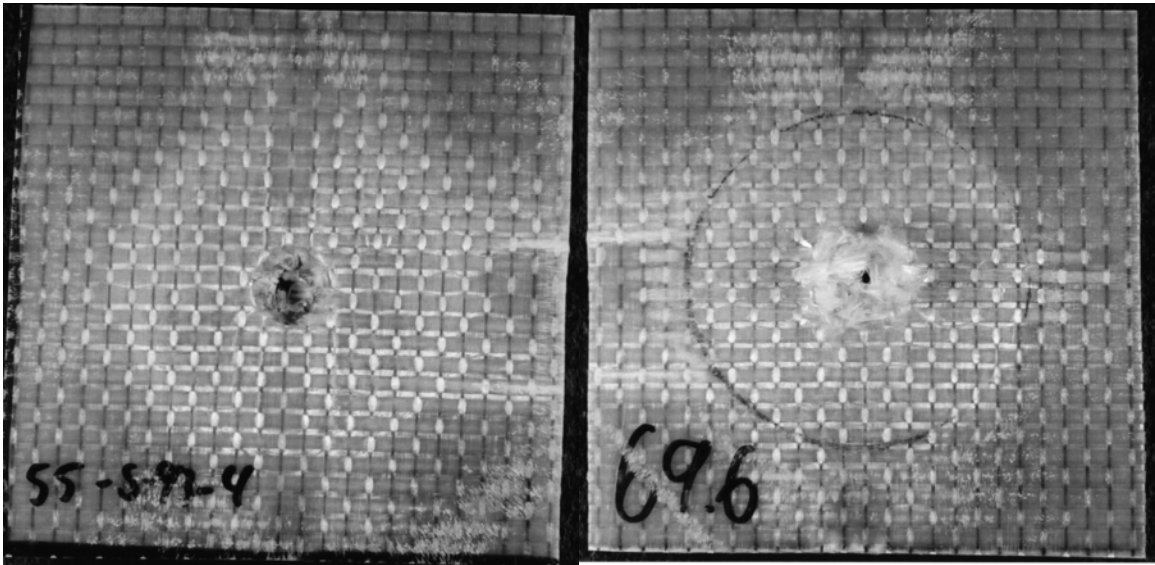
(a)

(b)



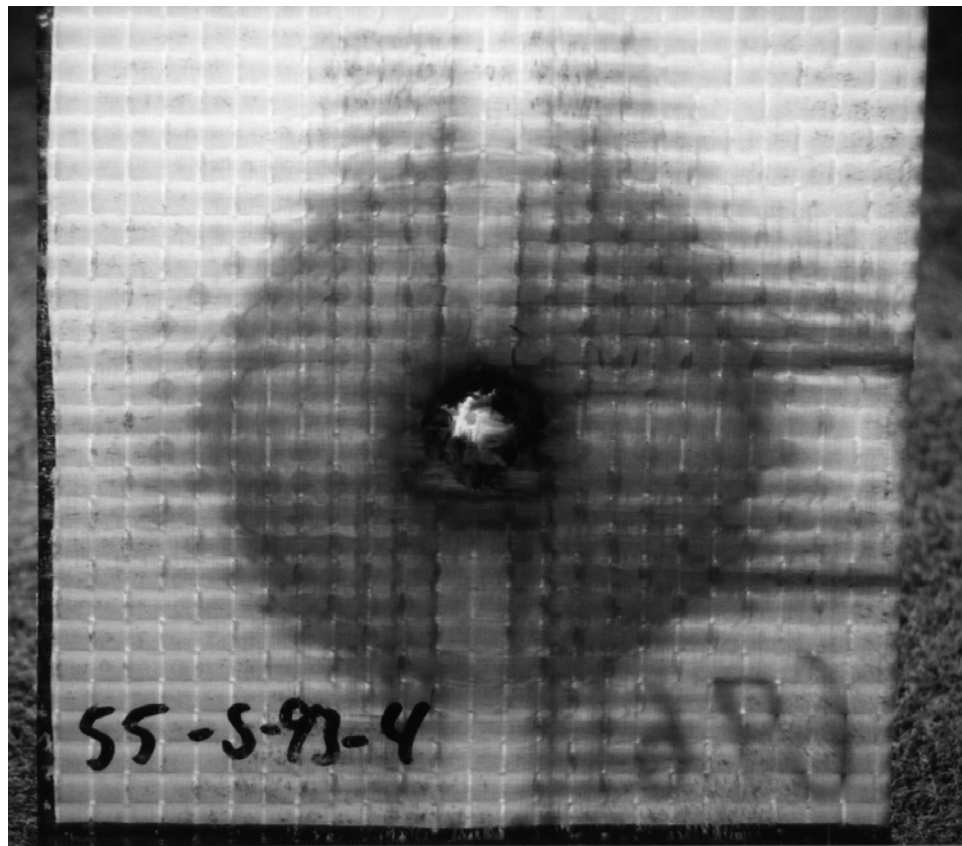
(c)

**Figure 4.31 Sub-Perforation (5 Strikes) Photography of 3D-S-93-4:  
(a) Front Face, (b) Rear Face, (c) Rear Face, Oblique**



(a)

(b)



(c)

**Figure 4.32 Post-Mortem (39 Strikes) Photography of 3D-S-93-7:  
(a) Front Face, (b) Rear Face, (c) Rear Face under Back-Lighting**

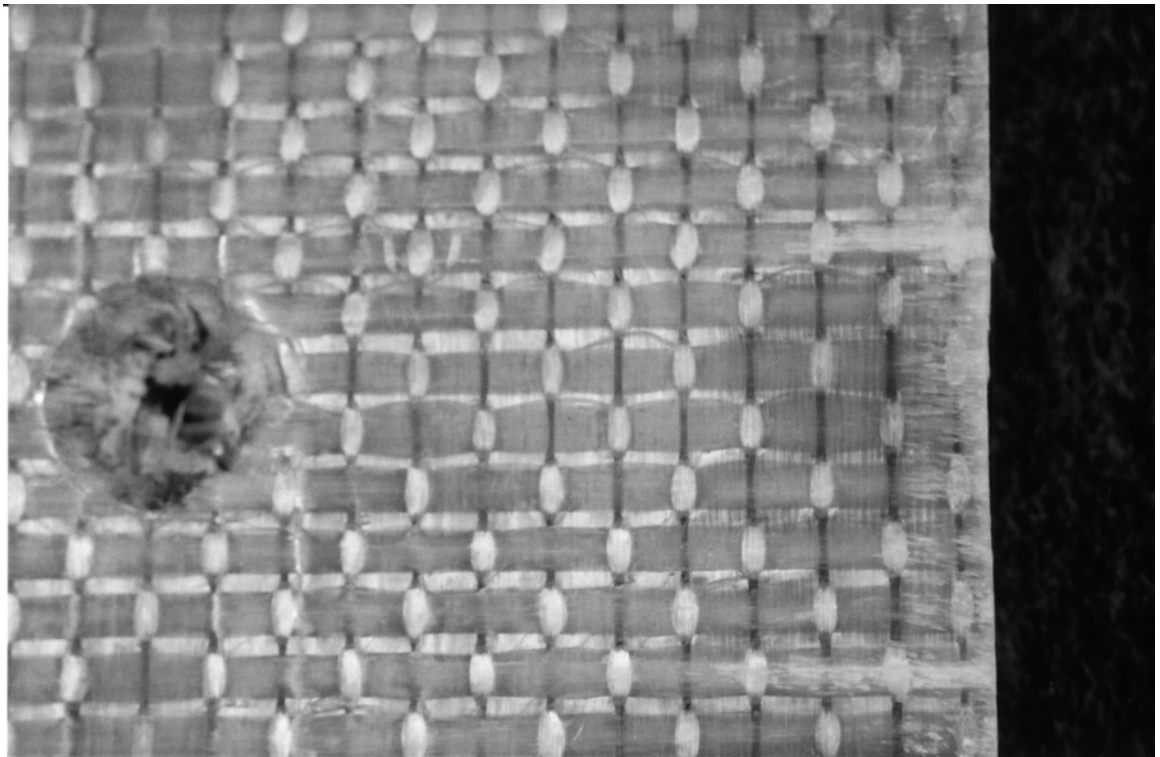
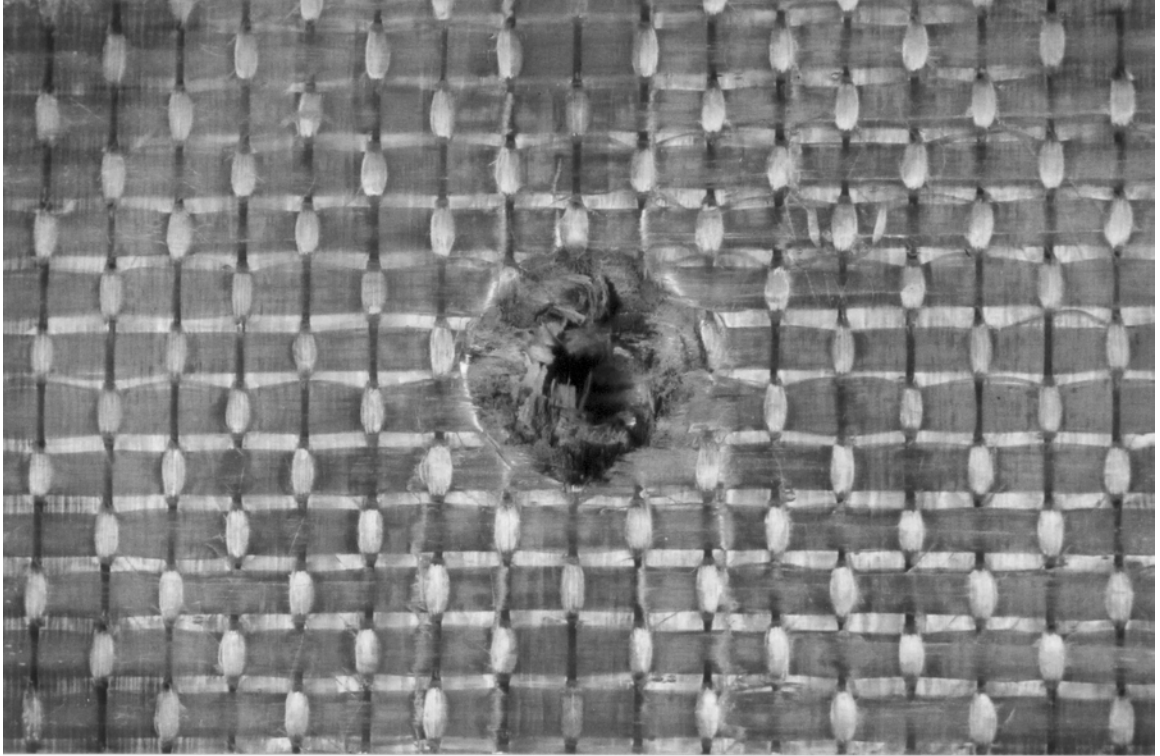


**Figure 4.33** Closer Views of Front Target Face (3D-S-93-7)

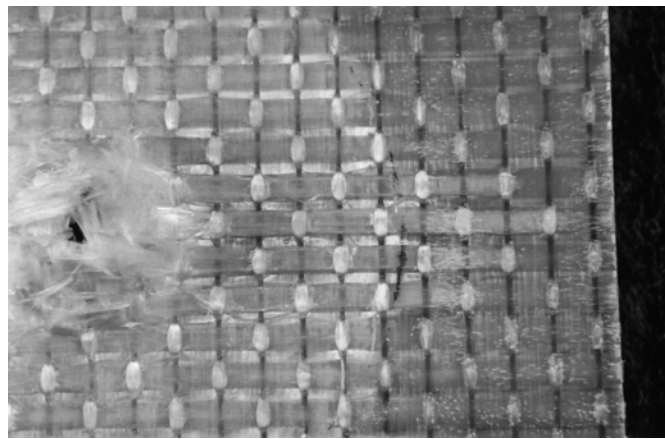
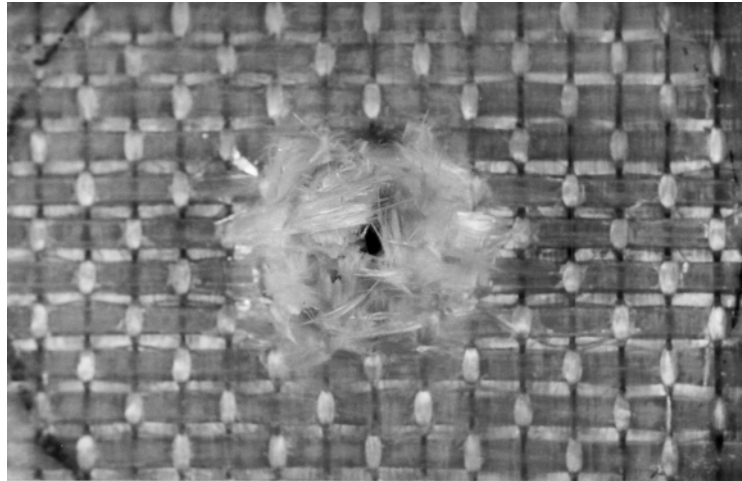


Figure 4.34 Closer Views of Rear Target Face (3D-S-93-7)

## 5. HIGH-VELOCITY IMPACT AND PERFORATION

This part of the investigation examines how the variation of fabric architecture of systems with comparable areal density and fiber-volume-fraction affects perforation resistance, strength, energy dissipation, and damage mechanisms in GFRP composite panels subjected to high-velocity perforation near the ballistic limit, at velocities ranging from 150 to 540 m/s. Three woven architectures were chosen as the fabric preforms for this investigation: a 2D plain-woven 24-ply laminate, a 3D orthogonally woven monolith, and a 3-ply laminate of 3D orthogonally woven lamina. The selected composite fibers were S2-glass, and a rubber-toughened vinyl-ester resin was chosen for the matrix material. These systems were chosen to compare systems of comparable areal-density but different fiber-architecture (Table 5.1). The 3D woven systems have fiber reinforcement in the  $z$ -direction. Furthermore, the 3D laminate has three times the number of sites of crimp in the  $z$ -yarns and the two internal planes separating the three layers lack  $z$ -reinforcement. This report is organized as follows: the details of the material preparation and fabrication are given in Section 5.2, a description of the experimental apparatus and method is presented in Section 5.3, the results are discussed in Section 5.4, and concluding remarks are made in Section 5.5.

### 5.1 Material Preparation and Fabrication

Three composite systems were examined, with different fabric architectures, but with comparable areal densities and thicknesses. The first composite system was a

conventional 2D plain-weave laminate with 12 layers (*2D-S-24x12*). The second material system was monolithic 3D orthogonal weave (*3D-S-270*). The third composite system (*3D-S-93x3*) was reinforced by three layers of 3D orthogonally woven fabric, such that the total areal density was nearly the same as for the other two systems. Further details of the material preparation and fabrication are provided in Section 3.1. Areal density, fiber-volume-fraction, and average thickness of each sample are given in Table 5.1. All three composite systems were derived from S2-glass fiber rovings in a matrix of Dow Derakane 8084 rubber-toughened epoxy/vinyl-ester. Based upon Equation (3.1), the estimated fiber-volume-fraction ranged from 0.49 to 0.54. As before, this selection of material systems permitted an isolation of the effects of fabric architecture.

**Table 5.1 S2-Glass/Rubber-Toughened-Epoxy-Vinyl-Ester Composite Systems for High-Velocity Impact**

<b>Composite System</b>	<b>Sample Designation</b>	<b>Measured Areal Density (kg/m<sup>2</sup>)</b>	<b>Fiber Volume Fraction</b>	<b>Thickness (mm)</b>
<b>2D-24x12</b> (12-ply, 2D Laminates)	<i>2D-S-24x12-4</i>	13.4	0.525	7.42
	<i>2D-S-24x12-5</i>	13.5	0.516	7.54
	<i>2D-S-24x12-6</i>	13.6	0.505	7.65
<b>3D-93x3</b> (3-Ply, 3D Laminates)	<i>3D-S-93x3-4</i>	12.9	0.538	7.01
	<i>3D-S-93x3-5</i>	13.0	0.532	7.09
	<i>3D-S-93x3-6</i>	13.0	0.532	7.09
<b>3D-270</b> (3D Monoliths)	<i>3D-S-270-4</i>	12.7	0.507	7.19
	<i>3D-S-270-5</i>	12.9	0.490	7.44
	<i>3D-S-270-6</i>	12.9	0.507	7.19

## 5.2 Experimental Procedures

The 19-mm powder gun, described in Section 2.2.2, is used to conduct impact experiments at ballistic velocities. The striking velocity and residual velocity of the projectile are used to calculate energy dissipation through a balance of kinetic energy (Equation 2.1). For these experiments, the projectile was designed to match the hemispherical nose geometry of the quasi-static and low-velocity penetrators of Chapters 3 and 4 (Figure 5.1). The work of quasi-static perforation, which was measured in Chapter 3, was used to estimate the ballistic limit in the following manner:

$$V_{BL} = \sqrt{\frac{2W_p}{m}} \quad (5.1)$$

where  $W_p$  is the average measured work of quasi-static perforation,  $m$  is the mass of the projectile, and  $V_{BL}$  is the estimated ballistic limit. A calibration of striking velocity and powder-charge yielded requisite powder to produce velocities close to the estimated ballistic limit, approximately 180 m/s. A third, larger charge was used to produce velocities far in excess of the ballistic limit. Post-mortem photography and scanning electron microscopy were used to characterize damage and failure mechanisms.

### 5.3 Results And Discussion

Striking velocities of approximately 150, 230, and 540 m/s were produced. The specific striking and residual velocities are listed in Table 5.2, as well as energy dissipation. The projectile rebounded at the lowest velocity for each material system and perforated the target in all other cases. The low residual velocities measured indicate that the ballistic limits are closer to 230 m/s than to 150 m/s. More data is needed to identify differences in ballistic limit; however, the monolithic 3D system (*3D-S-270*) had the lowest perforating striking velocity, 216 m/s, corresponding with the highest residual velocity, 79 m/s. Based on this information, the 3D monolith should have the lowest ballistic limit. Despite the coarseness of the velocity data, clear differences were observed in failure mechanisms. The remainder of Section 5.3 provides sequential

**Table 5.2 Striking Velocity, Residual Velocity, and Energy Dissipation**

<b>Composite System</b>	<b>Sample Designation</b>	<b>Striking Velocity (m/s)</b>	<b>Residual Velocity (m/s)</b>	<b>Energy Dissipation (J)</b>
<b>3D-270</b> (3D Monoliths)	<i>3D-S-270-4</i>	154	Rebound	656
	<i>3D-S-270-5</i>	216	79	1130
	<i>3D-S-270-6</i>	525	344	4380
<b>2D-24x12</b> (12-ply, 2D Laminates)	<i>2D-S-24x12-4</i>	155	Rebound	669
	<i>2D-S-24x12-5</i>	233	58	1420
	<i>2D-S-24x12-6</i>	539	344	4780
<b>3D-93x3</b> (3-Ply, 3D Laminates)	<i>3D-S-93x3-4</i>	152	Rebound	643
	<i>3D-S-93x3-5</i>	227	39	1390
	<i>3D-S-93x3-6</i>	508	*	*

\* Residual velocity device was damaged – no measurement obtained.

discussions of the photographic and micrographic record for the 3D monolithic system (*3D-S-270*), the 2D laminates (*3D-S-24x12*), and then the 3D laminates (*3D-S-93x3*).

Subjected to its lowest striking velocity of 154 m/s, the 3D monolith defeated the projectile, sending it back at an undetermined velocity. From Figure 5.2, it could be seen that fiber debonding extended to the edges of the panel on both front and rear faces. Figure 5.3 provides a closer view of the impacted face, where it could be seen that ruptured fiber rovings were bent back toward the projectile. Extensive matrix cracking was also observed (Figure 5.3). Scanning electron microscopy revealed a large amount of internal debonding (Figure 5.4).

The 3D monolith was perforated at a striking velocity of 216 m/s, indicating a ballistic limit between 154 and 216 m/s. Here, fiber debonding also extended to the edge of the panel. When loaded into a cartridge case, each projectile was separated from the smokeless powder (nitrocellulose) by a plastic shot cup whose petals were removed, allowing the powder to burn more completely before accelerating the projectile. At the striking velocity of 216 m/s, the projectile perforated the target, but the shot cup was caught in the newly created hole (Figures 5.5) with little residual transverse deformation (Figure 5.6). On the rear face, the straining and fracture of *z*-crimps was observed, as well as the sliding of surface weft through the *z*-crimps (Figure 5.7).

Subjected to the highest velocity of 525 m/s, the 3D monolith was perforated again. At this impact velocity, front face damage was confined to a small area (Figure 5.8a). However, back face damage was heavy, covering a wide area, and resulting in large residual transverse deformation (Figure 5.8b,c). Massive rupture of *z*-crimps was observed, and material streamed in from the sides toward the perforation site.

Struck at its lowest striking velocity of 155 m/s, the 2D laminate defeated the projectile, returning it at an undetermined velocity. On both front and rear faces, extensive delamination was observed, some of which grew to the edges of the panel (Figure 5.9a,b). Matrix cracking was also seen throughout the damaged area (Figure 5.9c).

The 2D laminate was perforated at a striking velocity of 233 m/s, implying a ballistic limit between 155 and 233 m/s. Again, the plastic wadding was trapped before it could pass completely through the perforated target (Figure 5.10). Except for the failure

mode of fiber-fracture, which occurred only at the perforation site, material damage in the form of delamination and matrix cracking was diffuse and widespread (Figure 5.10c).

Subjected to the high velocity of 539 m/s, the 2D laminate was obviously perforated again. The resulting damage pattern was virtually identical to that at the intermediate velocity, with the exception that the wadding was not caught. On the front face, fibers at the impact site are bent outward (Figure 5.11a), analogous to the walls of an impact crater in homogeneous, isotropic materials. Broken fibers on the rear face are bent in the direction of projectile travel (Figure 5.11b,c). Little residual transverse deformation was observed (Figure 5.11c). This behavior contrasts starkly with that of the 3D monolith under high-velocity impact.

Impacted at its lowest striking velocity of 152 m/s, the 3D laminate defeated the projectile, sending it back at an unknown velocity. Qualitatively, the damage pattern appeared to be no different than that of the 3D *monolith* subjected to a 154-m/s impact (Figure 5.12). The only noticeable difference was the appearance of a small area of fiber fracture on the rear face, opposite the point of impact (Figure 5.12b). Little residual transverse deformation was observed (Figure 5.12c).

The 3D laminate was perforated at a striking velocity of 227 m/s, suggesting a ballistic limit between 152 and 227 m/s. Similar to the other material systems struck at this approximate velocity, the wadding was caught as it passed through the hole (Figures 5.13a and 5.14a). The damage appearing on the front face was essentially the same as for the 3D monolith impacted at 216 m/s. The rear face exhibited more extensive damage,

including straining and fracture of the rear surface z-crimps and pull-through of the rear surface weft tows intersecting the impact site (Figures 5.13b, 5.14b, and 5.15).

Struck at the high velocity of 508 m/s, the 3D laminate was perforated. At this high velocity, the plastic wadding also cleared the hole. It was discovered that the projectile of the previous shot had rebounded from projectile catcher tube and damaged the residual velocity device; therefore, the residual velocity was not captured. The post-perforation appearance of the front face was similar to that of the 3D monolith under high-velocity impact (compare Figures 5.16a and 5.8a). The rear face was heavily damaged, with fiber-debonding extending to the panel edge on all sides. Fracture of rear face z-crimps was observed, as well as sliding of rear surface weft through unbroken z-crimps. In fact, one of the weft tows had slid through all z-crimps on one side of the perforation (Figures 5.16b, 5.17b, and 5.18).

#### **5.4 Conclusions**

This investigation examined how variations of fabric architecture in composite systems with comparable areal densities affect perforation resistance, strength, and distributions of energy dissipation of GFRP composite panels subjected to high-velocity impact and perforation. Three woven fabric preforms were investigated: a 24-ply 2D plain-weave laminate, a monolithic 3D orthogonal weave, and a 3-ply 3D orthogonal weave laminate. The projectile striking velocity and residual velocity were measured to provide the energy dissipation.

Small differences in energy absorption were observed, and more experiments are needed to precisely quantify these differences; however, the data from the present experiments indicate that the ballistic limits of the 2D and 3D laminates, comparable to each other, are significantly higher than the ballistic limit of the 3D monolith.

Failure modes and damage mechanisms varied among the different material systems. Matrix cracking, delamination or fiber-debonding, and fiber fracture were observed in all systems. For each striking velocity, the radial expansion of damage was smallest for the 2D laminate and largest for the 3D monolith. Debonding of the 3D systems often extended to the edges of the test panel. Post-mortem analyses revealed additional energy absorption mechanisms, which involved the crimped portion of *z*-tows in the 3D composites. This implies that failure may be controlled by manipulation of the properties of the *z*-tows. Damage mechanisms unique to the 3D systems included the straining and fracture of *z*-tows, as well as the sliding of weft tows through unbroken *z*-crimps on the rear target face. Velocity data indicated that the strength and capacity to absorb energy under high-velocity transverse puncture were comparable for the 2D and 3D laminates and superior to the 3D monolith.

**5.5 Figures**  
**(Chapter 5)**

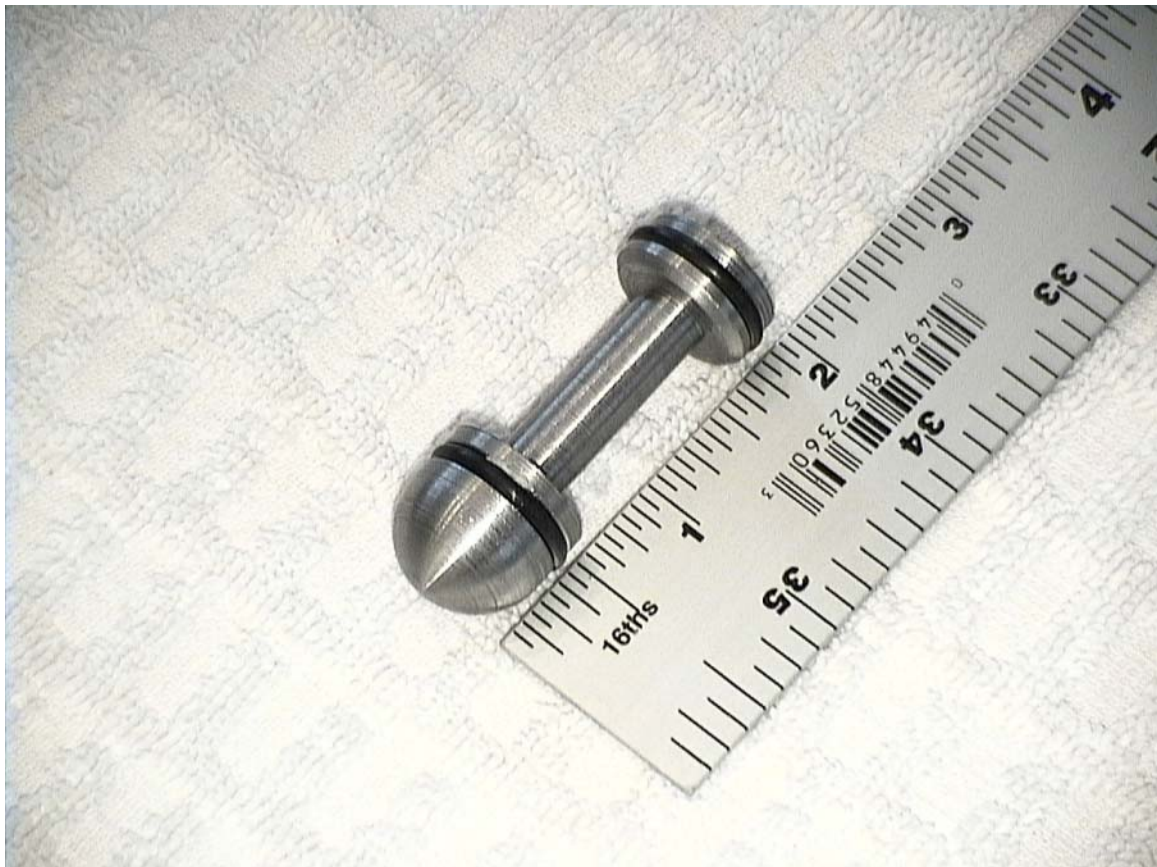
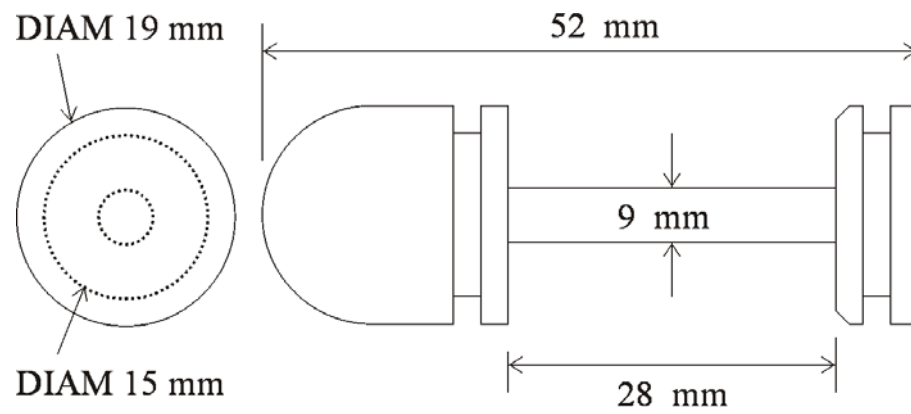
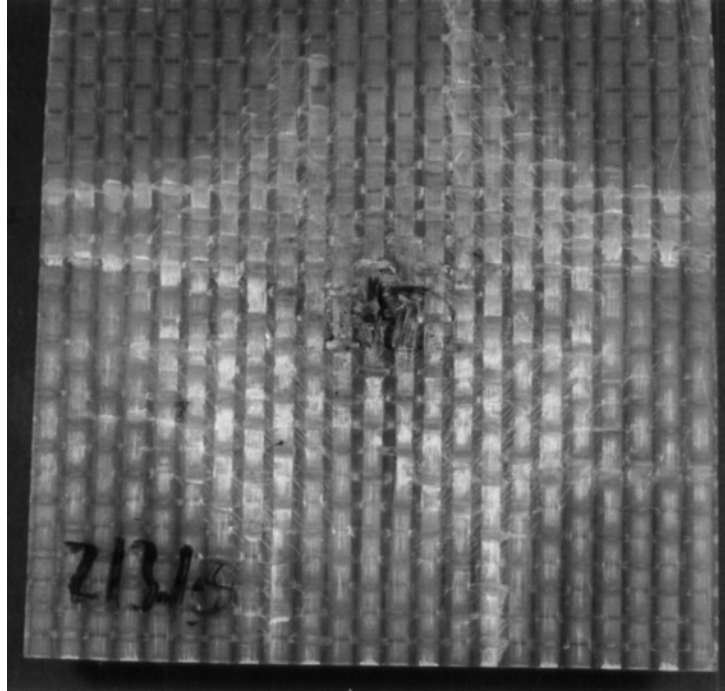
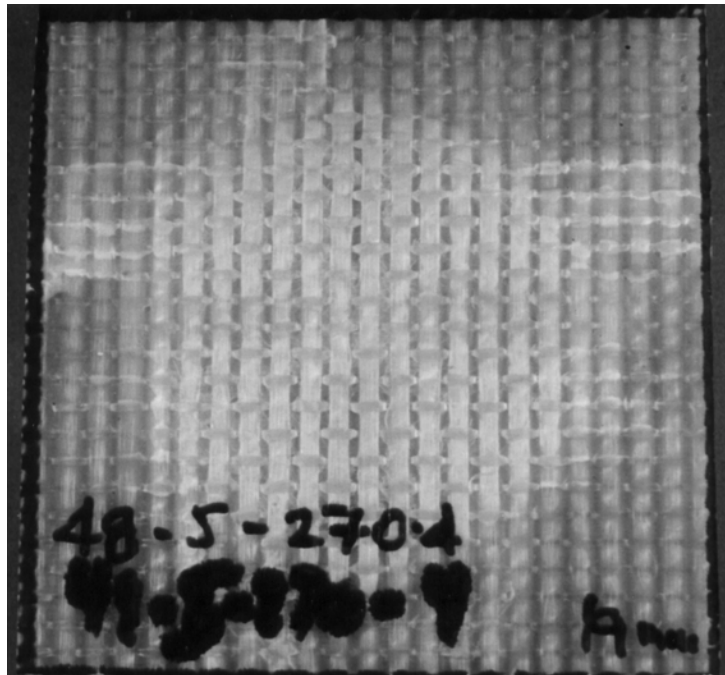


**Figure 5.1 19-mm Hemispherical-Nose Steel Projectile, 55.6 g  
(design by Rolin F. Barrett, Jr.)**



(a)



(b)

**Figure 5.2 Post-Mortem Photography of 3D-S-270-4 (154-m/s Striking Velocity):  
(a) Front Face, (b) Rear Face**

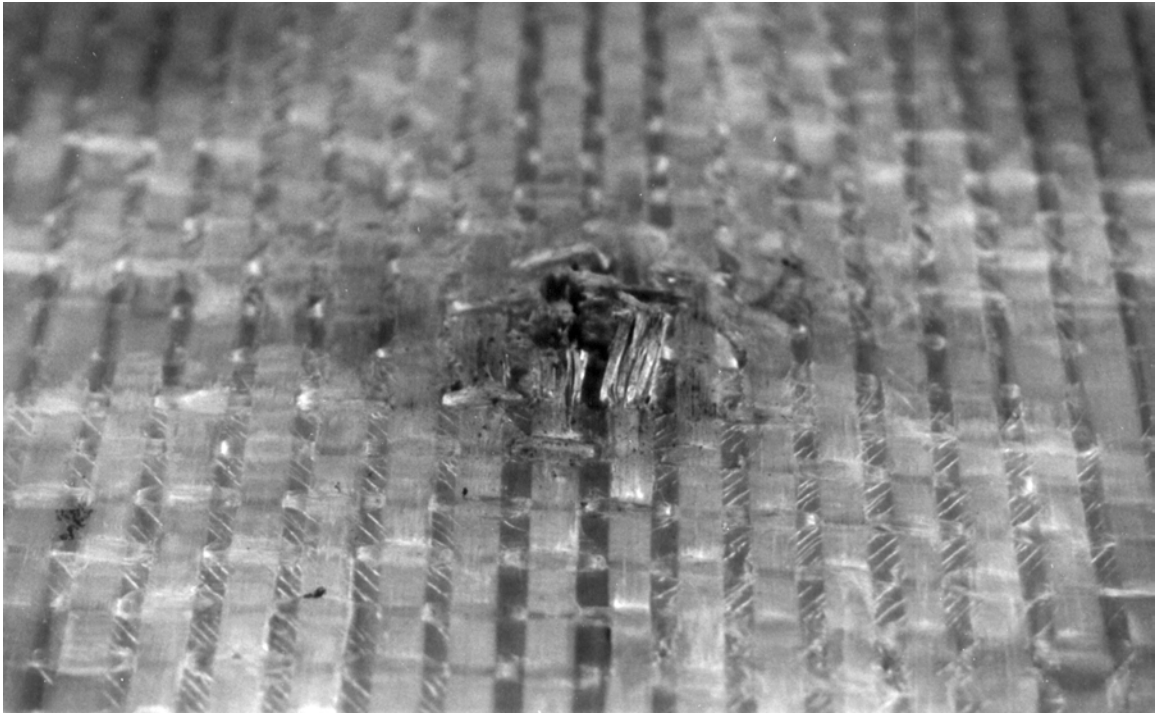
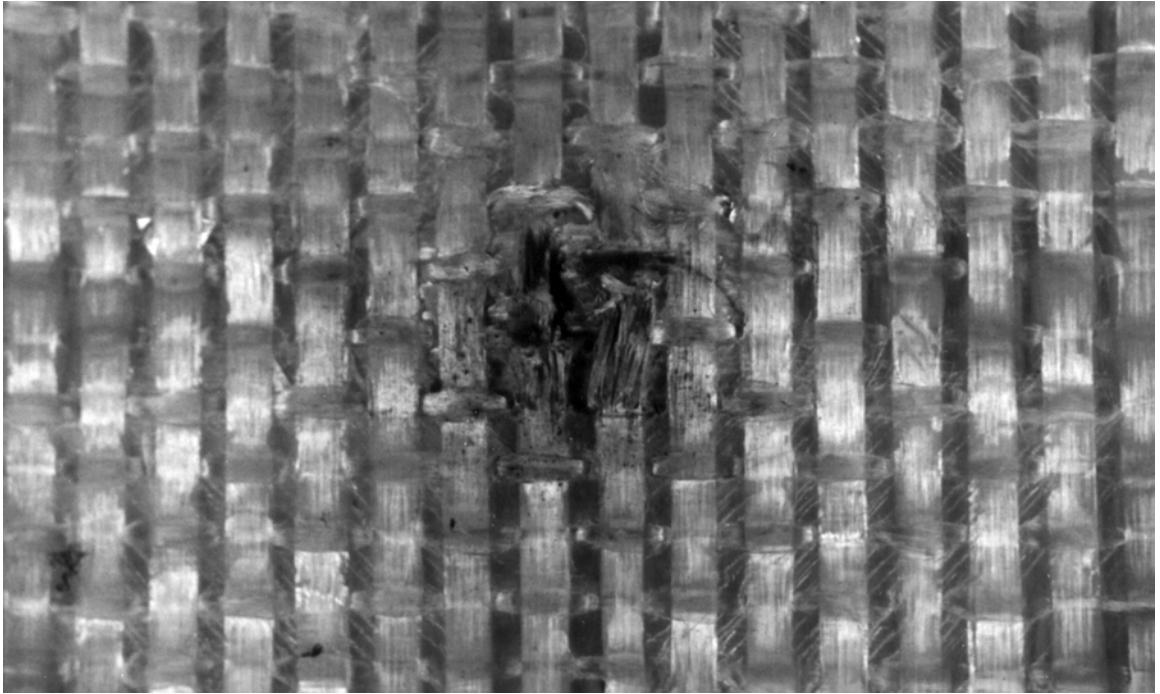


**Figure 5.3 Closer Views of Front Target Face (3D-S-270-4)**

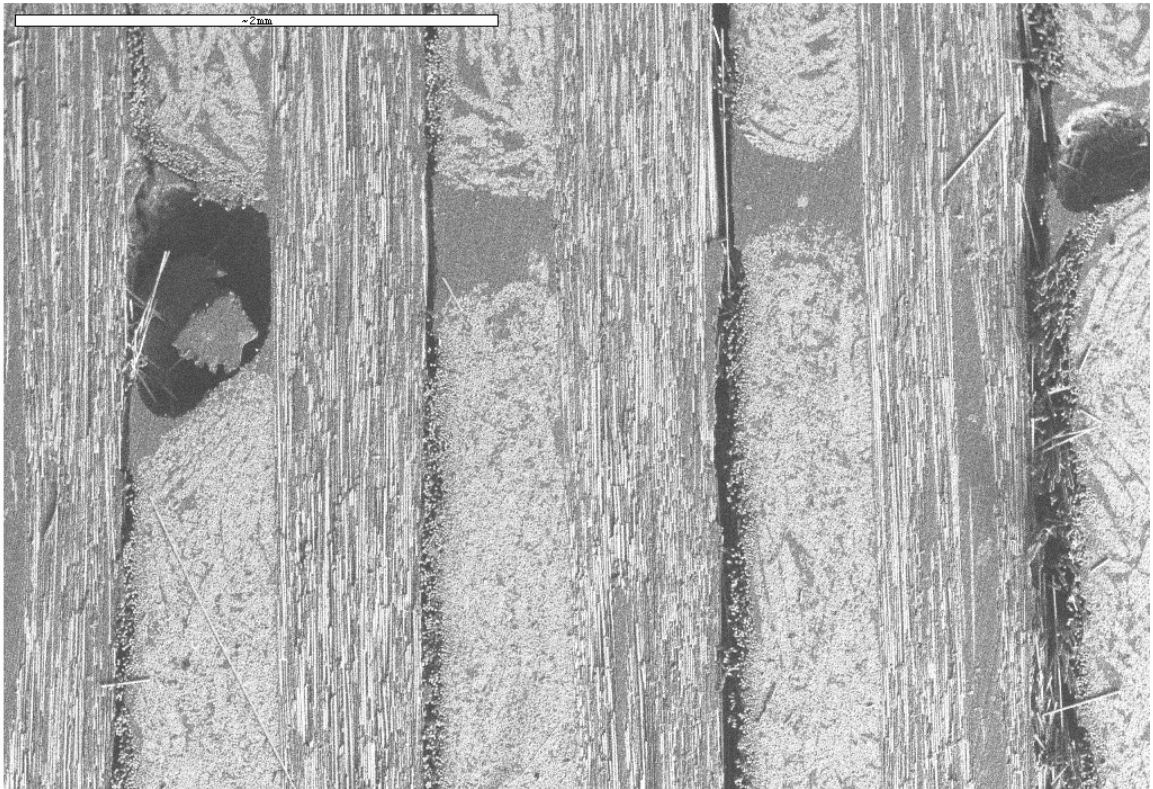
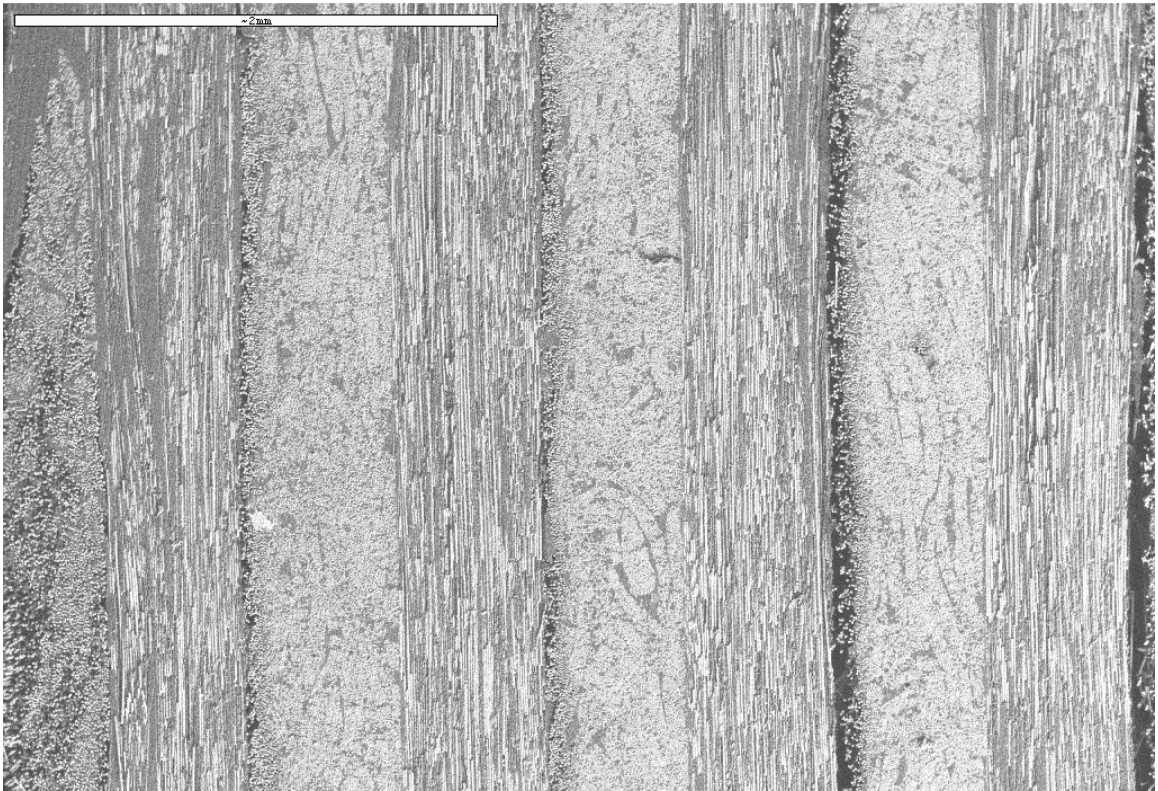
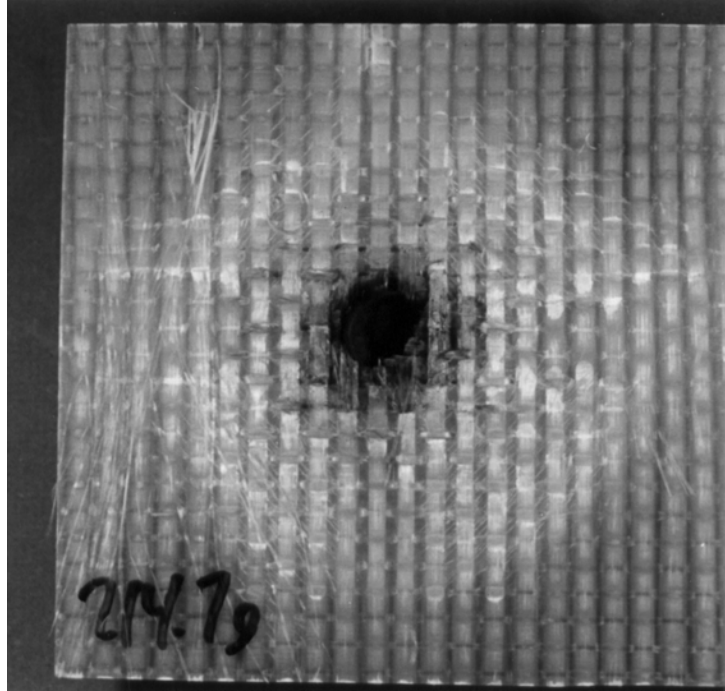
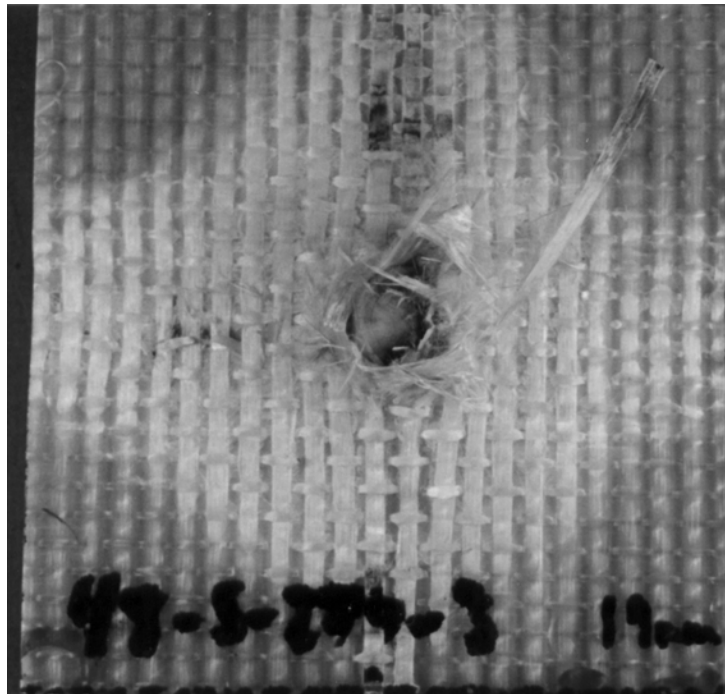


**Figure 5.4 Post-Mortem SEM (3D-S-270-4)**

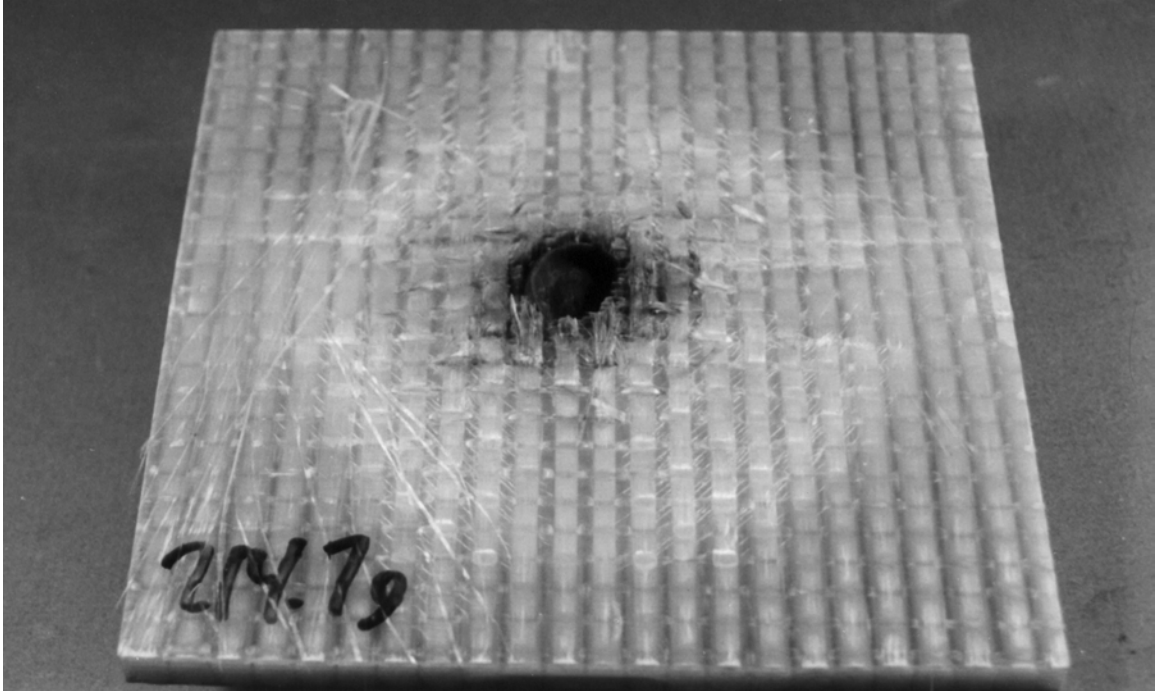


(a)

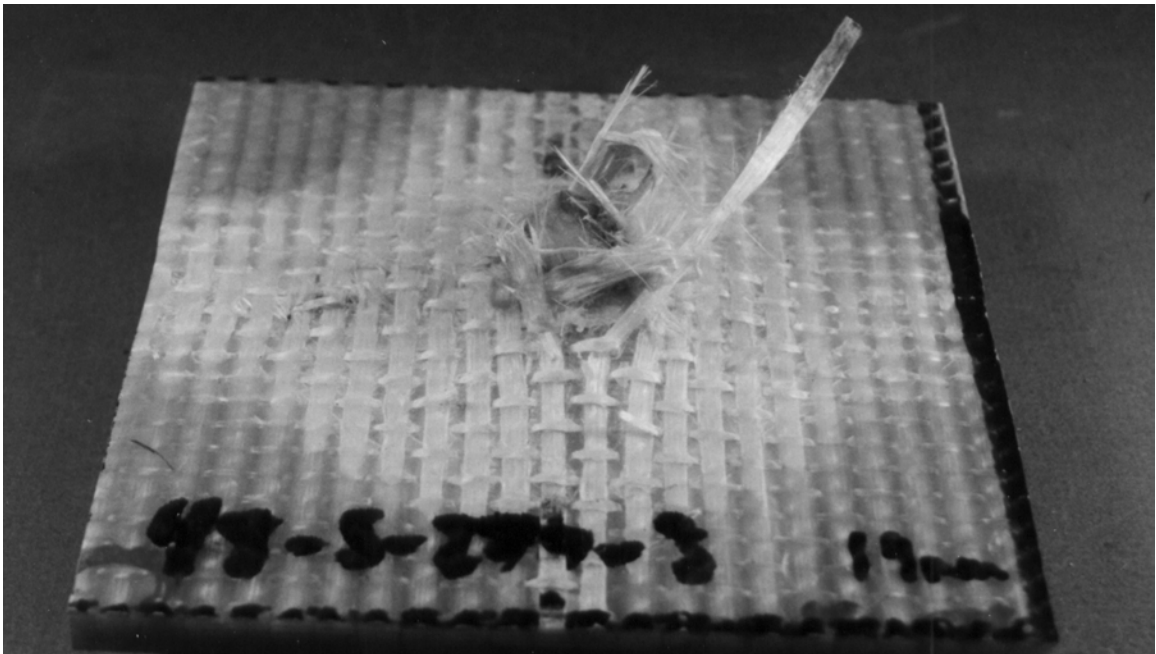


(b)

**Figure 5.5 Post-Mortem Photography of 3D-S-270-5 (216-m/s Striking Velocity):  
(a) Front Face, (b) Rear Face**



(a)



(b)

**Figure 5.6 Oblique Views of 3D-S-270-5: (a) Front Face, (b) Rear Face**

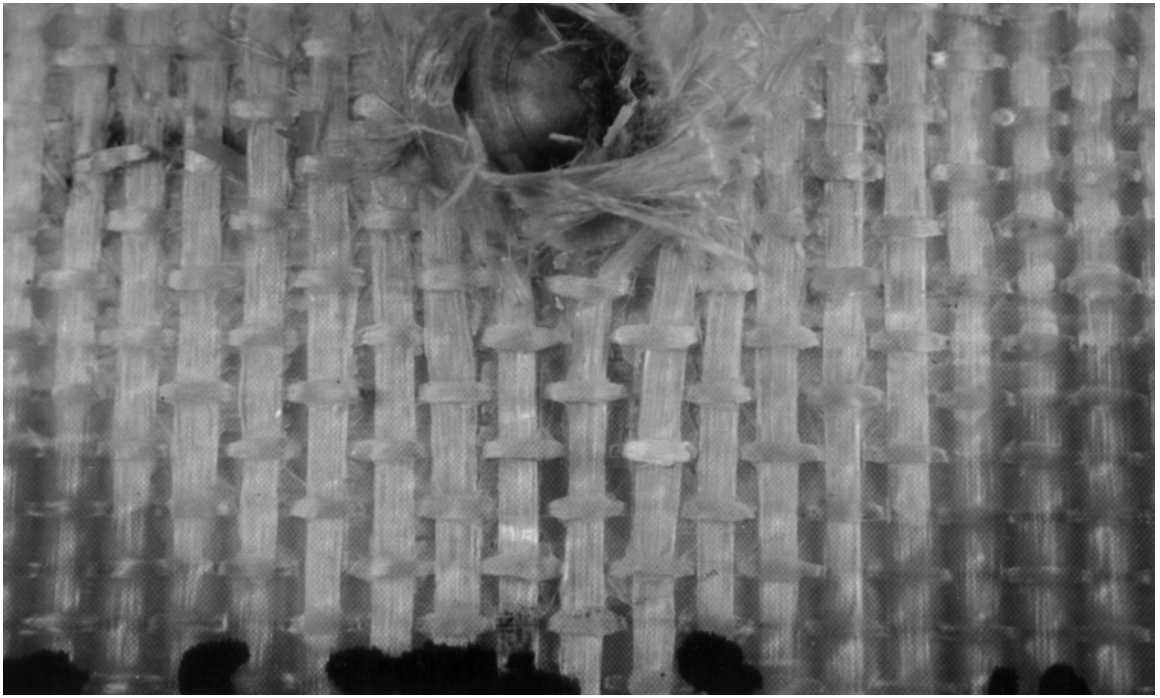
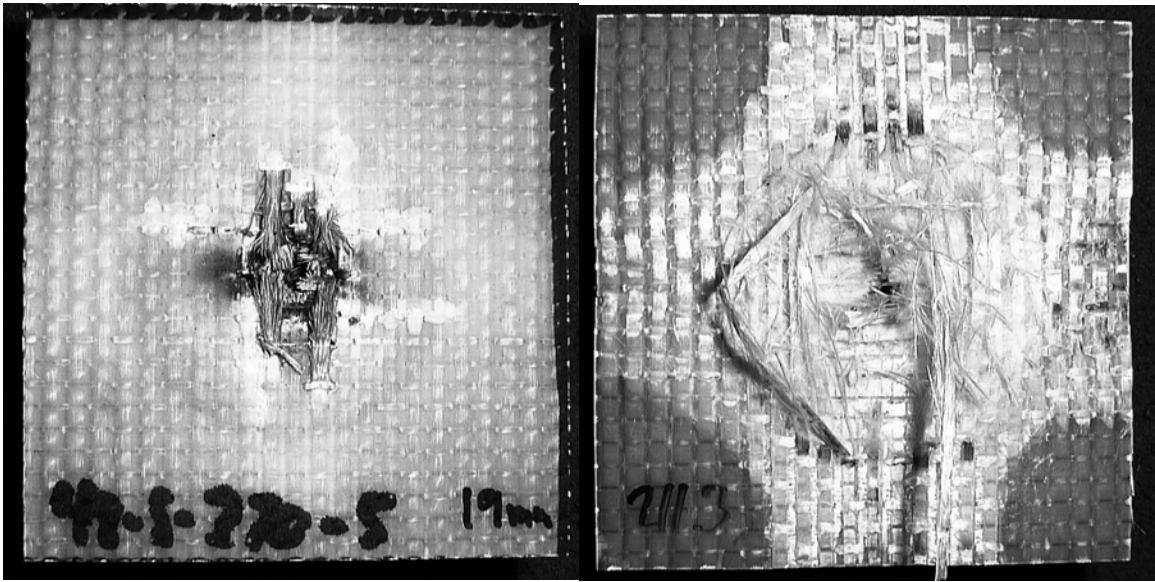


**Figure 5.7 Closer Views of Rear Target Face (3D-S-270-5)**



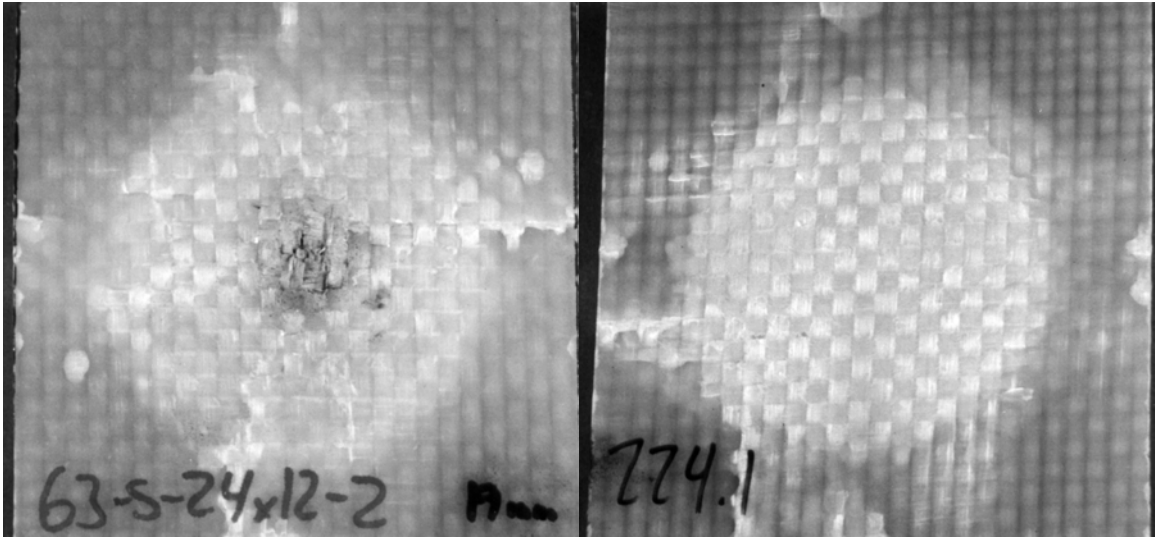
(a)

(b)



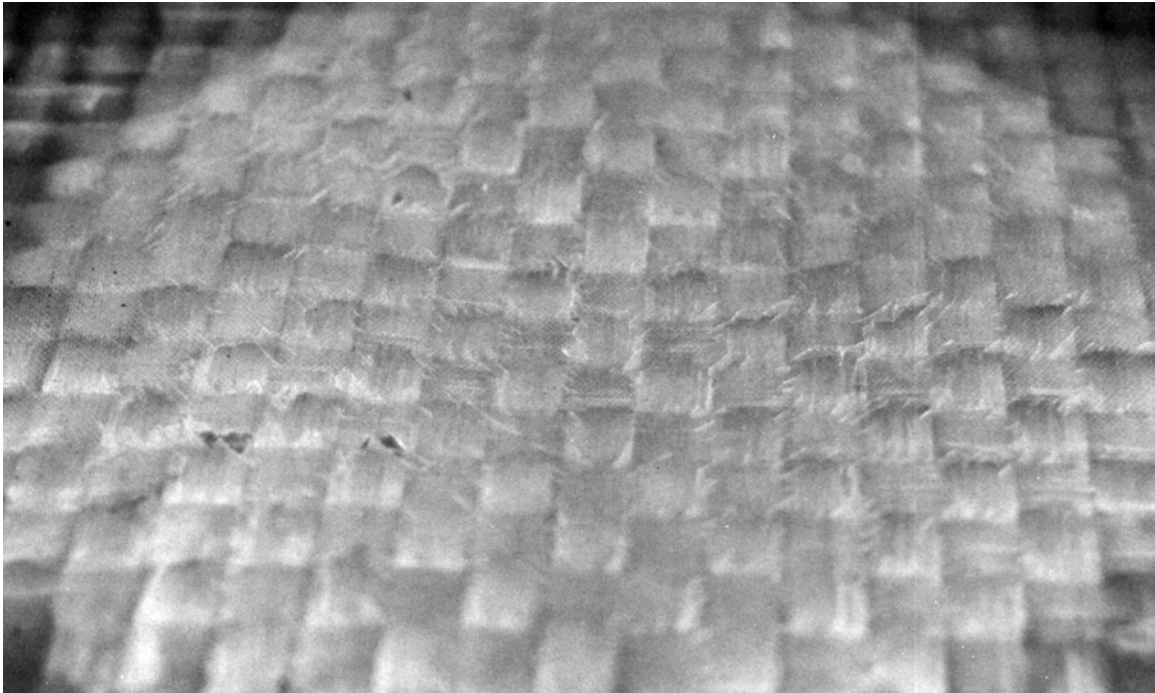
(c)

**Figure 5.8 Post-Mortem Photography of 3D-S-270-6 (525-m/s Striking Velocity):  
(a) Front Face, (b) Rear Face, (c) Rear Face, Oblique**



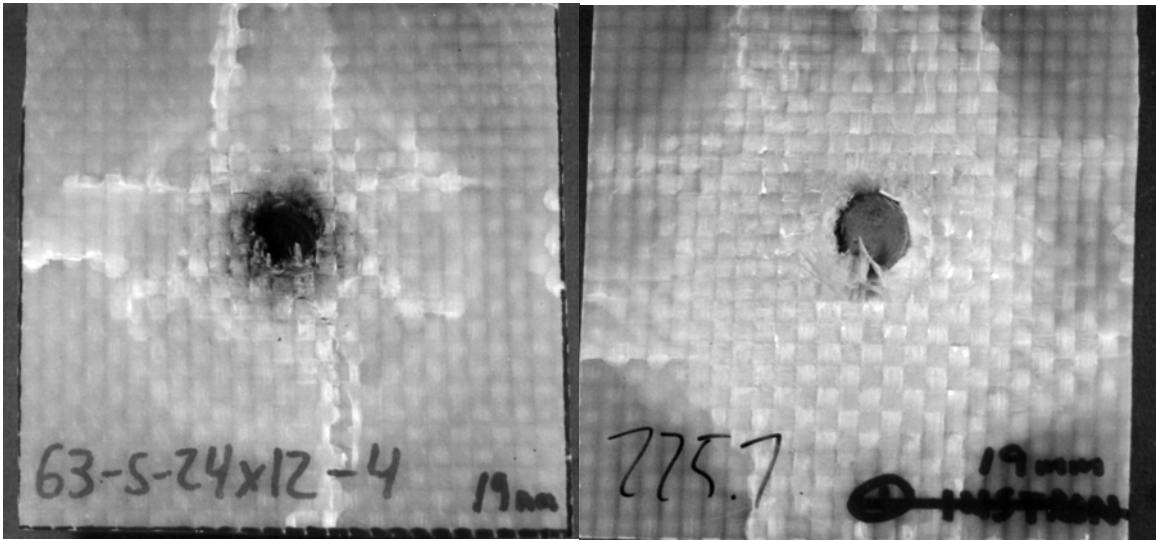
(a)

(b)



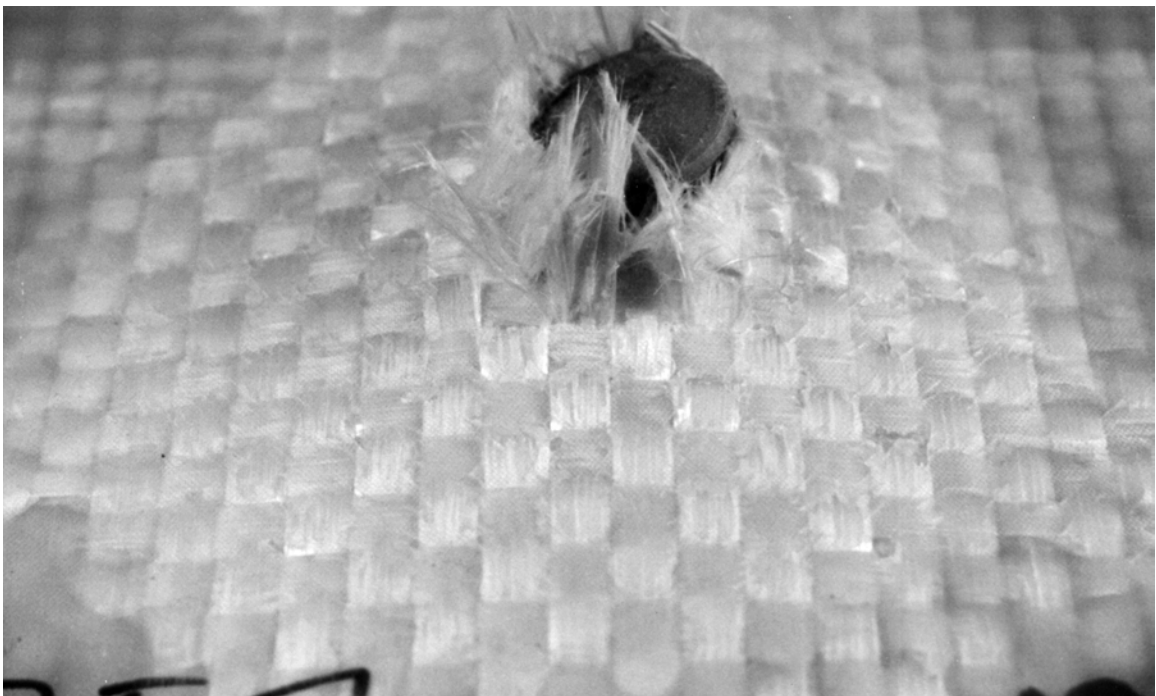
(c)

**Figure 5.9 Post-Mortem Photography of 2D-S-24x12-4 (155-m/s Striking Velocity):  
(a) Front Face, (b) Rear Face, (c) Rear Face, Oblique**



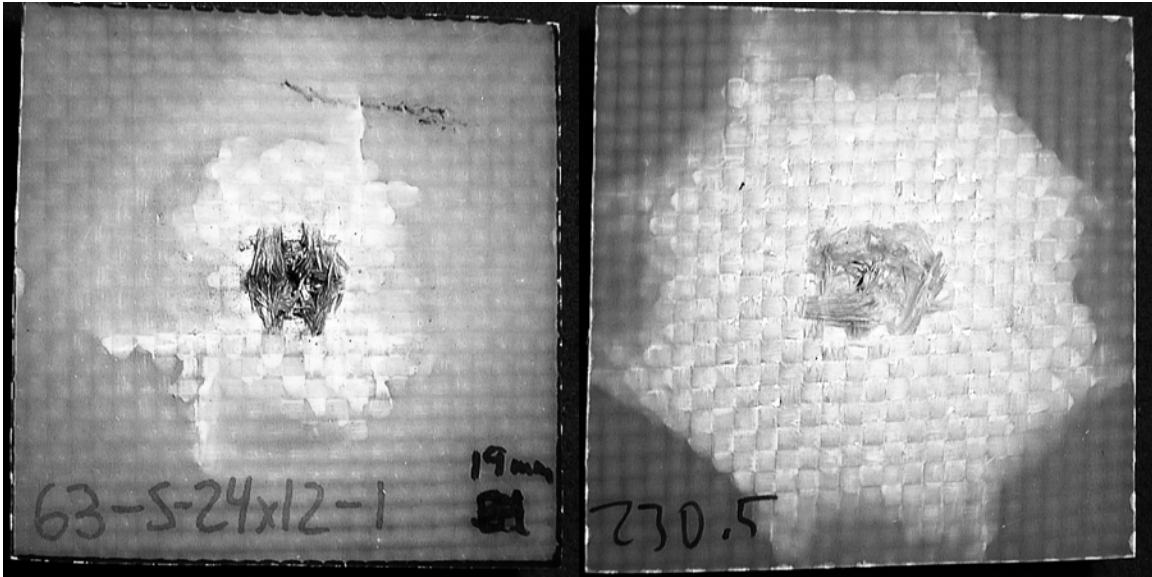
(a)

(b)



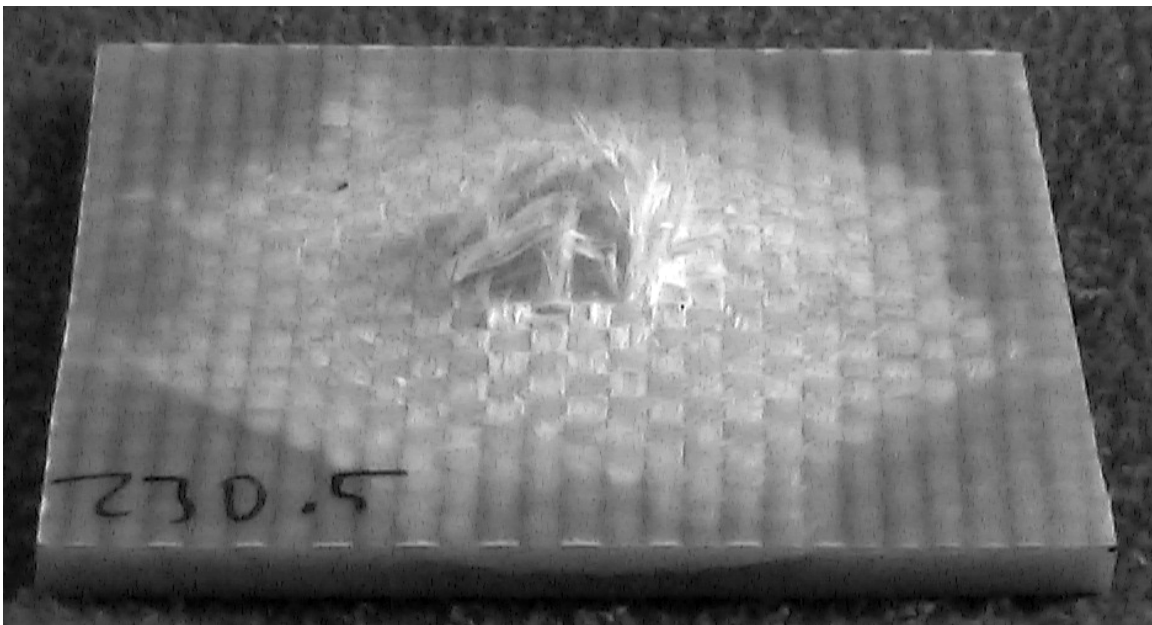
(c)

**Figure 5.10 Post-Mortem Photography of 2D-S-24x12-5 (233-m/s Striking Velocity):  
(a) Front Face, (b) Rear Face, (c) Rear Face, Oblique**



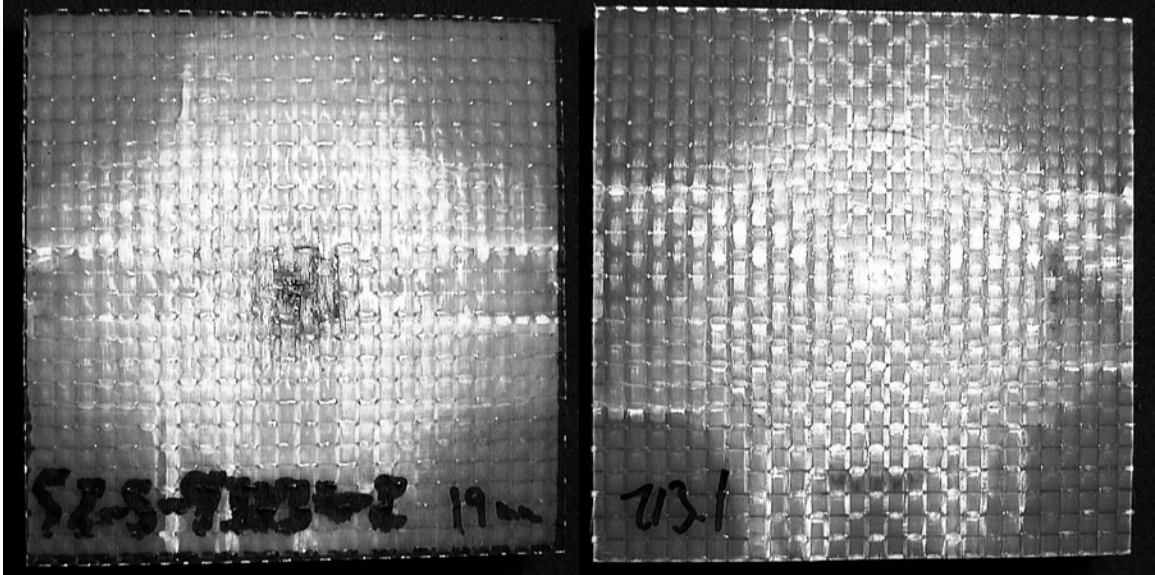
(a)

(b)



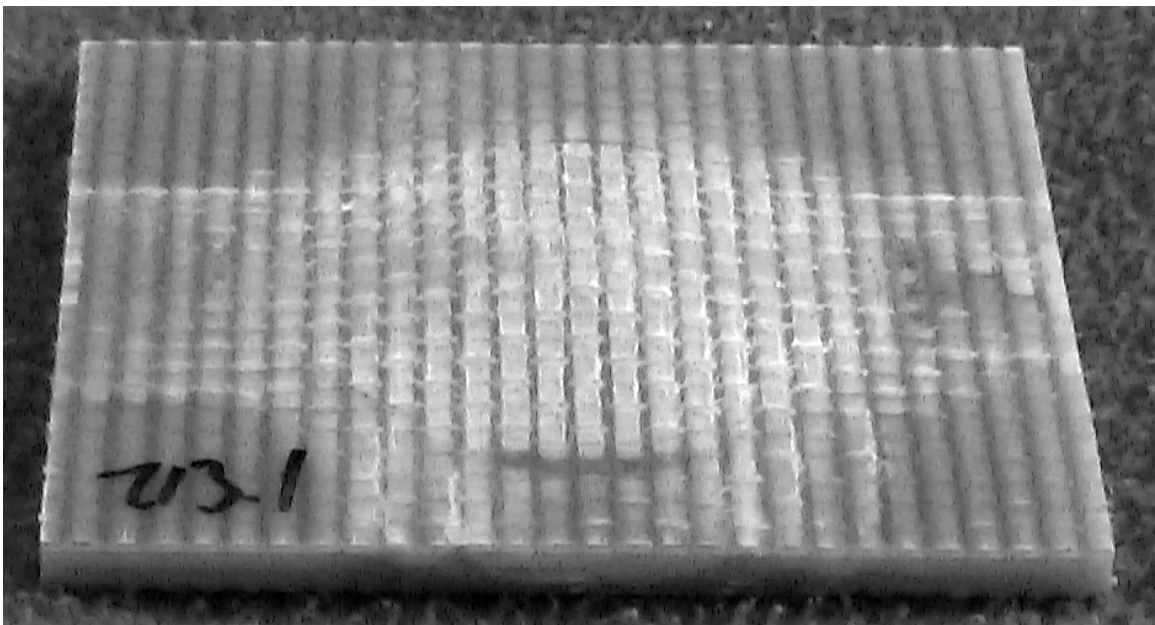
(c)

**Figure 5.11 Post-Mortem Photography of 2D-S-24x12-6 (539-m/s Striking Velocity):  
(a) Front Face, (b) Rear Face, (c) Rear Face, Oblique**



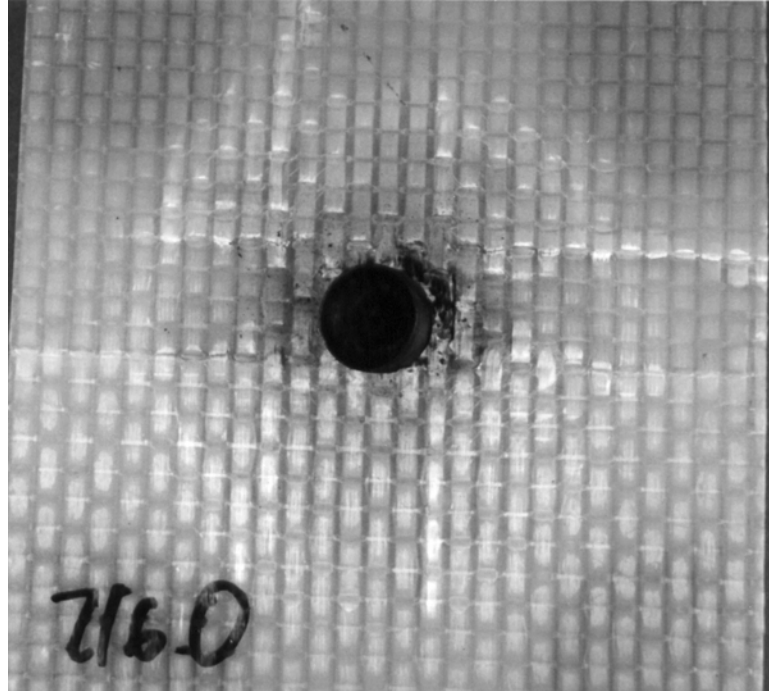
(a)

(b)

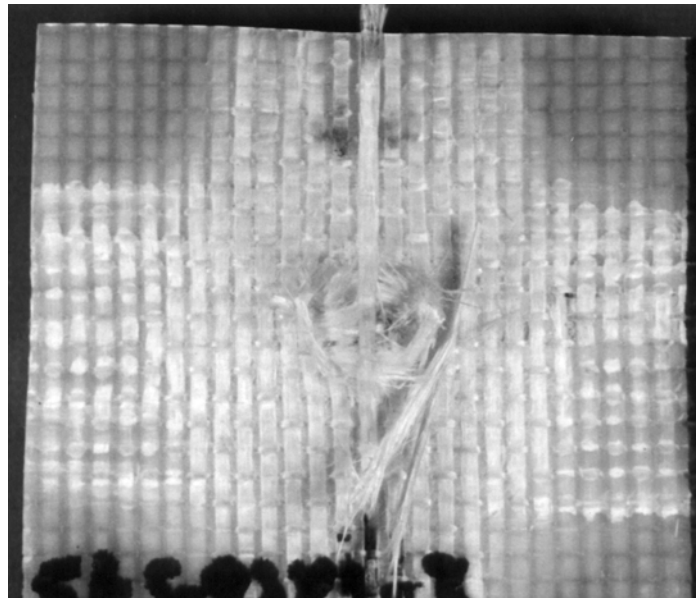


(c)

**Figure 5.12 Post-Mortem Photography of 3D-S-93x3-4 (152-m/s Striking Velocity):  
(a) Front Face, (b) Rear Face, (c) Rear Face, Oblique**



(a)



(b)

**Figure 5.13 Post-Mortem Photography of 3D-S-93x3-5 (227-m/s Striking Velocity):  
(a) Front Face, (b) Rear Face**

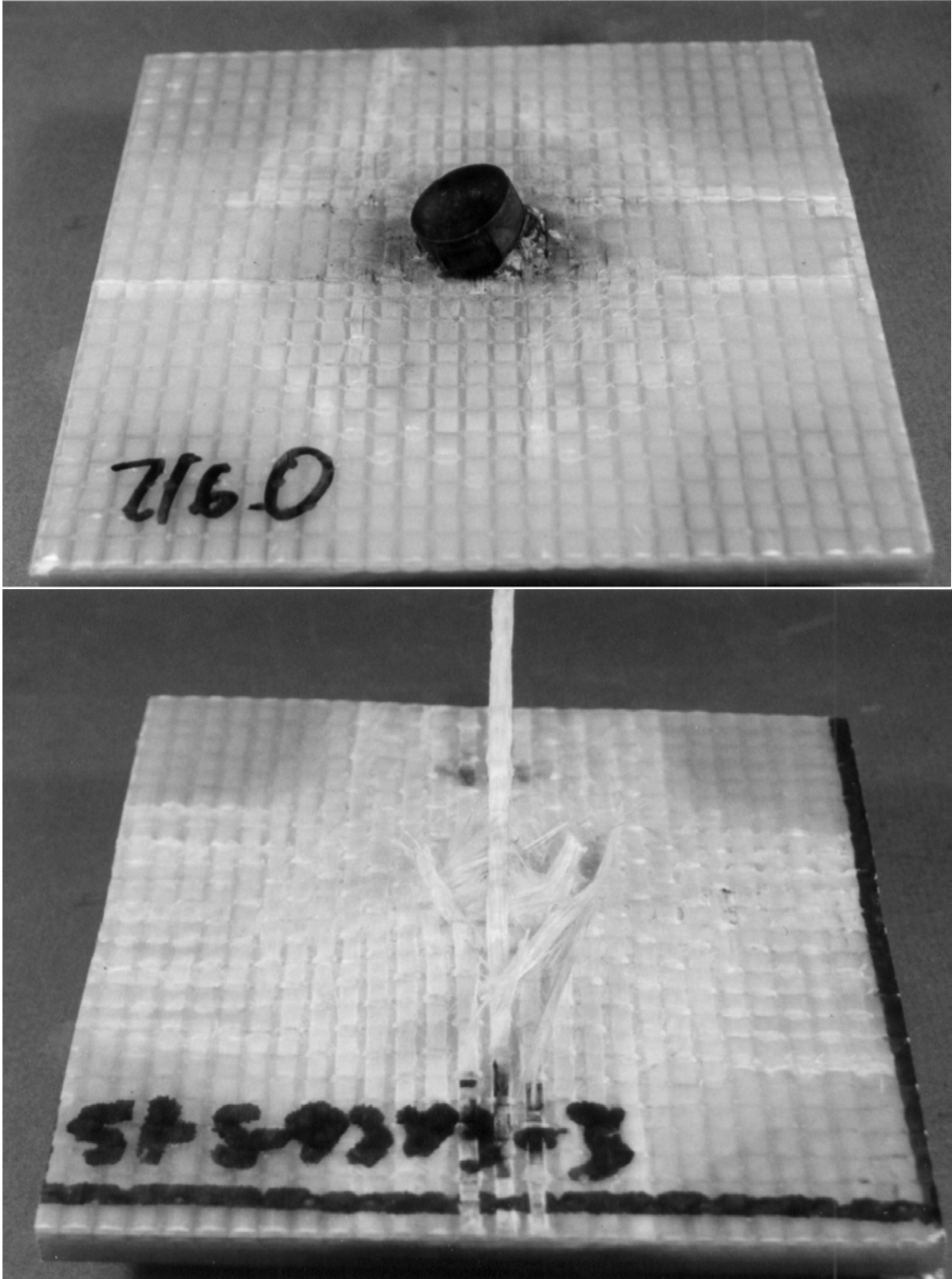


**Figure 5.14 Oblique Views of 3D-S-93x3-5: (a) Front Face, (b) Rear Face**

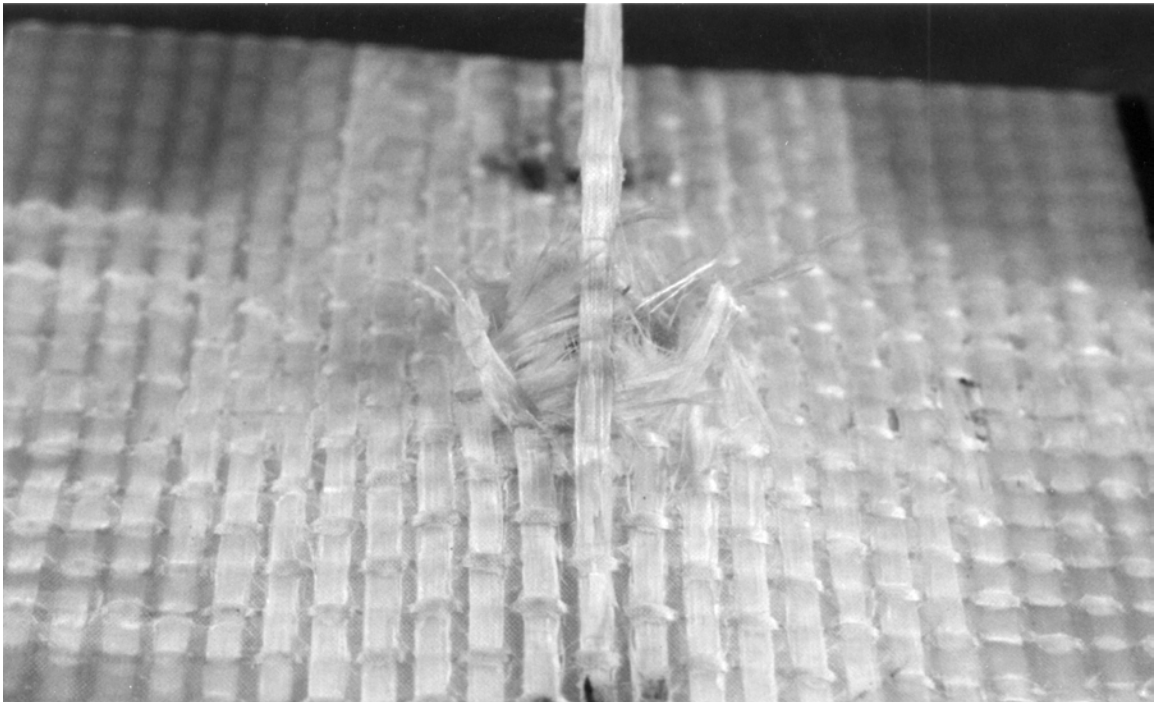
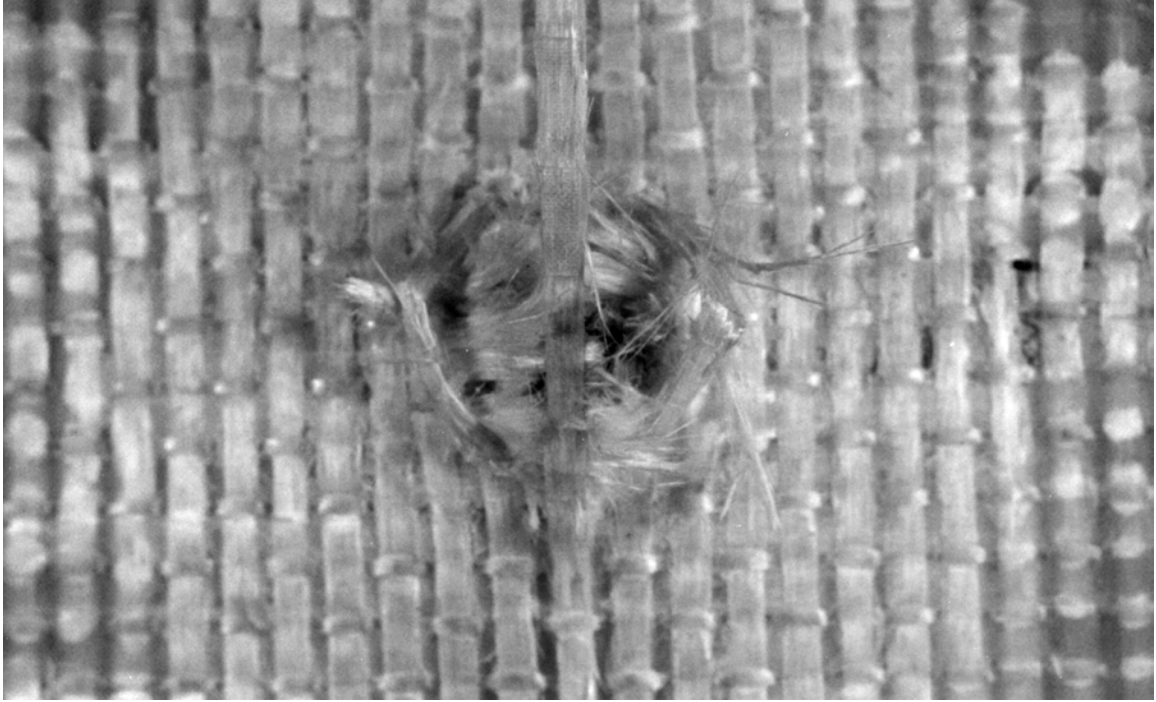
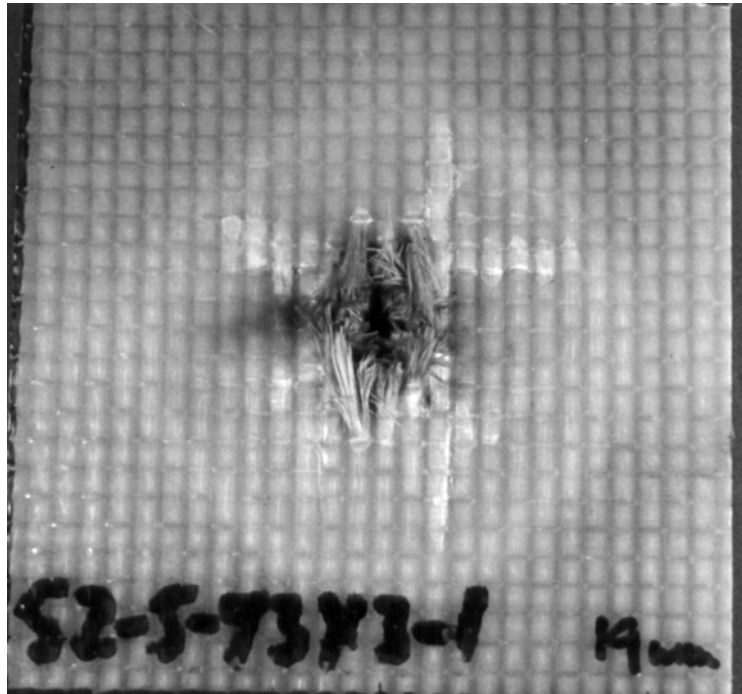
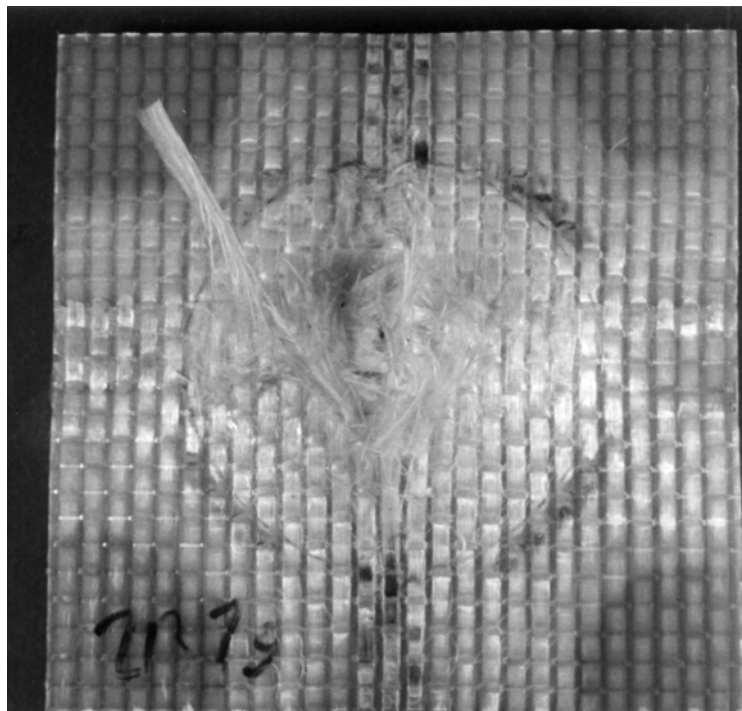


**Figure 5.15 Closer Views of Rear Target Face (3D-S-93x3-5)**



(a)

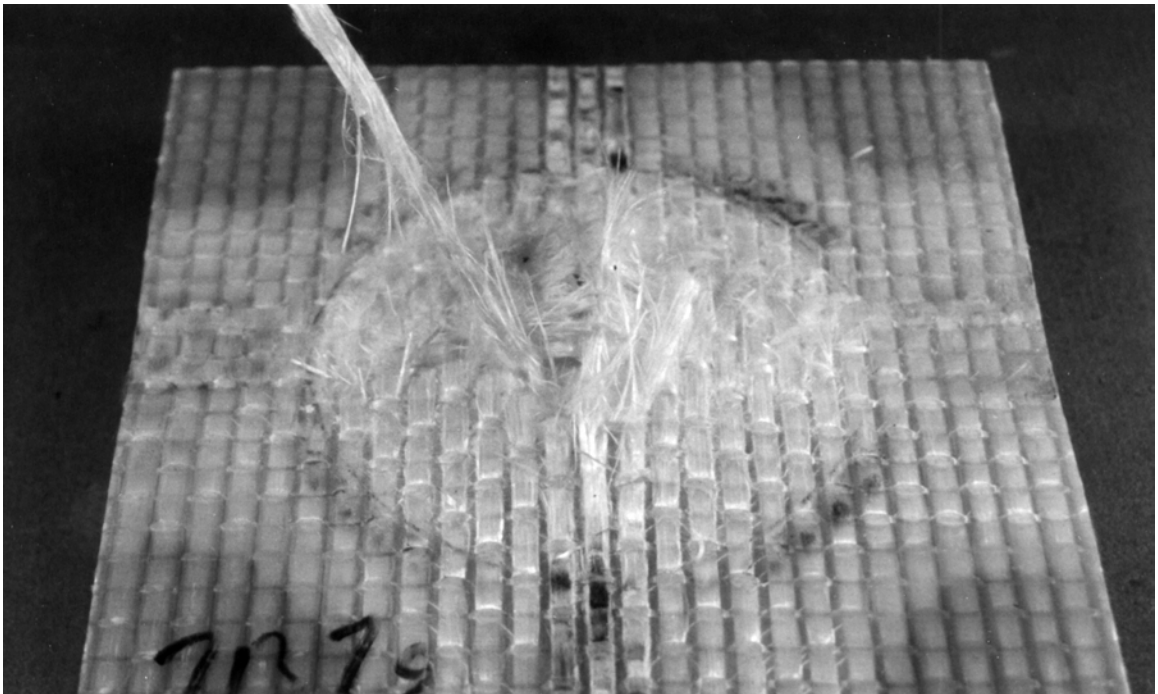


(b)

**Figure 5.16 Post-Mortem Photography of 3D-S-93x3-6 (508-m/s Striking Velocity):  
(a) Front Face, (b) Rear Face**



(a)



(b)

Figure 5.17 Oblique Views of 3D-S-93x3-6: (a) Front Face, (b) Rear Face

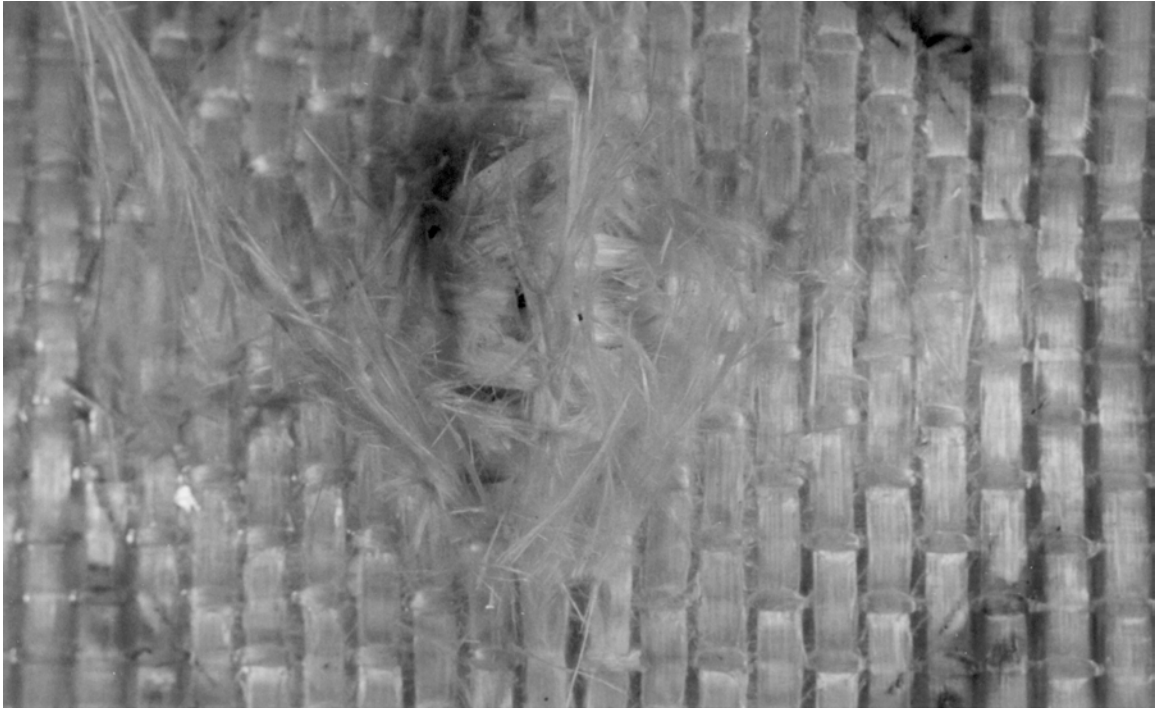


**Figure 5.18** Closer View of Rear Target Face (*3D-S-93x3-6*)

## 6. SUMMARY

The effects of the geometry of fabric reinforcement on resistance to perforation, progression of damage, and failure mechanisms in composite systems subjected to transverse impact at velocities ranging from quasi-static to ballistic regimes were investigated. Quantitative and qualitative comparisons were made, resulting in a better understanding of the complex behavior of these systems. Unique failure mechanisms were identified, energy dissipation was measured, and damage progression was characterized.

### 6.1 Failure Mechanisms

Failure mechanisms common to all of the systems under investigation, and at all impact velocities, included delamination (or fiber-debonding) and matrix cracking. This type of failure has been widely reported in the literature; however, new and unique modes of damage and failure for the 3D monolithic and 3D laminated composites were observed in this study. Extensive straining of the  $z$ -reinforcement of 3D orthogonal weaves was noted. In many cases, these tows were fractured. In addition, surface weft tows were frequently *pulled through* unbroken crimp of the  $z$ -tows. The frictional sliding of surface weft through  $z$ -crimps constitutes a new and significant mode of energy dissipation. It also suggests that manipulation of the relative properties of the in-plane and out-of-plane reinforcements can provide a means of controlling failure evolution in these systems.

## **6.2 Energy Dissipation**

The dissipation of energy for high-velocity impact and quasi-static perforation was comparable. Although a more precise comparison would require more data, the punch work measured under quasi-static perforation was consistent with the ballistic limits estimated from the high-velocity experiments. Based strictly upon the limited high-velocity data presented in this report, higher energy dissipation is expected at high velocities in comparison with quasi-static perforation. The cumulative energy dissipated under repeated low-velocity impacts was also consistent with other impact velocity regimes. In all experiments, the thick 3D monolithic systems performed the poorest. Raw measurements of energy dissipation typically showed comparable performance of the 2D and 3D laminates; however, normalization by target areal density revealed that the 3D laminates exhibited greater amount of perforation resistance and capacity for energy absorption.

## **6.3 Damage Progression**

Progression of damage was monitored under quasi-static and low-velocity impact. Backlighting of composite panels provided a new way to monitor internal damage progression in GFRP systems. For the quasi-static experiments, digital video was used in conjunction with backlighting and synchronized with the load-displacement data. Photography of specimens impacted once, five times, and after perforation, was used with both reflective lighting and backlighting. The photographs revealed extensive

internal delamination and fiber-debonding that could not be seen under reflective lighting.

#### **6.4 Conclusion**

Quasi-static and dynamic experiments were conducted on carbon/epoxy composites to investigate how porosity, fiber-volume fraction, and areal density affect mechanical response of 3D woven composites for different velocity regimes and loading conditions. The results of this investigation indicate that matrix-cellularization results in significant weight reduction, while structural performance and durability are maintained and energy is dissipated.

The effects of fabric architecture in GFRP composite systems with comparable areal density, thickness, and fiber-volume-fraction on perforation resistance, strength, and distributions of energy dissipation of panels subjected to quasi-static perforation were investigated. The penetration load was recorded and a novel view of internal damage progression was obtained by backlit videography. Matrix cracking, delamination or fiber debonding, and fiber fracture were observed in all systems. Damage mechanisms unique to the 3D systems included the straining and fracture of *z*-reinforcement tows. The radial spread of damage was larger for the 3D systems than for the 2D laminates, and fiber debonding of the 3D systems extended to the edges of the test panel. The strength and capacity to absorb energy were comparable for the 2D and 3D laminates and superior to the 3D monolith. This is attributed to the damage mechanisms unique to these geometries, involving the *z*-crimps; the introduction of two planes through the thickness,

which break z-reinforcement in the 3D laminates, increased the number of z-crimps by a factor of three.

Another part of the investigation examined how variation of the fabric architecture in composite systems affects perforation resistance, strength, and damage mechanisms of composite panels subjected to repeated low-velocity impact. Again, distinctive modes of failure for the various material systems were observed. Matrix cracking, delamination or debonding, and fiber fracture were dominant in all systems, but the unique damage mechanisms of the 3D systems, included the straining and fracture of z-tows, acted as additional means of energy absorption. As in the case of quasi-static perforation, the radial spread of damage was larger for the 3D systems than for the 2D laminates. After the occurrence of perforation, debonding of the 3D systems often extended to the edges of the test panel. The 3D systems survived more strikes and absorbed more total energy than the 2D laminates. This is attributed to the damage mechanisms unique to these reinforcement geometries. The tendency of the 3D orthogonal weaves to spread damage over a larger area is mainly due to the straightness of the fiber bundles.

The influence of fabric architecture on perforation-resistance, strength, and distributions of energy dissipation of composite panels subjected to high-velocity impact. Small differences in energy absorption were observed; however, the present results indicate that the ballistic limits of the 2D and 3D laminates, comparable to each other, are significantly higher than the ballistic limit of the 3D monolith. Failure modes for all systems included matrix-cracking, delamination or fiber-debonding, and fiber fracture.

For each of the three striking velocities, the radial expansion of damage was smallest for the 2D laminate and largest for the 3D monolith. Post-mortem analyses revealed additional energy absorption mechanisms, which involved the crimped portion of *z*-tows in the 3D composites. Damage mechanisms unique to the 3D systems included the straining and fracture of *z*-tows, as well as the sliding of surface weft through unbroken *z*-crimps on the rear target face. The strength and capacity to absorb energy under high-velocity transverse puncture were comparable for the 2D and 3D laminates but superior to the 3D monolith.

The 3D orthogonally woven fabric-reinforced composite monoliths and laminates exhibited unique modes of energy dissipation, involving the rear surface weft and the crimp of the *z*-tows on that face. These modes were observed at all velocity regimes examined (Figure 6.1). Modification of the properties of *z*-reinforcement (modulus, ductility, lubricity, tensile strength, *etc.*) should significantly influence the perforation resistance of the 3D composite systems.

The specific strength of fiber-reinforced polymer composite systems is in many cases superior to that of engineering metals and alloys. This report has provided a comparison of the behavior of composite plates with different geometries of fabric reinforcement and under various rates of transverse impact loading. Although the capacity for energy absorption did not vary dramatically, significant advantages of cellularization and lamination of 3D orthogonally woven fabric-reinforced composites were inferred. More studies are needed to develop and exploit the unique features of these systems.

**6.5 Figures**  
**(Chapter 6)**

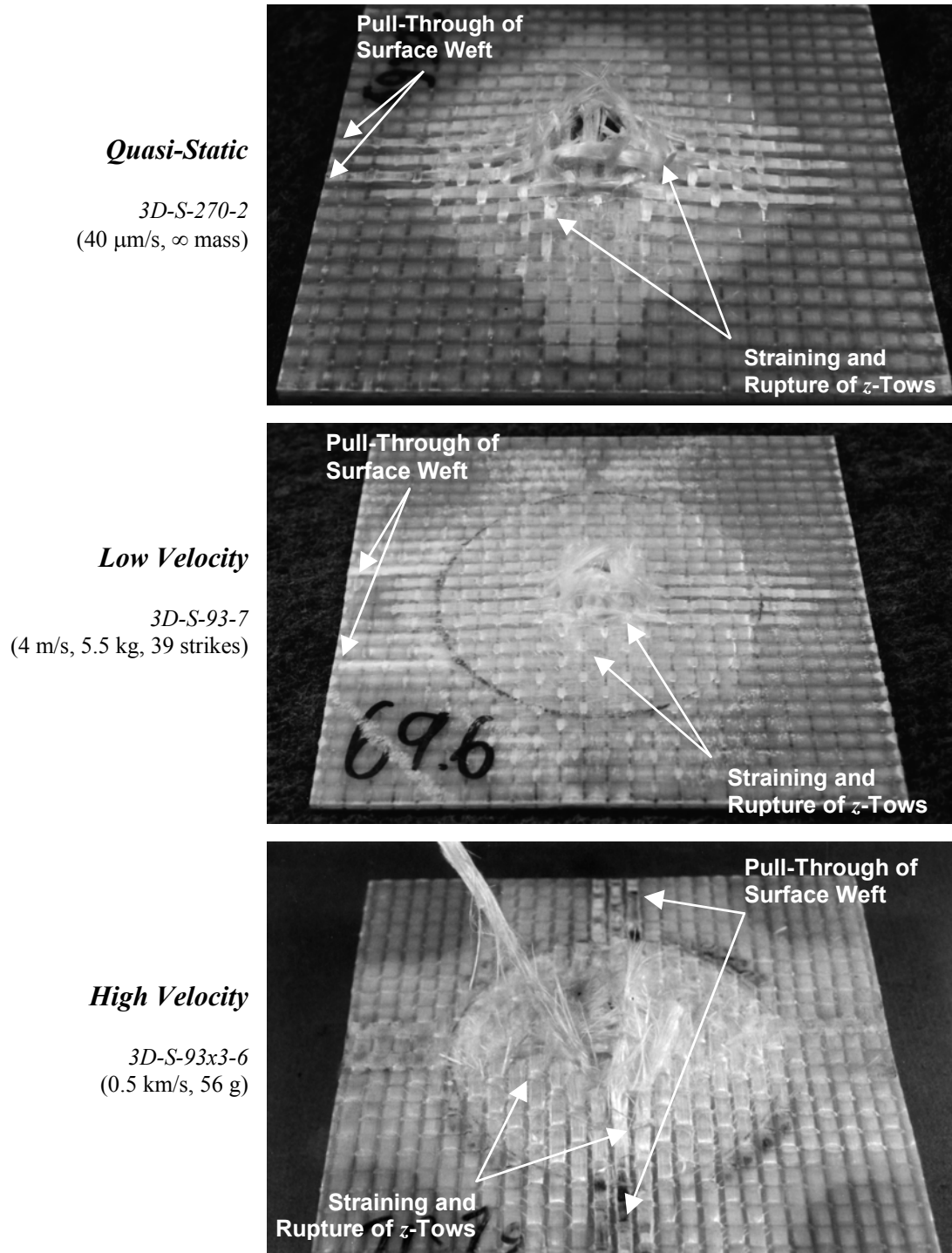


**Figure 6.1 Damage Mechanisms, Unique to 3D Orthogonally Woven Composites, Evident over a Wide Range of Penetration Velocities and for both 3D Monoliths and Laminates**

## 7. RECOMMENDATIONS FOR FUTURE STUDIES

One of the unfortunate limitations of many endeavors in the experimental study of composite materials is in the amount of available material. Such was the case in this investigation. Fortunately, this leaves room for a large number of future studies, as more material becomes available. Some recommendations for future study are enumerated below.

1. Precise determination of the ballistic limit of the composite systems examined in this report could verify the relationship of quasi-static, low-velocity, and ballistic perforation energies.
2. Variation of the size and geometry of the penetrator could determine the importance of these parameters and potentially reveal new damage mechanisms.
3. Significant benefits of the lamination of 3D reinforcement came to light in this investigation. A more detailed comparison of the effects of lamination of 2D and 3D systems should provide greater insight in the design trade-offs involving these systems.
4. Examination of the behavior of hybridized 2D/3D laminates may result in material systems with improved properties in comparison with strictly 2D or 3D laminates. A 3D orthogonal-weave face-layer has the potential to spread over a larger area the impact load onto a 2D plain-weave laminate backing.

## 8. LIST OF REFERENCES

- Allix, O. (2001). "A Composite Damage Meso-Model for Impact Problems." Composites Science and Technology **61**: 2193-2205.
- Anastasi, R. F. and C. Lopatin (2001). Application of a Fiber Optic Distributed Strain Sensor System to Woven E-Glass Composite. Hampton VA, NASA Langley Research Institute, Army Research Laboratory: 19.
- Azouaoui, K., S. Rechak, Z. Azari, S. Benmedakhene, A. Laksimi and G. Pluinage (2001). "Modelling of Damage and Failure of Glass/Epoxy Composite Plates Subject to Impact Fatigue." International Journal of Fatigue **23**: 877-885.
- Backman, M. E. and W. Goldsmith (1978). "The Mechanics of Penetration of Projectiles into Targets." International Journal of Engineering Science **16**: 1-99.
- Balasundharam, S. H. P. (1999). Ballistic Behavior of 3-D Fabrics. Master of Science. Textile Engineering and Science, North Carolina State University. Raleigh, NC.
- Baucom, J. N. (1999). Design Guidelines for Functionally Tailored Systems: Energy Absorption and Dissipation Mechanisms. ARO/MURI Interim Report 1999, Edgewood, MD.
- Baucom, J. N., M. A. Zikry and Y. Qiu (2000). Control of Failure Evolution in 3d Cellular Woven Composite Systems. ASME International Mechanical Engineering Congress and Exposition 2000, Orlando, FL, ASME.
- Baucom, J. N., M. A. Zikry and Y. Behai-El-Din (2001). Impact-Induced Damage Progression in 2-D and 3-D Woven Composite Systems. ASME International Mechanical Engineering Congress and Exposition 2001, New York, NY.
- Belingardi, G. and R. Vadori (2002). "Low Velocity Impact Tests of Laminate Glass-Fiber-Epoxy Matrix Composite Material Plates." International Journal of Impact Engineering **27**: 213-229.
- Bodner, S. R. and A. M. Rajendran (1997). Application of an Analytical Model for Ballistic Penetration to Composite Targets. Aberdeen Proving Ground, MD, Army Research Laboratory: 38.
- Bogdanovich, A. E. and K. Friedrich (1994). "Initial and Progressive Failure Analysis of Laminated Composite Structures under Dynamic Loading." Composite Structures **27**: 439-456.

- Bogdanovich, A. E. and R. L. Sierakowski (1999). "Composite Materials and Structures: Science, Technology and Applications - a Compendium of Books, Review Papers, and Other Sources of Information." Applied Mechanics Review **52**(12): 351-365.
- Cantwell, W., P. Curtis and J. Morton (1983). "Post-Impact Fatigue Performance of Carbon Fibre Laminates with Non-Woven and Mixed-Woven Layers." Composites **14**(3): 301-305.
- Cate, J. E. (1993). Impact Testing of Composite Laminates. Master of Science Thesis. Department of Mechanical and Aerospace Engineering, North Carolina State University. Raleigh, NC.
- Cheremisinoff, N. P. and P. N. Cheremisinoff (1995). Fiberglass Reinforced Plastics. New Jersey, Noyes Publications.
- Childers, B. A., M. E. Froggatt, S. G. Allison, T. C. Moore, Sr., D. A. Hare, C. F. Batten and D. C. Jegley (2001). Use of 3000 Bragg Grating Strain Sensors Distributed on Four Eight-Meter Optical Fibers During Static Load Tests of a Composite Structure. SPIE's 8th International Symposium on Smart Structures and Materials, Newport Beach, CA.
- Chocron-Benloulo, I. S., J. Rodríguez, M. A. Martínez and V. S. Gálvez (1997). "Dynamic Tensile Testing of Aramid and Polyethylene Fiber Composites." International Journal of Impact Engineering **19**(2): 135-146.
- Cox, B. N. (1995). Failure Models for Textile Composites. Hampton, VA, Langley Research Center, NASA: 142.
- Cox, B. N. and G. Flanagan (1997). Handbook of Analytical Methods for Textile Composites. Hampton, VA, Langley Research Center, NASA.
- Cunniff, P. M. (1992). "An Analysis of the System Effects in Woven Fabrics under Ballistic Impact." Textile Research Journal **62**(9): 495-509.
- Cunniff, P. M. (1996). "A Semiempirical Model for the Ballistic Impact Performance of Textile Based Personnel Armor." Textile Research Journal **66**(1): 45-59.
- Daniel, I. M., T.-W. Chou and P. Popper (1992). "Quantitative Porosity Characterization of Composite Materials by Means of Ultrasonic Attenuation Measurements." Journal of Nondestructive Evaluation **11**(1): 1-8.
- Davies, G. A. O., D. Hitchings and G. Zhou (1996). "Impact Damage and Residual Strengths of Woven Fabric Glass/Polyester Laminates." Composites, Part A: applied science and manufacturing **27A**: 1147-1156.

- Ellis, R. L., F. Lalande, H. Jia and C. A. Rogers (1998). "Ballistic Impact Resistance of Sma and Spectra Hybrid Composites." Journal of Reinforced Plastics and Composites **17**(2): 147-164.
- Espinosa, H. D., S. Dwivedi and H.-C. Lu (2000). "Modeling Impact Induced Delamination of Woven Fiber Reinforced Composites with Contact/Cohesive Laws." Computer methods in applied mechanics and engineering **183**: 259-290.
- Evans, A. G. and F. W. Zok (1994). "Review: The Physics and Mechanics of Fibre-Reinforced Brittle Matrix Composites." Journal of Materials Science **29**: 3857-3896.
- Flanagan, M. P. (1997). An Experimental Investigation of High Velocity Impact and Penetration Failure Modes in Textile Composites. Master of Science Thesis. Department of Mechanical and Aerospace Engineering, North Carolina State University. Raleigh, NC.
- Flanagan, M. P., M. A. Zikry, J. W. Wall and A. El-Shiekh (1999). "An Experimental Investigation of High Velocity Impact and Penetration Failure Modes in Textile Composites." Journal of Composite Materials **33**(12): 1080-1103.
- Fujii, K., M. Aoki, N. Kiuchi and E. Yasuda (2001, article accepted for publication). "Impact Perforation Behavior of Cfrps Using High-Velocity Steel Sphere." International Journal of Impact Engineering.
- Gellert, E. P., S. D. Pattie and R. L. Woodward (1998). "Energy Transfer in Ballistic Perforation of Fibre Reinforced Composites." Journal of Materials Science **33**: 1845-1850.
- Gellert, E. P., S. J. Cimpoeru and R. L. Woodward (2000). "A Study of the Effect of Target Thickness on the Ballistic Perforation of Glass-Fibre-Reinforced Plastic Composites." International Journal of Impact Engineering **24**: 445-456.
- Guo, N. and P. Cawley (1994). "The Non-Destructive Assessment of Porosity in Composite Repairs." Composites **25**(9): 842-850.
- Jang, B. Z., L. C. Chen, L. R. Hwang, J. E. Hawkes and R. H. Zee (1990). "The Response of Fibrous Composites to Impact Loading." Polymer Composites **11**(3): 144-157.
- Jenq, S. T. and J. J. Mo (1996). "Ballistic Impact Response of Two-Step Braided Three-Dimensional Textile Composites." AIAA Journal **34**(2): 375-384.
- Jenq, S. T., J. T. Kuo and L. T. Sheu (1998). "Ballistic Impact Response of 3-D Four-Step Braided Glass/Epoxy Composites." Key Engineering Materials **141-143**: 349-366.

- Kammerer, C. and A. Neme (1998). "Plane Behaviour at High Strain Rates of a Quasi-Unidirectional E-Glass/Polyester Composite: Application to Ballistic Impacts." European Journal of Mechanics, A/Solids **17**(3): 461-477.
- Khan, A. S., O. U. Colak and P. Centala (2001, accepted for publication). "Compressive Failure Strengths and Modes of Woven S2-Glass Reinforced Polyester Due to Quasi-Static and Dynamic Loading." International Journal of Plasticity.
- Kim, J.-K., M.-L. Sham, M.-S. Sohn and H. Hamada (2001). "Effect of Hybrid Layers with Different Silane Coupling Agents on Impact Response of Glass Fabric Reinforced Vinylester Matrix Composites." Polymer **42**: 7455-7460.
- Kumar, K. S. and T. B. Bhat (1998). "Response of Composite Laminates on Impact of High Velocity Projectiles." Key Engineering Materials **141-143**: 337-348.
- Kuo, W.-S. and L.-C. Lee (1999). "Elastic and Damage Behavior of Three-Dimensional Woven Composites Incorporating Solid Rods." Composites, Part A: applied science and manufacturing **30**: 1135-1148.
- Lee, S. M. and P. Zahuta (1991). "Instrumented Impact and Static Indentation of Composites." Journal of Composite Materials **25**(2): 204-222.
- Lee, S.-W. R. and C. T. Sun (1993). "A Quasi-Static Penetration Model for Composite Laminates." Journal of Composite Materials **27**(3): 251-271.
- Liu, D., B. B. Raju and X. Dang (1998). "Size Effects on Impact Response of Composite Laminates." International Journal of Impact Engineering **21**(10): 837-854.
- Liu, D., B. B. Raju and X. Dang (2000). "Impact Perforation Resistance of Laminated and Assembled Composite Plates." International Journal of Impact Engineering **24**: 733-746.
- Luo, R. K., E. R. Green and C. J. Morrison (2001). "An Approach to Evaluate the Impact Damage Initiation and Propagation in Composite Plates." Composites, Part B: engineering **32**: 513-520.
- Mahfuz, H., M. Saha, R. Biggs and S. Jeelani (1998). "Damage Tolerance of Resin-Infiltrated Composites under Low Velocity Impact - Experimental and Numerical Studies." Key Engineering Materials **141-143**: 209-234.
- Mahfuz, H., Y. Zhu, A. Haque, A. Abutalib, U. Vaidya, S. Jeelani, B. Gama, J. Gillespie and B. Fink (2000). "Investigation of High-Velocity Impact on Integral Armor Using Finite Element Method." International Journal of Impact Engineering **24**: 203-217.

- Mili, F. and B. Necib (2001). "Impact Behavior of Cross-Ply Laminated Composite Plates under Low Velocities." Composite Structures **2001**: 237-244.
- Mines, R. A. W., C. M. Worrall and A. G. Gibson (1998). "Low Velocity Perforation Behaviour of Polymer Composite Sandwich Panels." International Journal of Impact Engineering **21**(10): 855-879.
- Mines, R. A. W., A. M. Roach and N. Jones (1999). "High Velocity Perforation Behaviour of Polymer Composite Laminates." International Journal of Impact Engineering **22**: 561-588.
- Morye, S. S., P. J. Hine, R. A. Duckett, D. J. Carr and I. M. Ward (2000). "Modelling of the Energy Absorption by Polymer Composites Upon Ballistic Impact." Composites Science and Technology **60**: 2631-2642.
- Mouritz, A. P. and I. M. Hutchings (1992). "Compressive Failure of Silica-Filled Epoxy Resins: Influence of Matrix Strength, Interfacial Bond Strength and Porosity." Journal of Materials Science Letters **11**: 1100-1103.
- Mouritz, A. P. (2001). "Ballistic Impact Response and Explosive Blast Resistance of Stitched Composites." Composites, Part B: engineering **32**: 431-439.
- Naik, N. K. and Y. C. Sekher (1998). "Damage in Laminated Composites Due to Low Velocity Impact." Journal of Reinforced Plastics and Composites **17**(14): 1232-1263.
- Navarro, C. (1998). "Simplified Modelling of the Ballistic Behaviour of Fabrics and Fibre-Reinforced Polymeric Matrix Composites." Key Engineering Materials **141-143**: 383-400.
- O'Donnell, R. G. (1993). "Deformation Energy of Kevlar Backing Plates for Ceramic Armours." Journal of Materials Science Letters **12**: 1485-1486.
- Okafor, A. C., A. W. Otieno, A. Dutta and V. S. Rao (2001). "Detection and Characterization of High-Velocity Impact Damage in Advanced Composite Plates Using Multi-Sensing Techniques." Composite Structures **54**: 289-297.
- Olsson, R. (2001). "Analytical Prediction of Large Mass Impact Damage in Composite Laminates." Composites, Part A: applied science and manufacturing **32**: 1207-1215.
- Peters, E. C., F. Svek and J. M. J. Fréchet (1997). "Preparation of Large-Diameter 'Molded' Porous Polymer Monoliths and Control of Pore Structure Homogeneity." Chemistry of Materials **9**: 1898-1902.

- Peters, P. W. M., E. Martin and P. Pluvinage (1995). "Influence of Porosity and Fibre Coating on Engineering Moduli of Fibre-Reinforced Ceramics." Composites **26**: 108-114.
- Portanova, M. A. (1995). Evaluation of the Impact Response of Textile Composites. Hampton, VA, Langley Research Center, NASA: 1-53.
- Qiu, Y., W. Xu, Y. Wang, M. A. Zikry and M. H. Mohamed (2001). "Fabrication and Characterization of Three-Dimensional Cellular-Matrix Composites Reinforced with Woven Carbon Fabric." Composites Science and Technology **61**: 2425-2435.
- Schoeppner, G. A. and S. Abrate (2000). "Delamination Threshold Loads for Low Velocity Impact on Composite Laminates." Composites, Part A: applied science and manufacturing **31**: 903-915.
- Schonberg, W. P. (1998). "Using Composite Materials to Protect Spacecraft against Orbital Debris Impact Damage." Key Engineering Materials **141-143**: 573-584.
- Seale, M. D., B. T. Smith, W. H. Prosser and J. E. Masters (1994). "Lamb Wave Response of Fatigued Composite Samples." Review of Progress in Quantitative Nondestructive Evaluation **13B**: 1261-1266.
- Shen, W. Q. (1997). "Dynamic Response of Rectangular Plates under Drop Mass Impact." International Journal of Impact Engineering **19**(3): 207-229.
- Singletary, J. and A. E. Bogdanovich (2000). "3-D Orthogonal Woven Soft Body Armor." Journal of Industrial Textiles **29**(4): 287-305.
- Sirkis, J. S. and C. C. Chang (1998). Embedded Fiber-Optic Strain Sensors. Manual on Experimental Methods for Mechanical Testing of Composites. C. H. Jenkins. Lilburn, GA, The Fairmont Press: 63-84.
- Sun, C. T. and S. V. Potti (1996). "A Simple Model to Predict Residual Velocities of Thick Composite Laminates Subjected to High Velocity Impact." International Journal of Impact Engineering **18**(3): 339-353.
- Tarim, N., F. Findik and H. Uzun (2002). "Ballistic Impact Performance of Composite Structures." Composite Structures **56**: 13-20.
- Taylor, W. J., Jr. and J. R. Vinson (1990). "On the Behavior of Ballistic Impact into Flexible Protection Systems." AIAA Journal **28**(12): 2098-2103.
- Vinson, J. R. and J. A. Zukas (1975). "On the Ballistic Impact of Textile Body Armor." Journal of Applied Mechanics **42**: 263-268.

- Vinson, J. R. and J. M. Walker (1997). "Ballistic Impact of Thin-Walled Composite Structures." AIAA Journal **35**(5): 875-878.
- Walker, L., M.-S. Sohn and X.-Z. Hu (2002, accepted for publication). "Improving Impact Resistance of Carbon-Fibre Composites through Interlaminar Reinforcement." Composites, Part A: applied science and manufacturing.
- Walsh, T. F., B. L. Lee and J. W. Song (1998). "Penetration Failure of Spectra Polyethylene Fiber-Reinforced Ballistic-Grade Composites." Key Engineering Materials **141-143**: 367-382.
- Wu, E. and J. Wang (1995). "Behavior of Stitched Laminates under in-Plane Tensile and Transverse Impact Loading." Journal of Composite Materials **29**(17): 2254-2279.
- Xu, W. (2000). Development and Analysis of Three-Dimensionally Reinforced Cellular Matrix Composites. Doctor of Philosophy Dissertation. Fiber and Polymer Science, North Carolina State University. Raleigh, NC.
- Ying, Y. (1998). "Analysis of Impact Threshold Energy for Carbon Fibre and Fabric Reinforced Composites." Journal of Reinforced Plastics and Composites **17**(12): 1056-1075.
- Zee, R. H. and C. Y. Hsieh (1993). "Energy Loss Partitioning During Ballistic Impact of Polymer Composites." Polymer Composites **14**(3): 265-271.
- Zhou, G. (1998). "Damage Resistance and Tolerance in Thick Laminated Composite Plates Subjected to Low-Velocity Impact." Key Engineering Materials **141-143**: 305-334.
- Zhu, G., W. Goldsmith and C. K. H. Dharan (1992). "Penetration of Laminated Kevlar by Projectiles - I. Experimental Investigation." International Journal of Solids and Structures **29**(4): 399-420.